UNIVERSITY OF SOUTHAMPTON

FACULTY OF ENGINEERING AND THE ENVIRONMENT

national Centre for Advanced Tribology at Southampton

Microstructural and Nanomechanical Characterisation of Ni-Ti(-Cu) Shape Memory Alloy Thin Films for Tribology

by

Mauro Callisti

Thesis for the degree of Doctor of Philosophy

October 2014

UNIVERSITY OF SOUTHAMPTON

ABSTRACT

FACULTY OF ENGINEERING AND THE ENVIRONMENT

Doctor of Philosophy

MICROSTRUCTURAL AND NANOMECHANICAL CHARACTERISATION OF Ni-Ti(-Cu) SHAPE MEMORY ALLOY THIN FILMS FOR TRIBOLOGY

Mauro Callisti

Protective and functional coatings have been undergoing development for decades and further improvement to their mechanical and tribological properties are more and more challenging. Nowadays most research is aimed at improving the tribological behaviour of hard and functional coatings through the optimisation of their microstructure on the nanoscale. Over time significant breakthroughs have been achieved, however improving material performance is becoming harder. Combining different layers is another possible way of improving the tribological performance of functional coatings. The use of bonding layers can mitigate the differences in mechanical and thermal properties between coating and substrate and might change the behaviour of the coating system in a tribological scenario. As a consequence, the nature of this bonding interlayer plays an important role in the response of the coatings to the complex stress conditions taking place in a tribological system. Among the possible interlayer candidates a layer with the capability of accommodating large deformation, thus protecting the substrate from plastic deformation as well as improving the adhesion of the top layer to the substrate, could represent a suitable choice. One of the potential classes of materials satisfying the above requirements are the Ni-Ti based alloys which are known to exhibit superelastic properties also when sputter deposited.

In this study we first focus our investigation on the characterisation of sputter-deposited Ni-Ti based thin films. In particular, the Ni-Ti system is doped by a third element, Cu through which mechanical and microstructural properties can be changed

without detrimental effects on the typical functional properties of Ni-Ti alloys. The effects of Cu, in the range 0 – 20 at.%, and of the post-deposition heat treatments, with particular regard to annealing temperature, on mechanical and microstructural properties of sputter-deposited Ni-Ti(-Cu) thin films are investigated by nanoindentation, X-ray diffraction and transmission electron microscopy.

Based on the objective of using Ni-Ti(-Cu) thin films as the interlayer in tribological coatings, some of the Ni-Ti(-Cu) films are selected and integrated in a bilayer design. Among the tribological coatings self-lubricant W-S-C coatings are known for their excellent non-Amonton frictional behaviour with friction decreasing with increasing contact pressure. The low friction of W-S-C coatings is associated with the formation of a WS_2 tribolayer on the sliding surface. When the basal plane of the WS_2 tribolayer is aligned with the sliding direction, the friction coefficient drops to very low values owing to the weak bonding between chalcogenide atomic planes. The formation of the low-shear surface layer is directly related to contact pressure; therefore, a W-S-C coating is an ideal functional layer with which to study the effect of Ni-Ti(-Cu) interlayers on sliding properties.

W-S-C/Ni-Ti(-Cu) bilayer coatings are fabricated following a three-step process consisting of deposition and annealing of the Ni-Ti(-Cu) layers and subsequent deposition of the top functional layer. Mechanical and nano-scratch behaviour of these bilayers is investigated in order to study the functional role of different Ni-Ti(-Cu) interlayers on the response of the bilayers to nanoindentation and nano-scratch tests.

The tribological performance of W-S-C single layer and selected W-S-C/Ni-Ti(-Cu) bilayers are investigated by sliding tests in humid air under different test conditions in order to assess the potential beneficial effects of the interlayer on the tribological properties of W-S-C. Correlation between the tribological properties measured and microstructural changes induced by sliding is achieved by investigating the tested coatings by focused ion beam and transmission electron microscopy. Chemical changes on the sliding surfaces are also investigated by Raman spectroscopy in order to highlight possible differences in the tribolayer formation under different test conditions and for different Ni-Ti(-Cu) interlayers. The study is also aimed at understanding how the stress-induced martensitic transformation is activated in the interlayers during sliding.

TABLE OF CONTENTS

Declaration of authorship

Acknowledgements

List of symbols

Chapter 1: Shape memory alloy thin films 1

1. Introduction to Shape Memory Alloys 2
   1.1 Crystallography of martensitic transformation 3
   1.2 Thermodynamic perspective of martensitic transformation 5
   1.3 Superelastic and Shape Memory effects 8
2. Ni-Ti based thin films 11
   2.1 Ni-Ti(-Cu) thin films 12
   2.2 Fabrication process 14
   2.3 Crystallisation behaviour 16
   2.4 Microstructural properties of sputter-deposited Ni-Ti(-Cu) thin films 21
      2.4.1 Effects of annealing temperatures on the microstructure 21
3. Mechanical properties of Ni-Ti(-Cu) thin films 30
   3.1 Nanoindentation 31
   3.2 Nanoindentation of Ni-Ti(-Cu) thin films 33
4. Tribological properties and applications 47
5. Transition metal dichalcogenides coatings 54
   5.1 W-S-C coatings 57
      5.1.1 Deposition and microstructure 57
      5.1.2 Mechanical properties 60
      5.1.3 Tribological properties 63
6. Scope of the present research 71
7. Current approach and structure of the thesis 73

References 75
Appendix A 86

Chapter 2: Experimental methods and procedures 105

2.1 Chapter summary 105
2.2 Plasma-assisted Middle-Frequency Dual Magnetron Sputtering System 105
2.2.1 Calibration of the Ni-Ti(-Cu) deposition processes 105
2.2.2 Phase transformation in the binary Ni-Ti thin film 105
2.3 Post-deposition heat treatments 112
2.4 Microstructural and chemical characterisation 113
2.4.1 X-ray based techniques 113
2.4.2 Electron Microscopy 114
2.4.3 Microanalysis in TEM 118
2.4.4 (S)TEM samples preparation 119
2.5 Nanomechanical characterisation: Nanoindentation and Nano-scratch 120
2.6 Tribological characterisation 124

References 127

Chapter 3: Microstructure and mechanical properties of Ni-Ti(-Cu) thin films 128

3.1 Chapter summary 128
3.2 Coatings chemical composition and surface morphology 129
3.3 Structure 130
3.3.1 X-ray diffraction analysis 132
3.3.2 Transmission electron microscopy 135
3.4 Mechanical properties versus microstructure 145

References 152

Chapter 4: Grain refinement in Cu-doped Ni-Ti thin films 154

4.1 Chapter summary 154
4.2 Results and discussion 155

References 162

Chapter 5: Mechanical properties and nano-scratch behaviour of W-S-C/Ni-Ti(-Cu) bilayers 163

5.1 Chapter summary 163
5.2 Coatings composition 164
5.3 Microstructure 165
5.4 Mechanical properties 169
5.4.1 Nanoindentation 169
5.4.2 Nano-scratch 177

References 185
Appendix B 187

Chapter 6: Ni-Ti-Cu interlayers supporting low-friction functional coatings 189

6.1 Chapter summary 189
6.2 Coatings microstructure 190
6.3 Mechanical properties 195
6.4 Microstructural changes induced by sliding 197
6.5 Effects of the interlayer on the performance of W-S-C solid lubricant coating 202
6.6 Deformation of the W-S-C functional layer 207

References 209

Chapter 7: Conclusions and Future work 211

1. Conclusions 211
2. Suggestions for future work 216

Publications 221

DECLARATION OF AUTHORSHIP

I, Mauro Callisti, declare that this thesis and the work presented in it are my own and has been generated by me as the result of my own original research.

Microstructural and Nanomechanical Characterisation of Ni-Ti(-Cu) Shape Memory Alloy Thin Films for Tribology

I confirm that:

1. This work was done wholly or mainly while in candidature for a research degree at this University;
2. Where any part of this thesis has previously been submitted for a degree or any other qualification at this University or any other institution, this has been clearly stated;
3. Where I have consulted the published work of others, this is always clearly attributed;
4. Where I have quoted from the work of others, the source is always given. With the exception of such quotations, this thesis is entirely my own work;
5. I have acknowledged all main sources of help;
6. Where the thesis is based on work done by myself jointly with others, I have made clear exactly what was done by others and what I have contributed myself;
7. Parts of this work have been published as reported in the “Publications” section.

Signed:.....

Date:.....

Acknowledgement

I want to express my gratitude to those people that supported me during my Ph.D, as this important experience would not have been the same without them.

I would like to thank my supervisory team for their constant support over the past three years. I consider myself extremely lucky to have worked with good and very friendly people, who always made me feeling very comfortable in any circumstances.

My first and foremost thanks go to my main supervisor Dr. Tomas Polcar. At the beginning of my Ph.D, in my first meeting with him I remember one of his sentences: “I will support you, but it is your Ph.D”. Well, it was indeed like that! He supported my ideas with rationality, giving me the chance to shape my studies and find my way. I can firmly recognise how it contributed to my growth. I am grateful for the very instructive chats I had with him, his door having been always open. I am also very grateful to him to have given me the chance to share my achievements in very important international conferences, which further contributed to open my mind and where I could meet and socialise with many excellent researchers in our field. It also encouraged me to progress with enthusiasm and passion in my studies.

I would like to express my gratitude to my secondary supervisor Dr. Brian G. Mellor, who was a good sounding board and advisor, even before to start my Ph.D. I am very grateful for the useful chats and the precious advice provided by him especially in writing papers and scientific reports as well as on the subject of this thesis.

The research leading to some of the results showed in this thesis has received funding from the European Union Seventh Framework Programme under Grant Agreement 312483 - ESTEEM2 (Integrated Infrastructure Initiative–I3). In this context, I would like to thank Dr. Frans D. Tichelaar from the High Resolution Electron Microscopy Centre at Delft University of Technology in the Netherlands for his precious support in the TEM analyses, and for his valuable comments on transmission electron microscopy, which introduced me to the TEM world.

I express my gratitude to Dr. Jurgita Zekonyte and Dr. Richard Cook for the useful discussions I had on nanomechanical characterisation of materials by means of nanoindentation. I would like to further thank Dr. Zekonyte for XPS analysis and for useful discussions on it.

I thank Prof. Albano Cavaleiro at the University of Coimbra in Portugal for helping with the fabrication of W-S-C coatings and for letting me use some of the equipment in his laboratory. I would like to thank Mr. Petr Mutafov for helping with Raman spectra acquisition.

Finally, last but not least, I want to thank my family, which is always there, next to me, supporting my decisions and encouraging me to pursue and achieve all my goals.

Mauro Callisti

Southampton, October 2014

List of abbreviations

A_f	Austenite Finish Temperature
AFM	Atomic Force Microscopy
A_s	Austenite Start Temperature
BF	Bright Field
B2	austenitic phase (cubic)
B19’	martensitic phase (monoclinic)
CSM	Continuous stiffness measurements
CTA	Conventional Thermal Annealing
DC	Direct Current
DLC	Diamond-like Carbon
DSC	Differential Scanning Calorimetry
E	Elastic modulus
EDX	Energy Dispersive X-Ray Spectroscopy
ER	Electrical Resistance
FFT	Fast Fourier Transform
FIB	Focused Ion Beam
GP	Guinier-Preston
H	Hardness
HR-TEM	High Resolution Transmission Electron Microscopy
HAADF	High Angle Annular Dark Field
IFFT	Inverse Fast Fourier Transform
Lc	Critical load for delamination in scratch tests
MEMS	Micro – Electro – Mechanical – Systems
M_d	Critical temperature for austenite yielding
M_f	Martensite Finish Temperature
MF	Mid-frequency
M_s	Martensite Start Temperature
PVD	Physical Vapour Deposition
Ra	Average Roughness
RF	Radio Frequency

R_f	R-phase Finish Temperature
RMS	Root Mean Square Roughness
RPM	Rotation Per Minute
R_s	R-phase Start Temperature
SAEDP	Selected area electron diffraction pattern
SE	Superelasticity
SEM	Scanning Electron Microscopy
SIM	Stress Induced Martensite
SMA	Shape Memory Alloy
SME	Shape Memory Effect
T_E	Temperature of equilibrium
Tc	Crystallization temperature
TCR	Thermal Coefficient of Resistance
TEM	Transmission Electron Microscopy
T_H	Temperature hysteresis
TIM	Thermally-Induced Martensite
TMD	Transition metal dichalcogenide
TMT	Thermoelastic Martensitic Transformation
U	Mechanical driving force
XPS	X-Ray Photoelectron Spectroscopy
XRD	X-Ray Diffraction
ΔG	Variation in free energy
ΔG_c	Variation in chemical free energy
ΔG_{nc}	Variation in non-chemical free energy
ΔG_{net}	Combination of chemical and non-chemical free energy
ΔH	Variation of enthalpy
$\mathcal{E}_P$	Plastic strain
$\mathcal{E}_R$	Recoverable strain
$\mathcal{E}_T$	Transformation strain
σ_s	Critical stress for slip
$\sigma_s{}^{A\rightarrow M}$	Stress required to activate the Austenite-to-martensite transformation

Chapter 1 SHAPE MEMORY ALLOYS

The shape memory effect (SME) was first observed by Ölander [1, 2] *in an Au-Cd alloy in 1932, although it was not recognised as such, being viewed as a curious anomaly. A crystallographic explanation of the observed shape memory effect (SME) was first made in 1951* [3]*, leading to a number of publications which demonstrated the effect in other materials including In-Tl* [4] *and Cu-Zn* [5]*. In 1961 the first patents* [6, 7] *were filed for a SME device which used an Au-Ag-Cd alloy as a thermal actuator. The SME was first observed in Ni-Ti in 1961 at the US Naval Ordnance Laboratory and subsequent work led to the promotion of shape memory alloys (SMAs)* [8]*. Although the SME has been demonstrated in many alloys, including Cu-Al-Mn, Cu-Zn-Al-Co* [9, 10]*, U-Nb* [11]*, Fe-Mn-Si, Cu-Ni-Al, Ni-Mn-Ga* [12]*, Cu-Al-Ni* [13]*, only Ni-Ti alloys have achieved any marked industrial success over time, both with and without ternary alloying addition* [14, 15, 16, 17].

1. Introduction to Shape Memory Alloys

Here, a brief description is provided on the physical metallurgy of these alloys, while for a detailed explanation reference should be made to the review paper of *Wayman et al.* [18] and to that of *Otzuka et al.* [19].

Figure 1.1 shows the equilibrium phase diagram of the Ni-Ti system. Ni-Ti locates around the equiatomic composition region, while Ti_2Ni and $TiNi_3$ intermetallic compounds locate at 33.3 at.% Ni and 75 at.% Ni, respectively. These three intermetallic compounds are equilibrium phase. There is another phase, Ti_3Ni_4, which is not in equilibrium but is important as it affects shape memory behaviour.

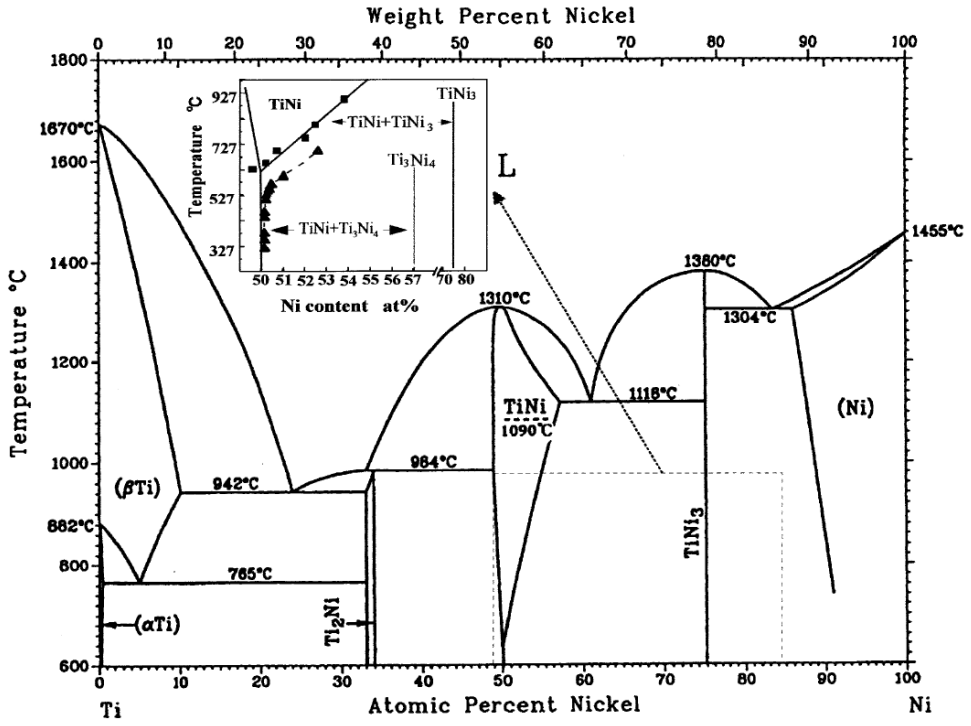

Figure 1.1 – Equilibrium phase diagram of the Ni-Ti system [20].

The term "Shape Memory Alloy" refers to the capability of such alloys to remember their low temperature shape after having suffered large deformations. This curious behaviour of Ni-Ti based alloys has its origin in the thermo-mechanical dependence of the austenite-to-martensite diffusionless solid state phase transformation on an atomic scale; this transformation is known as martensitic transformation. This transformation was observed first in carbon steels, where this reaction proceeds from an equilibrium austenite phase to a non-equilibrium (metastable) low temperature martensite phase. Since the martensite is metastable it will only form through very

rapid cooling, in fact the rate of growth is so high in these reactions that the volume change associated with the reaction is controlled almost entirely by the nucleation rate. However, in many martensitic transformations, as it is the case for Ni-Ti alloys, the low temperature phase is an equilibrium phase rather than a metastable one, therefore in this case the phase transformation occurs by the fast growth martensitic mode even with very slow cooling rates. The martensitic transformation taking place in Ni-Ti alloys can be explained in terms of both crystallographic structural changes and thermodynamics.

1.1 Crystallography of martensitic transformation

The parent phase of the Ni-Ti has a CsCl-type B2 superlattice, while the native phase (martensite) is three-dimensionally close packed and can have a B19' monoclinic or B19 orthorhombic structure, as shown in Figure 1.2. The martensitic transformation occurs in such a way that the interface between the martensite variant and the parent phase becomes an undistorted and unrotated plane (invariant plane or habit plane) in order to minimise the strain energy.

The crystallographic characteristics of the martensitic transformation are now understood by phenomenological crystallographic theory, which states that the transformation consists of the following three operational processes: (i) a lattice deformation creating the martensitic structure from the parent phase, (ii) a lattice invariant shear (twinning, slip or faulting) and (iii) a lattice rotation. The lattice invariant shear is generally twinning, which is reversible, in shape memory alloys. Structurally, martensite forms through a twinning type process that is very similar in nature to deformation twinning where this must involve a pure shear and preserve the lattice structure, allowing only some rotations. For a pure shear three non-coplanar vectors are required which must retain their mutual lengths and angles upon transformation.

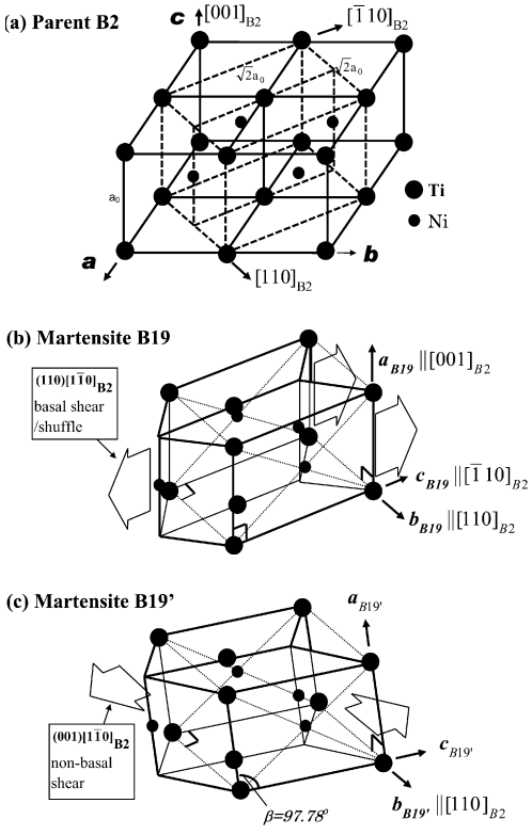

Figure 1.2 – Structure relationship among B2 parent phase and two kinds of martensite, B19 and B19': (a) the parent phase B2 structure with a FCT cell delineated; (b) orthorhombic martensite B19, formed by shear/shuffle of the basal plane (1 1 0)$_{B2}$ along [11 0] direction; (c) monoclinic martensite B19' , which is viewed as a B19 structure sheared by a non-basal shear (0 0 1)[11 0]$_{B2}$, the modulus of which corresponds to c_{44} [19].

As an example Figure 1.3 (a) shows untwined material as a semicircle that undergoes pure shear into an ellipse. It can be seen that the only two planes undistorted during the shear process are planes K^1 (known as the twinning plane) and K^2, whereas the only direction above the twinning plane that does not change length during the transformation is OA. Therefore the non-coplanar vectors that retain their mutual lengths and angles must lie within these planes.

The nature of the atom movement during twinning is illustrated in Figure 1.3 (b), where the first atoms above the twinning plane move by a vector *t*, whereas the adjacent plane of atoms moves relative to its neighbour by the same vector *t*. This is a cooperative motion since all atoms move through the same vector relative to its neighbour. It means that a large strain is produced by many smaller cooperative atom movements. As the twins grow predominantly in directions parallel to the K^1 planes, they have a plate like morphology.

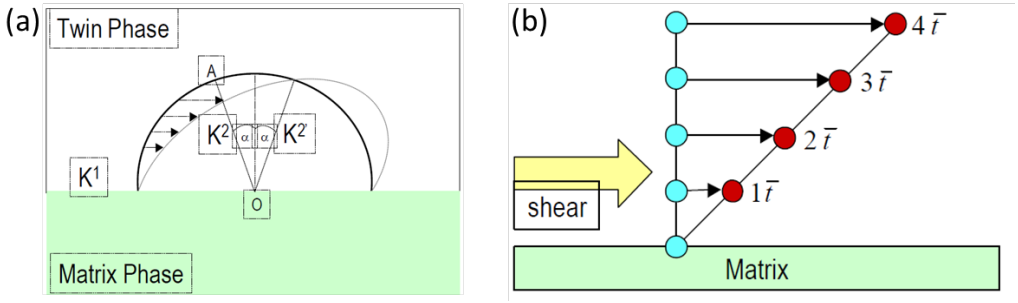

Figure 1.3 – Schematic representation of the twinning process: (a) semicircle of material undergoing shear transformation, (b) shear strain as a result of atom motion in twinning planes [19].

The transformation is thus produced by an invariant plane strain, where the movement of each point is a linear function of the distance from the invariant plane. Experimental observations by optical microscopy clarified that the martensitic habit plane is only an invariant plane on a macroscopic scale and that the shape strain is only homogenous on a macroscopic level.

1.2 Thermodynamic perspective of martensitic transformation

From a thermodynamic perspective, martensite forms because it has a lower free energy than the corresponding parent phase. As there is no compositional change associated with the transformation the free energy curves as a function of temperature may be represented as in Figure 1.4. In this diagram the temperature T_E represents the point where the two phases are in thermodynamic equilibrium and the difference in free energy (ΔG) between martensite and parent phase is zero. As there is a strong nucleation barrier to the formation of martensite, significant undercooling is necessary before enough free energy is available to provide the driving force for the nucleation of the martensite phase. In Figure 1.4, the term $\Delta G^{P\rightarrow M}$, at temperature M_s, represents the variation in free energy required to start the martensitic transformation. Usually, the term M_f is used to indicate the finish temperature of the above mentioned transformation. The same considerations can be adopted for the inverse transformation, where superheating is required to activate the phase

transition from martensite to austenite which starts at the temperature A_s and finishes at A_f, (A refers to the austenite phase).

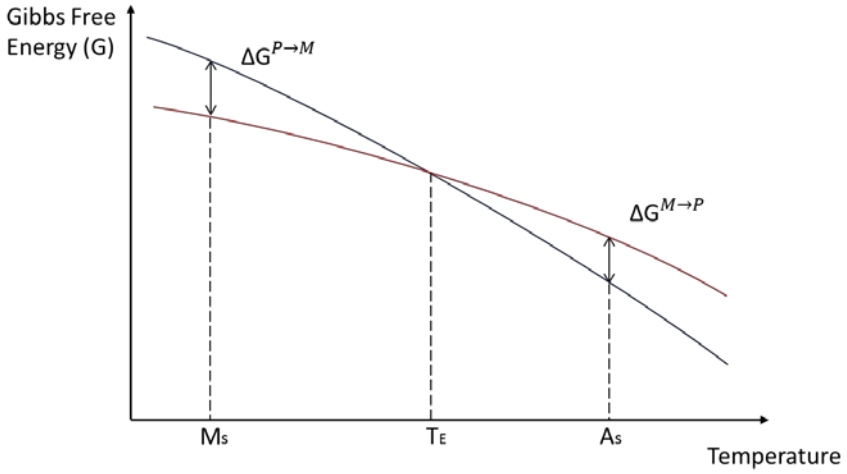

Figure 1.4 – Free energy curves for the martensite and parent phases [19].

The variation of free energy (ΔG_{net}) can be seen as the interplay of various energy terms operating during the transformation. In particular three terms are considered, i.e. a chemical energy term (ΔG_c) resulting from the structural change from parent to martensite, a surface energy term (ΔG_s) resulting from the formation of internal interfaces during the transformation, and an elastic strain energy term (ΔG_e) stored in the system as the transformation proceeds on cooling. These contributions can be subsequently stored in two main terms, where the first takes into account the variation of the chemical free energy (ΔG_c) and the second takes into account the non-chemical free energies (ΔG_{nc}). The presence of the non-chemical free energy explains why the transformation start temperatures are not the same as the finish temperatures. In particular, as the transformation proceeds further cooling or heating is required to overcome the concomitant increase in ΔG_{nc} resulting from the formation of the new phase.

The martensitic transformation can be divided in two categories: thermoelastic and non-thermoelastic. The former shows a lower variation or hysteresis in the formation of parent phase during heating and cooling, compared to the non-thermoelastic transformation. This is because a much smaller driving force is required for thermoelastic transformations due to the greater mobility of the parent/martensite interface. In non-thermoelastic transformations, during cooling below M_s, martensite grows to its limiting size and upon further cooling, additional transformation only

occurs by the nucleation of new plates, whereas old plates will not grow even at lower temperatures. However, during the thermoelastic transformation, further cooling below M_s causes additional transformation due to the growth of old plates as well as of new plates. It is the thermoelastic transformation that is at the heart of the memory effect. Thermoelastic transformations stop when the free energy available to drive the reaction is counterbalanced by the strain energy generated in the parent matrix. Because of the very small volume change, plastic flow does not occur and a balance is achieved between the elastic strain energy made available by the lower free energy state of the martensitic phase. It is the balance that defines the term thermoelastic. Therefore as the temperature is lowered, new equilibrium is created. The rate at which the bulk interface moves is governed by how fast the temperature is lowered.

Another important factor affecting the martensitic formation is whether or not a stress is applied to the system. In particular, an applied stress will either have a positive or a negative effect on the amount of the chemical free energy required for martensite nucleation. Figure 1.5 shows how the stress applied to the parent phase at the temperature between M_s and T_E will provide an additional mechanical driving force U, which is added to the chemical driving force ΔG_c.

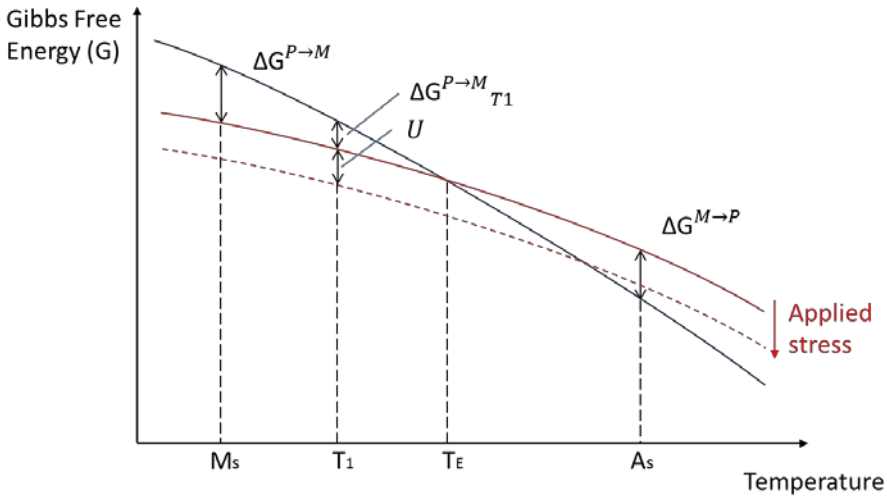

Figure 1.5 – The effect of applied stress on the free energy of transformation [19].

The driving force U is a linear combination of the applied stress in relation to the orientation of the transforming plate. In particular, when a martensitic reaction starts by stressing a polycrystalline parent phase in which the orientation of each grain is

randomly distributed, a martensite plate with an orientation that yields a maximum value of U will be formed first. In the example in Figure 1.5, U represents the critical mechanical driving force for transformation to occur at temperature T_1.

1.3 Superelastic and Shape Memory effects

Figure 1.6 shows by using a simple two-dimensional model how shape memory and superelastic (or pseudo-elastic) effects manifest themselves in terms of shape strain and stress-strain constitutive relationship. If an alloy, at a temperature below M_f, is deformed by a tensile stress (curve A), and subsequently unloaded then an apparent plastic strain will remain. If the alloy is now reheated to a temperature above A_f (the red arrow in Figure 1.6) then the apparent plastic strain will fully recover and the alloy will be restored to its original shape. This is known as the one-way shape memory effect, and the formation of martensite is related to the thermal energy supplied to the system (TIM, thermal-induced martensite).

If the same alloy is deformed in a similar manner at a temperature between A_f and M_d (temperature at which plastic strain is energetically more favorable than martensitic transformation), when it is unloaded, the strain is simultaneously recovered (curve B). This effect is known as superelasticity and the formation of martensite is related to the applied stress (SIM, stress-induced martensite).

Again, the structural changes that take place in Figure 1.6 can be thought in two dimensional terms, as shown in Figure 1.7. During the deformation in the curve A, the alloy starts in the twinned martensite condition, during loading de-twinning occurs and the structure becomes a deformed martensite resulting in a macroscopic shape change.

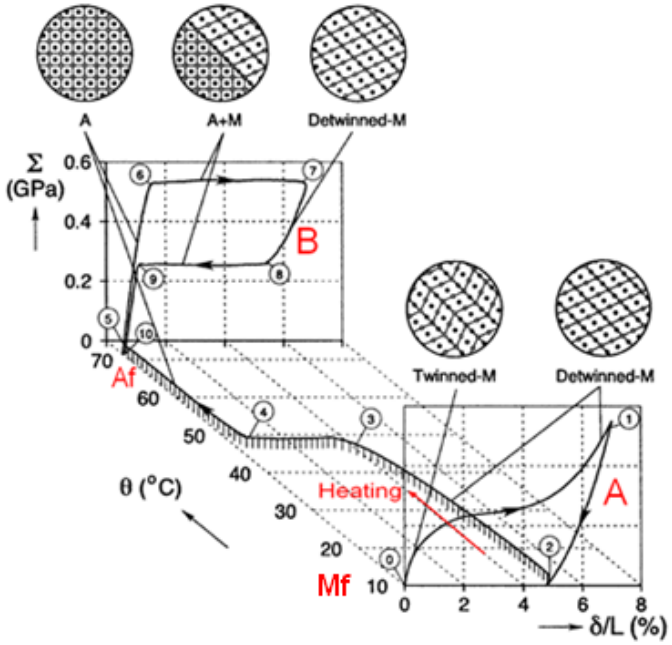

Figure 1.6 – Stress-strain-temperature relationship in Shape Memory Alloys [21].

When the alloy is unloaded the deformed martensite structure remains resulting in the apparent plastic strain. If the alloy is now reheated to a temperature above A_f then the original parent phase structure and orientation is restored via a thermoelastic type of transformation. When the alloy is cooled back down to below M_f the twinned martensite structure is restored. It should be noted that the transformation between parent phase and self-accommodating martensite results in no macroscopic shape change. Thus a one-way shape memory effect is achieved where the total maximum strain that can be recovered, without any real plastic deformation occurring, depends upon the shape memory alloy system, and typically it is in the range of 1 – 6 % for polycrystalline alloys.

If the alloy can be trained to remember a hot shape and cold shape (i.e. deformed martensite shape) then a two-way memory effect may be established, where the component may be cycled between two different shapes without any external stress being applied. In this case the self-accommodation of the martensite variants will be lost on cooling and predominant variants form resulting in a memorised shape change. Subsequent heating results in the inverse transformation to the parent phase and another shape change to the second memorised shape.

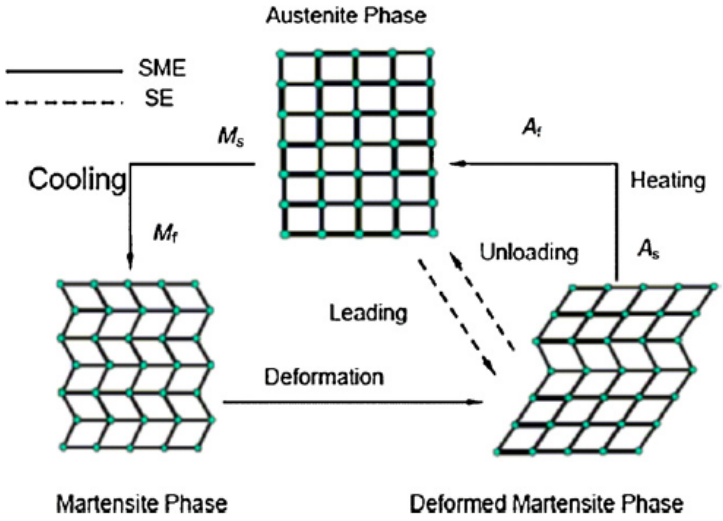

Figure 1.7 – Two-dimensional model of the structural changes involved with shape memory transformations [22].

Similarly with superelasticity, the martensite transformation takes place under the influence of stress, though in two-way SME the stresses are internal rather than external. These forces may be induced in a number of ways, usually referred to as training the alloy. Through training, the nuclei of the internal stress field which control the martensitic transformation upon cooling are created inside the parent phase. These sites must be stable with respect to the transformation and are usually a certain pattern of irreversible defects such as dislocations caused by deformation or second phase particles or precipitates created through stress ageing.

Figure 1.7 can also explain the origin of the superelastic effect displayed by curve B in Figure 1.6. In this case, the alloy is deformed at a temperature above A_f and the martensitic transformation is entirely stress induced. The symmetrical parent phase is changed into the lower symmetry deformed martensite phase directly. Upon unloading, the decreasing stress and surrounding elasticity of the matrix results in the martensite plates shrinking back and the original parent phase structure being restored.

Figure 1.8 provides a map in terms of temperature/stress, where conditions for superelasticity (also referred as pseudo-elasticity) and shape memory effect are shown.

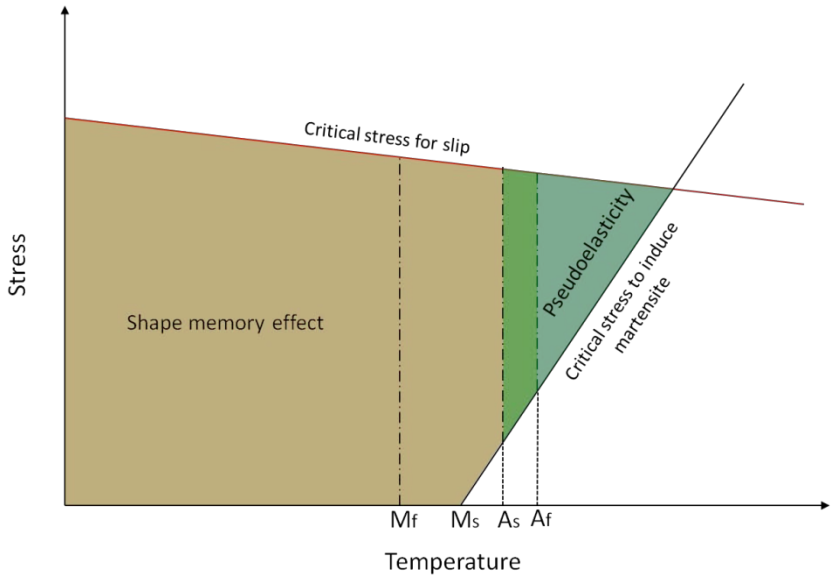

Figure 1.8 – Shape memory and superelasticity as a function of stress and temperature coordinates [19].

Therefore, depending upon the temperature and stress coordinates, the alloy will either exhibit superelasticity and/or shape memory effect. The critical stress to induce martensite from the austenitic phase approximately is found to scale linearly with the temperature.

2. Ni-Ti based thin films

The reversible stress- and thermal-induced martensitic transformation, particularly in Ni-Ti based compositions, has attracted much attention from different engineering fields. Furthermore, the fact that the shape memory and superelastic effects have also been demonstrated in Ni-Ti based thin films makes these attractive candidates for actuation devices in micro-electro-mechanical systems (MEMS), owing to their significantly increased response rate, resulting from their increased surface-to-volume ratio, compared to bulk Ni-Ti alloys.

Although considerable breakthroughs have been achieved by means of extensive research, there are still some concerns regarding the use of these films in industrial applications on account of the inability to control precisely their response to external stimuli. Moreover, in addition to this limitation, low hardness further limits their field of application. To counter these deficiencies much effort has been directed to making

Ni-Ti thin films more attractive and the use of a third element as dopant has emerged as an effective approach for changing or modulating their properties. Typically, elements such as: Cu, Pt, or Pd are used to replace Ni atoms, while Zr or Hf, but also Cu are used as replacements for Ti.

Among the possible candidate dopant elements copper has been widely used to replace both Ni and Ti in Ni-Ti thin films in order to reduce the composition sensitivity of the transformation temperatures, as well as to reduce temperature hysteresis (T_H), stabilize the shape memory effect and increase the actuation rate and the recoverable strain, also under a stress as high as 1 GPa [23]. These properties make Ni-Ti-Cu films more suitable for engineering applications. The following sections provide an overview of the current state of knowledge, on fabrication and characterization of Ni-Ti and Ni-Ti-Cu thin films.

2.1 Ni-Ti(-Cu) thin films

With respect to micro-scale actuation, SMAs possess the highest known actuation force compared to other actuation methods, such as electrostatic, thermal and piezoelectric [24]. SMA thin films can be electrically driven using joule heating; their high surface-to-volume ratio produces high cooling rates, which is ideal for a high frequency response. Moreover, Ni-Ti based systems have been particularly popular for the relatively high work density they can produce during recovery ($\sim 10^7\ J/m^3$) [25].

Popular methods for the fabrication of these films include laser ablation, cathodic arc plasma ion plating, flash evaporation, vacuum evaporation, and sputtering. The techniques other than sputtering often produced films with non-uniform film thickness and composition, therefore they are incompatible with MEMS processing, by considering also their low deposition rates [26].

Therefore, sputtering deposition has often been chosen to produce Ni-Ti based films, because of its ability to control film thickness and composition as well as to produce films with excellent mechanical properties and extremely fine grain sizes [27, 28, 29, 30, 31, 32, 33, 34].

Both SME and SE have proved to be very sensitive to small changes in composition [35], an aspect which has restricted system reliability and manufacturability of Ni-Ti MEMS devices. At the same time, the strong dependence of transformation temperatures on composition was exploited to change the transformation temperatures range, making these smart films suitable for hostile environments, even though the control of composition is probably one of the most sensitive issues in PVD techniques. Overtime different solutions were adopted in order to improve this aspect, as reported in the following sections.

Sputter-deposited Ni-Ti based thin films deposited at room temperature (without any deliberate substrate heating), are generally amorphous, therefore, as the martensitic transformation is associated with a change in crystalline structure, the as-deposited films must be annealed above ~ 500°C [36, 37] to crystallise, though the crystallisation process is sensitive to the film stoichiometry [37, 38]. Conversely, it has been found that, for Ti-rich Ni-Ti based films, it is possible to carry out the crystallisation process during deposition, due to the lower crystallization temperature of such compositions [39].

Ishida et al. [40] demonstrated that thermal treatment post-deposition has a significant role on the subsequent thermomechanical and shape memory properties of the deposited films, due to the nucleation and growth of different types of precipitates, both in the grain interior and at the grain boundaries [41].

The following sections provide an overview on the fabrication, microstructural and thermal-mechanical characterization of Ni-Ti based films. Particular attention was directed to Ni-Ti-Cu ternary films, which are widely considered as the most promising composition for MEMS applications [42], owing to their stabilizing effect on the SME as well as for their reduced hysteresis temperature [43, 44] and high actuation speed [45], compared to Ni-Ti films [46]. For these reasons, most of the research carried out so far, focused on the characterization of the functional properties of these films in relation to the sputtering process, post-deposition thermal treatments, microstructure and composition [47], as well as on the physical processes involved during film growth and crystallization [48].

2.2 Fabrication process

Ni-Ti thin films, produced in the amorphous state, were first made by *Thomas et al.* [19] in 1982 using electron irradiation and a high voltage electron microscope. Although these films were amorphous, it was a monumental step in the development of SMA thin films. In 1983, *Sekiguchi et al.* [49] produced the first crystallised Ni-Ti thin film using vacuum deposition and were the first to confirm SME in thin films. Four years later, *Kim et al.* [50] used magnetron sputtering to deposit films with $Ni_{56}Ti_{44}$ composition. Although the film composition was not close to the desired equiatomic composition and did not undergo martensitic transformation, their work verified the possibility of using sputter deposition techniques to produce reliable and sufficient shape memory thin films [19]. Since that discovery, a lot of research has been carried out in order to understand better the role of the deposition parameters on film properties, as well as the possibility of real-time structure design of magnetron sputtered Ni-Ti based thin films [51].

Using appropriate targets for the constituent elements of the film represented the first issues, especially for achieving a desired chemical composition. Many solutions have been adopted over time to produce Ni-Ti films by magnetron sputtering, with a desired composition from an alloy target. Ti has a lower sputtering yield [52], a variable angular distribution [53, 54, 55] and a different sticking coefficient [56], compared to Ni. For these reasons, films obtained by using an equiatomic Ni-Ti alloy target are normally Ni-rich [57]. The solutions adopted to compensate for Ti deficiency, basically consists in making the target richer in Ti by using a Ti-rich target or including in the erosion zone of the target, Ti chips [58, 59]. *Ho et al.* [28, 52] showed that by using a single Ni-Ti target it is possible to reduce Ti loss, by heating the target to temperature above 400°C during deposition, which also improved the compositional uniformity of the deposited films [60]. Recently, it has been reported that by controlling the power ratio of separate targets (e.g. Ti, Ni, Cu single targets or Ni-Ti alloy, Ti and Cu single targets), precise composition control is possible [61, 62, 63, 64].

The other important parameter to be properly set in magnetron sputtering deposition is the partial pressure during deposition, which has been shown to influence the surface morphology, grain size of Ni-Ti(-Cu) films as well as deposition rate and density [65]. *Chu et al.* [66] found that films deposited at high pressure ($\geq$ 7 mTorr) had a well-

defined clustered columnar structure. A high partial pressure is likely to decrease the energy of sputtered atoms by collision, resulting in a decrease in surface diffusion and so the columnar structure developed contained structural defects [67, 68]. Conversely, the film grown at low partial pressures ($\leq$ 0.5 mTorr), exhibited a dense structure and columnar grains were evidently not seen for both Ni-Ti and Ni-Ti-Cu compositions. Under extremely high partial pressure (> 10 mTorr), argon atoms absorbed on the film surface interfered with the surface diffusion of sputtered atoms and caused columnar sputtered films to grow, producing brittle Ni-Ti based films with some cracks [64, 69].

As-deposited Ni-Ti based films can be amorphous or crystalline in structure depending on the deposition temperature. Sputter deposition processes, conducted at low temperatures, produced amorphous structures for Ni-Ti based thin films [70]. Low sputter deposition temperatures can also contribute to the formation of columnar structures and voided boundaries [71], due to the effect of deposition pressure [72].

Conversely, sputter depositions conducted at a high temperature, above the crystallisation temperature for Ni-Ti based films, produced a fully crystalline structure, making the post-sputtering annealing process unnecessary [70]. Ni-Ti films were also deposited at a temperature of approximately 300°C to gain partial crystallisation [73, 74] or to induce structural relaxation [75], followed by annealing at a higher temperature (e.g. 500°C) for a short time, to gain full crystallisation [58].

Since shape memory and superelastic properties are associated with a crystalline structure, Ni-Ti based films need to be annealed after deposition in order to promote the crystallization process [38, 39, 41]. Due to the reactive nature of titanium, the post-deposition annealing treatment is generally conducted under high vacuum conditions, in order to reduce the oxygen content within the chamber. Over time, two different post-deposition thermal treatments were adopted in order to crystallize sputter deposited Ni-Ti based films: (i) solution treatment at temperatures much higher (700 – 900°C) than the crystallization one (T_c = 450 – 550°C, depending of the composition [76]), in order to homogenise the film and produce a crystalline structure, and subsequent annealing at temperatures $\geq T_c$ [40] in order to promote microstructural changes; (ii) annealing the films directly at temperatures higher than the T_c [77], thus avoiding double treatments. Among these heat treatments, annealing the films directly at temperatures $\geq T_c$ [77] became a standard [20] for Ni-Ti based films.

It is well known that the transformation temperatures of Ni-Ti based films are strongly related to the chemical composition of the matrix, and a slight shift in compositions (especially regarding the Ni content), might produce a shift in transition temperatures of 100°C.

In binary Ni-Ti films it was generally observed that Ti-rich and near equi-atomic compositions show a martensitic structure at room temperature ($M_f <$ ambient temperature), while Ni-rich compositions are austenitic at room temperature ($A_f >$ ambient temperature) [78, 79]. Moreover, it has been widely confirmed that transition temperatures are affected by annealing temperature and duration. Transformation temperatures increase with increasing annealing temperature [80] and annealing time [40], although the dependence on annealing time is not fully understood.

In particular, as the annealing process produces precipitates of different phases in both grain interior and at grain-boundaries, it is believed that precipitates in the grain interior affect the local stress field which in turn affects the transformation temperatures. This phenomenon occurs when the precipitates are coherent with the matrix (i.e. GP zones). On the other hand, the formation and growth of semi-coherent precipitates, with increasing annealing temperature, reduces the Ni or Ti content in the grain, thus changing the Ni/Ti ratio of the matrix and consequently the transformation temperatures [81]. Similar effects were observed in ternary Ni-Ti-Cu thin films, where for both Ti-rich [82] and (Ni,Cu)-rich [83] compositions, transformation temperatures increased with increasing copper content and annealing temperature.

These findings have confirmed that the thermal as well as mechanical properties of Ni-Ti based films are governed surely by the grain size but also by a balance between two factors: precipitate evolution, and matrix composition.

2.3 Crystallisation behaviour

The crystallization process consists of two major events, i.e. nucleation and crystal growth. In a general system consisting of solute and solvent, nucleation is the step where the solute atoms dispersed in the solvent start to gather into clusters gaining stability, and subsequently constitute the nuclei. It is at the nucleation stage that

atoms arrange in a defined and periodic manner that defines the crystal structure. Crystal growth is the subsequent growth of the formed nuclei. Nucleation and growth continue to occur simultaneously while supersaturation exists. Supersaturation is the driving force for the crystallization process; hence the rate of nucleation and growth is driven by the existing supersaturation in the solution. Depending on the conditions, either nucleation or growth may be dominant over the other, and as a result, crystals with different sizes and shapes are obtained [84].

Many compounds (e.g. Ni-Ti based alloys), have the ability to crystallize with different crystal structures, a phenomenon called polymorphism. Each polymorph is in fact a different thermodynamic solid state, and crystal polymorphs of the same compound exhibit different physical properties.

The first study on the crystallization behaviour of sputter deposited Ni-Ti thin films was carried out by *Chen et al.* [38]. The behaviour of free-standing and substrate-attached Ni-rich and Ti-rich Ni-Ti films was analysed after different thermal treatments and by different methods. This research revealed a difference in behaviour between free-standing and substrate-attached films, due to the presence of compressive residual stress in the latter, which encouraged the crystallization process. Specifically, for the substrate-attached film a lower activation energy was estimated by XRD analyses (i.e. by monitoring peaks position and intensity over time and by using the Arrhenius law), compared to that calculated by the Avrami's and Kissenger's methods for the free-standing film (see Figure 1.9).

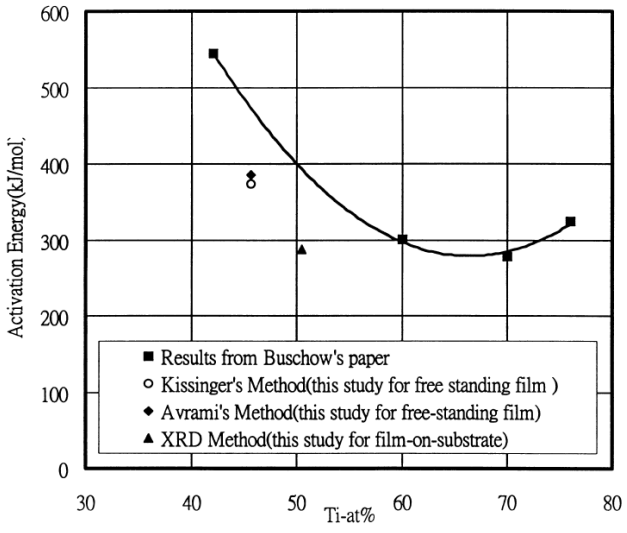

Figure 1.9 - Activation energy calculated by different methods for different Ni-Ti compositions [38].

For bulk Ni-Ti alloys, the activation energy has been correlated with the alloy composition (Figure 1.9), i.e. the activation energy decreased with increasing Ti content [85] and showed a minimum in the range 60 – 70 at.% Ti. Compared to the data found for Ni-Ti bulk alloys, the activation energy for thin films showed lower values [39].

Liu et al. [86] analysed by DSC the crystallization process of a slightly Ni-rich Ni-Ti thin film, during both continuous heating and isothermal annealing. In the former case, the activation energy for crystallization was determined by the Kissenger (411 kJ/mol) and Augis & Bennett methods (311 kJ/mol), while in the second case, using the Arrhenius law, a value of 424 kJ/mol was calculated. The agreement between the values calculated for both annealing treatments indicated a similar nucleation and growth mechanism in the different annealing methods. The large Avrami exponent ($n > 3$) found in the stage of crystallisation for the Ni-rich Ni-Ti film suggested a diffusion-controlled growth mechanism. On the other hand, for a near-equiatomic Ni-Ti film, *Vestel et al.* [87] found an Avrami exponent between 2.1 (2 - site saturation) and 2.6 (3 - continuous nucleation). Moreover, they found by TEM (Figure 1.10) on a partially crystallised Ni-Ti film that nucleation occurred at the free surface, where the growth of the surface-nucleated phase continued until lateral impingement occurred, after which a columnar mode persisted in the direction normal to the film surface with the same growth rate for all the columnar grains.

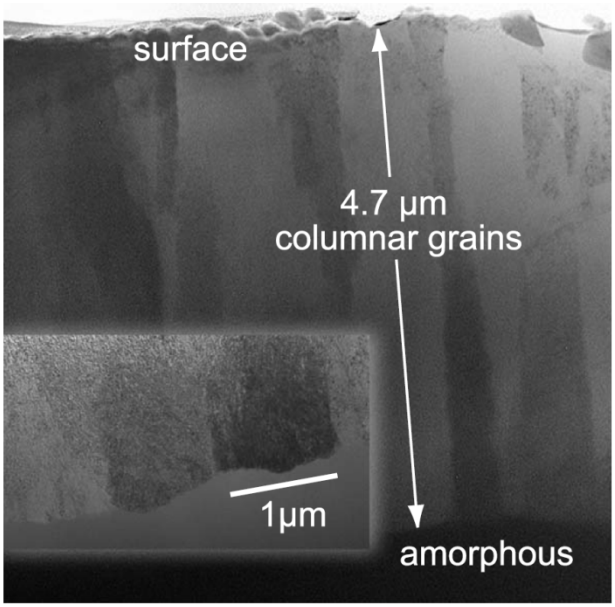

Figure 1.10 – TEM image showing the structure of a near-equiatomic NiTi film resulting from surface nucleation of columnar grains (top) growing into remnant amorphous phase (bottom). The inset shows the interface growing grains/amorphous structure [87].

Wang et al. [37] observed that surface heterogeneous nucleation in Ni-Ti films can be avoided by "insulating" the inner part of the film by Ni-rich domains along the film surfaces (Figure 1.11) so as to make the nucleation more difficult at the film surfaces and promoting a continuous nucleation within the inner part of the layer. TEM observations showed that disk-like grains as large as about 75 times the layer thickness can be produced.

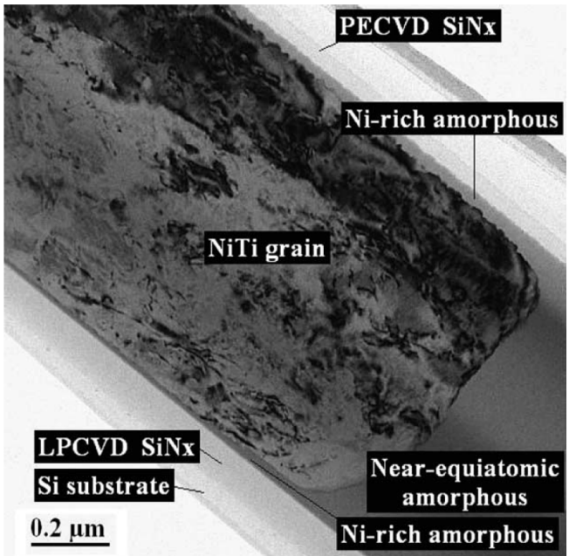

Figure 1.11 – Cross-section TEM image of a partially crystallised film [37].

Ni et al. [88] studied the compositional effects on the crystallisation kinetics of Ni-Ti thin films by comparing the crystallisation behaviour of a near-equiatomic (50.4 at.% Ti) and a Ti-rich (52.6 at.% Ti) Ni-Ti thin films. These films were annealed *in-situ* in the TEM at 495°C, while the microstructural changes were recorded through a CCD camera. The near-equiatomic system exhibited an incubation time[1] and an annealing time for total crystallisation of 60 and 210 seconds, respectively. Crystals grew spherically until they reached the film surface, after which they grew laterally in a disk shape. With continued heating, the growth of crystals continued until impingement with other crystals, after that their isotropic growth was impeded, thus causing them to deviate from a circular shape. The circular shape of the crystals suggested a non-diffusional crystallisation process and the crystal growth remained constant throughout the transition. Conversely, the Ti-rich Ni-Ti sample subjected to the same heat treatment as the near-equiatomic sample, exhibited a much longer incubation

[1] Time required before the first crystallite is formed.

time (180 seconds) and a longer crystallisation time (450 seconds). In this sample, crystals exhibited a spherical shape only at the very beginning, while as the crystallisation processed further the nucleation process changed significantly. In fact, small crystals formed and rapidly populated unoccupied areas. The shape of these crystals deviated from the circular shape and the resulting grain size was about 60 % smaller compared to the near-equiatomic system.

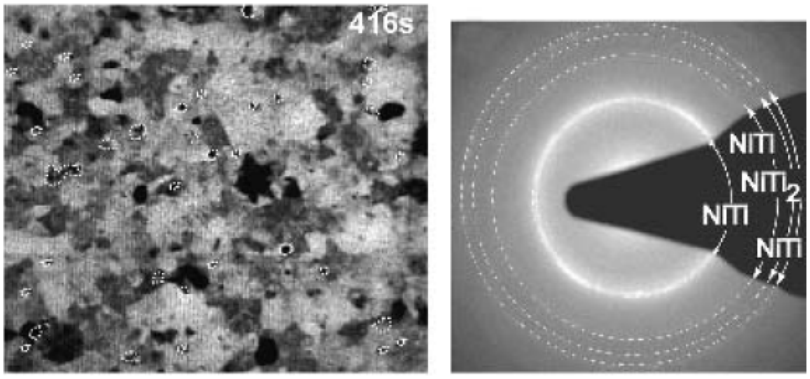

Figure 1.12 – TEM image of the resulting microstructure and the corresponding electron diffraction patter for the off-stoichiometric NiTi film. The dark domains correspond to the Ti_2Ni precipitates [88].

The final microstructure (Figure 1.12) consisted of irregular crystalline domains and of Ti_2Ni precipitates segregated at the grain boundaries, which were supposed to have grown in the vicinity of the Ni-Ti crystals. The formation of these precipitates was a consequence of the sluggish crystallisation process observed for the off-stoichiometric Ni-Ti composition.

Chen et al. [89] investigated the effects of Cu addition on the crystallisation behaviour of Ni-Ti thin films by comparing two films with very similar Ti content, i.e. $Ti_{49.93}Ni_{50.07}$ and $Ti_{49.96}Ni_{40.09}Cu_{9.95}$. The binary system (416 kJ/mol) exhibited an activation energy, calculated by the Kissinger's method, higher compared to the ternary system (388 kJ/mol). Cu addition (likely substitution of Ni by Cu atoms) lowered the onset temperature and the crystallisation activation energy, suggesting that amorphous Ni-Ti films are more stable compared to the Cu-doped Ni-Ti systems. According to the analyses performed by *Chen and Park* [90], the stability of amorphous alloys is dominated by the strength of interactions between constituent atoms. The relative strength of interaction between constituent atoms can be evaluated by comparing their enthalpy of mixing. Ni-Ti exhibits a larger negative enthalpy of mixing than Ti-Cu, while Ni-Cu has a positive enthalpy of mixing (weakest chemical bonding). Therefore, it

was assumed that Cu addition, with the formation of weaker bonding in the amorphous film between different constituent atoms in the short-range ordered clusters, lowered the stability of the amorphous structure.

The effects of copper on the crystallization process of Ni-Ti thin films were also investigated by *Xu et al.* [48]. It was found that by adding a small amount of Cu (1.3 at.%), Ni-Ti-Cu thin films exhibited crystallization temperatures and activation energies similar to those of pure Ni-Ti films. *In-situ* TEM observations revealed that crystallization of Ni-Ti-Cu films, at different temperatures, was characterized by a higher growth rate and a lower nucleation rate, with concomitantly larger crystals than those observed in Ni-Ti. From the temperature dependence of the growth rate and incubation time, it was deduced that copper additions decreased the activation energy for growth but increased it for nucleation.

2.4 Microstructural properties of sputter-deposited Ni-Ti(-Cu) thin films

The chemical compositions and the fabrication process (deposition and heat treatment) of crystalline Ni-Ti(-Cu) films has a significant impact on the overall performance of these materials. In particular, for a given chemical composition of the film, the resulting microstructure and consequently the mechanical and functional properties (shape memory and superelastic effects) can still be strongly changed by the post-deposition annealing processes chosen. In the following section, an overview about the microstructural changes induced by different annealing temperatures on Ni-Ti(-Cu) films with different composition ratios is proposed.

2.4.1 Effects of annealing temperatures on the microstructure

The crystalline structure is achieved by atom densification and crystallisation during the annealing process. This indispensable post-deposition heat treatment is characterised mainly by the annealing temperature and annealing time, which in turn

are greatly influenced by the nucleation rate and crystallite growth velocity. As discussed in section 2.3 nucleation rate and crystallite growth are affected by the film composition [88]. Usually, bigger grain sizes for Ni-Ti thin films are observed for increasing annealing temperature and time, even though in some cases this phenomenon is only evident for high annealing temperatures and specific compositions [91]. Annealing at a high temperature or for a long time may change the microstructure and introduce second phase segregations or precipitates [58, 40]. Therefore, many types of precipitates can be formed both in the grain interior and/or at the grain boundary according to the precipitation process described by the Ostwald step rule [92]. Ni-Ti(-Cu) compositions are generally classified in relation to the Ti content with respect to the Ni (+ Cu) content, therefore for the binary system Ni-rich, Ti-rich and near-equiatomic compositions are distinguished. On the other hand, for the ternary Ni-Ti-Cu compositions Ti-rich and (Ni, Cu)-rich Ni-Ti-Cu compositions are distinguished; Table 1.1 briefly summarise the different precipitates that can be observed for the different composition ratios.

Table 1.1. Precipitates found in Ni-rich, Ti-rich binary NiTi compositions and for Ti-rich and (Ni, Cu)-rich ternary NiTiCu compositions annealed for 1 hour at different temperatures. In the ternary system rhe formation of precipitates is affected also by the Cu content other than by the Ni/Ti ratio [41, 80, 93, 94, 95].

Composition [at. %]	Precipitates
Ni-rich Ni-Ti	Ni4Ti3, Ni3Ti
Ti-rich Ni-Ti	Ti2Ni, GP zone
Ti-rich Ni-Ti-Cu	Ti2Ni, Ti2Cu, TiCu, GP zone
(Ni, Cu)-rich NiTiCu	Ti(Ni,Cu)2, TiCu

Regarding Ti-rich Ni-Ti compositions, *Zhang et al.* [96] found that the annealing process of a Ti-rich $Ti_{51.1}Ni_{48.9}$ thin film, carried out at 550°C for 1 hour, promotes the formation of Guinier-Preston (GP) zone with a disk-like shape (about 30 nm diameter and a few nanometres thick) as shown in Figure 1.13. It was found that GP zones have positive effects on the mechanical and functional properties of these films, as the coherent strain field, between the GP zones and matrix, provides a resistance to the movement of dislocations and, at the same time, allows the twinning deformation of martensite variants to occur.

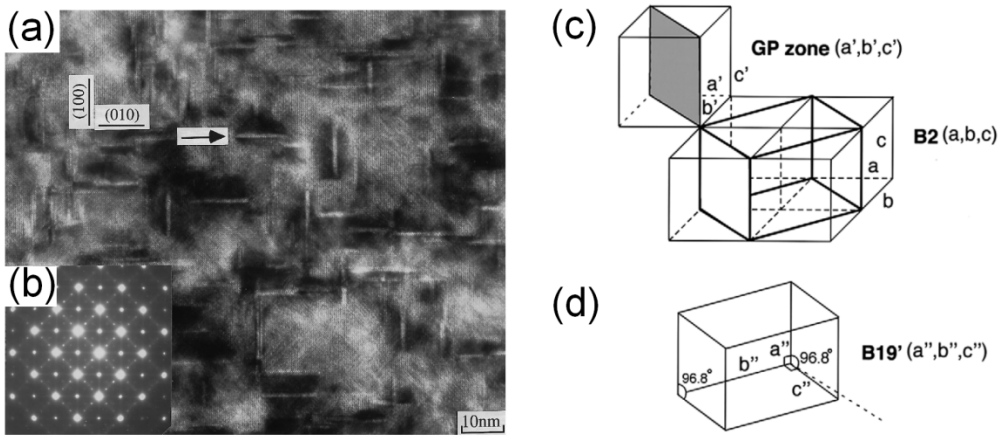

Figure 1.13 - Bright-field TEM image of GP zone in the B2 matrix (a) and the corresponding SADP (b). Schematic representation of the crystallographic relationship among GP zones, B2 parent phase (c) and B19' martensitic phase (c - d) [68, 97].

In fact, HR-TEM observation (see Figure 1.14) showed that the martensite twin variants can move across the GP zones, elastically distorting them during the transition. In this manner, a large strain transformation is still possible; furthermore as the deformation process involves mainly the twinning process, an almost complete recovery upon heating, is possible.

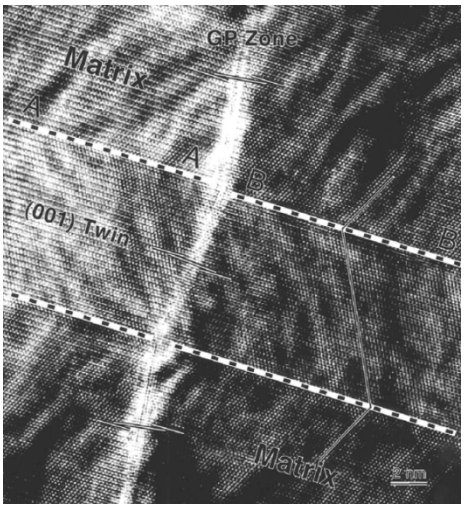

Figure 1.14 - High-resolution electron microscopy image of a (001) deformation twin intersecting a GP zone in a sample deformed to 8.1% [96].

These results were further confirmed in other studies [98], in which the microstructural evolution of deformed B19' martensite in Ti-rich $Ti_{51.1}Ni_{48.9}$ films, was analysed by transmission electron microscopy, at different strain levels. Additionally, it

was pointed out that the GP zones do not have much influence on the twinning mode during the martensite deformation process.

Zhang et al. [97] also found that by annealing a Ti-rich Ni-Ti film at a high temperature, such as 600°C for 1 hour, semi-coherent spherical Ti_2Ni precipitates grew in the Ni-Ti grains interior (Figure 1.15). HR-TEM observations show that the presence of these precipitates may disturb the growth of martensite variants or stop these completely, as illustrated in Figure 1.15, resulting in noticeable plastic deformation or a reduction of the accommodated deformation. Additionally, the presence of GP zones reduced the M_s, due to the higher amount of energy needed to deform elastically these disk-like precipitates during the twinning process.

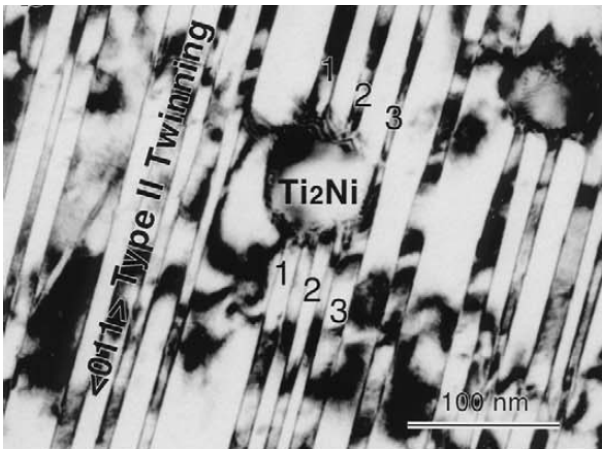

Figure 1.15 – TEM image of the stress-induced martensite with (011) type II twinning plates in a Ti–48.5at.%Ni thin film, showing that Ti_2Ni precipitates can impede the growth of martensite plates [97].

On the other hand, for equiatomic Ni-Ti compositions annealed at 500°C for 1 hour, no precipitates were observed according to the Ni-Ti phase diagram, thus plastic deformation was easily introduced. However, in these films, the martensitic transformation took place without significant resistance, and thus the transformation strain[2] ($\mathcal{E}_T$) was also quite large (5.5%) as for Ti-rich Ni-Ti compositions (see appendix A for further details about the effects of different precipitates on the functional behaviour of Ni-Ti(-Cu) thin films).

Ni-rich Ni-Ti thin films have attracted less attention in the research community owing to the fact that Ni-Ti thin films have been investigating mostly for MEMS applications, where transformation temperatures at or above room temperatures are often required. Usually, Ni-rich Ni-Ti thin films exhibit a M_s temperature lower or much lower

[2] Strain produced during the martensitic transformation.

than room temperature. In terms of precipitation process, as reported in Table 1.1, Ni-rich Ni-Ti thin films form Ni_4Ti_3 plate precipitates in the grain interior, although Ni_3Ti were also reported with a disk-like shape [73, 81]. *Ishida et al.* [40] investigated the microstructure of Ni-rich $Ni_{51.3}Ti_{48.7}$ thin films, solution treated at 700°C for 1 hour and then annealed at various temperatures between 300 and 500°C for different times (1, 10 and 100 hours). The grain size in these films was found to be almost constant (1 µm), whereas the size of the Ti_3Ni_4 precipitates increased with increasing annealing temperature and time (from a few nm at 300°C to about 450 nm at 500°C). These precipitates were found to be densely distributed in the grains interior for annealing at low temperatures, while their density distribution decreased for higher annealing temperatures [68].

The microstructure of ternary Ni-Ti-Cu thin films was investigated by changing the Cu content for Ti-rich and (Ni, Cu)-rich Ni-Ti-Cu compositions and annealing these systems at different temperatures in the range 500 – 700°C.

According to the summary proposed in Table 1.1, for Ti-rich Ni-Ti-Cu films, different precipitates can be formed in relation to the Cu content. In particular GP zone and Ti_2Ni were found when the films were annealed at low (500°C) and higher temperatures (≥600°C), respectively. However, depending on the Cu content and for Ti contents well above 50 at.%, Ti_2Cu plate precipitates are observed [99], although the conditions under which these phases appear are not fully clear, their formation being affected by both chemical composition ratio between constituent elements and annealing temperature. Table 1.2 summarises the microstructural evolution of $Ti_xNi_{(84.5-x)}Cu_{15.5}$ thin films in relation to the Ti content and for different annealing temperatures.

Table 1.2. Phases formed in $Ti_xNi_{(84.5-x)}Cu_{15.5}$ films annealed at 773, 873, 973 K for 1 hour. The parentheses represent precipitates observed in B2 grain interiors [99].

Ti content (at.%)	773 K	873 K	973 K
55.4	Ti_2Cu (–)	$Ti_2Cu + Ti_2Ni$(–)	$Ti_2Cu + Ti_2Ni$(–)
53.2	Ti_2Cu (GP zone)	$Ti_2Cu + Ti_2Ni(Ti_2Cu + Ti_2Ni)$	$Ti_2Cu + Ti_2Ni(Ti_2Ni)$
51.5	– (GP zone)	$Ti_2Cu + Ti_2Ni(Ti_2Cu + Ti_2Ni)$	$Ti_2Cu + Ti_2Ni(Ti_2Ni)$
50.7	– (GP zone)	– ($Ti_2Cu + Ti_2Ni$)	$Ti_2Ni(Ti_2Ni)$
48.6	$Ti(NiCu)_2(Ti(NiCu)_2)$	$Ti(NiCu)_2(Ti(NiCu)_2)$	$Ti(NiCu)_2(Ti(NiCu)_2)$
46.2	$Ti(NiCu)_2(Ti(NiCu)_2)$	$Ti(NiCu)_2(Ti(NiCu)_2)$	$Ti(NiCu)_2(Ti(NiCu)_2)$
44.6	– ($Ti(NiCu)_2$)	$Ti(NiCu)_2(Ti(NiCu)_2)$	$Ti(NiCu)_2(Ti(NiCu)_2)$

For Ti-rich Ni-Ti-Cu compositions, GP zones are almost always observed for annealing temperatures close to that of crystallisation (~ 500 ± 50°C is generally observed), whereas for higher annealing temperatures Ti_2Cu and Ti_2Ni are formed.

Similar effects of coherent GP zones and semi-coherent Ti_2Ni spherical precipitates on the martensitic transformation, as those found on Ti-rich Ni-Ti films, were observed in Ti-rich Ni-Ti-Cu thin films. Films containing GP zones showed a smaller transformation hysteresis (strain versus temperature), despite the films containing semi-coherent spherical Ti_2Ni, owing to the capacity of the elastically deformed GP zones to exert a back stress on the matrix during the reverse martensitic transformation. This phenomenon was further confirmed by HR-TEM observations performed on Ti-rich $Ti_{51.5}Ni_{33.1}Cu_{15.4}$ films annealed at different temperatures.

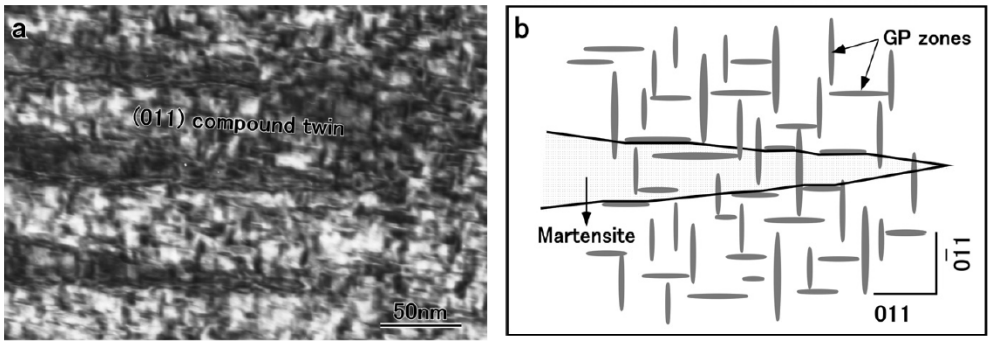

Figure 1.16 – BF TEM Image of several (011) martensitic fingers in $Ti_{51.5}Ni_{33.1}Cu_{15.4}$ film annealed at 773 K for 1 hour with GP zones (a), schematic illustration of a (011) martensite variant tip interacting with GP zones (b) [100].

Figure 1.16 shows GP zones that were elastically deformed when the growing martensite variants met them in the length direction, conversely, they represented an obstacle when the martensite variants met them in the width direction, the martensite plate sometimes changing direction or width and producing a martensite finger with a wavy shape [101]. Further increase of the annealing temperature led to the suppression of the GP zones and to the growth of Ti_2Ni spherical precipitates, semi-coherent with the B2 matrix, which limited or inhibited the growth of martensite variants in the parent phase [100], as shown in Figure 1.17.

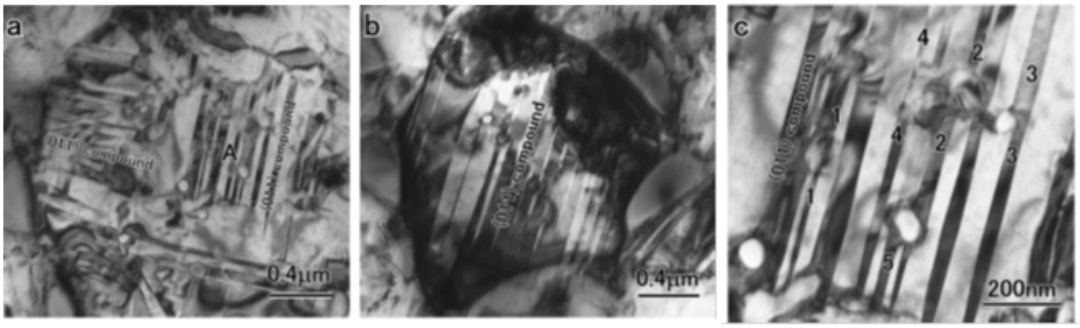

Figure 1.17 - (a) Bright field image of (011) compound twins in $Ti_{51.5}Ni_{33.1}Cu_{15.4}$ thin film annealed at 500°C for 1 hour with spherical Ti_2Ni precipitates. (b) A grain with single-pair (011) compound twins. (c) Enlarged bright field image of region A in (a) [100].

Further studies were carried out by increasing the Cu content up to 37.3 at.%, keeping the Ti level constant at about 51.5 at.%, so as to evaluate the changes in microstructure introduced by higher Cu contents. TEM analyses (Figure 1.18) revealed that films with 23.4 at. % Cu and annealed at 500 and 600°C, contained many precipitates within the grains (GP zones and coherent Ti_2Cu plate precipitates). Ti_2Cu coherent plate-like precipitates were found to have a similar effect as the GP zones on the martensitic transformation. No precipitates were observed in the grain interior for annealing temperature of 700°C.

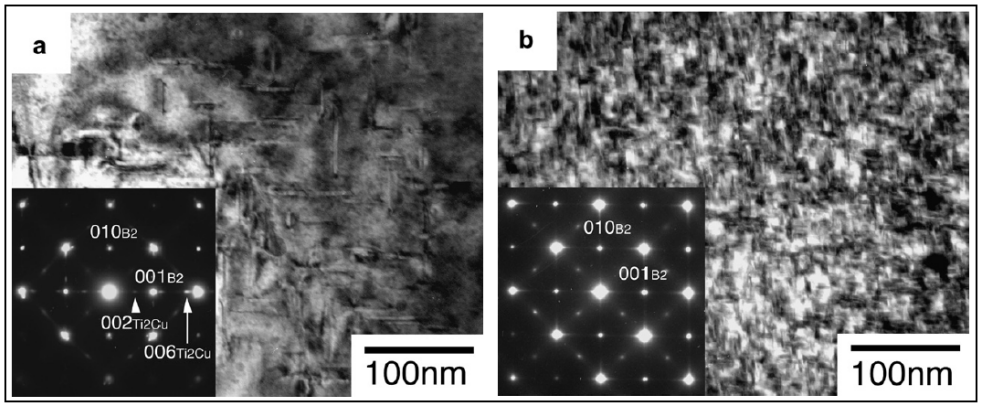

Figure 1.18 – Precipitates within the grains and corresponding electron diffraction patterns of $Ti_{51.4}Ni_{25.2}Cu_{23.4}$ films annealed at (a) 600°C and (b) 500°C for 1 hour [102].

For a higher Cu content (27.6 at.%), films annealed at 500°C showed precipitates within the grains (Ti_2Cu), but no precipitates were observed in the grain interior for annealing temperatures of 600 and 700°C. When the Cu content was further increased, no precipitates were detected at all within the grains. For a Cu content

lower than 15.4 at.% semi-coherent Ti_2Ni precipitates appeared in the B2 grain owing to the Ti content being above 50 at.%. Interestingly, TEM observations revealed that the grain size of the $Ti_{51.4}Ni_{25.2}Cu_{23.4}$ film was approximately 1 µm irrespective of the annealing temperature, while it decreased with increasing Cu content (Figure 1.19). The 33.1 and 37.5 at.% Cu, films annealed at 500°C, showed extremely small grain sizes (120 and 50 nm, respectively), compared to the other films [102].

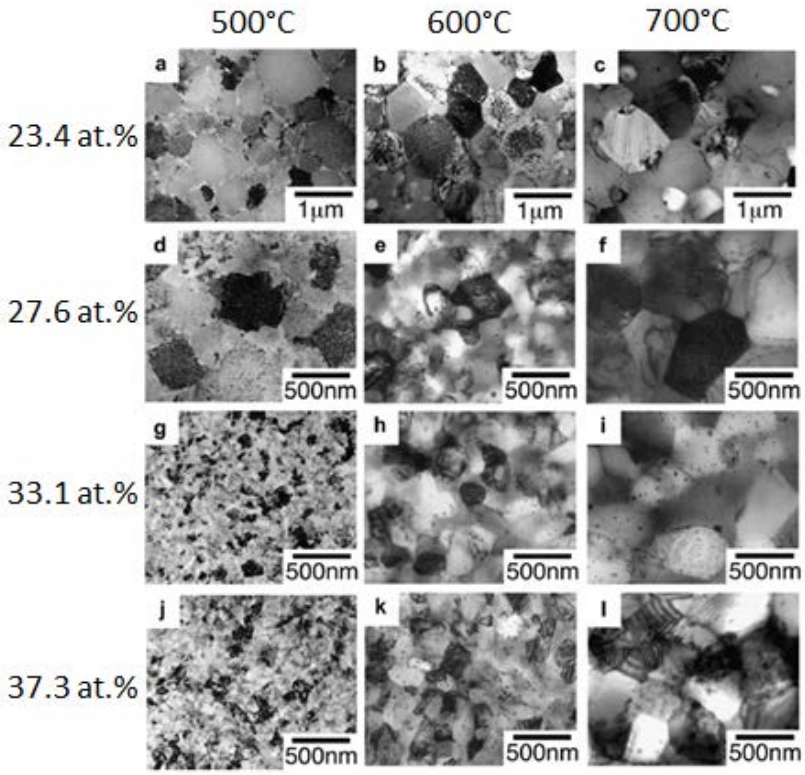

Figure 1.19 - Structures of (a – c) $Ti_{51.4}Ni_{25.2}Cu_{23.4}$, (d – f) $Ti_{51.3}Ni_{21.1}Cu_{27.6}$, (g – i) $Ti_{51.2}Ni_{15.7}Cu_{33.1}$, and (j – l) $Ti_{51.4}Ni_{11.3}Cu_{37.3}$ films annealed at (a, d, g, j) 500, (b, e, h, k) 600, (c, f, i, l) 700°C for 1 hour [102].

Ishida et al. [103] led some investigations on (Ni,Cu)-rich Ti-Ni-Cu thin films, with a Cu content ranging between 6.2 – 33.5 at.%, to assess the effects of the post-deposition annealing process as well as that of Cu content on the microstructure. As also found for Ti-rich Ni-Ti-Cu compositions, the grain size of (Ni, Cu)-rich Ni-Ti-Cu films decreased with increasing Cu content, while it resulted unaffected by the annealing temperature for a Cu content $<$ 28 at.%; conversely for a higher Cu content slightly coarsened grains were observed with increasing annealing temperature.

X-ray diffraction analyses, for films annealed at 500, 600 and 700°C for 1 hour, revealed the presence of two phases: $Ti(Ni,Cu)_2$ and TiCu for different annealing

temperatures. For annealing at 500°C, $Ti(Ni,Cu)_2$ plate precipitates, coherent with the B2 matrix, were found for a Cu content below 27.8 at.%, while for higher Cu content, i.e. 33.5 at.%, TiCu precipitates, still coherent with the B2 matrix, were found rather than $Ti(Ni,Cu)_2$.

In all the films annealed at 500°C $Ti(Ni, Cu)_2$ plate precipitates were observed, except for the film with 33.5 at.% Cu, where TiCu precipitates were found instead. These precipitates were densely distributed in the grains interior of films annealed at 500°C, while their density decreased in the grains interior of films annealing at 600 and 700°C to compensate the formation of grain boundary precipitates. In fact, $Ti(Ni, Cu)_2$ plate precipitates in the grain interior were found to coarsen with increasing annealing temperature, thus losing their interfacial coherency with the B2 matrix. $Ti(Ni, Cu)_2$ formed in the films annealed at 500°C were found to have the same effects as the GP zones on the martensitic transformation, the $Ti(Ni, Cu)_2$ being as thin as GP zones. Conversely, coarse $Ti(Ni, Cu)_2$ in the B2 matrix of films annealed at 600°C were found to seriously impede the growth of martensitic plates, as is clearly shown in Figure 1.20. Such a detrimental effect enhanced with coarsening of the $Ti(Ni, Cu)_2$ with increasing annealing temperature [94]. The $Ti(Ni, Cu)_2$ precipitates were found to have a thickness of about 1 – 2 nm, much smaller compared to the thickness of TiCu precipitates (~ 7 nm). Such a difference was attributed to the misfit strain between matrix and precipitates, which was higher for the $Ti(Ni, Cu)_2$ precipitates.

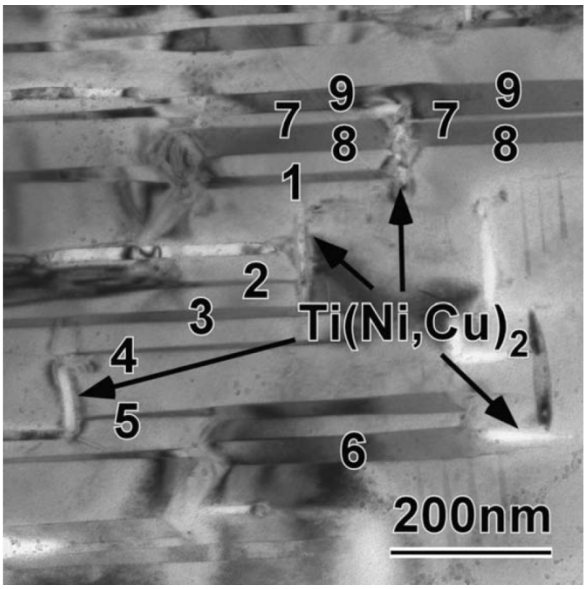

Figure 1.20 – Resistance of the coarse $Ti(Ni, Cu)_2$ precipitates to the growth of martensite in Ni-Ti-Cu thin films annealed at 600°C [94].

However, grain boundary precipitates become prominent with increasing annealing temperature at the expense of precipitates in the grain interior. A phase with a granular morphology was segregated at the grain boundary for films with Cu content $<$ 23.3 at.%, while plate precipitates were found at the grain boundary for Cu content $>$ 27.8 at.%. These two different phases at the grain boundaries corresponded to TiCu and Ti(Ni, $Cu)_2$ phases, respectively. As the solubility of Ni in the B2 matrix was reported to decrease with increasing Cu content, Ni atoms were expected to be removed from the matrix with increasing Cu content, thus causing a change in chemical composition of the grain boundary precipitates from TiCu to Ti(Ni, $Cu)_2$ for low Cu content ($\leq$ 23.3 at.%). On the other hand, for films with high Cu content ($\geq$ 27.8 at.%), TiCu precipitates were found at the grain boundaries already in the early stage of the precipitation process, while with increasing annealing temperature these precipitates evolved toward a Ti(Ni, $Cu)_2$ composition and structure. This transition was thought to be activated by the diffusion of Ni from the grain interior to the grain boundaries with increasing annealing temperature [103].

3. Mechanical properties of Ni-Ti(-Cu) thin films

Sputter deposited thin films were characterized by experimental techniques, as either free-standing films, where the measured properties were intrinsic to the film itself, or as a film attached to the substrate, where the measured properties can be affected by the substrate. Based on this difference, the experimental technique employed to characterise free-standing films was micro-tensile test (details are reported in the appendix A), whereas the substrate-attached thin films were characterized by nanoindentation.

3.1 Nanoindentation

With the growing interest in characterization of small volumes of material, micro-indentation and especially nanoindentation techniques play an important role in probing the mechanical and functional properties of thin films.

Indentation testing is a simple method that consists of probing a sample whose mechanical properties are unknown with another material whose properties are known. This technique was a development of the Vickers/Brinell hardness, which in turn has its origins in Mohs hardness scale, where materials that are able to leave a permanent scratch in another were ranked harder with diamond assigned the maximum value of 10 on the scale [104]. Nanoindentation is an indentation test in which the length scale of the penetration is measured in nanometres. Apart from the displacement scale involved, the main difference from conventional hardness testing in most nanoindentation testing is the indirect measurement of the contact area[3]. In fact, while in normal indentation the contact area is calculated by measuring directly the imprint left on the sample surface, in nanoindentation tests the imprint left on the surface is too small to be conveniently measured directly. Therefore the determination of the indenter geometry is determined by indenting a standard test specimen (fused silica, whose elastic modulus and Poisson's ratio are known) at different maximum loads (see ref. [104] for further details). Therefore by combining information such as penetration depth and geometry of the tip, it is possible to derive the contact area at full load. For this reason nanoindentation is also known as depth-sensing indentation.

The maximum penetration depth, for a specific load, together with the slope ($S = dP/dh$) of the unloading curve, measured at the tangent to a data point at maximum load (Figure 1.21), lead to a measure of both hardness and elastic modulus of the sample material. The procedure outlined by Oliver and Pharr [105] is one of the most widely used for calculating hardness and elastic modulus from nanoindentation data.

[3] Area of contact between indenter and sample projected on a plane normal to the loading direction.

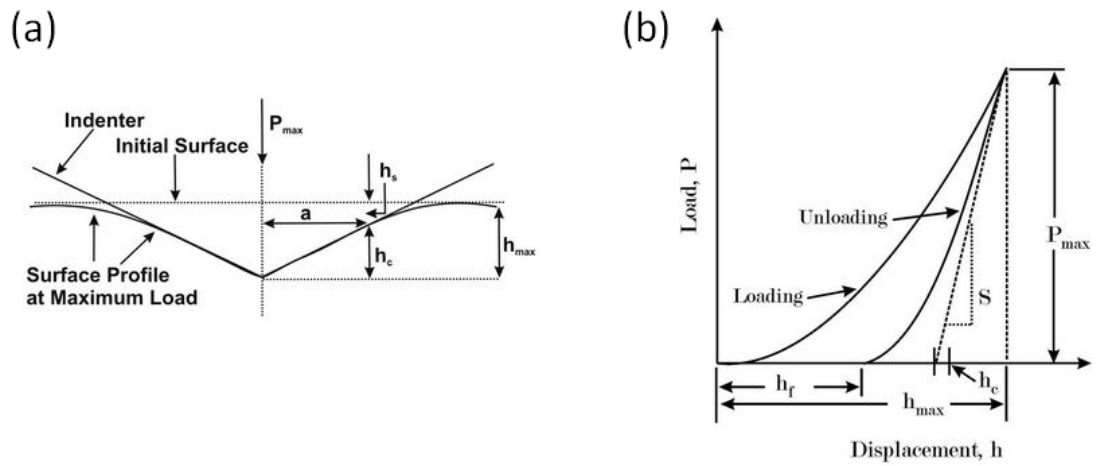

Figure 1.21 – Nanoindentation: (a) schematic representation of the indentation process: P_{max} (maximum load), a (contact radius), h_{max} (maximum penetration depth), h_c (contact depth), h_s (depth at the contact boundary), h_f (residual depth); (b) corresponding (schematic) load-displacement curve [104].

Regarding probes used to test materials' surface, Berkovich tips are generally used in small-scale indentation studies owing to the fact that edges of the pyramid are more easily constructed to meet a single point compared to the four-sides Vickers pyramid. Berkovich tip is a three-sided pyramid with a face angle of 65.3°, which gives the same projected area-to-depth ratio as the Vickers indenter. The tip radius of Berkovich tips ranges between 50 – 250 nm.

Nanoindentation revealed to be a useful technique through which mechanical properties such as hardness and elastic modulus can be consistently measured and combined together[4] in order to provide information about the performance of tested materials particularly for tribological applications; properties such as: wear resistance and toughness can be evaluated – see ref. [106, 107] for details. Furthermore load – displacement data can be used to define other useful parameters with the aim to characterise the functional behaviour of the probed materials and correlate it to the mechanical properties as well. Particularly, the capability of a material to absorb energy (during impact as a practical example) can be quantified by calculation of the area enclosed by the load – displacement curve (usually referred as plastic work, W_p). Similarly, the capability of a material to absorb and restore energy after being probed can be quantified by calculating the area underneath the unloading curve (usually

[4] The most used combinations are H/E_r and H^3/E_r^2 ratios which provide information about wear behaviour and resistance to plastic deformation, respectively [142, 143].

referred as elastic work, W_e). Even in this case, the combination[5] of elastic and plastic works gives details about the functional behaviour of the material. The functional behaviour of tested materials can similarly evaluated by combining the maximum (h_{max}) and residual depth (h_f) to define parameters such as the depth recovery ratio defined as ($h_{max} – h_f$)/ h_{max} [108]. Some of these concepts are employed to characterise Ni-Ti(-Cu) thin films as it is reported in the following sections.

Nanoindentation is also employed to measure other mechanical properties of the tested material such as: creep, strain-hardening exponent, fracture toughness and viscoelastic properties. More advanced methods are employed to study residual stresses in thin films, material properties at high/low temperatures, fretting, impact and fatigue even in specific environment (liquid, level of humidity).

3.2 Nanoindentation of Ni-Ti(-Cu) thin films

With the growing interest in characterization of small volumes of material, nanoindentation techniques are playing an important role in probing the mechanical and functional properties of shape memory alloy thin films. A number of authors have used nanoindentation as a means of characterizing the properties of these films, and most of these works focused on investigating Ni-Ti based thin films. Because of the particular functional aspects related to shape memory materials, in addition to the thermomechanical characterization, functional characterization by nanoindentation measurements was also of particular interest.

One of the first studies performed on Ni-Ti thin films by nanoindentation was carried out as a comparison with the bulge test, with the aim of evaluating the complementarity of these techniques for the examination of the thermomechanical behaviour of Ni-Ti films. The investigation provided clear evidence of the phase transformation induced during penetration, as well as valuable information about the mechanical properties for both the martensitic and austenitic phases. Young's modulus

[5] The W_p/W_{tot} ratio is known as plasticity index which, in the case of nanoindentation, can be taken as the ratio of the area enclosed between the loading-unloading curves to the area under the loading part of the curve. This index provides information about the plastic behaviour of probed material during the contact [142] and is distinct from the plasticity index associated with contact of surface of varying roughnesses.

and hardness were found to decrease with increasing penetration depth, in the nano- and micro-scale [109].

Ni-Ti based thin films are usually amorphous in the as-deposited condition; therefore an annealing process is required to have fully crystalline and thus functional layers. Nanoindentation was employed to understand how the mechanical properties of Ti-rich Ni-Ti thin films evolve during the crystallisation process. $Ni_{48.3}Ti_{51.7}$ thin films (1.1 µm thick) with different degrees of crystallization, showed that the crystalline regions, in the partially crystallised film (region B in Figure 1.21), behaved like the fully crystallised film, with a lower Young's modulus compared to the amorphous region [110].

On the other hand, the amorphous region in the partially crystallised film (region A in Figure 1.21) exhibited a higher hardness and Young's modulus compared to the as-deposited film. The observed increase in mechanical properties in the amorphous region of the partially crystalline film was attributed to a structural relaxation.

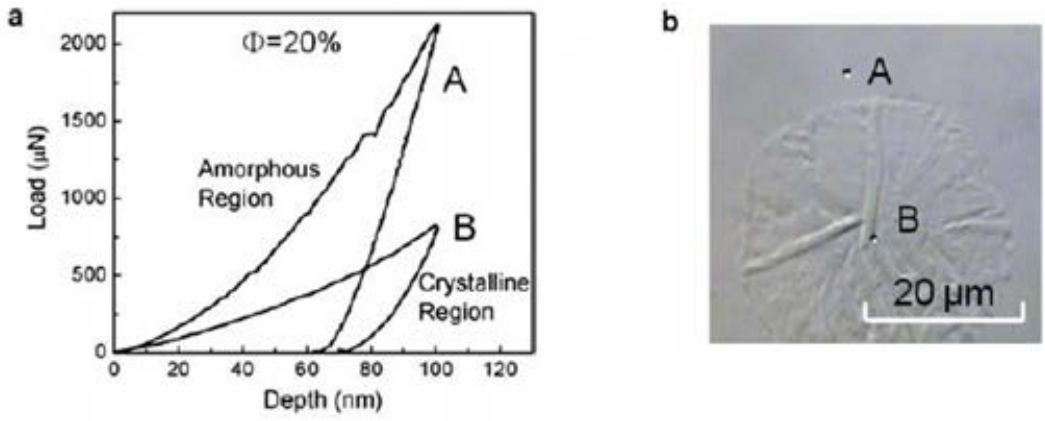

Figure 1.21 – Nanoindentation of partially crystalline Ni-Ti thin film: (a) a typical bimodal load–displacement response of a partially crystallized film, (b) the corresponding interferometry image indicating the indentation locations (A and B) [110].

Basically, during annealing an atomic rearrangement occurs prior to the nucleation and growth processes of crystallisation, consequently the film became less glassy and developed a short-range ordered structure. For this Ti-rich $Ni_{48.3}Ti_{51.7}$ thin film a systematic softening accompanied the crystallisation process, although the opposite behaviour was observed for a $Ni_{48.6}Ti_{51.4}$ thin film (4 µm thick) by *Zhang et al.* [111], where the lower hardness for the amorphous film was attributed to the low compressive stress state and disordered structure compared to the crystalline

structure. These differences suggest that the deposition process plays a significant role on the subsequent mechanical properties of these films and different evolution in hardness and elastic modulus during annealing can be expected depending on the deposition process itself.

The film thickness may also play a role in the change in mechanical properties, as the residual stress generated in the amorphous as-deposited films was found to be affected by the film thickness, i.e. by decreasing the thickness especially below 200 nm the residual stress in the film drastically increases [112]. The Ar gas pressure was also found to affect the residual stress in the film, i.e. a higher residual stress was found for a higher gas pressure regardless of the film thickness in the range 0.2 – 3.5 μm, although thinner films showed higher residual stress regardless of the fabrication process (deposition at room temperature followed by annealing or deposition at high temperature) [70].

Nanoindentation measurements carried out on as-deposited and annealed Ni-rich $Ni_{60}Ti_{40}$ thin films (500 nm thick) showed a higher Young's modulus and hardness for the annealed films. These mechanical properties exhibited a slight increasing trend as the load applied increased in both the amorphous and crystalline state (see Figure 1.22) [113].

The film composition affects the transformation temperatures and consequently the dominant phase at a specific temperature. Considering that most of the potential applications involving shape memory alloy thin films are around room temperature, nanoindentation studies on Ni-Ti thin films were often carried out at ambient temperature.

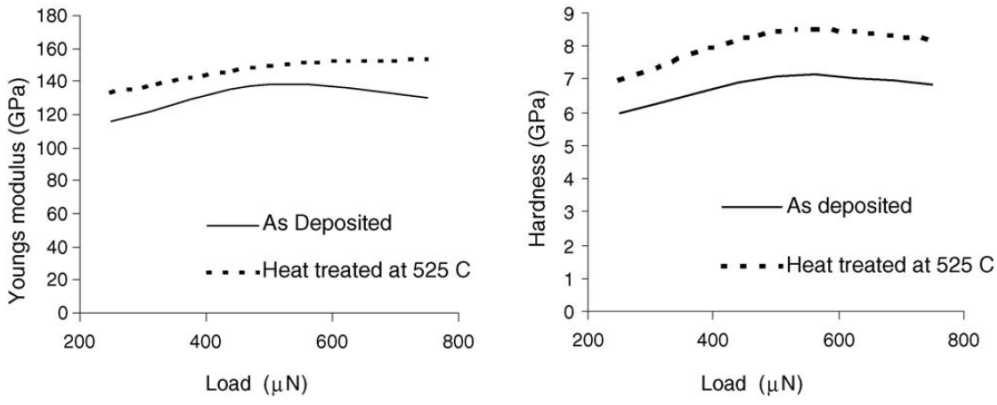

Figure 1.22 - Variation of Young's modulus and hardness with load for the as deposited and amorphous films [113].

Mechanical properties at a specific test temperature are affected by the film chemical composition. In fact, Ni-rich Ni-Ti films (normally austenitic at ambient temperature) exhibit higher hardness and elastic modulus compared to Ti-rich and near-equiatomic Ni-Ti films (normally martensitic at ambient temperature) [78]. Furthermore, it was reported that for Ti-rich Ni-Ti thin films, by shifting the chemical composition away from the equiatomic condition (i.e. increasing amount of Ti) higher hardness and elastic modulus were found [114].

A more direct comparison in mechanical properties between austenitic and martensitic Ni-Ti thin films, as well as the reliability of nanoindentation, as a means of interrogating the mechanical properties of materials that undergo a thermally-induced phase transformation, was recently reported by *Huang et al.* [115]. Specifically, *in-situ* heating nanoindentation experiments were carried out in order to demonstrate the similar themo-mechanical properties of a Ni-rich and Ti-rich Ni-Ti thin film in their austenitic state.

Table 1.3. The Young's modulus and hardness of Ni-Ti shape memory thin films [115].

		Mechanical properties at room temperature (GPa)			Mechanical properties at 110°C (GPa)	
Sample	Composition	Phase	Modulus	Hardness	Modulus	Hardness
A	Ti–48.3 at. % Ni	Martensite	73.7 ± 4.2	2.5 ± 0.3	89.0 ± 2.1	4.0 ± 0.2
B	Ti–50.8 at. % Ni	Austenite	80.1 ± 2.1	4.4 ± 0.1	92.8 ± 3.1	4.2 ± 0.2

The increase in Young's modulus with increasing temperature for the film B (Table 1.3) was attributed to the transformation of residual martensite to austenite. Very similar results in terms of mechanical properties (Table 1.3) were observed in the films tested at 110°C in their austenitic state, i.e. film A austenitic at 110°C and film B austenitic at both ambient temperature and at 110°C. The similar load-displacement curves found at 110°C for Ni-rich Ni-Ti film (sample A in table 1.3) and the Ti-rich Ni-Ti film (sample B in table 1.3) corroborated the significant effect of the phase transformation on the mechanical response of sputtered Ni-Ti films, as well as the capability of this hot stage test to measure these changes.

Kumar et al. [116] investigated the effects of substrate and annealing temperatures on the mechanical properties of Ti-rich Ni-Ti thin films. $Ni_{48.8}Ti_{51.2}$ films (1 µm thick) were

deposited by heating the substrate at two different temperatures followed by annealing for 4 hours at different temperatures.

In particular, films deposited at 300°C were annealed at 300, 400, 500 and 600°C, while those deposited at 400°C were annealed at 400, 500 and 600°C. These films exhibited an amorphous structure in the as-deposited and annealed ($<$ 400°C) conditions, while a crystalline structure was formed for annealing at temperatures $\geq$ 500°C. Figure 1.23 shows that mechanical properties were not affected by the substrate temperatures below 400°C and by the subsequent annealing process at temperatures below 400°C, as no microstructural changes were introduced in the films for depositing/annealing at temperatures $\leq$ 400°C.

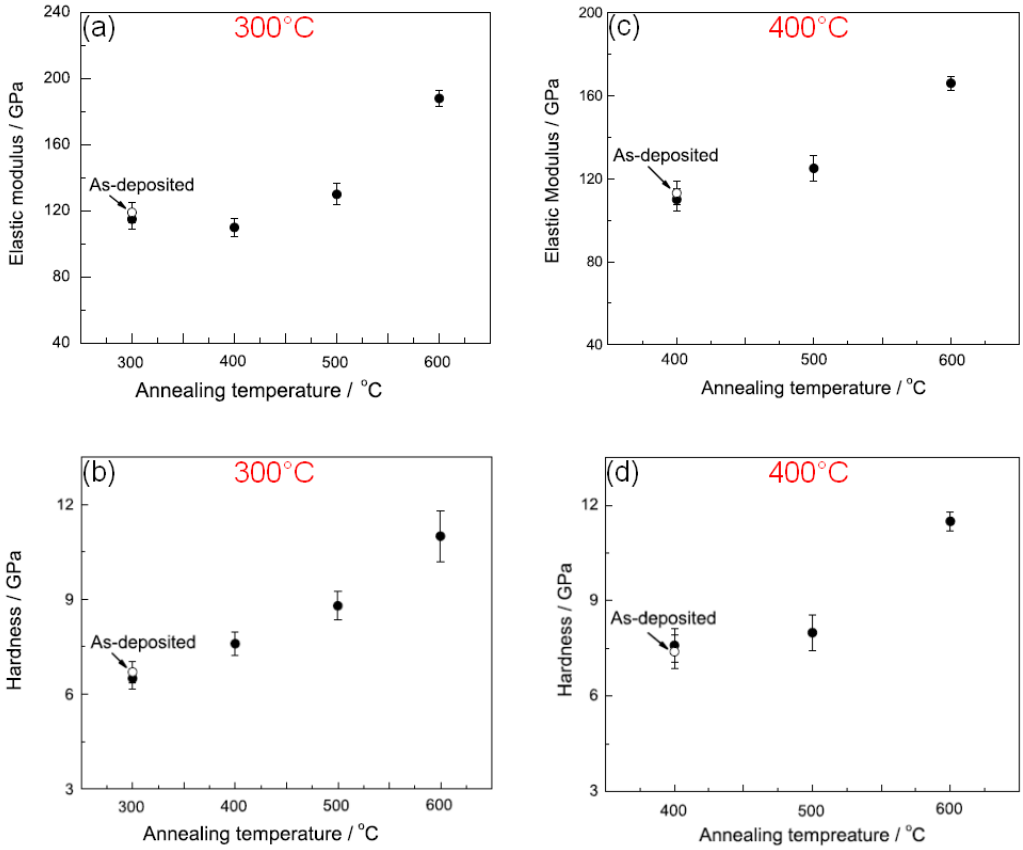

Figure 1.23 – Variation of elastic modulus and hardness for films deposited at 300°C ((a) and (b)) and 400°C ((c) and (d)) [116].

The high hardness showed in Figure 1.23 was attributed to the high compressive stress found in these films. By annealing at temperatures $\geq$ 500°C a clear increase in mechanical properties was observed (see Figure 1.23) owing to the degree of crystallisation increasing with the annealing temperature. In this case, increasing mechanical properties were found with increasing annealing temperature according to

the results reported by *Zhang et al.* [111] and conversely to the results found in another study [110, 113] previously mentioned. In fact *Zhang et al.* found that when as-deposited $Ti_{51.3}Ni_{48.7}$ thin films were annealed at 450°C for 1 hour, the maximum penetration depth decreased and the recovered depth increased compared to the amorphous film, whereas further increases in annealing temperature produced the opposite effect. The Oliver and Pharr method, applied to the load-displacement curves, provided an increasing micro-hardness (from 8 to 15 GPa) and Young's modulus (from 125 to 170 GPa), when the annealing temperature increased from 450°C to 600°C. The rising trend for mechanical properties was ascribed to the degree of crystallization at the lower annealing temperatures, and to the presence of precipitates, which improved the resistance to plastic deformation of the crystalline thin films, at the higher annealing temperatures. This further highlighted the strong relationship between the fabrication process as well as post-deposition thermal treatments, on the subsequent nanoindentation response of Ni-Ti thin films.

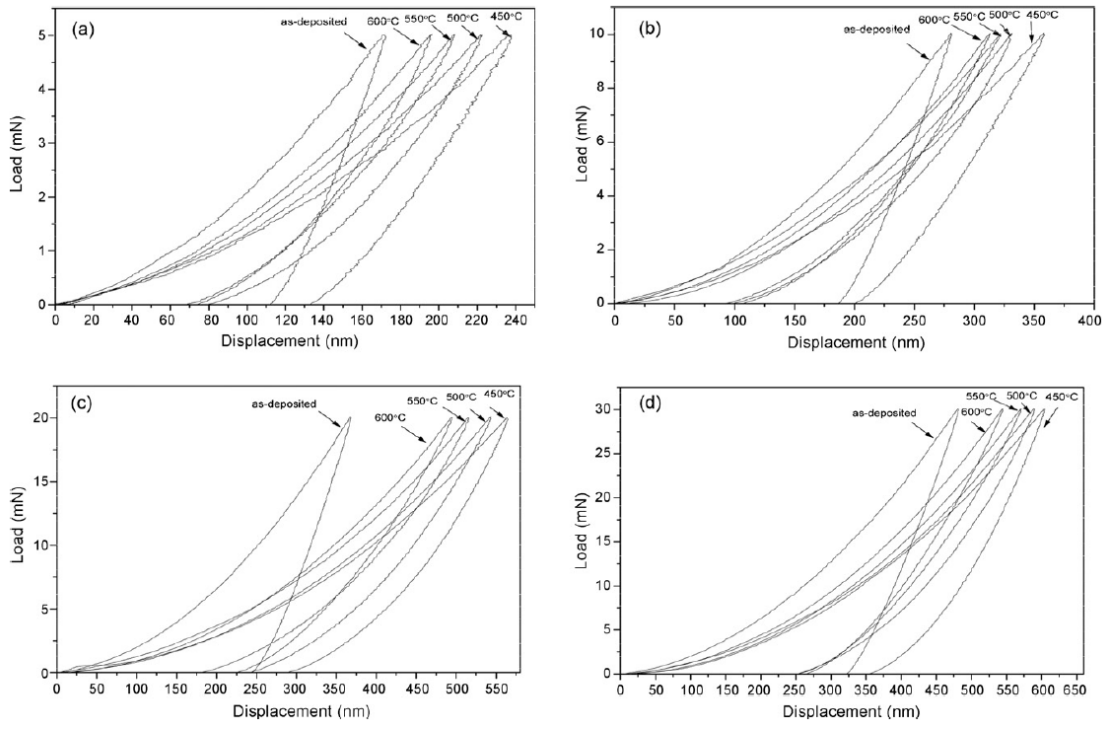

Figure 1.24 - Representative nanoindentation load-displacement curves for as-deposited and annealed Ti-Ni thin films at different temperatures under (a) 5 mN, (b) 10 mN, (c) 20mN and (d) 30 mN [80].

Figure 1.24 shows the load-displacement curves obtained at different loads for a $Ni_{51.7}Ti_{48.3}$ thin film (6.5 µm thick) annealed for 1 hour at 450, 500, 550 and 600°C. The

film in its as-deposited condition resulted stiffer compared to the annealed films. The load-displacement data allowed the calculation of the elastic and dissipated work and consequently, the definition of an energy recovery ratio (elastic to total work ratio) shown in Figure 1.25, through which the superelastic behaviour was characterized. In particular, it was found that with increasing annealing temperature, the energy recovery ratio increased, achieving a maximum value of about 70 % after annealing at 550°C, whereas further increases in annealing temperature produced a diminution of the aforementioned ratio, due to the shift in transformation temperatures. This shift was related to the formation of Ni_4Ti_3 precipitates in the grain interior, which decreased the Ni/Ti ratio thus allowing the presence of martensite at the test temperature [80].

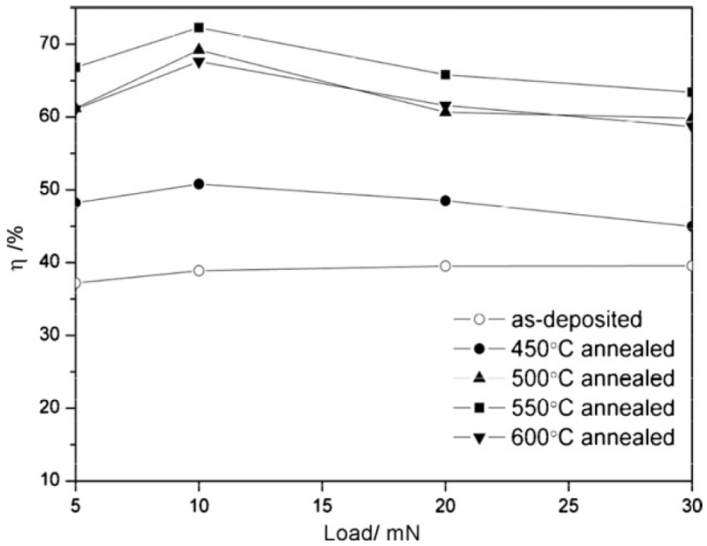

Figure 1.25 - Load dependence of the energy recovery ratio η for as-deposited and annealed $Ni_{51.7}Ti_{48.3}$ thin film at 450, 500, 550 and 600°C, respectively [80].

Nanoindentation in combination with AFM was employed to evaluate the shape memory effect in Ti-rich Ni-Ti thin films (1.7 and 10 µm thick) [25]. The profile of the residual depth left on the surface after indentation by a Berkovich tip (100 nm tip rounding) was imaged before and after heating above A_f. The depth recovery ratio was defined as the depth recovery after heating divided by the depth before heating. Figure 1.26 shows the depth recovery ratio in relation to the residual depth for different film thicknesses and type of tip.

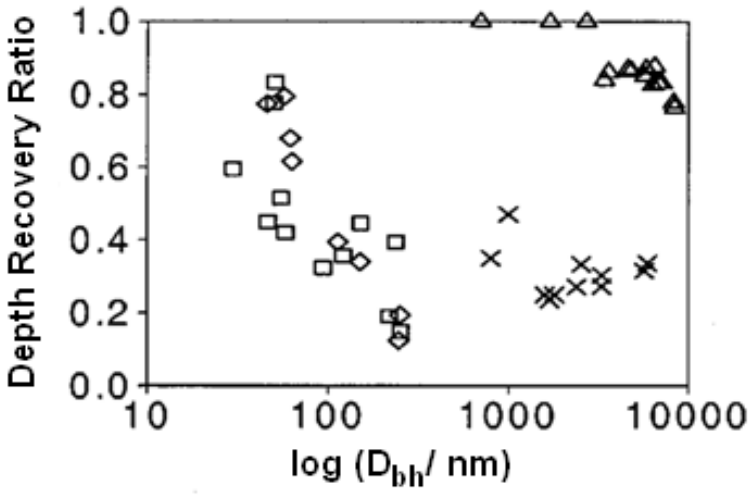

Figure 1.26 – Comparison of nanoindentation results for 1.7 (square) and 10 µm (rhombus) thick thin films to spherical (triangle) and Vickers (cross) micro-indentation [25].

For penetration depths lower than 100 nm an increase in depth recovery ratio was observed and ascribed to the tip rounding of the indenter. It was suggested that pyramidal tips such as: Berkovich and Vickers generate a high stress field underneath the indented surface, thus promoting plastic deformation. On the contrary, by using a spherical indenter a much weaker stress field is generated (less plastic deformation) and larger shape recovery can be achieved upon heating. A similar result was found for superelastic Ni-Ti layers (1 – 2 µm thick) annealed for 1 hour at 500°C. In particular the dissipation energy was quantified by probing superelastic layers by two different tips, i.e. spherical tip (15 µm tip radius) and cube-corner diamond tips (nominal tip radius equal to 116, 240 and 685 nm) [117]. Figure 1.27 shows that dissipation energy[6] increases with maximum indentation load by using the spherical tip and the cube-corner tip with a radius of 685 nm (for smaller radii no superelasticity was observed). For a given load, a significantly larger amount of energy was dissipated with the sharper tip.

This phenomenon was explained by considering the intensification of the stress field generated in the vicinity of the tip, which is much higher when a sharper tip is used. In particular, the higher stress generated by a sharper tip enhance the energy dissipated by mainly two mechanisms: (a) the martensitic variant generated during phase transformation must overcome the internal stress generated during the phase change

[6] Area within the load-displacement hysteresis.

in order to shrink back to the parent austenitic matrix and (b) energy can be dissipated as frictional heat due to the interaction between the boundaries of the imperfect austenitic matrix and the martensite.

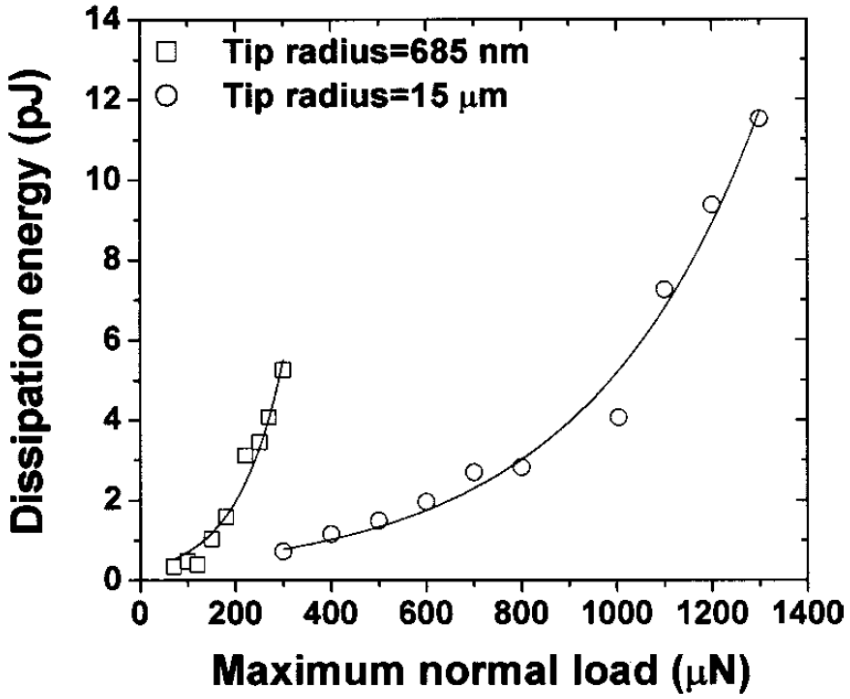

Figure 1.27 – Effects of maximum normal load and tip radius on the dissipation of energy in indented superelastic Ni-Ti films [117].

The same Ni-Ti film mentioned above was tested by cyclic nanoindentation (at the same location on the film surface) by using a cube-corner diamond tip (685 nm tip rounding) at a constant penetration depth of about 20 nm [118]. The energy dissipated in every cycle decreased and became constant after about 20 cycles. It was suggested that the stress-induced martensite crystals underwent repeated rearrangements to obtain energetically favourable orientations for their nucleation and growth in the austenitic matrix.

This process decreased the strain mismatch at the austenite/martensite boundaries and the number of possible twin variants, and consequently the energy dissipation necessary to overcome the abovementioned strain mismatch. Stress-induced defects also contributed to increasing the energy dissipation through frictional heat, which however mitigated after about 20 cycles.

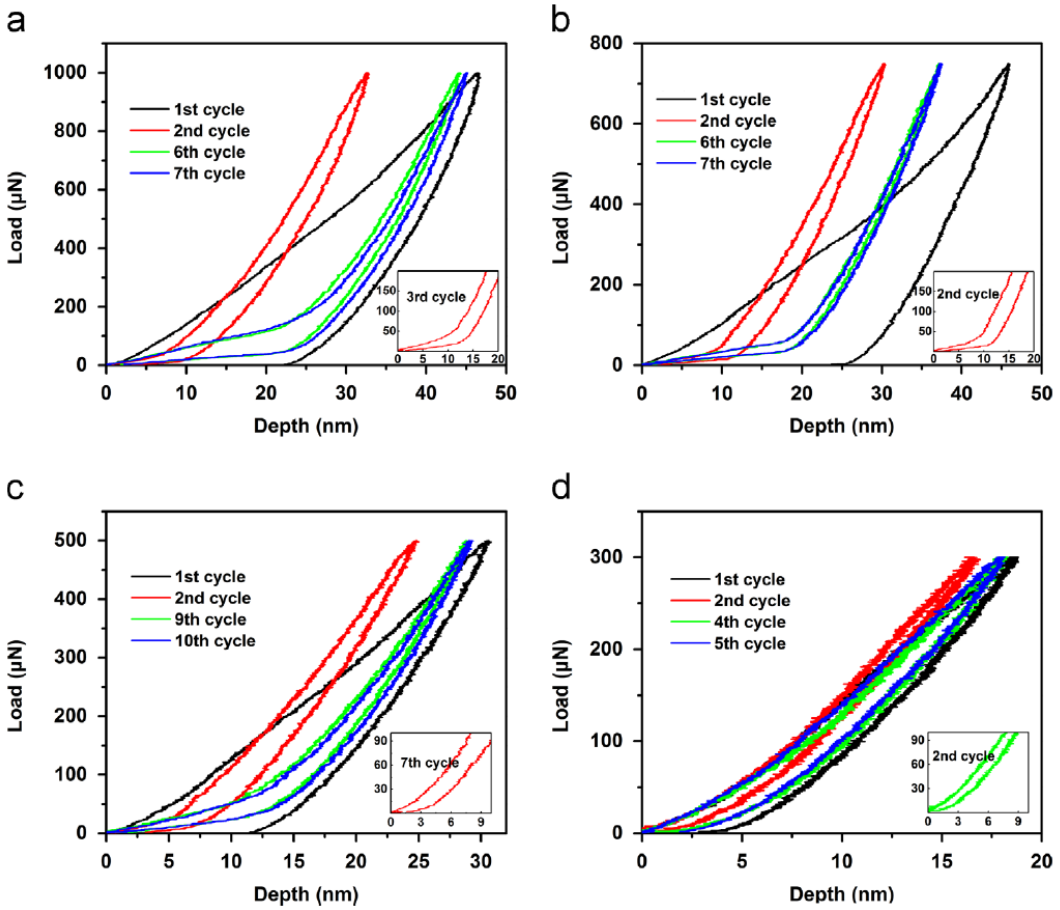

Figure 1.28 – Cyclic load-displacement curves of TiNi film under different maximum loads: (a) 1 mN, (b) 0.75 mN, (c) 0.5 mN and (d) 0.3 mN [119].

After this training consisting of 20 cycles the nucleation and growth of the martensitic crystals and the subsequent detwinning process occurred at a lower energy compared to the initial Ni-Ti microstructure.

Multiple nanoindentation experiments were carried out on a thinner Ni 49±0.4 at.% – Ti films (500 nm thick) in order to assess its superelastic properties [119] by using a Berkovich diamond tip (250 nm nominal tip rounding). Even in this case steady-state superelasticity was achieved after 6 consecutive cycles with a maximum load of 1 mN (Figure 1.28 (a)). For lower loads a larger number of cycles were needed (i.e. 9 cycles for a load of 05 mN, Figure 1.28 (c)) to attain steady-state superelasticity, thus suggesting that more cyclic deformation is required at lower stress level. For a very low load (0.3 mN) the load-displacements curves achieved steady-state after 4 cycles (Figure 1.28 (d)), however a different deformation mechanism took place. In order to gather more insight into the deformation behaviour of the film, the load-displacement curves were converted to nominal stress-strain curves as showed in Figure 1.29.

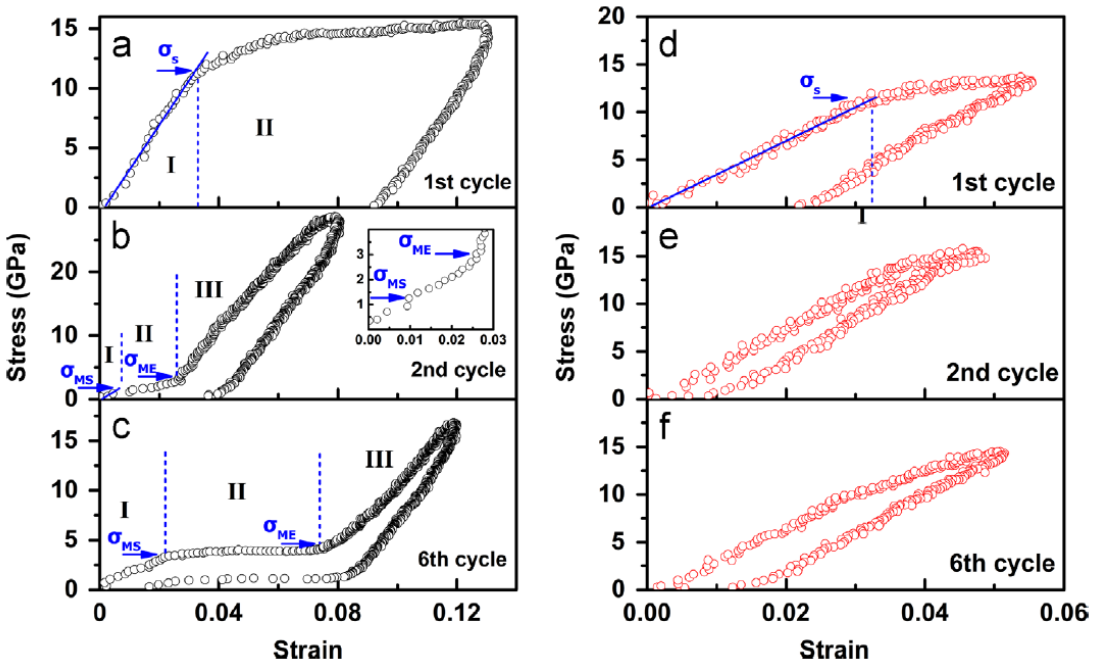

Figure 1.29 – Calculated indentation stress-stain curves for maximum load of 1 mN (left column) and 0.3 mN (right column) in different indentation cycles. (a),(d) 1st cycle (I: B2 elastic ; II: B2 plastic); (b),(e) 2nd cycle (I: B2 elastic; II: B2-B19'; III: B19' elastic); and(c),(f) stabilized cycle (I: B2 elastic; II: B2-B19'; III: B19' elastic).

In the first cycle (Figure 1.29 (a)) an elastic (I) and plastic (II) deformation behaviour was observed and attributed to the inverse Hall-Petch relationship owing to the small grains found in this film (40 nm in average with subgrains as small as 7 – 13 nm). A large dislocation density was found by TEM underneath the indented surface after the first cycle, which was found to increase the critical stress for slip of the austenitic matrix, as the film exhibited a considerable higher hardness after the first cycle. In Figure 1.29 (b) and especially in Figure 1.29 (c) the typical stress-strain curve corresponding to the stress-induced martensitic transformation was found.

On the other hand, for a lower load (i.e. 0.3 mN) the deformation behaviour of the film was mostly dominated by the elastic deformation of austenite as evident in Figure 1.29 (d) – (f). This result suggested that for low load no plastic deformation of the austenitic phase was induced; plastic deformation increases the critical stress for slip (work hardening) of the austenitic phase itself. Consequently no relevant evidence of the stress-induced martensitic transformation was observed. In order to have a stress-induced martensitic transformation, the critical stress for slip in the film has to be higher than the critical stress for induced phase transformation. It was proposed that

the repeated deformation cycles induced by nanoindentation caused the formation of dislocations, which increased the critical stress for slip of the austenitic matrix on one hand and a stress-induced grain growth in this nano-crystalline Ni-Ti film on the other hand. Typically, the stress required to induce martensitic transformation decreases with increasing grain size. Therefore, these simultaneous effects made the stress-induced martensitic transformation energetically more favourable than plastic deformation of the nano-crystalline structure.

Wood et al. [108] performed the first investigation on the characterization of binary Ni-Ti ternary Ni-Ti-Cu thin films (2 µm thick) by nanoindentation at different test temperatures. It was suggested that in order to investigate the functional properties of these films, a spherical diamond tip (10 µm tip radius) is suitable owing to the lower stress gradient introduced by this type of tip compared to pyramidal shapes. In terms of load-displacement curves, the transition from an elastic-plastic response (typical for martensitic films) to the superelastic response is shown in Figure 1.30, where a progressive decrease of both maximum and residual penetration depth with increasing temperature up to A_f (100°C) was clearly observed.

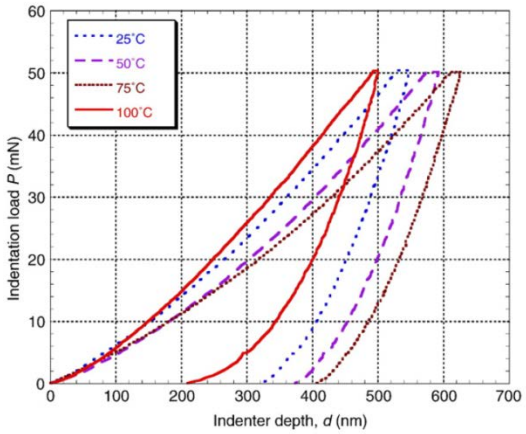

Figure 1.30 - Load-displacement plots obtained during indentation of a Ti-50.2at.% Ni thin film, carried out at various temperatures around and below A_f, using a small spherical (r = 10 µm) indenter [108].

The superelastic effect was quantified for Ni-Ti and Ni-Ti-Cu films by comparing the remnant depth ratio[7] obtained for indentations in a range of temperatures between M_f and A_f (Figure 1.31). It was found that once a sufficient austenitic volume fraction was thermally-induced in the film a significant decrease in remnant depth ratio was

[7] Ratio between the residual depth and the depth at maximum load.

observed, thus suggesting that most of the deformation was recovered upon unloading by the inverse (martensite → austenite) phase transformation.

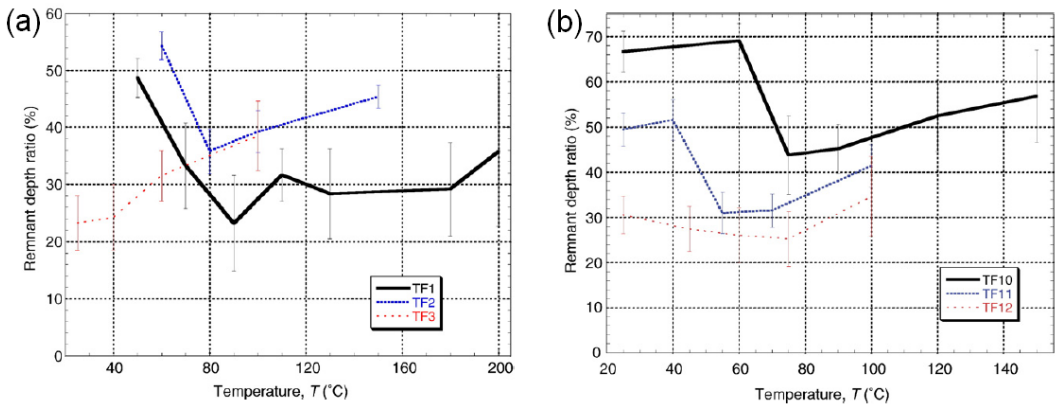

Figure 1.31 – Plot of remnant depth ratio as a function of the test temperature for a penetration depth of 200 nm for: (a) $Ni_{47.2}Ti_{52.8}$ (TF1) with A_f = 70°C, $Ni_{49.4}Ti_{50.6}$ (TF2) with A_f = 85°C and $Ni_{51.2}Ti_{48.8}$ (TF3) with A_f = 20°C; (b) $Ni_{47.6}Ti_{51}Cu_{1.4}$ (TF10) with A_f = 75°C, $Ni_{40.2}Ti_{51}Cu_{8.8}$ (TF11) with A_f = 55°C and $Ni_{34.4}Ti_{53}Cu_{12.6}$ (TF12) with A_f = 60°C [108].

Similar results were found for ternary Ti-rich Ni-Ti-Cu thin films with Cu content up to 12.6 at.%, even though no evidence of superelastic effect was detected for Cu content above 10 at.%, due to the brittleness of the film.

Further investigations on the mechanical properties of ternary $Ti_xNi_{90-x}Cu_{10}$ (37 at.% < x < 67 at.%) thin films (600 nm thick) annealed for 1 hour at 500°C were carried out by *Zarnetta et al.* [120].

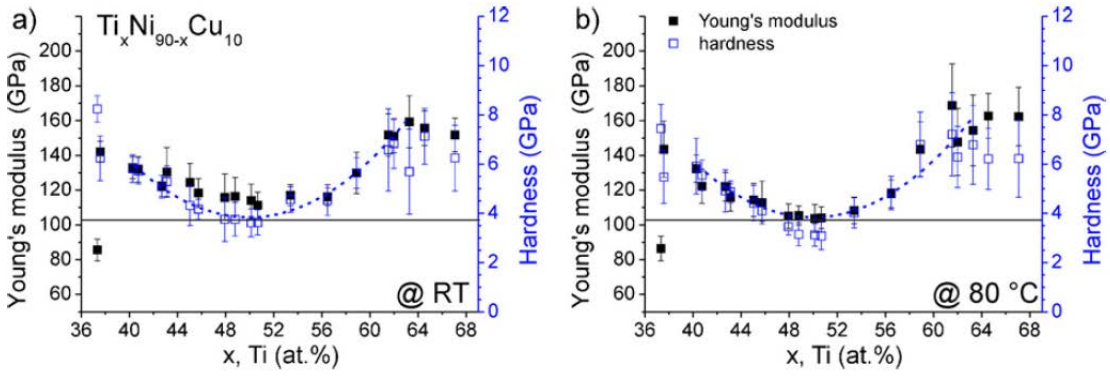

Figure 1.32 - Composition dependencies of Young's modulus and hardness for TixNi(90−x)Cu10 SMA thin film samples: (a) at RT and (b) at 80°C. Error bars indicate the standard deviation within each set of either 49 or 25 indents [120].

In particular continuous stiffness measurement (CSM) at both ambient (< M_f) and high temperature (> A_f) were carried out by using a Berkovich diamond tip (tip rounding of

100 nm), and Young's modulus and hardness were evaluated according to the procedure outlined by Oliver and Pharr for a penetration depth of 100 nm. Mechanical properties (and scatter in the data as well) were found to increase as the compositions deviated from a Ti content of 50 at.% (Figure 1.32).

The trends observed were ascribed to the formation of different types of precipitates according to those reported in Table 1.1 and Table 1.3, which resulted in strengthening off-stoichiometric compositions, as well as limiting grain growth during annealing, with a subsequent hardening effect according to the Hall-Petch relationship.

The high-angle annular dark field (HAADF) images in Figure 1.33 show the microstructure of Ni-rich and Ti-rich Ni-Ti-Cu films. It is seen that for both off-stoichiometric compositions the grain size is found to be significantly smaller (50 – 100 nm) compared to the films with a Ti content close to 50 at.%. However, for high Ti content (see Figure 1.33 (c)) the grain size was found to increase again.

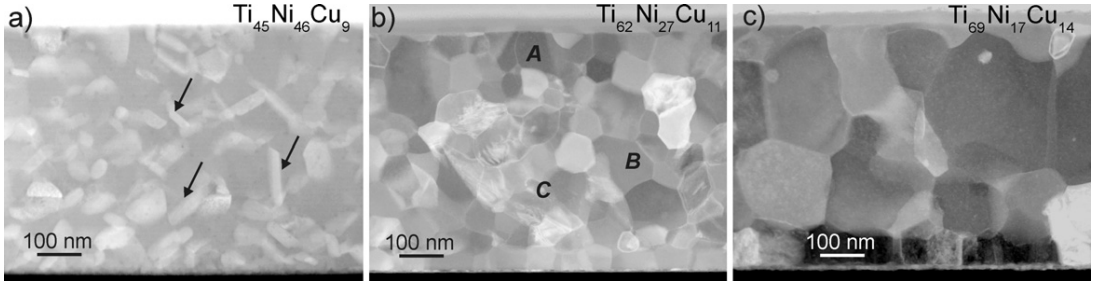

Figure 1.33 – HAADF TEM images of Ni-rich (a) $Ti_{45}Ni_{46}Cu_9$ and Ti-rich (b) $Ti_{62}Ni_{27}Cu_{11}$ and (c) $Ti_{69}Ni_{17}Cu_{14}$ thin films annealed at 500°C. Arrows in (a) highlight $Ti(Ni, Cu)_2$ precipitates. Letters A, B and C in (b) indicate different Ti-rich Ni-Ti-Cu phases. A TiO_2 oxide layer 30±10 nm on the surface is found for all the layers [120].

This increase in grain size corresponded to a slight decrease in hardness and a levelling off in Young's modulus (Figure 1.32 (a)) measured at room temperature. The presence of precipitates large compared to the layer thickness (see Figure 1.33 (a)) caused a bimodal distribution of the load-displacement curves. In particular the expected higher mechanical properties of the precipitates compared to the Ni-Ti-Cu matrix led to an overall stiffening of the load-displacement curves especially for off-stoichiometric compositions.

Similar trends for hardness and Young's modulus were observed when the films were tested at 80°C, as seen in Figure 1.32 (b). However, slightly lower values were found at

high temperature compared to those obtained at ambient temperature. Although the trend of the Young's modulus in relation to the film composition was confirmed also by stress-temperature measurements, from which elastic modulus was calculated, the reason behind the lower values found at higher temperature was not clear.

4. Tribological properties and applications

Tribology is the science and engineering of interacting surfaces in relative motion. The subject of tribology deals with the friction contact, which is the region of interaction of bodies in contact. Various processes of a physical (including mechanical, electrical, magnetic and heat), chemical and biological nature occur at the friction contact. The friction force, i.e. the resistance to the relative displacement of bodies, is one of the main manifestations of these processes. Wear of contacting surfaces is the other manifestation of the processes that occur in contact interactions. Wear is a progressive loss of material from surfaces resulting from this frictional contact. The precision of machines is impaired by wear, sometimes wear leads to machine failure. Thus the study of wear and the elaboration of methods to improve wear resistance are important problems for tribology. These discussions lead to another definition of tribology which is the science of friction, lubrication and wear of materials. Tribology can be considered as an applied science, since the reduction of energy losses and the deleterious effects of friction and wear on the environment are the main purposes of tribological investigation [121].

The tribological properties as well as the potential use of Ni-Ti based thin films in tribological applications have been investigated from about a decade. Due to the unusual functional properties of these alloys also in the form of sputter deposited thin films, self-healing surfaces and complex bilayer[8] coatings have been fabricated and characterised.

[8] Tribological layer deposited on top of a Ni-Ti layer.

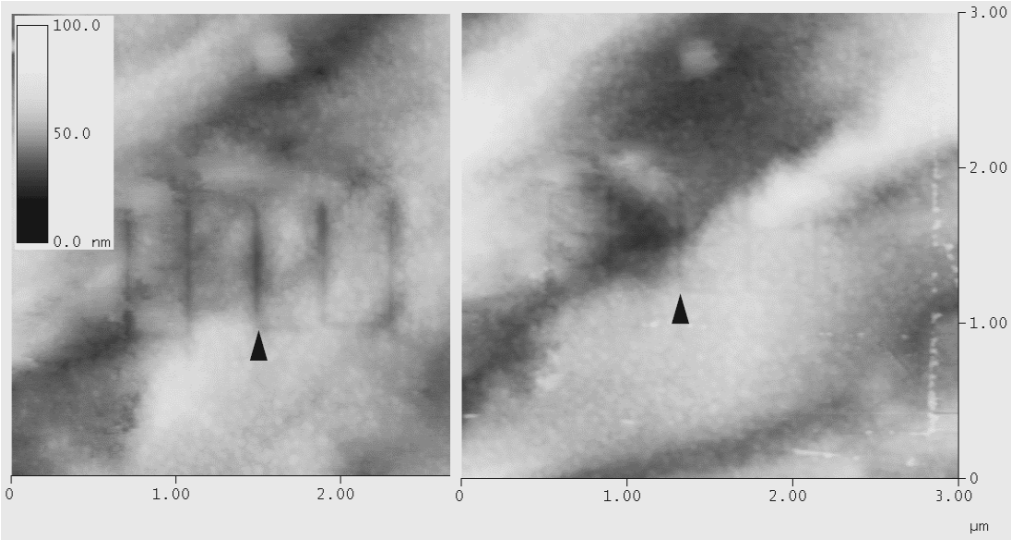

Figure 1.34 – AFM topographical maps of nano-scratches before (left) and after (right) heating above A_f. Although recovery of the nanoscale scratches is nearly complete, a residual scar remained after transformation [122].

The concept of self-healing Ni-Ti based thin films was proved by using a 10 µm thick martensitic Ni-Ti film [122]. Many nano-scratches were produced on the surface of the film by using a Berkovich tip with a constant applied load of 20 µN. The scratched surface was analysed by an atomic force microscope (AFM) before and after heating the sample above A_f. Figure 1.34 shows the nano-scratches before and after heating, where after the thermally-induced transformation the recovery of the scratches was nearly completed. Similar experiments were also conducted on austenitic Ni-Ti thin film, where the same results were observed in terms of shape recovery upon unloading owing to the superelastic effect.

The generally poor tribological properties of Ni-Ti thin films have been addressed by *Fu et al.*, who investigated the possibility of improving the tribological performance of a $Ni_{50.2}Ti_{49.8}$ film (3.5 µm thick) by coating the layer with a hard coating, such as TiN (300 nm thick) [123]. The scratch test was employed to evaluate the adhesion between layers, while tribological properties were investigated by using a ball-on-disk tribometer (1 – 5 N normal load) with an alumina ball as counterpart (ϕ = 9.5 mm) and for a sliding distance of 300 metres at 0.2 m/s. Differential scanning Calorimetry (DSC) analyses performed on the TN/Ni-Ti bilayer showed that the presence of the top layer did not inhibit the functional behaviour of the Ni-Ti layer, which underwent thermally-induced phase transformation. Stress-temperature measurements carried out on Ni-Ti

single layer and TN/Ni-Ti bilayer showed a similar transformation stress for the two coating systems and a slightly smaller residual stress in the bilayer.

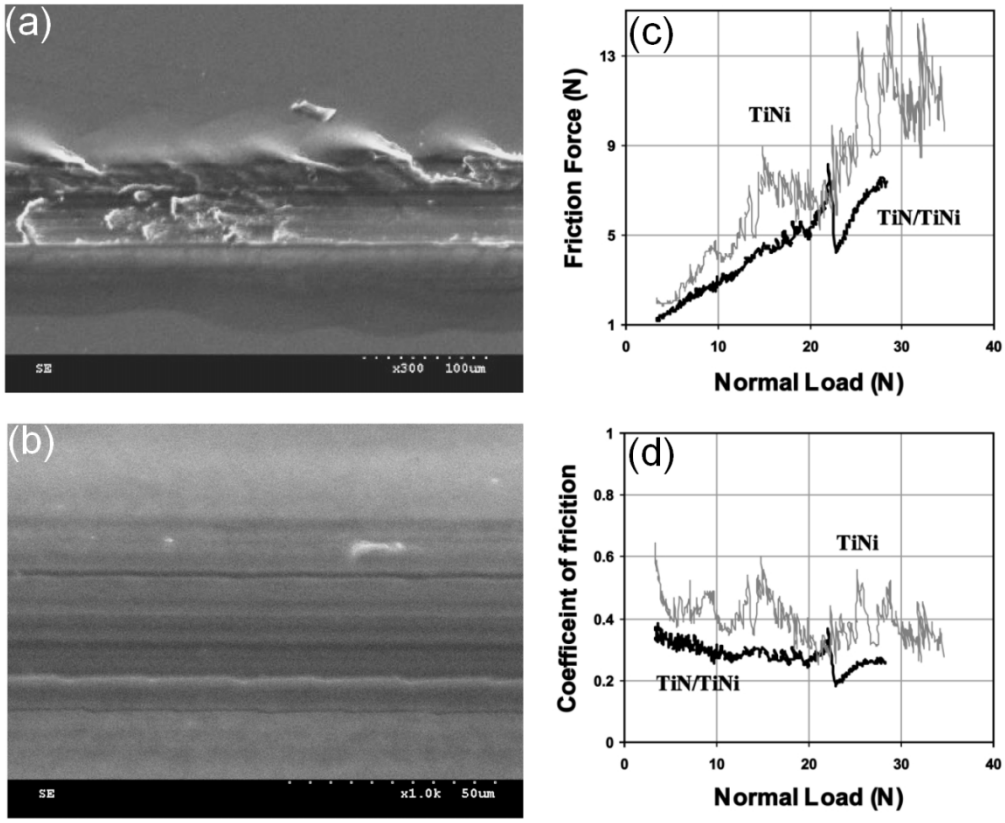

Figure 1.35 - Scratch track of (a) Ni-Ti and (b) TiN/Ni-Ti films. Scratch test results are reported in terms of (c) friction force versus normal load and (d) coefficient of friction versus normal load [123].

Examination of the scratch track obtained for the Ni-Ti film (Figure 1.35 (a)) revealed severe ploughing and delamination. The friction force versus normal load curve (Figure 1.35 (c)), obtained by the scratch test, indicated a quite poor load bearing capacity for Ni-Ti, and the average coefficient of friction around 0.4. On the other hand, Figure 1.35 (b) for the TiN/Ni-Ti bilayer shows that only slight scratches were produced on the surface and a lower wear damage obtained. By using the TiN top layer the load bearing capacity of Ni-Ti was slightly improved and the friction coefficient decreased below 0.3. The sliding wear test corroborated the higher friction coefficient exhibited by the bare Ni-Ti film compared to the TiN/Ni-Ti bilayer, which exhibited a friction coefficient of 0.15 for a normal load of 1 N. The wear track of the TiN/Ni-Ti bilayer exhibited only a few scratches without significant wear damage. On the contrary, at a higher applied

load (5 N), the bilayer exhibited spallation and the delaminated area became important, thus causing an increase in friction coefficient up to 0.4 – 0.5.

Wangyang Ni et al. [107] used both austenitic ($Ni_{51.8}Ti_{48.2}$) and martensitic ($Ni_{49.5}Ti_{50.5}$) Ni-Ti thin films (4 µm thick) annealed at 550°C for 1 hour, as well as a Cr layer (4 µm thick) as an interlayer between a CrN hard coating (1 µm thick) and a softer substrate (Al) to produce different bilayer coatings (the same top layer but different interlayer material), the aim bring to improve the adhesion between the outer layer and the substrate as well as to improve the tribological performance of the hard coatings. As a reference case CrN coatings were deposited directly on the Al substrate with a thickness of 1 and 5 µm. Nanoindentation measurements provided information about the mechanical properties of different coating designs as summarised in Table 1.4.

Table 1.4. Nanoindentation properties of aluminium substrate, interlayer materials (S1: austenitic, S2: martensitic and Cr), and CrN hard coating evaluated on nanoindentation curves for a load between 8 and 10 mN [124].

Materials	Al	S1($Ni_{51.8}Ti_{48.2}$)	S2($Ni_{49.5}Ti_{50.5}$)	Cr	CrN
H(GPa)	0.94	4.7	2.4	6.7	23.0
E(GPa)	77.6	95.0	89.3	318.4	257.0
Poisson's ratio	0.34	0.3	0.3	0.21	0.3
H/E^*	0.012	0.049	0.027	0.026	0.102
Depth recovery ratio	0.067	0.33	0.23	0.16	0.64
Work recovery ratio	0.070	0.35	0.23	0.17	0.70

These results indicated that the hardness to reduced modulus ratio (H/E_R), depth recovery ratio[9] and work recovery ratio[10] decreased in the following sequence for each single layer separately deposited: austenite, Cr, martensite and aluminium, whereas the hardness decreased in the following sequence: Cr, austenite, martensite and Al. On the other hand, it was found that the H/E_R ratio was strongly dependent on the interlayer material, layer thickness and indentation depth. Specifically, nanoindentation measurements carried out on different Cr-SMA-Al layered coatings with and without a Ni-Ti interlayer, showed that the 5 µm CrN/Al coating exhibited higher hardness compared to the 1 µm CrN/Al coating, but the Cr-S1-Al system

[9] Ratio between the recoverable indentation depth and the indenter displacement at maximum load.
[10] Ratio between the elastic work enclosed by the unloading curve and the total work enclosed by the loading curve.

presented a higher H/E_R, owing to the superelasticity of the Ni-Ti interlayer. Figure 1.36 shows how hardness and H/E_R changed at different penetration depths for different layered coatings.

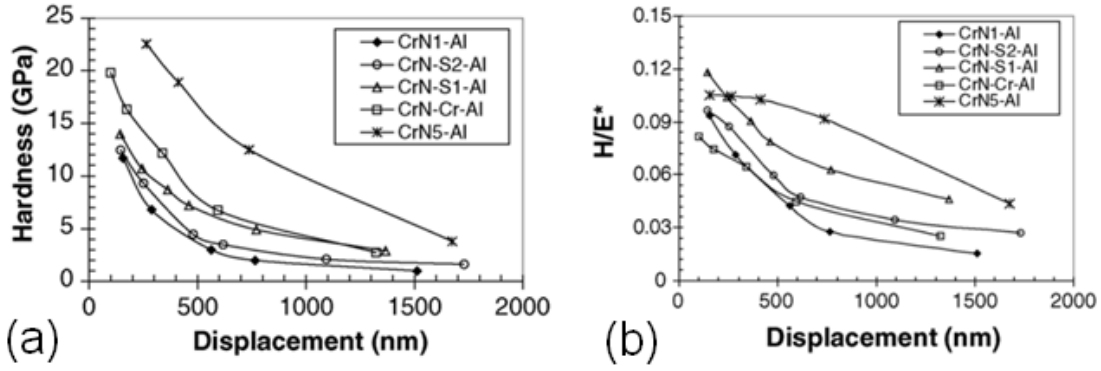

Figure 1.36 - Mechanical properties of the coatings at various depths: hardness (a), and ratio of hardness to reduced modulus (b). S1: austenitic Ni-Ti layer; S2: martensitic Ni-Ti layer [107].

The adhesion of the CrN layer in different coating designs was evaluated by a scratch test performed by increasing the load in the range 0 – 6 N by using a spherical tip (213.4 µm tip rounding). SEM observations (Figure 1.37) of the end of the scratches showed that by using a superelastic Ni-Ti or a Cr interlayer, the adhesion was improved, as no coating delamination was observed in these samples. On the other layered and single CrN coatings delamination occurred as a result of the compressive stress ahead of the indenter. The difference in scratch behaviour between the layered coatings using austenitic and martensitic Ni-Ti interlayers was attributed to the capability of the austenitic layer to accommodate strain in a reversible manner.

A comparative investigation, carried out by dry pin-on-disk wear tests, on the coatings reported in Table 1.4 showed that the CrN-martensite-Al and the CrN(1 µm)-Al failed after 1100 and 3000 cycles, respectively, accompanied by an abrupt increase in friction coefficient. On the other hand, the coating durability was improved when a Cr and especially Ni-Ti superelastic interlayer were used. However, a significant difference was observed in the friction coefficient of the above mentioned layered coatings. In fact, while friction increased and stabilised around 0.8 for the CrN-Cr-Al coating, a much lower and stable friction coefficient (~ 0.3) was found for the CrN-S1-Al coating. The improved frictional behaviour of CrN-S1-Al coating was attributed to the high H/E_R achieved by using the Ni-Ti superelastic interlayer, as the plowing contribution to the

friction coefficient is expected to be lower for materials with higher H/E_R ratio (see Table 1.4).

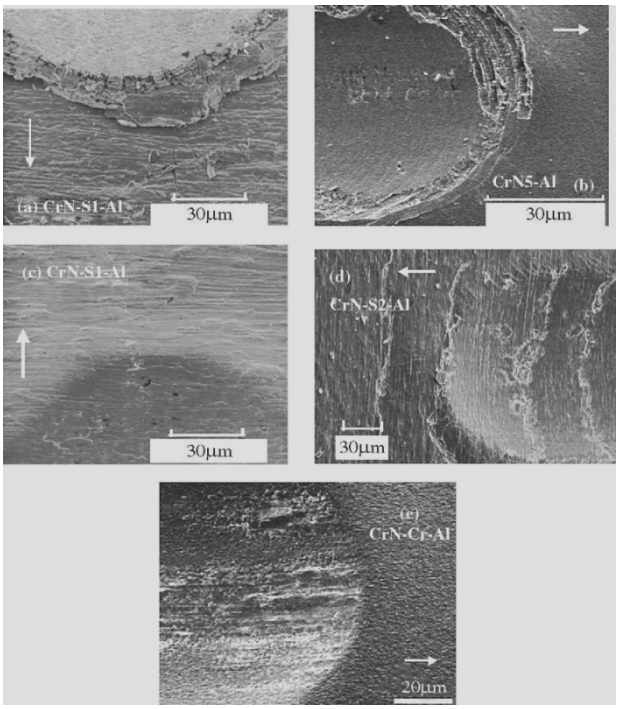

Figure 1.37 - SEM images of the end of scratches on 1 μm CrN-Al (a), 5 μm CrN-Al (b), CrN-S1-Al (c), CrN-S2-Al (d), and CrN-Cr-Al (e) (the arrow indicates the scratch direction) [107].

The wear loss of these layered and non-layered coatings is reported in Figure 1.38, where it is clearly seen that the layered coatings fabricated by using austenitic Ni-Ti and Cr as interlayer exhibited the lowest wear loss compared to the other coatings, which instead showed higher wear loss owing to adhesion problems with the substrate. By comparing the mechanical properties of the Cr and austenitic Ni-Ti interlayers, it was seen that the layered coating using the interlayer with higher H/E_R ratio, i.e. austenitic Ni-Ti, exhibited a lower wear loss, even though the CrN-Cr-Al coating exhibited a higher hardness than the CrN-S1-Al coating. In Figure 1.36 (b) the CrN-S1-Al exhibited a higher H/E_R compared to the CrN-Cr-Al coating at different indentation depths.

This result was rationalised by considering that the wear loss in the two layered coatings mentioned above occurred by gradual material removal or gradual wear was caused by plastic deformation rather than elastic deformation followed by fracture, as confirmed by SEM observations. In particular, materials with higher H/E_R are expected

to have a more elastic response to the contact, i.e. larger elastic work during indentation, therefore a smaller accumulative strain and thus a better wear resistance.

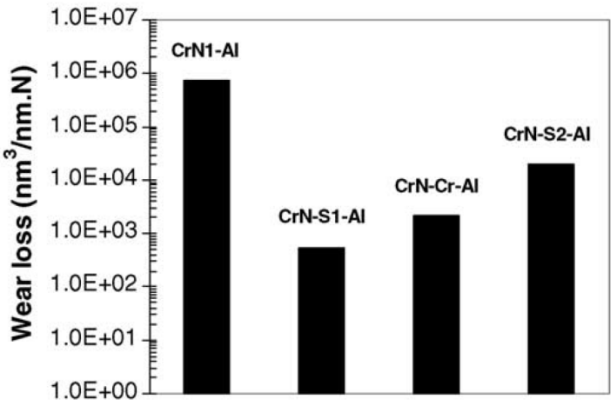

Figure 1.38 – Wear losses of the layered and non-layered coatings [107].

Zhang et al. [125] investigated the use of $Ni_{48.3}Ti_{51.7}$ films (15 and 21 µm thick) as an interlayer between metal substrates (Al) and hard coatings: CrN (3.9 µm thick) and DLC (2.5 µm thick) as a means to enhance coating adhesion and to protect the underlying metal from plastic deformation. Scratch tests carried out above and below A_f for CrN-NiTi-Al and CrN-Al systems, showed an increased critical load for delamination when the testing temperature was above A_f, indicating that the improved performance was attributable to the superelastic effect (Figure 1.39).

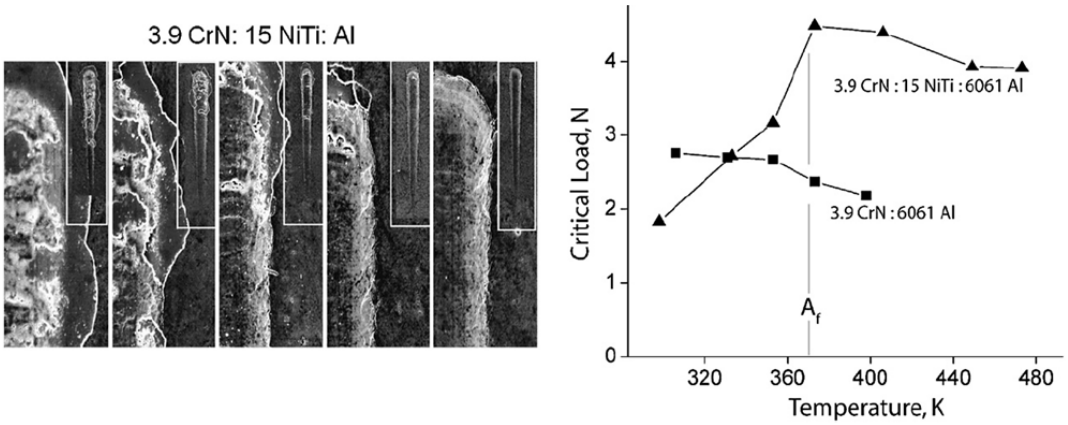

Figure 1.39 - Results of temperature-controlled scratch tests with an increasing load from 0 to 5 N over 1 mm scratch length. The micrographs at the upper row are scratch terminations (with full scratch tracks in the insets) for the (3.9)CrN:(15)NiTi:Al (µm) system. The graph on the right hand side shows the critical load for onset of delamination, as determined by the onset of acoustic emission during scratch tests [125].

Ball-on-disk tests, performed at different temperatures around A_f, were carried out by using a 200 µm tip radius spherical probe at 0.49 and 0.98 N loads for 50 – 1000 revolutions. Tests showed that the wear rates for temperatures above A_f were a factor of 50 less than those determined at a temperature below A_f, indicating much lower wear loss by using a superelastic interlayer rather than a martensitic interlayer. Similar investigations were carried out on a DLC-NiTi-Al system, and comparable results to those of the CrN-NiTi-Al system were found for temperatures below A_f.

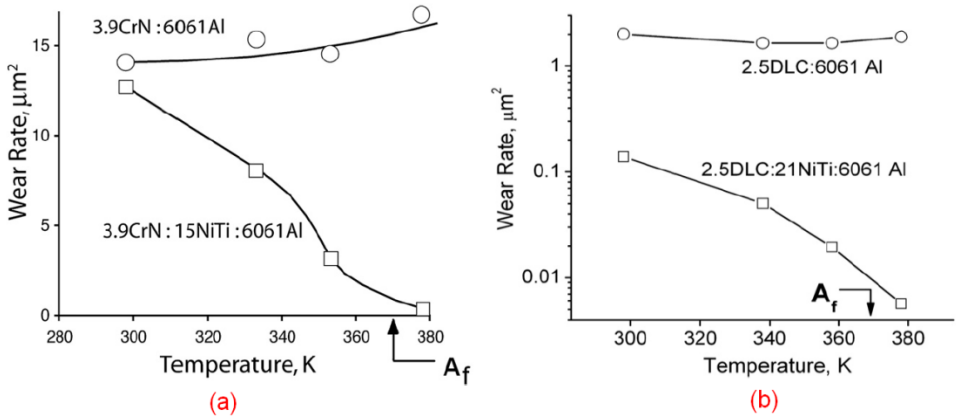

Figure 1.40 - Results of ball-on-disk wear tests for (a) CrN and (b) DLC coated aluminum with and without Ni-Ti interlayers [125].

However, wear tests performed above A_f for the DLC-NiTi-Al system, showed an enhancement in wear resistance by a factor of 150 compared to the wear loss achieved at temperatures below A_f, much higher than that obtained for the CrN-NiTi-Al system (Figure 1.40). This difference was attributed to the higher hardness and Young's modulus of DLC compared to CrN, as well as to the fact that the Ni-Ti interlayer was 21 µm thick in DLC-NiTi-Al and 15 µm in CrN-NiTi-Al.

5. Transition metal dichalcogenides coatings

Transition metal dichalcogenides (TMD) are a large group of compounds with different properties and often with several crystallographic structures. However, the structure exhibiting low friction is hexagonal, which gives the structure a lamellar architecture.

Furthermore, in order to achieve low friction, i.e. low shear resistance, a certain electronic structure is also required [126, 127, 128]. This further shrinks the number of possible candidate materials to Mo and W disulphides and diselenides.

The lamellar structure associated with the above mentioned systems exhibits a highly anisotropic behaviour. These lamellar structures can be seen as a stacking of layers, where the transition metal layer is stacked between two layers of dichalcogenides [126]. Each metal atom is coordinated with six chalcogenide atoms, three on each side of the metal plane, with one metal atom and three chalcogenide atoms located at the corners of triangular prisms (Figure 1.41).

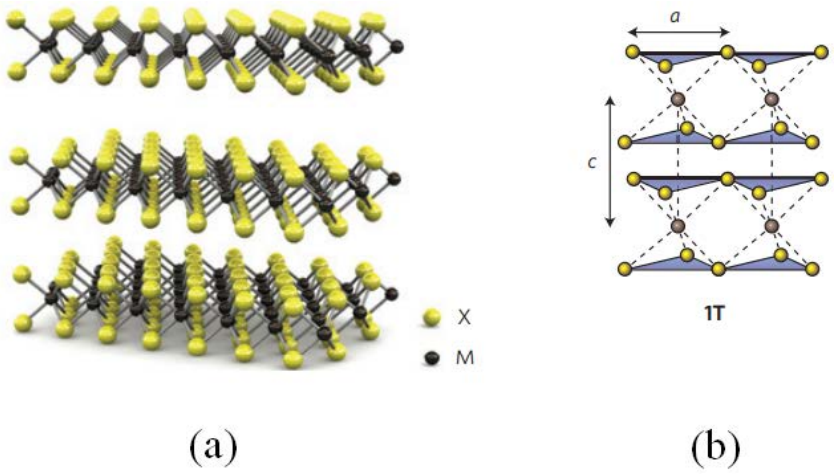

Figure 1.41 – Structure of TMD materials: (a) three-dimensional schematic representation of a typical MX_2 structure, with the chalcogen atoms (X) in yellow and the metal atoms (M) in grey; (b) schematic of the structural type 1T, i.e. tetragonal symmetry, one layer per repeat unit, octahedral coordination [129].

The metal atoms have strong covalent bonding to each other within their plane, with chalcogenide atoms sticking out of their side of the plane. Since all molecular orbits are filled, there are only weak interactions with the chalcogenide atoms in the adjacent planes. Also the structure contains no unsaturated or dangling bonds, except at the edge of a plane or at defects. Since the electrons are located preferentially close to the metal atoms, the negative charge is contained within the layers, which create a net positive charge on the surface of the layers. This results in an electrostatic coulomb repulsion between the planes, which provides the material with low friction shear strength. The only TMDs that exhibit this structure are: $MoSe_2$, MoS_2, WSe_2 and WS_2.

Despite the excellent tribological properties exhibited by the above reported TMDs, there are some drawbacks that limit their use in industrial applications. Among these

weaknesses, the most relevant is related to the extreme sensitive of TMDs to environmental attack. In particular, when sliding in air, oxidation occurs owing to the high reactivity with oxygen of the non-oriented layers (also called TMD platelets), thus producing metal oxides, which in turn increases the friction. On the other hand, when the basal planes are well oriented, i.e. parallel to the sliding direction, no oxidation occurs. Another aspect not less relevant that further limits the use of TMDs is their low hardness when compared to other low-friction coatings, i.e. diamond-like carbon (DLC). Moreover, though the adhesion of TMDs to the substrate has been improved by the use of a thin metallic interlayer (Ti or Cr), it is still limited. As a consequence, the load-bearing capability is very low and TMDs coatings peel off the substrate under high contact pressures [130].

In order to overcome the above mentioned limitations, without deteriorating significantly the unique tribological properties of TMDs, several solutions have been considered, i.e. alloying TMDs with non-metallic, metallic elements and compounds. Although general improvements were observed from alloying TMDs with compounds, the most successful solution resulted in alloying TMDs with metallic (Cr or Ti being the most promising) and/or non-metallic elements (C and N) to produce C- or N-doped TMDs, or quaternary systems [131, 132, 133, 134]. By using metallic elements, coatings were characterised by a prevalence of TMD phase compared to the alloying element, with a limited interaction between them. On the contrary, TMDs alloyed with non-metallic elements showed usually a higher non-TMD content; moreover reactions between the alloying element and chalcogenides and transition metal are expected [130].

In the late nineties, the concept of coatings produced by alloying TMDs with carbon attracted much attention owing to the combination of the excellent frictional properties of TMDs in vacuum and in dry air with those of DLC in humid environments. Furthermore, an improvement in mechanical properties, particularly the hardness, was obtained. The basic concept behind this combination was to fabricate coatings able to switch their tribological behaviour according to the environment, with particular reference to the humidity, i.e. in humid environment a predominant response by the DLC structure, while in dry atmosphere and in vacuum a response by the TMDs structure. This property was called “chameleon behaviour” [135], though the authors that coined this concept substantially did not further proof this behaviour, which was

not observed later in other studies [130]. C-doped TMDs exhibited improved mechanical properties, i.e. hardness and load-bearing capability, compared to the pure TMDs coatings. The carbon matrix also contributed at protecting the TMD platelets during the reorientation, thus permitting low friction in oxygen-containing and humid environments. The following sections focus on TMD-C coatings, in particular to the ternary W-S-C system.

5.1 W-S-C coatings

In this section a review on the fabrication of W-S-C coatings by PVD techniques (reactive magnetron sputtering and magnetron co-sputtering of WS_2 and C target) and of their mechanical properties, as well as their tribological behaviour in different environments is proposed. The above mentioned properties are discussed in relation to the deposition processes and the chemical composition.

5.1.1 Deposition and microstructure

W-S-C coatings were deposited both by magnetron co-sputtering (single WS_2 and C target) and reactive magnetron sputtering (by using CH_4 and Ar^+) [136]. It was observed that the presence of oxygen as an impurity as well as the S/W ratio in the coatings was affected by the deposition process. In particular, in the reactively deposited coatings the O at.% decreased in a more pronounced way, compared to the co-sputtered ones, with increasing C at.%, while the S/W ratio decreased progressively with increasing C at.% until reaching unity. On the other hand, in the coatings deposited by co-sputtering the S/W ratio was almost unaffected. The lower O at.% and S/W ratio observed in reactively deposited coatings was attributed to the presence of active species (i.e. C and H atoms) in the deposition chamber. These active species promote reactions with oxygen and sulphur during deposition, thus producing gases such as: CO, CO_2 and H_2S, which are pumped out of the chamber.

The microstructure of W-S-C coatings is affected both by the deposition process and the C content. In general, it was observed that regardless of the deposition process, with increasing C at.% (below 30 at.% a columnar structure was still present) a lower porosity is obtained and coatings exhibit a featureless cross-sectional morphology for a high C content (~ 72 at.%).

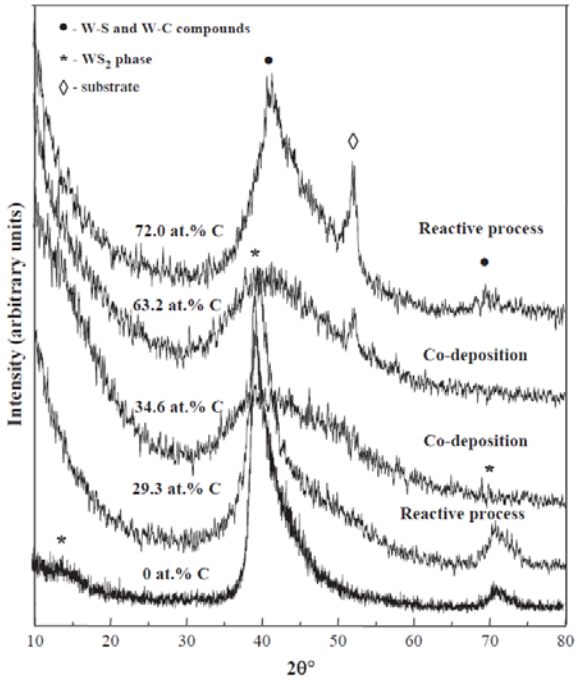

Figure 1.42 – XRD diffractograms of reactively deposited and co-sputtered W-S-C coatings [136].

Reactively deposited WS_2 coatings exhibited a crystalline structure (Figure 1.42) characterised by the type I structure (basal planes oriented normal to the film surface). The main peak at $2\theta \approx 40°$ was indexed as (100) of the WS_2 phase. The long tail for the higher diffraction angles corresponded to a turbostratic[11] stacking of (10L) planes (L = 1, 2, 3,..), while the peak located at $2\theta \approx 72°$ corresponds to the (110) planes. On the other hand, by introducing carbon a loss of crystallinity was observed; moreover, in the latter case traces of W-C compounds were also detected. Therefore, by reactive magnetron sputtering, coatings consisting of WS_2 and W-C domains embedded in a C-rich matrix were obtained. Conversely, the co-sputtered coatings exhibited an amorphous structure regardless of the C at.%.

The differences in microstructure as a function of the deposition process were further investigated by fabricating W-S-C coatings (1 – 2 µm thick) by three different processes: (1) using a reactive gas, i.e. CH_4, (2) co-sputtering from separate targets, i.e.

[11] Crystal structure in which basal planes have slipped out of alignment.

WS_2 and C, and (3) co-sputtering from a C target embedded with WS_2 pellets within the erosion track [137].

The first difference between coatings deposited by the above mentioned processes is related to the chemical composition and in particular to the oxygen content. In all the films the S/W ratio was lower than 2 (stoichiometric condition) owing to the preferential re-sputtering effect of sulphur atoms by the energetic species during deposition.

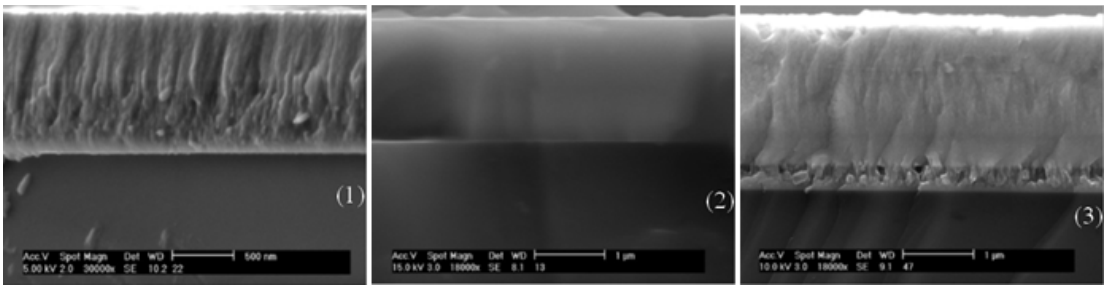

Figure 1.43 – SEM micrographs showing cross-section morphology of W-S-C deposited in different processes; see text for details [137].

The film obtained by process (3) exhibited the highest O content, while the film produced by process (2) the lowest O content. The film produced by (2) exhibited a featureless cross-sectional morphology suggesting an amorphous microstructure (Figure 1.43), while the films fabricated by (1) and (3) exhibited a porous columnar structure confirming the higher O content. The amorphous film showed the lowest RMS value (12.9 nm), while the highest value (85 nm) was showed by the film deposited by the method (1).

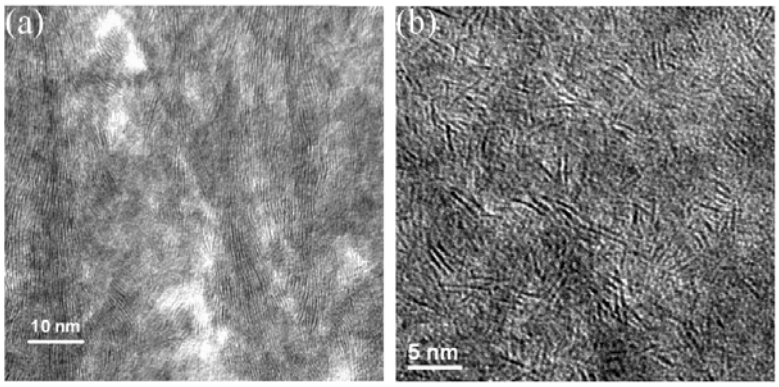

Figure 1.44 – HR-TEM images of W-S-C coatings with (a) 33 at.% C and (b) 51 at.% C [138].

The structure of W-S-C coatings deposited by method (3) was further investigated by HR-TEM for coatings with different C content [138]. The coatings with 27 at.% C exhibited WS_2 platelets (5-10 nm in size) preferentially oriented perpendicular to the coating surface (Figure 1.44 (a)). The coating with 49 at.% C was described as a nanocomposite material consisting of randomly oriented WS_2 platelets (3 nm in length) embedded in an amorphous carbon matrix (Figure 1.44 (b)). For high C content, i.e. 66 at.%, a featureless structure was observed, where the size of WS_2 platelets was probably further reduced. No evidence of WC was revealed by different techniques (i.e. XPS, Raman spectroscopy, TEM).

5.1.2 Mechanical properties

Mechanical properties such as hardness and critical load (resistance to scratch) were found to depend on the deposition process and on the C content (Figure 1.45). The C-doped WS_2 coatings, regardless of the deposition process, exhibited a higher hardness compared to the pure WS_2 coatings (< 3 GPa), i.e. in general one order of magnitude higher.

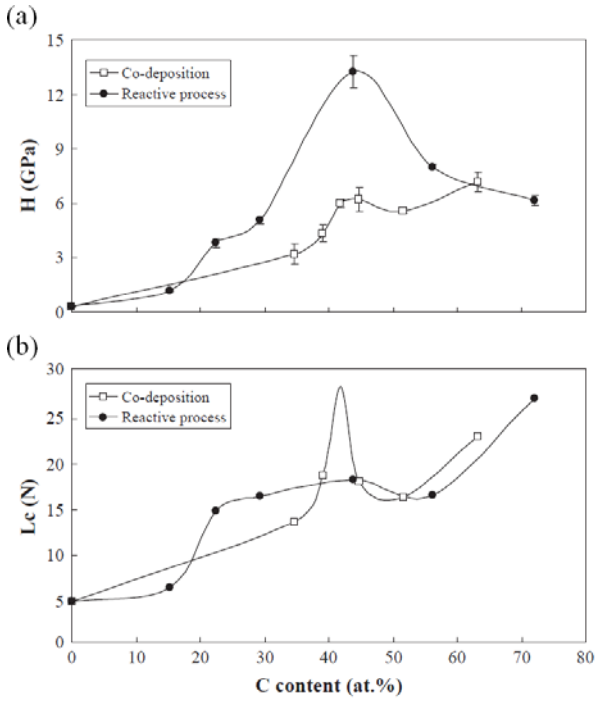

Figure 1.45 – Mechanical properties of W-S-C coatings as a function of the C content: (a) hardness and (b) adhesive critical load [136].

It was attributed to the microstructural changes caused by C in the coatings. In particular, carbon addition increased the compactness of the coatings by promoting the growth of a less porous structure compared to pure WS_2 coatings, which usually exhibit a porous columnar structure. The other effect of C addition was the formation of nano-grains. However, regardless of the C content, reactively deposited W-S-C films (~ 2 µm thick) exhibited a higher hardness compared to the co-sputtered ones. This difference was attributed to the lower S/W ratio in reactively deposited coatings, which encouraged the formation of carbides. In these coatings the highest hardness (~ 13 GPa) was obtained for 40 at.% C, while for a higher C content, the formation of C-phases (softer than carbides) caused a drop in the hardness. The hardness reported above for the reactively deposited coating is significantly higher than the values found in most of the studies reported in the literature. In fact, in other works [139], a similar trend of the hardness in relation to the C content was observed for reactively deposited coatings, but a maximum hardness of about 5 GPa was found for a C content of 54 at.%. On the other hand, the highest elastic modulus (75 GPa) was found for a C content of 28 at.%.

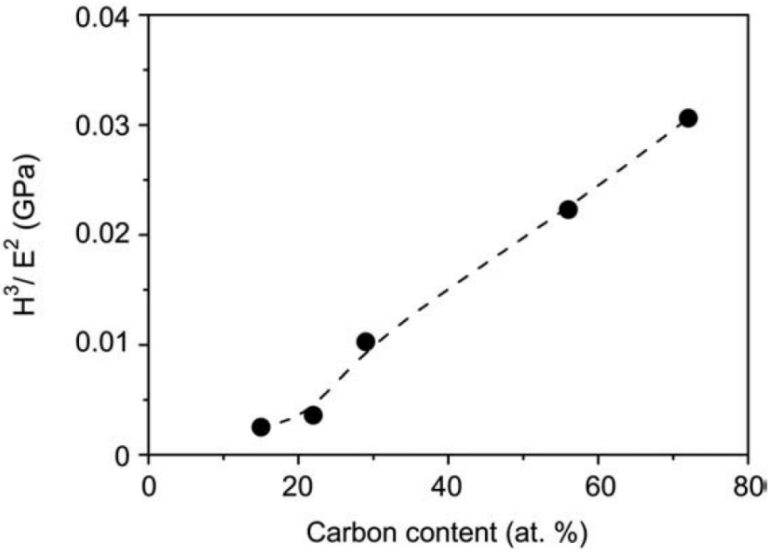

Figure 1.46 – The variation of H^3/E^2 with the C at.% [139].

The evaluation of H^3/E^2, referred as an index providing information about the elasticity exhibited by a film, showed that with increasing C at.%, a more elastic response to the indentation was observed for W-S-C films (Figure 1.46).

Doping WS_2 with C also represented a good method for improving the adhesion. In fact regardless of the deposition process the critical load (Lc) increased (Figure 1.45 (b)) with increasing C at.% [136]. As expected, the maximum depth increased by increasing the applied load and the hardest coating exhibited the lowest maximum depth [139].

The mechanical properties of W-S-C coatings (~ 2 µm thick) deposited by the three different processes, again reported here for clarity: (1) using a reactive gas, i.e. CH_4, (2) co-sputtering from separate targets, i.e. WS_2 and C targets, and (3) co-sputtering from C target embedded with WS_2 pellets, were investigated [137]. Nanoindentation measurements showed that the films produced by method (2) exhibited the lowest creep at a maximum load of 2 mN. Figure 1.47 shows the load-displacement curves for the films investigated and the measured mechanical properties.

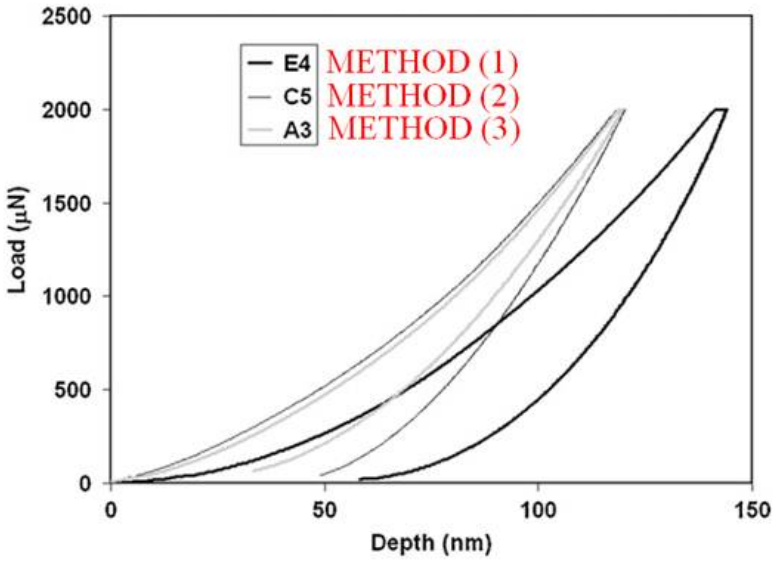

Film	Modulus (GPa)	S.D. (GPa)	Hardness (GPa)	S.D. (GPa)
E4	66.0	3.6	4.6	0.34
C5	76.0	3.2	7.4	0.55
A3	74.0	2.1	9.4	0.51
WS_2	38.0	2.1	0.53	0.03
C	112.0	12.1	9.6	1.3

Film designation	O (at.%)	C (at.%)	S (at.%)	W (at.%)	Thickness (µm)
E4 (reactively sputtered)	4.0	54.0	21.0	21.0	1.0
C5 (co-sputtered, 2 targets)	2.0	50.0	26.0	22.0	2.0
A3 (co-sputtered)	5.0	49.0	28.0	18.0	2.0

Figure 1.47 – Load vs. Displacement curves, measured mechanical properties and chemical composition of W-S-C coatings deposited by different methods [137].

The higher elastic modulus of the coating deposited by method (2) was attributed to both the amorphous structure and the low porosity obtained with this deposition process. The higher hardness of the film deposited by method (3), was attributed to the higher oxygen content in this coating. Hardness of ~ 10 GPa for W-S-C (40 at.% C) coatings deposited by method (3) was also reported in other studies [138, 140], where the increased hardness was attributed both to the higher compactness of the coatings and to the smaller size of the WS_2 platelets randomly oriented in the C matrix.

Mechanical parameters such as: H/E (indicative of the fracture toughness of the coating) and H^3/E^2 (indicative of the elasticity exhibited by the coating) were higher for the film deposited by method (3) and lowest for the coatings deposited by method (1).

The adhesion of reactively deposited W-S-C coatings to the substrate was slightly enhanced by the use of a thin Ti interlayer (~ 300 nm thick). However, the critical load (Lc) was found to scale with the C content [137]. In fact, the Lc (only 5 N for the WS_2) increased to about 7 N for low C at.%, but increased up to 50 N for a C content of ~ 64 at.%. This trend was attributed to an increasing amount of C diffusing toward the Ti interlayer with increasing C content in the coating. It may have led to an interfacial mixing with the formation of TiC, which improved adhesion.

5.1.3 Tribological properties

The tribological properties of W-S-C coatings deposited in reactive mode or by co-sputtering were evaluated mostly by tribotests, such as: pin-on-disk or reciprocating sliding tests. These tests are performed in order to study the role of the WS_2 platelets, embedded in the C matrix, on the tribological properties of W-S-C coatings. Scratch tests were also used to measure the coefficient of friction and the wear rate of as-deposited W-S-C coatings, as well as to compare coatings fabricated by different deposition processes.

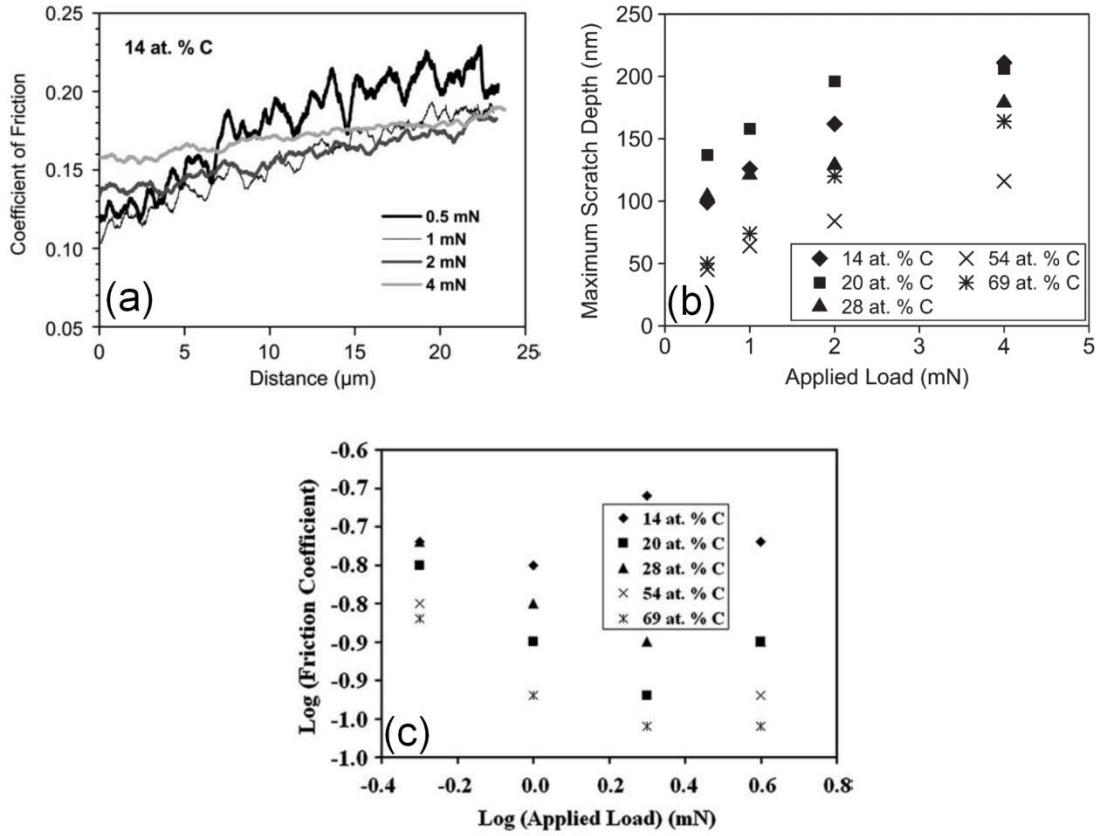

Figure 1.48 – Scratch tests on reactively deposited W-S-C coating [139].

The coefficient of friction was measured by scratch tests for reactively deposited W-S-C coatings with different C contents, by using different loads and scratch distances [139]. It was found that with increasing C at.% the coefficient of friction decreased (Figure 1.48 (c)). On the other hand, regardless of the C at.%, the friction increased monotonically with increasing scratch distance owing to the material piling up in front of the tip during sliding (Figure 1.48 (a)). It was also reported that with increasing applied load, the maximum scratch depth increased (Figure 1.48 (b)), while the coefficient of friction decreased (deduced from the log-log plot in Figure 1.48 (c)).

As reported in the previous section, W-S-C coatings have been fabricated by different deposition processes. Scratch tests were also used to compare the tribological properties of W-S-C coatings deposited according to the processes mentioned in section 5.1.1. It was reported (Figure 1.49) that the coefficient of friction is the highest for the film deposited by method (1), while it is the lowest for the film deposited by method (2).

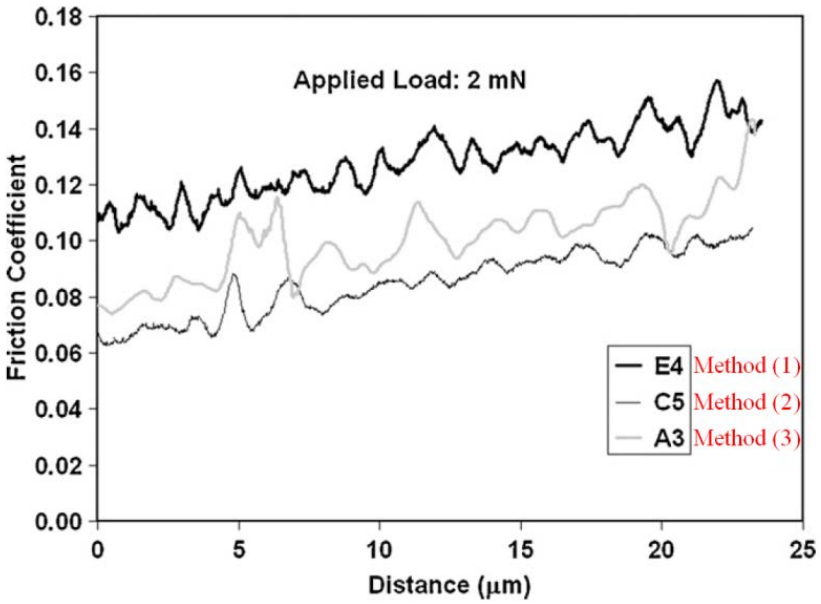

Figure 1.49 – Coefficient of friction vs. sliding distance at a constant load of 2 mN for W-S-C coatings deposited by different methods (see text for details) [137].

The reason behind this behaviour was attributed mostly to the presence of W-C nano-grains in the film deposited by reactive sputtering, i.e. method (1), which inhibited the easy glide of sandwiched layers of dichalcogenides. On the contrary, the film deposited by method (2) did not show any carbides, thus allowing easy glide between layers. The surface roughness also could have played a role on the higher coefficient of friction measured for the coating deposited by method (1). No significant dependence of the coefficient of friction on the applied load during scratch tests was observed, which suggested ploughing as the main friction dissipation mechanism rather than adhesion. On the contrary, pin-on-disk tests performed on W-S-C coatings deposited by the method (3) clearly showed that the coefficient of friction decreases with increased applied load, regardless of the temperature in the contact area induced by frictional heating, which is the typical behaviour observed for TMDs [138].

The weak relationship between applied load and coefficient of friction obtained by scratch test might suggest that a single-pass scratch test is not suitable for observing the effects of the re-oriented WS_2 platelets on the tribological behaviour of W-S-C coatings. A single-pass scratch might be seen as the first lap of a pin-on-disk test.

Pin-on-disk tests allowed the effects of the chemical composition, with particular regard to the C content, on the coefficient of friction, particularly on its trend in relation to the sliding distance [140] to be highlighted. Coatings with C content up to

51 at.% showed high friction in the first hundred laps (running-in), which was followed by a drop in friction corresponding to the steady state regime. On the other hand, for coatings with 66 at.% C a high coefficient of friction was observed during the entire test (Figure 1.50).

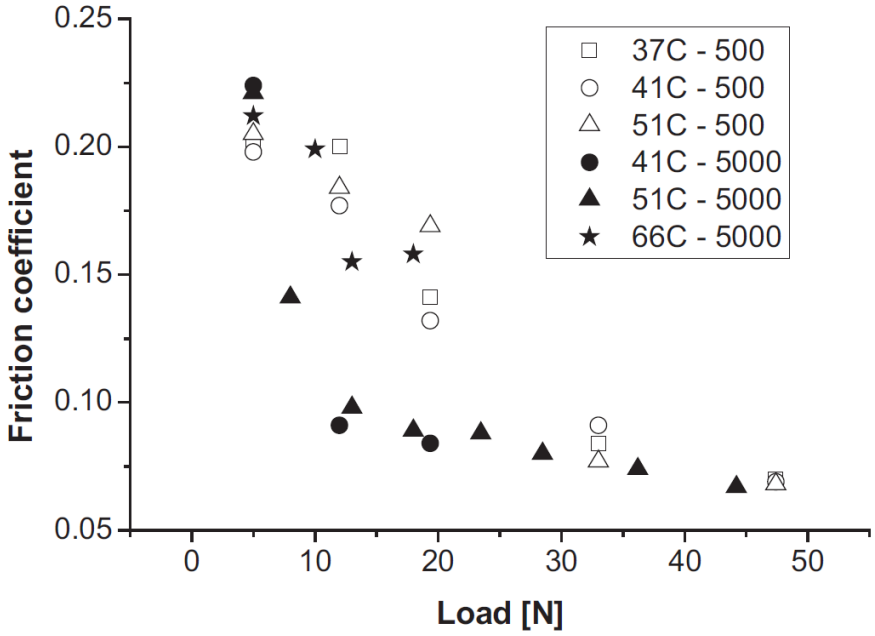

Figure 1.50 – Coefficient of friction of W-S-C coatings as a function of the load and for different number for laps [140].

Coatings with 51 at.% C exhibited a fluctuating wear rate (from 0.55 x 10-6 $\mathrm{mm}^3 \cdot \mathrm{N}^{-1} \cdot \mathrm{m}^{-1}$ for a load of 5 N to 1.36 x 10-6 $\mathrm{mm}^3 \cdot \mathrm{N}^{-1} \cdot \mathrm{m}^{-1}$ for 18 N), which stabilised at 0.9 x 10-6 $\mathrm{mm}^3 \cdot \mathrm{N}^{-1} \cdot \mathrm{m}^{-1}$for a load of 18 N. The coating containing 41 at.% C exhibited a constant low wear rate, i.e. small increase from 0.6 x 10-6 $\mathrm{mm}^3 \cdot \mathrm{N}^{-1} \cdot \mathrm{m}^{-1}$ for 5 N to 1.06 x 10-6 $\mathrm{mm}^3 \cdot \mathrm{N}^{-1} \cdot \mathrm{m}^{-1}$for a load of 19 N.

Raman spectroscopy performed on the as-deposited coating and within the wear track showed a decrease of the Ic/Iws_2 ratio (Ix: integrated area of all the peaks corresponding to the element "x" in the Raman spectrum) within the wear track, regardless of the C content. Moreover, the Ic/Iws_2 ratio further decreased with the contact pressure and/or number of laps. It was suggested that the formation of a WS_2-rich layer within the wear track, which becomes thicker with increased contact pressure and/or number of laps.

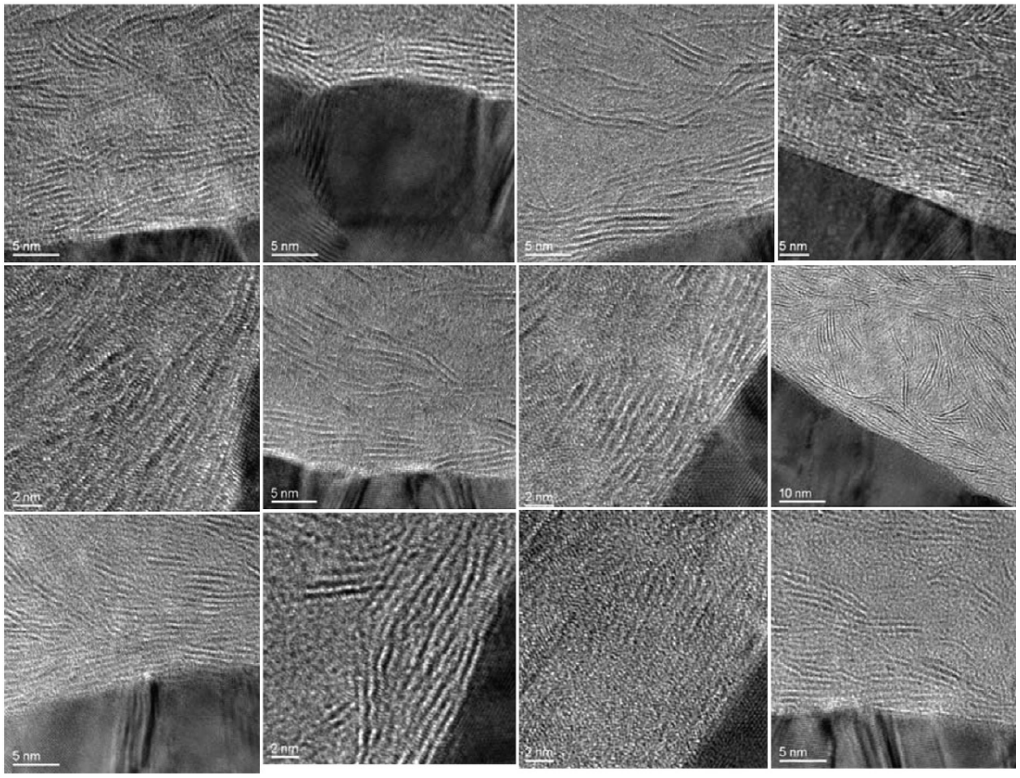

Figure 1.51 – HR-TEM images of the cross-sections of the wear track prepared by Focused Ion Beam. The black area in the image represents a protective layer deposited on the wear track after the tribotests. The preferred orientation of the TMD platelets is clearly visible compared to the as-deposited coating shown in Fig. 4 [130].

The formation of this tribolayer (tens of nanometres thick [138]), observed for TMD coatings by HR-TEM (Figure 1.51), is the reason behind the friction reduction during sliding, although a slightly different frictional mechanism was found in W-S-C coatings compared to pure WS_2. The amount of well oriented WS_2 platelets on the contacting surfaces was thought to affect also wear rate. In W-S-C coatings with high C content, the amount of WS_2 available within the contacting surface is lower and as a consequence more material has to be removed before low friction and wear is achieved. This might be the explanation behind the higher wear rate measured in C-rich coatings.

As mentioned previously, the tribological properties of TMD coatings are strongly sensitive to the environment, with particular regard to the oxygen content. W-S-C coatings, with different C contents, deposited by process (3) were tested in dry nitrogen and in humid air (RH, 5 – 70 %) [138]. In dry air (RH < 5 %), the coatings exhibited a very low coefficient of friction (0.03 – 0.06), which increased almost linearly up to 0.2 for RH < 40 %, regardless of the C content. For RH > 40 %, C-rich (> 41

at.%) coatings exhibited a lower sensitivity to the humidity, thus showing a lower coefficient of friction with respect to C-poor coatings. On the contrary, the coatings with the highest C content (66 at.%) exhibited the highest coefficient of friction and wear rate for sliding in dry air, while coatings with 33 and 37 at.% C showed the best wear resistance even in humid air. The hardest coating, i.e. W-S-C with 41 at.% C with a hardness of 10 GPa, showed the highest wear in humid air.

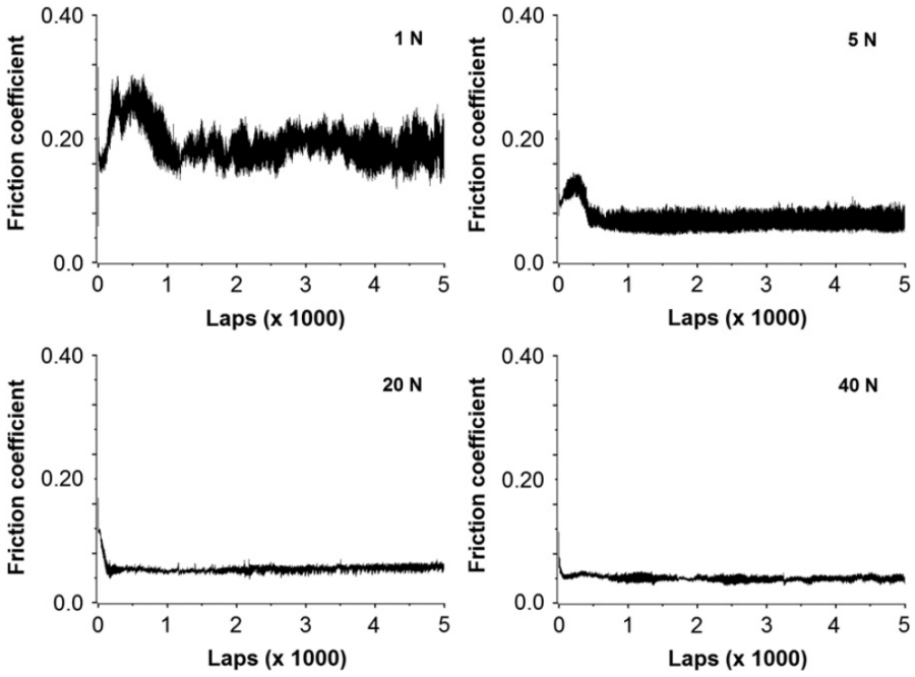

Figure 1.52 – Friction curves from sliding test under different contact pressures [138].

The different wear behaviour of the coatings with high and low C content was ascribed to the different amount of self-lubricant WS_2 material available on the interacting surfaces to form the tribolayer at the beginning of the tribotests, where high friction forces cause severe damage to the coating surface. However, contrary to the friction, the wear rate resulted almost unaffected by the humidity.

The tribological properties of W-S-C coatings deposited by co-sputtering from single WS_2 and C targets, i.e. process (2), were also investigated [141]. Even in this case, a decreasing coefficient of friction with applied load was observed. Compared to the W-S-C coatings deposited by process (3), a similar friction and improved wear behaviour was observed. Moreover, it was found that the running-in stage decreased with increasing contact pressure owing to a faster formation of the tribolayer (Figure 1.52). A unusual behaviour, in terms of coefficient of friction, was observed during the

running-in and in the early steady state stage during the sliding test. In particular, the coefficient of friction decreased dramatically at the beginning of the sliding test, while it increased with increasing number of laps after an initial stage of about 100 laps (Figure 1.53). The microstructural evolution of the wear track during the sliding test was monitored by in-situ Raman spectroscopy, by pausing the sliding test every few laps and acquiring the spectrum in the wear track without removing the sample and unloading the ball. A correlation between the Ic/Iws_2 ratio and the coefficient of friction for different laps was observed (Figure 1.53).

At the beginning of the test, the coefficient of friction dramatically dropped owing to the formation of the WS_2-rich tribolayer, as also suggested by the decrease of the Ic/Iws_2 ratio. Interestingly, after 100 laps the coefficient of friction as well as the Ic/Iws_2 ratio increased with increasing number of laps.

The Raman spectrum acquired on the ball surface at the end of the long sliding test suggested the formation of a C-rich layer. It led the authors to assume that the increasing coefficient of friction observed in Figure 1.53 was attributed to the wear of the interacting bodies. The wear caused an increase of the contact area and thus a consequent decrease of the contact pressure, which led to a higher coefficient of friction.

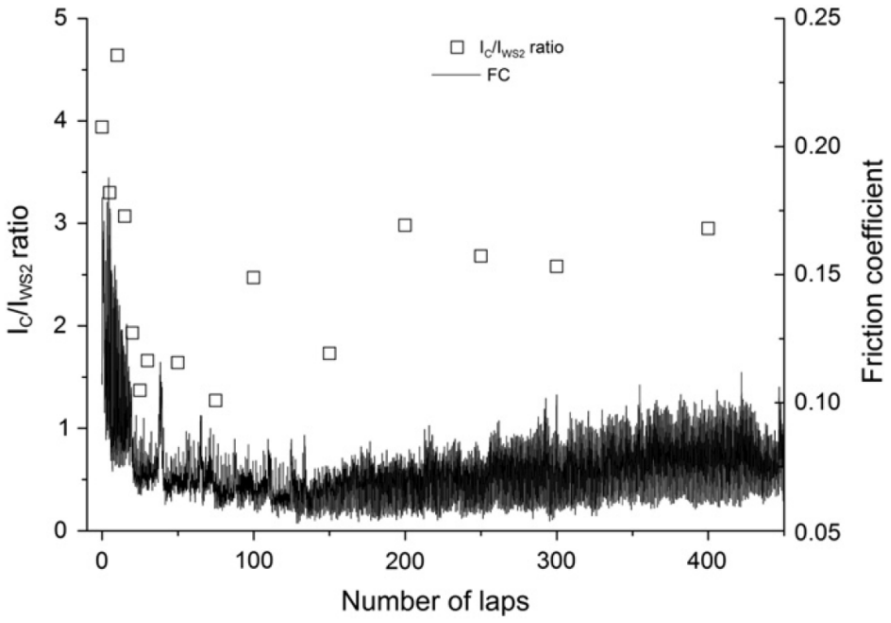

Figure 1.53 – Ic/Iws2 ratio of Raman peaks and friction coefficient during the running-in process (load 5 N) [141].

Hardness measurements were carried out within the wear track in an attempt to characterise the mechanical properties of the tribolayer formed after the tribotest [141]. The maximum penetration depth within the wear track was set at 35 nm as a compromise to limit surface effects and to indent sufficient material. However, a hardness very close to that of the as-deposited coating (9 GPa) was found, thus indicating that, at least at this depth, no significant changes in hardness are caused by the tribolayer formation.

6. Scope of the present research

The current state of the art on sputter-deposited Ni-Ti-based thin films covers a vast range of investigations aimed at assessing the microstructural and functional properties of these films in relation to their fabrication process, post-deposition heat treatments and chemical composition. With particular regard to Cu-doped Ni-Ti thin films, although these ternary films have been receiving much attention owing to their promising properties for applications, some of the effects of doping Ni-Ti with Cu are still missing in the literature.

Several studies reported experimental evidence about the grain refinement induced by Cu addition in Ti-rich and Ni-rich Ni-Ti thin films. Considering that the grain size in Ni-Ti-Cu films is not affected by the annealing temperature in the range 500 – 700°C, the grain size is determined by the crystallisation process taking place during annealing of the as-deposited amorphous structure. A very few studies investigated the kinetic of crystallisation of Ni-Ti and Ni-Ti-Cu films. In the former case, it was reported that off-stoichiometric compositions exhibit a more complex and sluggish crystallisation process. Regarding the ternary Ni-Ti-Cu compositions it was reported that Cu addition (only a small amount, i.e. 1.3 at.% was investigated) decreased the activation energy for crystal growth but increased it for nucleation, which should led to the formation of less grains of bigger size. However, this result contradicts the experimental evidence, as with increasing Cu content smaller grains were observed. Furthermore, most of the transmission electron microscopy investigations reported in literature on Ni-Ti-Cu films, were carried out by analysing thin foils from the top view[12] thus missing information through the films thickness, which can provide precious evidence about grain growth. Therefore, the effects of Cu addition on the microstructure, with particular regard to the grain size, of Cu-doped Ni-Ti thin films are still missing in the literature and represent therefore one of the aims of the present research.

As mentioned previously, several investigations were carried out on Ni-Ti-Cu films by changing systematically the film composition. These investigations were primarily aimed at understanding how the functional properties of Ni-Ti thin films are affected by the Cu content in view of a potential application of Ni-Ti-Cu films as MEMS.

[12] Electron beam normal to the substrate.

However, only a few studies reported the mechanical properties of Ni-Ti binary films in relation to their chemical composition and no investigations reported specifically the effects of Cu content on the mechanical properties of Ni-Ti-Cu thin films. Hardness and elastic modulus as well as combinations of these mechanical parameters in relation to the films composition are important aspects to take in account when designing novel coatings systems. Therefore, the present research was also aimed at evaluating how the microstructural changes induced by Cu addition as well as the necessary post-deposition heat treatment affect the mechanical properties of sputter-deposited Ni-Ti(-Cu) thin films. Nanoindentation was adopted with the aim of characterising the thin films at nano-scale.

A very important area of development among the tribology community is represented by the ongoing effort of improving crack resistance of functional tribological coatings by designing multilayer[13] systems. A very few studies showed that adhesion and tribological performance (friction and wear) of hard coatings can be improved by the interposition of a Ni-Ti layer (4 – 21 μm thick) between the substrate and the hard coating. These improvements were ascribed to the superelastic properties of the Ni-Ti interlayer. However, these bilayer coatings were considered as a black box and no microstructural investigations were carried out in order to assess the actual response of the bilayer structure to the loading conditions taking place in a tribological scenario. Furthermore, the fabrication process of Ni-Ti-based thin films is rather expensive; therefore thinner layers might be more suitable from production on large scale.

In the research reported in this thesis, a novel thin bilayer system was fabricated by magnetron sputtering and characterised from mechanical, structural and tribological point of view at nano-scale, before and after testing. The bilayer system consisted of the interposition of a Ni-Ti(-Cu) thin layer, with different Cu contents, between a W-S-C transition metal dichalcogenide coating and the substrate. This functional top layer has been selected as despite its excellent frictional properties, often these coatings exhibit adhesion problems, which limit their lifetime in service. The study was aimed at understanding and correlating the microstructural and mechanical properties of different Ni-Ti(-Cu) interlayers to the tribological performance of the corresponding bilayer coatings. Nanoindentation is adopted to assess the mechanical behaviour of bilayers with different interlayers, while nano-scratch and tribotests are employed to

[13] Coating consisting of several or many layers.

evaluate the tribological behaviour of these coatings. Advanced analysis techniques such as focused ion beam, X-ray based techniques and transmission electron microscopy are employed in order to investigate the microstructure of as-deposited and tested coatings.

7. Current approach and structure of the thesis

In this study we are interested in exploring and understanding the effects of Cu additions on the microstructural and mechanical properties of sputter deposited Ni-Ti thin films. Furthermore, we aim to use these thin films as an interlayer between a tribological top layer (W-S-C) and the substrate with the objective of improving the tribological performance of functional layers. Of interest is the correlation between microstructural and mechanical properties of the Ni-Ti(-Cu) interlayers with the tribological performance of the bilayer coatings[14]. With these aims in mind the current research is subdivided essentially in two parts where the microstructural and mechanical properties of Ni-Ti(-Cu) thin films are first investigated and correlated. In the second part of the research the tribological properties of the bilayer coatings are explored and related to microstructure and mechanical properties of single and bilayer coatings. Structural, mechanical and tribological properties are investigated by means of different experimental techniques as summarised in Chapter 2.

Amorphous Ni-Ti(-Cu) thin films with different Cu content are deposited and subsequently annealed at different temperatures in order to produce different microstructures, especially in terms of precipitates in the grains interior. The microstructure of the films is investigated by X-ray diffraction and (scanning) transmission electron microscopy, while the mechanical properties are measured by multiple-loading nanoindentation measurements (Chapter 3).

A microstructural investigation is aimed at understanding the unknown grain refinement induced by Cu addition in Ni-Ti thin films. Particularly, a HR-TEM investigation is aimed at characterising the grain boundary microstructure and

[14] Bilayers consist of the same top layer and of a Ni-Ti-(Cu) interlayer with different Cu contents.

chemical composition, which are discussed in relation to the crystallisation process taking place in Ni-Ti-Cu films (Chapter 4).

In the second part of this study, the effects of Ni-Ti(-Cu) interlayer, in relation to different Cu contents, on the mechanical properties and resistance to adhesion damage of W-S-C self-lubricant coatings is addressed by a comparative study performed with the aid of nanoindentation, nano-scratch and nano-friction measurements (Chapter 5).

The tribological performance of W-S-C/Ni-Ti(-Cu) bilayers are investigated by pin-on-disc wear tests and correlated to the mechanical and microstructural properties of the bilayers. Surface chemical analysis is carried out on the sliding surfaces by Raman spectroscopy, while the microstructural changes produced in the subsurface are studied by transmission electron microscopy. TEM lamellae are produced by focused ion beam within the wear tracks. Therefore, a microstructural investigation on different bilayer systems and testing conditions is undertaken in this research (Chapter 6).

References

[1] A. Olander, “An electrochemical investigation of solid cadmium-gold alloys,” *Journal of the American Chemical Society,* vol. 54, pp. 3819-3833, 1932.

[2] A. Olander, “The crystal structure of AuCd,” vol. 83, pp. 145-148, 1932.

[3] L. C. Chang and T. A. Read, “Plastic Deformation and Diffusionless Phase Changes in Metals- The Gold-Cadmium Beta Phase,” *Transactions of the AIME,* vol. 191, pp. 47-52, 1951.

[4] M. W. Burkart and T. A. Read, “Diffusionless Phase Change in the Indium-Thallium System,” *Journal of Metals,* pp. 1516-1524, 1953.

[5] E. Hornbogen and R. Feder, “Über den Einfluss von Spannungen und das Auftreten von Umwandlungsplastizität bei der Beta-Beta-Umwandlung des Messings,” *Zeitschrift fur Metallkunde,* vol. 47, pp. 427-433, 1956.

[6] L. Muldawer and R. Feder, “Temperature Responsive Cadmium-Silver-Gold Alloys,” *US Patent 3,012,882,* 1961.

[7] L. Muldawer and R. Feder, “Temperature Responsive Cadmium-Silver-Gold Alloys,” *US Patent 3,012,883,* 1961.

[8] F. E. Wang, W. J. Buehler and S. J. Pickart, “Crystal Structure and a Unique “Martensitic” Transition of TiNi,” *Journal of Applied Physics,* vol. 36, pp. 3232-3239, 1965.

[9] J. Guilemany, B. Mellor and J. Fernandez, “A comparison of the two-way shape-memory effect achieved by stabilised stress-induced martensite training in β and martensitic Cu-Zn-Al-Co alloys,” *Materials Letters,* vol. 13, pp. 105-108, 1992.

[10] B. Mellor, J. Guilemany, J. Miguel, J. Fernandez, A. Amengual, F. Lovey and V. Torra, “Stabilized stress induced martensite - Its use in two way shape memory training process,” *Scripta Metallurgica et Materialia,* vol. 24, pp. 241-244, 1990.

[11] R. Jackson, J. Boland and J. Frankeny, “Pseudo-Plastic Behavior of Uranium-Niobium Alloys,” *US Patent 3,567,523,* 1971.

[12] C. Liu, Z. Gao, X. An, H. Wang, L. Gao and W. Cai, “Surface characteristics and nanoindentation study of Ni-Mn-Ga ferromagnetic shape memory sputtered thin films,” *Applied Surface Science,* vol. 254, pp. 2861-2865, 2008.

[13] J. V. Humbeeck, “The martensitic transformation,” *in Mechanical Spettroscopy, R. Shaller, G. Fantozzi and G. Gremaud,* pp. 382-415, 2001.

[14] J. V. Humbeeck and R. Stalmans, “Shape memory alloys, types and functionalities,” *in*

Encyclopaedia of Smart Materials, pp. 951-964, 2002.

[15] H. Y. Kim, Masashi and S. Miyazaki, “Crystallization process and shape memory properties of Ti-Ni-Zr thin films,” *Acta Materialia,* vol. 57, pp. 1920-1930, 2009.

[16] R. Zarnetta, A. Savan, S. Thienhaus and A. Ludwig, “Combinatorial study of phase transformation characteristics of a Ti-Ni-Pd shape memory thin film composition spread in view of microactuator applications,” *Applied Surface Science,* vol. 254, pp. 743-748, 2007.

[17] S. Sanjabi, Y. Cao and Z. Barber, “Multi-target sputter deposition of Ni50Tix-50Hfx shape memory thin films for high temperature microactuator application,” *Sensors and Actuators A,* vol. 121, pp. 543-548, 2005.

[18] C. Wayman and J. Harrison, “The Origins of the Shape Memory Effect,” *Journal of Materials,* vol. 41, pp. 26-28, 1989.

[19] K. Otsuka and X. Ren, “Physical metallurgy of Ti-Ni-based shape memory alloys,” *Progress in material sciences,* vol. 50, pp. 511-678, 2005.

[20] S. Miyazaki, Y. Q. Fu and W. M. Huang, Thin Film Shape Memory Alloys, Cambridge: Cambridge Unversity Press, 2009.

[21] J. Shaw, “Thermomechanical Model for a 1- Shape Memory Alloy Wire with Propagating Instabilities,” *Internation Journal of Solids and Structures,* vol. 39, pp. 1275-1305, 2002.

[22] A. Saigal and M. Fonte, “Solid, shape recovered “bulk” Nitinol: Part I—Tension–compression asymmetry,” *Materials Science and Engineering A,* vol. 528, pp. 5536-5550, 2011.

[23] A. Ishida, M. Sato and Z. Gao, “Properties and applications of Ti-Ni-Cu shape-memory-alloy thin films,” *Journal of Alloys and Compounds,* pp. In Press, Corrected Proof, 2012.

[24] P. Neukomn, H. Bornhauser, T. Hochuli, R. Paravinci and G. Schwarz, “Characteristics of Thin-wire Shape Memory Actuators,” *Sensors and Actuators,* Vols. A21-A23, pp. 247-252, 1990.

[25] G. Shaw, D. Stone, A. Johnson, A. Ellies and W. Crone, “Shape memory effect in nanoindentation of nickel-titanium thin films,” *Spplied physics letters,* vol. 3, 14 July 2003.

[26] F. YongQing, D. Hejun, W. Huang, S. Zhang and M. Hu, “TiNi-based thin films in MEMS applications: a review,” *Sensors and Actuators A ,* vol. 112, pp. 395-408, 2004.

[27] W. D. Bosscher and H. Lievens, “Andances in magnetron sputter sources,” *Thin Solid Films,* vol. 351, pp. 15-20, 1999.

[28] K. K. Schuegraf, Handbook of thin-film deposition process and techniques: principles,

methods, equipment, and applications, Noyes Publications, 1988.

[29] J. Musil and J. Vlecek, "A perspective of magnetron sputtering in surface engineering," *Surface and Coatings Technology,* vol. 112, pp. 162-169, 1999.

[30] R. Arnell and P. Kelly, "Recent advances in magnetron sputtering," *Surface and Coatings Technology,* vol. 112, pp. 170-176, 1999.

[31] P. Kelly and R. Arnell, "Magnetron sputtering: a review of recent developments and applications," *Vacuum,* vol. 56, pp. 159-172, 2000.

[32] D. Gibson, I. Brinkley, E. Waddell and J. Walls, "Closed field magnetron sputtering: new generation sputtering process for optical coatings," *Applied Multilayers Ltd., Coalville, Leicestershire, UK.*

[33] G. Brauer, B. Szyszka, M. Vergohl and R. Bardorf, "Magnetron sputtering – Milestones of 30 years," *Vacuum,* vol. 84, pp. 1354-1359, 2010.

[34] S. Miyazaki, K. Nomura, A. Ishida and S. Kajiwara, "Recent Developments in Sputter-Deposited Ti-Ni-Base Shape Memory Alloy Thin Films," *J. Phys., France 7,* vol. IV, 1997.

[35] S. Patrick, C. Chaterine, P. B. Le, A. Manabu and F. Hiroyuki, "Effect of the composition and thermal annealing on the transformation temperatures of sputtered TiNi shape memory alloy thin films," *Thin Solid Films,* vol. 401, pp. 52-59, 2001.

[36] A. G. Ramirez, H. Ni and H.-J. Lee, "Crystallization of amorphous sputtered NiTi thin films," *Materials Sciences and Engineering A,* Vols. 438-440, pp. 703-709, 2006.

[37] X. Wang and J. J. Vlassak, "Crystallization Kinetics of amorphous NiTi shape memory alloy thin films," *Scripta Materialia ,* vol. 54, pp. 925-930, 2006.

[38] J. Chen and S. Wu, "Crystallization behaviour of r.f.-sputted TiNi thin films," *Thin Solid Films,* vol. 339, pp. 194-199, 1999.

[39] J.-L. Seguin, M. Bendahan, A. Isalgue, V. Esteve-Cano, H. Carchano and V. Torra, "Low temperature crystallized Ti-rich NiTi shape memory alloy films for microactuators," *Sensors and Actuators,* vol. 74, pp. 65-69, 1999.

[40] A. Ishida, M. Sato, A. Takei, K. Nomura and S. Miyazaki, "Effect of Aging on Shape Memory Behaviour of Ti-51.3 At. Pct Ni Thin Films," *Metallurgical and Materials Transactions A,* vol. 27 A, p. 3753, 1996.

[41] Y. Yang, H. Jia, Z. Zhang, H. Shen, A. Hu and Y. Wang, "Transformation in sputter-deposited thin films of NiTi shape memory alloy," *Materials Letters,* vol. 22, pp. 137-140, 1995.

[42] H. Zhang and C. Qiu, "Characterization and MEMS application of low temperature TiNi(Cu) shape memory thin films," *Materials Science and Engineering A,* Vols. 438-440,

pp. 1106-1109, 2006.

[43] K. Hori, T. Namazu and S. Inoue, “Effect of Cu content on the shape memory behaviour of Ti-Ni-Cu alloy thin films prepared by triple-source dc magnetron sputtering,” *Thin Solid Films,* vol. 518, pp. 26-28, 2010.

[44] S. Miyazaki, T. Hashinaga and A. Ishida, “Martentisic transformations in sputter-deposited Ti-Ni-Cu shape memory alloy thin films,” *Thin Solid Films,* Vols. 281-282, pp. 364-367, 1996.

[45] H. Du and Y. Fu, “Deposition and characterization of Ti1-x(Ni,Cu)x shape memory alloy thin films,” *Surface and Coatings Technology,* vol. 176, pp. 182-187, 2004.

[46] T. Matsunaga, S. Kajiwara, K. Ogawa, T. Kikuchi and S. Miyazaki, “High strength Ti-Ni-based shape memory thin films,” *Materials Science and Engineering A,* Vols. 273-275, pp. 745-748, 1999.

[47] R. Lobel, S. Thienhaus, A. Savan and A. Ludwig, “Combinatorial fabrication and high-throughput characterization of a Ni-Ti-Cu shape memory thin film composition spread,” *Materials Science and Engineering A,* Vols. 481-482, pp. 151-155, 2008.

[48] Y. Xu, X. Huang and A. Ramirez, “Crystallization of amorphous NiTiCu thin films,” *Journal of Alloys and Compounds,* vol. 480, pp. L13-L16, 2009.

[49] S. Y., F. K. and F. T., “Proc. 32nd Materials Society Annual Conf.,” p. 65, 1983.

[50] K. J.J., M. P. and S. D.A., *Scripta Metall.,* vol. 20, p. 243, 1986.

[51] N. Schell, R. Martins and F. B. Fernandes, “Real-time and in-situ structural design of functional NiTi SMA thin films,” *Applied Physics A,* vol. 81, pp. 1441-1445, 2005.

[52] K. K. Ho and G. P. Carman, “Sputter deposition of NiTi thin film shape memory alloy using a heated target,” *Thin Solid FilmS,* vol. 370, pp. 18-29, 2000.

[53] V. Chernysh, V. Tuboltsev and V. Kulikauskas, “Angular distribution of Ni and Ti atoms sputtered from a NiTi alloy under He and Ar ion bombardment,” *Nuclear Instruments and Methods in Physics Research B,* vol. 140, pp. 303-310, 1998.

[54] M. Ren, L. Wang, D.Xu and B. Cai, “Sputter-deposited Ni-Ti-Cu shaped memory alloy thin films,” *Materials and Design,* vol. 21, pp. 583-586, 2000.

[55] M. Cai, Y. Fu, S. Sanjabi, Z. Barber and J. Dickinson, “Effect of composition on surface relief morphology in TiNiCu thin films,” *Surface & Coatings Technology,* vol. 201, pp. 5843-5849, 2007.

[56] K. K. Ho, K. Mohanchandra and G. P. Carman, “Examination of the sputtering profile pf NiTi under target heating conditions,” *Thin Solid Films,* vol. 413, pp. 1-7, 2002.

[57] F. Gong and Y. W. H.M. Shen, “Fabrication and characterization of sputtered Ni-rich NiTi thin films,” *Materials Letters,* vol. 25, pp. 13-16, 1995.

[58] I. Akira, S. Morio, T. Atsushi and M. Shuichi, “Effect of Heat Treatment on Shape Memory Behaviour of Ti-rich Ti-Ni Thin Films,” *Materials Transactions, JIM,* vol. 36, no. 11, pp. 1349-1355, 1995.

[59] A. Ishida, M. Sato, A. Takei, K. Nomura and S. Miyazaki, “Effect of Aging on Shape Memory Behaviour of Ti-51.3 At. Pct Ni Thin Films,” *Metallurgical and Materials Transactions A,* vol. 27 A, p. 3753, 1996.

[60] K. Mohanchandra, K. K. Ho and G. P. Carman, “Compositional uniformity in sputter-deposited NiTi shape memory alloy thin films,” *Materials Letters,* vol. 62, pp. 3481-3483, 2008.

[61] T. Lehnert, H. Grimmer, P. Boni, M. Horisberger and R. Gotthardt, “Characterization of shape-memory alloy thin films made up from sputter-deposited Ni/Ti multilayers,” *Acta Materialia,* vol. 48, pp. 4065-4071, 2000.

[62] E. Quandt, C. Halene, H. Holleck, K. Feit, M. Khol, O. Schlobmacher, A. Skokan and K. Skrobanek, “Sputter deposition of TiNi, TiNiPd and TiPd films displaying the two-way shape-memory effect,” *Sensors and Actuators A,* vol. 53, pp. 343-439, 1996.

[63] P. Krulevitch, P. Ramsey, D. Makowiecki, A. Lee, M. Northrup and G. johnson, “Mixed-sputter deposition of Ni-Ti-Cu shape memory films,” *Thin Solid Films,* vol. 274, pp. 101-105, 1996.

[64] S. Sanjabi, S. K. Sadrnezhaad, K. A. Yates and Z. H. Barber, “Growth and characterization of TixNi1-x shape memory thin films using simultaneous sputter deposition from separate elemental targets,” *Thin Solid Films,* vol. 491, pp. 190-196, 2005.

[65] N. Frantz-Rodriguez, A. Bosseboeuf, E. Dufour-Gergam, V. Stambouli-Sènè, G. Nouet, W. Seiler and J.-L. Lebrun, “Composition and structure of NiTiCu shape memory thin films,” *Journal of Micromechanics and Microengineering,* vol. 10, pp. 147-151, 2000.

[66] J. Chu, Y. Lai, T. Lin and S. Wang, “Deposition and characterization of TiNi-base thin films by sputtering,” *Materials Sciences and Engineering A,* vol. 277, pp. 11-17, 2000.

[67] N. Kaiser, “Review of the fundamentals of thin-film growth,” *Applied Optics,* vol. 41, no. 16, p. 3053, 2002.

[68] S. Miyazaki and A. Ishida, “Martensitic transformation and shape memory behaviour in sputter-deposited TiNi-base thin films,” *Materials Sciences and Engineering A,* Vols. 273-275, pp. 106-133, 1999.

[69] F. Yongqing and HejunDu, “RF magnetron sputtered TiNiCu shape memory alloy thin film,” *Materials Science and Engineering A,* vol. 339, pp. 10-16, 2003.

[70] Y. Fu, H. Du and S. Zhang, "Sputtering deposited TiNi films: relationship among processing, stress evolution and phase transformation behaviours," *Surface and Coatings Technology,* vol. 167, pp. 120-128, 2003.

[71] I. Petrov, P. Barna, L. Hultman and J. Greene, "Microstructural evolution during film growth," *J. Vac. Sci. Technol A,* vol. 21, p. S117, 9 June 2003.

[72] M. J. Vestel and D. S. Grummon, "Precipitates and lamellar microstructures in NiTi films," *Materials Sciences and Engineering A,* vol. 378, pp. 437-442, 2004.

[73] B. G. Priyadarshini, S. Aich and M. Chakraborty, "An investigation on phase formations and microstructures of Ni-rich Ni-Ti Shape memory alloy thin films," *Metallurgical and Materials Transactions A,* vol. , p. 3284, 2010.

[74] A. Ishida and M. Sato, "Ti-Ni-Cu shape memory alloy thin film formed on polyimide substrate," *Thin Solid Films,* vol. 516, pp. 7836-7839, 2008.

[75] X. Huang and A. Ramirez, "Structural relaxation and crystallization of NiTi thin film metallic glasses," *Applied Physics Letters,* vol. 95, p. 121911, 2009.

[76] P.-Y. Hsu and J.-M. Ting, "Growth and characteristics of TiNICu thin films," *Thin Solid Films,* Vols. 420-421, pp. 524-529, 2002.

[77] A. Ishida, M. Sato and S. Miyazaki, "Mechanical properties of Ti-Ni shape memory thin films formed by sputtering," *Materials Sciences and Engineering A,* Vols. 273-275, pp. 754-757, 1999.

[78] S. Sanjabi and Z. Barber, "The effect of film composition on the structure and mechanical properties of NiTi shape memory thin films," *Surface & Coatings Technology,* vol. 204, pp. 1299-1304, 2010.

[79] P. Surbled, C. Clearc, B. L. Pioufle, M. Ataka and H. Fujita, "Effect of the composition and thermal annealing on the transformation temperatures of sputtered TiNi shape memory alloy thin films," *Thin Solid Films,* vol. 401, pp. 52-59, 2001.

[80] X. Cao, X. Cao and Q. Zhang, "Nanoscale indentation behaviour of pseudo-elastic Ti-Ni thin films," *Journal of Alloys and Compounds,* vol. 465, pp. 491-496, 2008.

[81] L. Tong, Y. Li, F. Meng, H. Tian, W. Zheng and Y. Wang, "Investigation on the mechanical properties of sputtered TiNi thin films," *Journal of Alloys and Compounds,* vol. 494, pp. 166-168, 2010.

[82] A. Ishida and M. Sato, " Microstructure and shape memory behaviour of annealed Ti51.5Ni(48.5-x)Cux (x=6.5-20.9) thin films," *Philosophical Magazine,* vol. 87, no. 35, pp. 5523-5538, 11 December 2007.

[83] A. Ishida and M. Sato, "Shape Memory behaviour of annealed Ti48.5Ni(51.5-x)Cux (x=6.2-33.5) thin films," *Philosophical Magazine,* vol. 88, no. 16, pp. 2439-2448, 1 June

2008.

[84] P. B. Barna and M. Adamik, “Growth mechanisms of policrystalline thin films,” *Research Istitute for Techinical Physics.*

[85] Y. Lei, H. Zhao, W. Cai, X. An and L. Gao, “Cristallization kinetics of NixTi1-x alloy thin films,” *Physics B,* vol. 405, pp. 947-950, 2010.

[86] K. Liu and J. Duh, “Kinetics of the crystallization in amorphous NiTi thin films,” *Journal of Non-Crystalline Solids,* vol. 353, pp. 1060-1064, 2007.

[87] M. J. Vestel, D. S. Grummon, R. Gronsky and A. P. Pisano, “Effect of temperature on the devetrification kinetics of NiTi films,” *Acta Materialia,* vol. 51, pp. 5309-5318, 2003.

[88] H. Ni, H.-J. Lee and A. G. Ramirez, “Compositional effects on the crystallization kinetics of nickel-titanium thin films,” *Journal of Materials Research,* vol. 20, no. 7, July 2005.

[89] J. Z. Chen and S. K. Wu, “Crystallisation temperature and activation energy of rf-sputtered near-equiatomic TiNi and Ti50Ni40Cu10 thin films,” *Journal of Non-Crystalline Solids,* vol. 288, pp. 159-165, 2001.

[90] H. S. Chen and B. K. Park, “Role of chemical bonding in metallic glasses,” *Acta Metallurgica,* vol. 21, no. 4, pp. 349-400, 1973.

[91] C. X. L. Zhang and J. Wu, “Grain size estimations of annealed Ti-Ni shape memory thin films,” vol. 432, no. 4/25, pp. 318-322, 2007.

[92] E. Machlin, An Introduction to Aspects of Thermodynamics and Kinetics Relevant to Materials Science, Third ed., Elsevier Science & Technology Books, 2007.

[93] A. Ishida, M. Sato and K. Ogawa, “Microstrucure and Shape-memory behaviour of annealed Ti51.5-Ni33.1-Cu15.4 thin films,” *Philosophy Magazine Letters,* vol. 86, no. 1, pp. 13-20, January 2006.

[94] X. Meng, M. Sato and A. Ashida, “Structure of martensite in sputter-deposited (Ni,Cu)-rich Ti-Ni-Cu thin films containing Ti(Ni,Cu)2 precipitates,” *Acta Materialia,* vol. 57, pp. 1525-1535, 2009.

[95] F. M. B. Fernandes, R. Martines, M. T. Nogueira and R. J. Silva, “Structural characterisation of NiTi thin film shape memory alloys,” *Sensors and Actuators A,* vol. 99, pp. 55-58, 2002.

[96] J. Zhang, M. Sato and A. Ishida, “Influence of Guiner-Preston zones on deformation in Ti-rich Ti-Ni thin films,” *Philosophical Megazine Letters,* vol. 82, no. 5, pp. 257-264, 2002.

[97] J. Zhang, M. Sato and A. Ishida, “On the Ti2Ni precipitates and Guinier-Preston zones in Ti-rich Ti-Ni thin films,” *Acta Materialia,* vol. 51, pp. 3121-3130, 2003.

[98] J. Zhang, M. Sato and A. Ishida, “Deformation mechanism of martensite in Ti-rich Ti-Ni shape memory alloy thin films,” *Acta Materialia,* vol. 54, pp. 1185-1198, 2006.

[99] A. Ishida, M. Sato and Z. Gao, “Effects of Ti content on microstructure and shape memory behavior of TixNi(84.5-x)Cu15.5 (x = 44.6-55.4) thin films,” *Acta Materialia,* vol. 69, pp. 292-300, 2014.

[100] X. Meng, M. Sato and A. Ishida, “Structure of martensite in Ti-rich Ti-Ni-Cu thin films annealed at different temperatures,” *Acta Materialia,* vol. 56, pp. 3394-3402, 2008.

[101] X. Meng, M. Sato and A. Ishida, “Influence of Ti2Cu precipitates on B19 martensite structure in a Ti-rich Ti-Ni-Cu thin film,” *Philosophical Magazine Letters,* vol. 88, no. 8, pp. 575-582, August 2008.

[102] A. Ishida and M. Sato, “Microstructures of crystallized Ti51.5Ni48.5-xCux (x=23.4-37.3) thin films,” *Intermetallics,* no. 19, pp. 900-907, 2011.

[103] A. Ishida, M. Sato and K. Ogawa, “Microstructure of annealed Ti48.5Ni(51.5-x)Cux (x=6.2-33.5) thin films,” *Philosophical Magazine,* vol. 88, no. 16, pp. 2427-2438, 1 June 2008.

[104] A. C. Fisher-Cripps, Nanoindention, Second, Ed., Spring, 2004.

[105] W. C. Oliver and G. M. Pharr, “Measurement of hardness and elastic modulus by instrumented indentation: Advances in understanding and refinements to methodology,” *Journal of Material Research,* vol. 19, no. 1, pp. 3-20, 2004.

[106] A. Leyland and A. Metthews, “On the significance of the H/E ratio in wear control: a nanocomposite coating approach to optimised tribological behaviour,” *Wear,* vol. 259, pp. 1-11, 2000.

[107] W. Ni, Y.-T. Cheng, M. Lukitsch, A. M. Wainer, L. C. Lev and D. S. Grummon, “Novel layered tribological coatings using a superelastic NiTi interlayer,” *Wear,* vol. 259, pp. 842-848, 2005.

[108] A. Wood, S. Sanjabi, Y. Fu, Z. Barber and T. Clyne, “Nanoindentation of binary and ternary Ni-Ti-based shape memory alloy thin films,” *Surface & Coatings Technology,* vol. 202, pp. 3115-3120, 2008.

[109] S. Moyne, C. Poilane, K. Kitamura, S. Miyazaki, P. Delobelle and C. Lexcellent, “Analysis of the thermomechanical behaviour of Ti-Ni shape memory alloy thin films by bulging and nanoindentation procedures,” *Materials Science and Engineering A,* Vols. 273-275, pp. 727-732, 1999.

[110] X. Huang, J. S. Juan and A. Ramirez, “Evolution of phase transformation behaviour and mechanical properties with crystallization in NiTi thin films,” *Scripta Materialia,* vol. 63, pp. 16-19, 2010.

[111] L. Zhang, C. Xie and J. Wu, "Effect of annealing temperature on surface morphology and mechanical properties of sputter-deposited Ti-Ni thin films," *Journal of Alloys and Compounds,* vol. 427, pp. 238-243, 2007.

[112] D. Konig, P. Buenconsejo, D. Grochla, S. Hamann, J. Pfetzing-Micklich and A. Ludwig, "Thickness-dependence of the B2-B19 martensitic transformation in nanoscale shape memory alloy thin films: Zero-hysteresis in 75 nm thick Ti51Ni38Cu11 thin films," *Acta Materialia,* vol. 60, pp. 306-313, 2012.

[113] A. N. Kumar, C. S. Nair, M. Kannan and S. Jayakumar, "TEM and nanoindentation studies on sputtered Ti40Ni60 thin films," *Materials Chemistry and Physics,* vol. 97, pp. 308-314, 2006.

[114] P. Tall, S. Ndiaye, A. Beye, Z. Zong, W. Soboyejo, H.-J. Lee, A. Ramirez and K. Rajan, "Nanoindentation of Ni-Ti Thin Films," *Materials and Manufacturing Processes,* vol. 22, pp. 175-179, 2007.

[115] X. Huang, J. Nohava, B. Zhang and A. Ramirez, "Nanoindentation of NiTi shape memory thin films at elevated temperatures," *International Journal of Smart and Nano Materials,* vol. 2, no. 1, pp. 39-49, March 2011.

[116] A. Kumar, S. Sharma, S. Bysakh, S. Kamat and S. Mohan, "Effect of substrate and annealing temperature on mechanical properties of Ti-rich NiTi films," *J. Mater. Sci. Technol.,* vol. 26(11), pp. 961-966, 2010.

[117] X. -. G. Ma and K. Komvopoulos, "Nanoscale pseudoelastic behaviour of indented titanium-nickel films," *Applied Physics Letters,* vol. 83, no. 18, pp. 3773-3775, 2003.

[118] X. -. G. Ma and K. Komvopoulos, "Pseudoelasticity of shape-memory titanium-nickel films subjected to dynamic nanoindentation," *Applied Phyisics Letters,* vol. 84, no. 21, pp. 4274-4276, 2004.

[119] G. Pan, Z. Cao, M. Wei, L. Xu, J. Shi and X. Meng, "Superelasticity of TiNi thin films induced by cyclic nanoindentation deformation at nanoscale," *Materials Science & Engineering A,* no. 600, pp. 8-11, 2014.

[120] R. Zarnatta, S. Kneip, C. Somsen and A. Ludwig, "High-throughput characterization of mechanical properties of Ti-Ni-Cu shape memory thin films at elevated temperature," *Materials Science and Engineering A,* vol. 528, pp. 6552-6557, 2011.

[121] I. GORYACHEVA, Contact Mechanics in Tribology, Dordrecht: Kluwer Academic Publishers, 1998.

[122] W. Crone, G. Shaw, D. Stone, A. Johnson and A. Ellis, "Shape Recovery after Nanoindentation of NiTi thin films," *Society for Experimental Mechanics, 2002 SEM Annual Conference Proceedings, Carlotte, NC,* 2003.

[123] Y. Fu, H. Du and S. Zhang, “Deposition of TiN layer on TiNi thin films to improve surface properties,” *Surface & Coatings Technology,* vol. 167, pp. 129-136, 2003.

[124] W. Ni, Y.-T. Cheng, M. J. Lukitsch, A. M. Weiner, L. C. Le and D. S. Grummon, “Effects of the ratio of hardness to Youngs' modulus on the frictrion and wear behaviour of bilayer coatings,” *Applied Physics Letters,* vol. 85, no. 18, pp. 4028-4030, 2004.

[125] Y. Zhang, Y.-T. Cheng and D. S. Grummom, “Novel tribological systems using shape memory alloys and thin films,” *Surface & Coatings technology,* vol. 202, pp. 998-1002, 2007.

[126] W. Jamison and S. Cosgrove, “Friction Characteristics of Transition-Metal Disulfides and Diselenides,” *A. S. L. E. Transactions,* vol. 14, pp. 62-72, 1971.

[127] P. Fleischauer and R. Bauer, “The Influence of Surface Chemistry on MoS2 Transfer Film Formation,” *A. S. L. E. Transactions,* vol. 30, pp. 160-166, 1987.

[128] P. Fleischauer, J. Lince, P. Bertrand and R. Bauer, “Electronic Structure and Lubrication Properties of MoS, A Qualitative Molecular Orbital Approach,” *Langmuir,* vol. 5, pp. 1009-1015, 1989.

[129] Q. H. Wang, K. Kalantar-Zadeh, A. Kis, J. Coleman and M. S. Strano, “Electronics and optolectronics of two-dimentional transition metal dichalcogenides,” *Nature Nanotecnology,* vol. 7, pp. 699-712, 2012.

[130] T. Polcar and A. Cavaleiro, “Review on self-lubricant transition metal dichalcogenides nanocomposite coatings alloyed with carbon,” *Surf. Coat. Tech.,* vol. 206, pp. 686-695, 2011.

[131] J. Pimental, M. Danek, T. Polcar and A. Cavaleiro, “Effects of rough surface patterning on the tribology of W-S-C-Cr self-lubricant coatings,” *Tribology International,* vol. 69, pp. 77-83, 2014.

[132] T. Polcar, F. Gustavsson, T. Therslaff, S. Jacobson and A. Cavaleiro, “Complex frictional analysis of self-lubricant W-S-C/Cr coating,” *Faraday Discussion,* vol. 156, pp. 383-401, 2012.

[133] J. Sundberg, H. Nyberg, E. Sarhamaar, F. Gustavsson, T. Kubart, T. Nyberg, S. Jacobson and U. Jansson, “Influence of Ti addition on the structure and properties of low-friction W-S-C coatings,” *Surface & Coatings Technology,* vol. 232, pp. 340-348, 2013.

[134] H. Nyberg, J. Sundberg, E. Sarhamaar, F. Gustavsson, T. Kubart, T. Nyberg, U. Jansson and S. Jacobson, “Extreme friction reductions during initial running-in of W-S-C-Ti low-friction coatings,” *Wear,* vol. 302, pp. 987-997, 2013.

[135] A. A. Voevodin and J. S. Zabinski, “Supertough wear-resistant coatings with "chameleon" surface adaption,” *Thin Solid Films,* vol. 370, p. 223, 2000.

[136] M. Evaristo, A. Nossa and A. Cavaleiro, “W-S-C sputtered films: Influence of the carbon alloying method on the mechanical properties,” *Surface & Coating Technology,* vol. 200, pp. 1076-1079, 2005.

[137] M. Roy, T. Koch and A. Paushitz, “The influence of sputtering procedure on nanoindentation and nanoscratch behaviour of W-S-C film,” *Applied Surface Science,* vol. 256, pp. 6850-6858, 2010.

[138] T. Polcar, M. Evaristo and A. Cavaleiro, “Self-Lubricating W-S-C Nanocomposite Coatings,” *Plasm. Process. Polym.,* vol. 6, pp. 417-424, 2009.

[139] T. Koch, M. Evaristo, A. Pauschitz, M. Roy and A. Cavaleiro, “Nanoindentation and nanoscratch behaviour of reactive sputtered deposited W-S-C film,” *Thin Solid Films,* vol. 518, pp. 185-193, 2009.

[140] T. Polcar, M. Evaristo and A. Cavaleiro, “Friction of Self-Lubricant W-S-C Sputtered Coatings Sliding Under Increasing Load,” *Plasm. Process. Polym.,* vol. 4, pp. S541-S546, 2007.

[141] J. V. Pimentel, T. Polcar, M. Evaristo and A. Cavaleiro, “Examination of the tribolayer formation of a self-lubricant W-S-C sputtered coating,” *Tribology International,* vol. 47, pp. 188-193, 2012.

[142] B. D. Beake, V. M. Vishnyakov and A. J. Harris, “Relationship between mechanical properties of thin nitride-based films and their behaviour in nano-scratch tests,” *Tribology International ,* vol. 44, pp. 468-475, 2011.

[143] A. Leyland and A. Matthews, "On the significance of the H/E ratio in wear control: a nanocomposite coating approach to optimised tribological behaviour", Wear, vol. 246, pp. 1-11, 2000.

Appendix A

1. Details on the functional behaviour of Ni-Ti(-Cu) thin films in relation to the microstructure

The interaction between the martensitic transformation and the precipitates formed in the grain interior by the post-deposition heat-treatment have been studied mostly by measuring the hysteresis behaviour (strain versus temperature) of the thin films during thermal cycles at different applied constant stresses. This kind of test consists of loading (constant stress) the film at high temperature, cooling it down to induce the martensitic transformation, and finally heating the sample up to the starting temperature while the strain is measured [1].

Although by the type of test mentioned above the direct and inverse martensitic transformation is thermally-induced, the hysteresis curves allowed understanding how the microstructure (as a consequence of different post-deposition heat treatments), and particularly the interaction between growing martensitic plates and precipitates affects the functional behaviour of these thin films. Figure A.1 shows typical strain – temperature curves measured for different applied stresses; the typical parameters evaluated on these curves are specified in the figure.

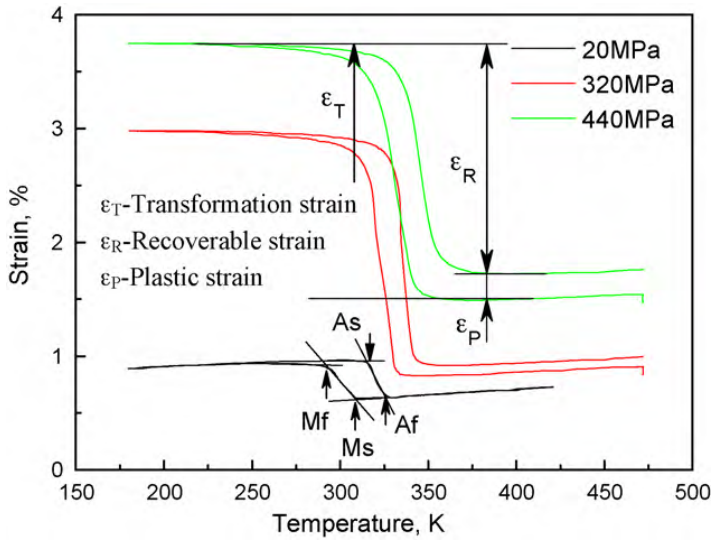

Figure A.1 – Strain versus temperature curves measured during heating and cooling under constant stresses for a $Ti_{44.6}Ni_{40.1}Cu_{15.3}$ thin film annealed at 700°C [2].

Numerous investigations have been carried out on Ni-Ti(-Cu) films of different compositions, i.e. Ti-rich, Ni-rich and near equi-atomic for binary Ni-Ti, and Ti-rich and (Ni,Cu)-rich for ternary Ni-Ti-Cu. In the following sections a brief summary of the functional behaviour of Ni-Ti(-Cu) films is reported according to different chemical compositions and microstructures.

1.1 Ti-rich Ni-Ti thin films

Based on observations in bulk Ti-rich Ni-Ti alloys, it was thought that the microstructure of films annealed at relatively low temperatures or for a short time, would be unstable. Thus when the heat-treatment does not reach equilibrium in Ti-rich films, non-equilibrium conditions can exist making transformation temperatures and shape memory behaviour sensitive to the post-fabrication thermal-treatment [3].
The effects of thermal treatment on the shape memory behaviour of Ti-rich Ni-Ti thin films were systematically investigated for the first time by *Ishida et al.* [4]. They found that when annealing at temperatures slightly higher (500°C) than T_c, Ti-rich plate precipitates were formed on the {100} planes of the B2 phase, with perfect coherency (GP zones). These precipitates conferred on the austenitic phase a higher strength, resulting in excellent shape memory properties [5]. After annealing at intermediate temperatures (550 – 600°C), a mixture of Ti-rich plate precipitates (GP zones, coherent with the B2 phase) and equilibrium Ti_2Ni spherical precipitates (semi-coherent with the B2 phase), were formed in the grain interior [6]. At a higher annealing temperature (700°C), only equilibrium spherical Ti_2Ni precipitates grew at the grain boundaries, degrading the shape memory behaviour. On the other hand, a very similar grain size (3 μm) was found for the different annealing temperatures and time, except for films annealed for 1 h at 500°C where a smaller grain size was measured.

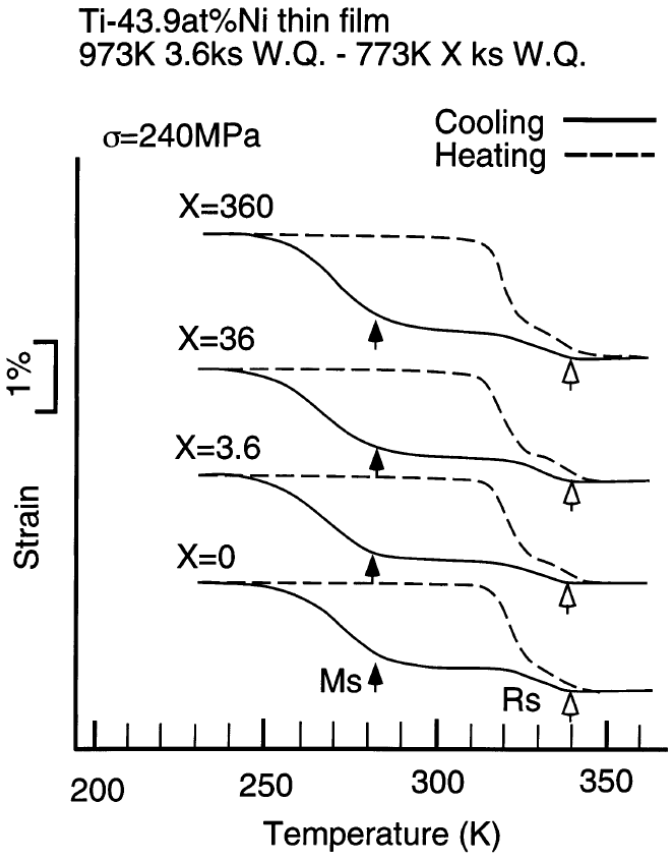

Figure A.2 - Effect of aging time on the shape memory behaviour in Ti-43.9at%Ni thin film [3].

Strain – temperature measurements, under constant applied stress, revealed marked differences for different annealing temperatures and time (Figure A.2). Specifically, all the annealed films except for those annealed at 700°C for 100 hours showed a two-stage phase transformation, associated with the R-phase. It was believed that the presence of the R-phase is linked to the existence of Ti-rich or Ni-rich plate precipitates [7]. The R-phase was exploited to produce two-way shape memory micro-actuators [8, 9], owing to its quite small hysteresis and stability during thermal cycles, compared to the large hysteresis associated with the martensitic transformation.

Strain – temperature measurements revealed that the critical stress for slip (σ_s, the stress for which the plastic strain first exceeds 0.02%, in the strain-temperature measurement), rapidly increased when the annealing temperature was below 823 K while above this temperature, σ_s was almost constant (100 MPa), as shown in Figure A.3 a. It was interesting to note that the critical temperature of 823 K coincides with the heat-treatment temperature above which subnanometric non-equilibrium plate precipitates were no longer observed. The maximum σ_s (260 MPa) was obtained for the specimen heat treated at about 690 K for about 2 hours.

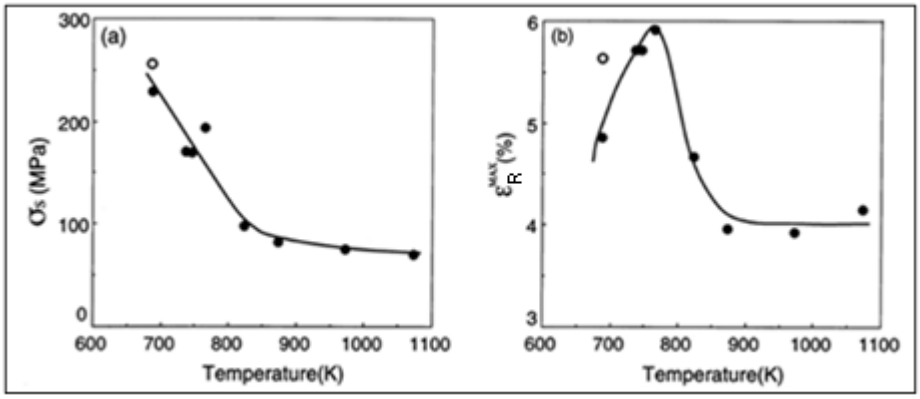

Figure A.3 - Variation in (a) critical stress for slip and (b) the maximum recoverable strain as a function of heat-treatment temperature [3].

On the other hand, Figure A.3 b shows that the recoverable strain ($\varepsilon\varepsilon_R$= total strain – plastic strain) increased with annealing temperature up to 500°C achieving a maximum value of about 6%. Higher annealing temperature caused a decrease in recoverable strain to about 4% due to the growth of semi-coherent spherical precipitates in the grain interior, which hindered martensite growth. The strain-temperature hysteresis also provided an estimate of the transformation temperatures, which were found to increase with increasing annealing temperature and time [3].

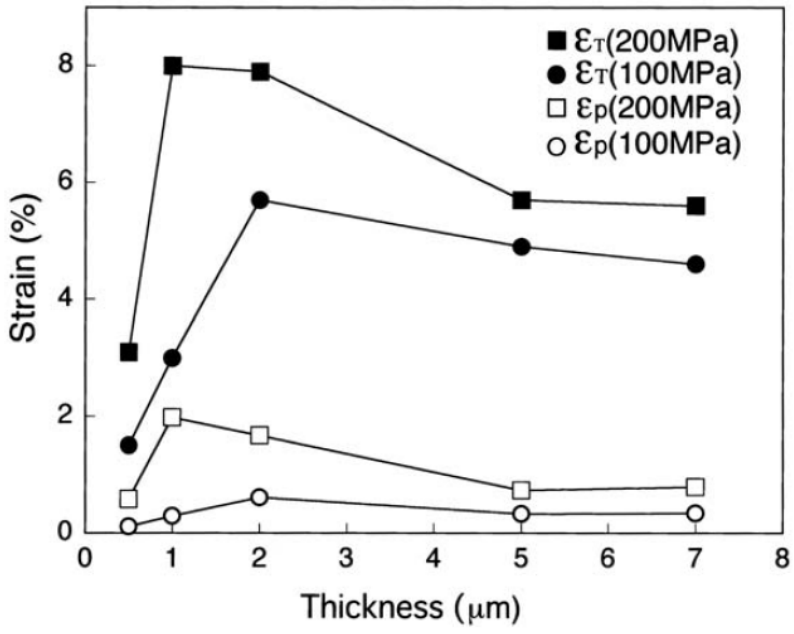

Figure A.4 - Transformation (ε_T) and plastic (ε_P) strains of Ti-50.0 at.%Ni thin films as a function of thickness [10].

The film thickness exhibited a marked effect on the shape memory behaviour of equi-atomic Ni-Ti thin films, as pointed out by *Ishida et al.* [10]. In particular, strain measurements during thermal cycles carried out for different constant tensile stresses, showed that both transformation and residual strain were characterized by a maximum, which shifts towards lower thicknesses with increasing applied stress (Figure A.4).

1.2 Ni-rich Ni-Ti thin films

Ishida et al. [11] investigated the shape memory behaviour of Ni-rich $Ni_{51.3}Ti_{48.7}$ thin films, solution treated at 700°C for 1 hour and then aged at various temperatures between 300 and 500°C for different times (1, 10 and 100 hours). The grain size in these films was found to be almost constant (1 µm), which was also observed for Ti-rich compositions, whereas the size of the Ti_3Ni_4 precipitates increased with increasing annealing temperature and time (from a few nanometres at 350°C to about 450 nm at 500°C).

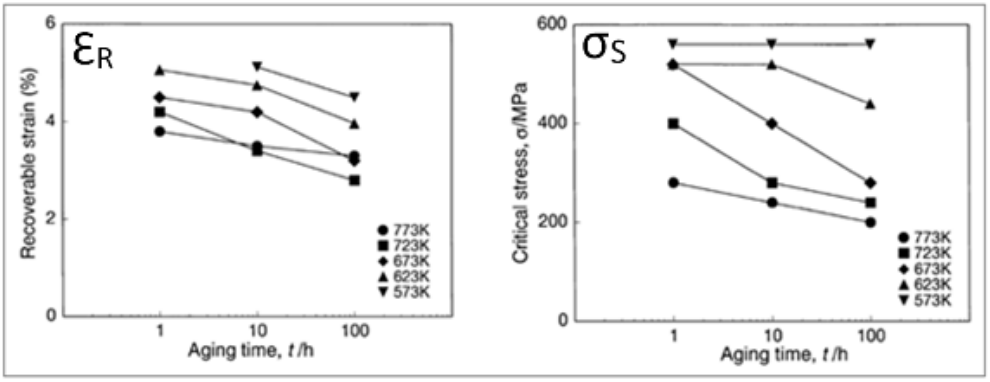

Figure A.5 - Maximum recoverable strain and critical stress for inducing slip deformation of Ti-51.3 at.% Ni thin films aged at various temperatures as a function of aging time [11].

A decreasing trend was observed for ε_R and σ_S (Figure A.5) with increasing aging time and temperature. For the $Ni_{51.3}Ti_{48.7}$ thin film, it was noted that for precipitates with diameter less than 100 nm, higher values of σ_s were measured, see Figure A.6 (a). The maximum recoverable strain (ε_R) tended to decrease with the precipitate diameter,

see Figure A.6 (b). This trend was attributed to the lower critical stress for slip, which likely became lower than the stress required to rearrange the martensitic phase.
These results highlighted the important role of Ti_3Ni_4 precipitates on the functional and mechanical behaviour of Ni-rich Ni-Ti thin films.

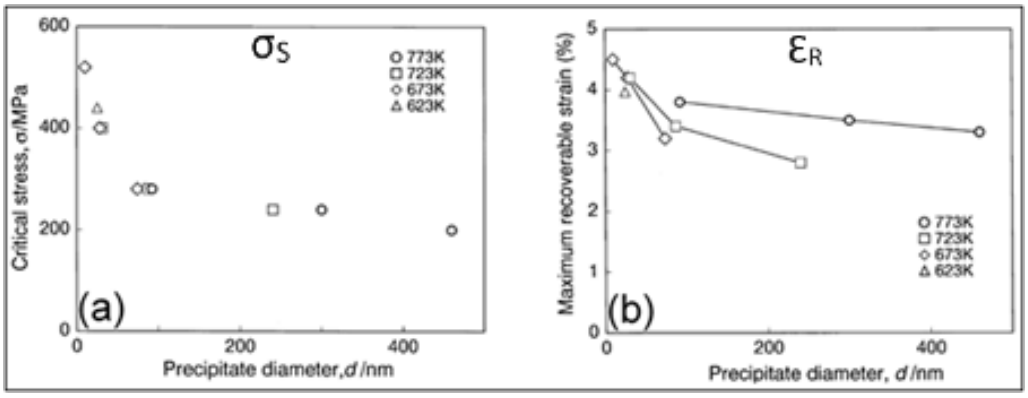

Figure A.6 - Relationship between the critical stress for slip (a) and the maximum recoverable strain (b) in relation to the Ti_3Ni_4 precipitate diameter formed in the Ti-51.3 at. pct Ni thin films aged at various temperatures for various times [3].

In particular, it was generally observed that fine precipitates increase the critical stress for slip (precipitation hardening effect) and at the same time allow larger deformation to be accommodated through the martensitic transformation. On the other hand, coarser precipitates encourage permanent deformation with a consequent degradation of the functional behaviour. The presence of these precipitates in the grain interior, was thought to favour the formation of the intermediate R-phase (rhombohedral structure) in the grain before the formation of the B19' martensitic phase, thus producing a two-step phase transformation [3].

1.3 Ni-Ti-Cu thin films

Matsunaga et al. [12] performed the first comparative study between binary Ni-Ti and ternary Ni-Ti-Cu thin films heat treated by the same method (i.e. annealing at T_c and T_c - 50°C for 1 hour). They found that a ternary $Ni_{43}Ti_{50.8}Cu_{6.2}$ thin film, notwithstanding the larger grain size with respect to the binary $Ni_{48.2}Ti_{51.8}$ film, exhibited a recovery

stress double than that of the binary film and a shape recovery strain of about 5 %, as well as a thermal hysteresis 50 % narrower than that of $Ni_{48.2}Ti_{51.8}$ film. The higher critical stress for slip (40 % higher) found for the ternary film was attributed not only to the solid solution hardening obtained by solid solution substitution of Ni by Cu atoms, but also to a change in the Burgers vector of dislocations in the B2 matrix compared to the binary system. This change further complicated dislocation movement through the plate precipitates formed in Ni-Ti-Cu films for heat treatments close to T_c.

Ishida et al. [13] performed a similar comparative study between a Ti-rich $Ni_{48.5}Ti_{51.5}$ and a Ti-rich $Ti_{51.5}Ni_{33.1}Cu_{15.4}$ thin film, annealed at 500, 600 and 700°C for 1 hour. Even though the two compositions underwent the same thermal treatments and similar precipitation mechanisms, marked differences were observed in their microstructure and consequently their shape memory behaviour (Figure A.7). In particular, the plate precipitates found in the ternary film, i.e. Ti_2Cu, survived and maintained a coherent interface with the B2 matrix when the film was annealed up to 600°C, while spherical precipitates were observed for annealing at higher temperatures. On the other hand, in the binary film GP zones together with semi-coherent Ti_2Ni spherical precipitates were already observed for annealing at 500°C, while GP zones disappeared for annealing at higher temperatures. These microstructural evolutions reflected in the shape memory behaviour of these films.

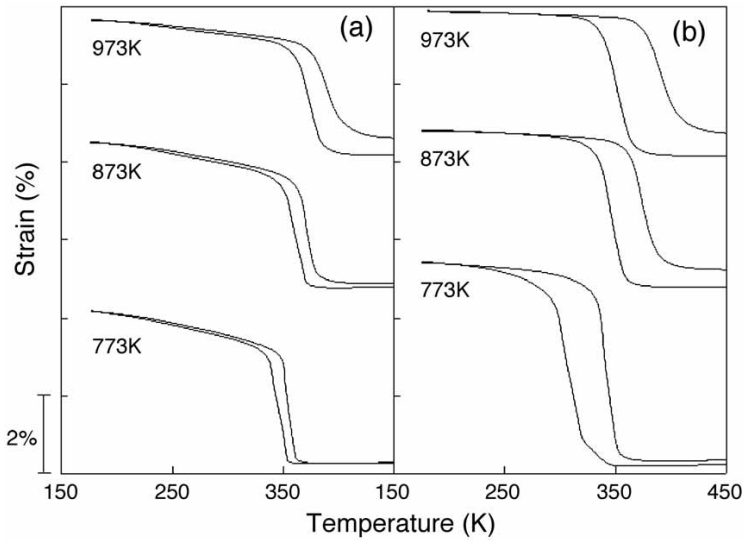

Figure A.7 - Strain–temperature curves at 360 MPa of (a) $Ti_{51.5}Ni_{33.1}Cu_{15.4}$ and (b) $Ti_{51.5}Ni_{48.5}$ thin films annealed at 500, 600 and 700°C for 1 hour [13].

The ternary film showed a lower ε_T owing to the B2 – B19 transformation (B2 – B19' in Ni-Ti films exhibit higher transformation strain), which was found to decrease slightly with increasing annealing temperature. On the other hand, residual strain was found to increase with increasing annealing temperature, due to the evolution of the plate precipitates toward a semi-coherent interface with B2 and a spherical shape. Nevertheless, due to the stabilizing effect of Cu on the coherent Ti_2Cu plate precipitates, a smaller increase in residual strain was observed for the ternary composition compared to the binary Ni-Ti film. The temperature hysteresis (T_H) for thin films annealed at each temperature was significantly reduced for the ternary composition compared to the $Ni_{48.5}Ti_{51.5}$ thin film.

The effects of the substitution of Ni for Cu on the functional behaviour of Ti-rich Ni-Ti thin films were systematically investigated by *Ishida et al.* [14], by keeping constant the Ti content at 51.5 at.%, and varying the Cu content in the range 6.5 – 20.9 at.%. All the films were annealed at various temperatures (i.e. 500, 600 and 700°C) for 1 hour, to produce a crystalline structure. Transmission electron microscopy revealed that the annealing temperature did not affect the grain size, as also observed in a previously reported study [11] for different compositions, whereas by adding Cu, the grain size decreased from 4 μm to 800 nm.

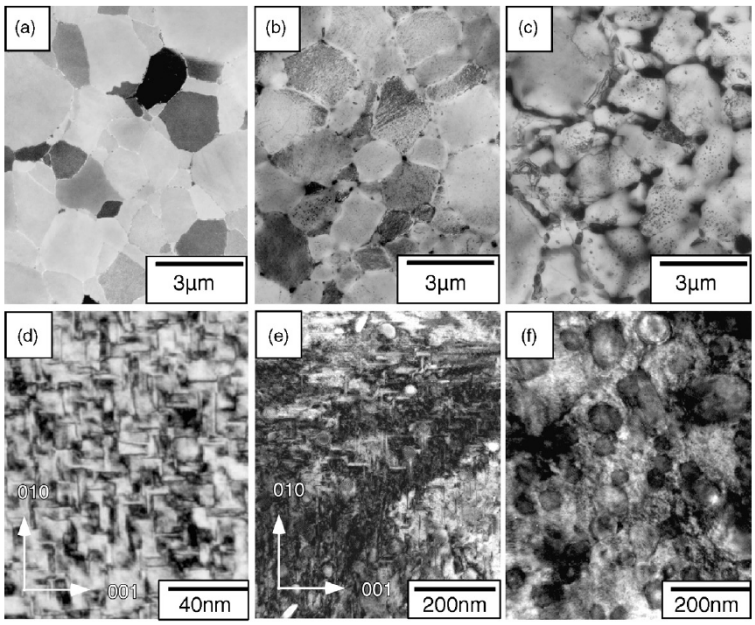

Figure A.8 - Structures of $Ti_{51.6}Ni_{36.8}Cu_{11.6}$ thin films annealed at (a, d) 500°C, (b, e) 600°C and (c, f) 700°C for 1 hour. Images (d – f) show the grain interiors of (a – c), respectively [15].

Furthermore, with increasing annealing temperature different precipitates were observed in both the grain interior and grain boundaries. The formation and structure of precipitates was related to the film composition, and the following evolution with increasing annealing temperature for a Ni-Ti-Cu composition was proposed: (a) formation of GP zones (plate Ti_2Ni precipitates are formed for a Cu content lower than 11.6 at.%, while Ti_2Cu plate precipitates replaces GP zones for Cu content > 11.6 at.%), after annealing at 500°C; (b) formation of plate Ti_2Cu precipitates (coherent with the Ni-Ti matrix), and spherical Ti_2Ni precipitates (semi-coherent with the Ni-Ti matrix), after annealing at 600°C; (c) formation of spherical Ti_2Ni precipitates within the Ni-Ti grains and grain boundary precipitation of Ti_2Ni and Ti_2Cu phases, after annealing at 700°C [15]; Figure A.8 shows the microstructural evolution of the $Ti_{51.6}Ni_{36.8}Cu_{11.6}$ films annealed at various temperatures.

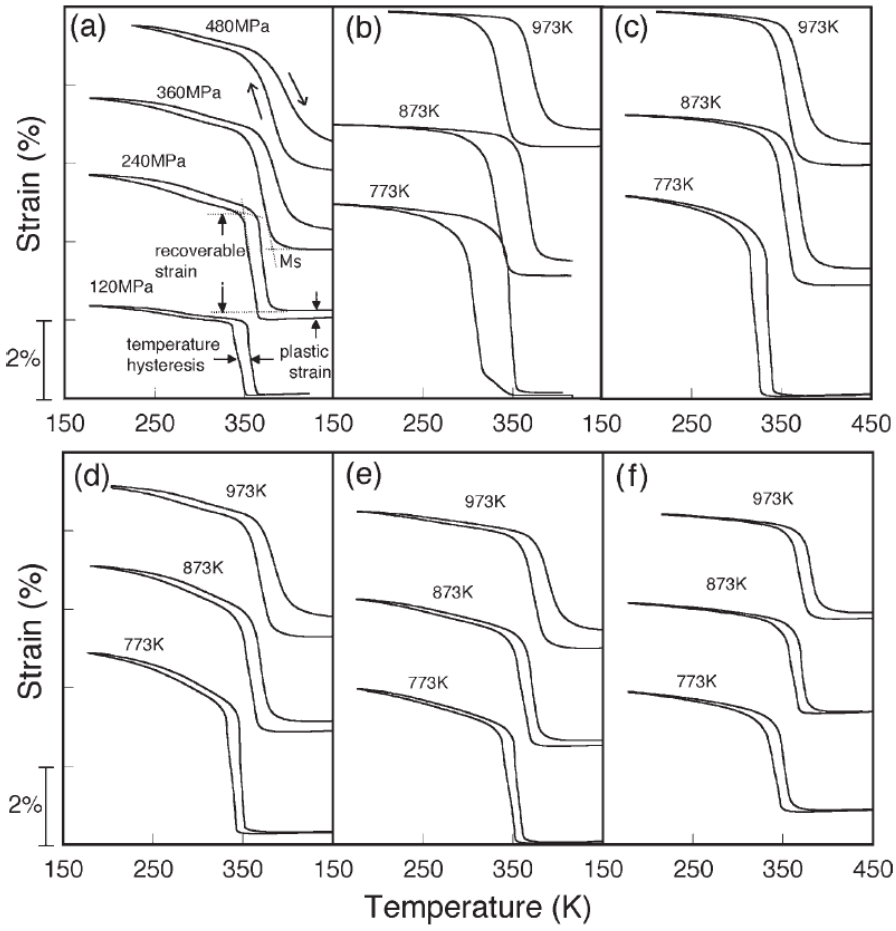

Figure A.9 - (a) Strain – temperature curves at various stresses of $Ti_{51.6}Ni_{36.8}Cu_{11.6}$ thin film annealed at 873 K for 1 h and strain – temperature curves at 360MPa of (b) $Ti_{51.5}Ni_{48.5}$, (c) $Ti_{51.9}Ni_{41.6}Cu_{6.5}$, (d) $Ti_{51.6}Ni_{36.8}Cu_{11.6}$, (e) $Ti_{51.5}Ni_{33.1}Cu_{15.4}$ and (f) $Ti_{51.7}Ni_{27.4}Cu_{20.9}$ thin films annealed at 500, 600 and 700°C for 1 hour [14].

The shape memory behaviour of each film was characterized by strain-temperature measurements at various constant stresses and in Figure A.8 clear differences can be observed in relation to the Cu content and annealing temperature. Films with a Cu content above 10 at.% exhibited a two-stage phase transformation, i.e. B2↔B19↔B19', except the film with 20.9 at.% Cu where only the B2↔B19 transformation was observed, as can be seen in Figure A.9. The typical parameters evaluated on the strain-temperature curves are summarised in Figure A.10. It was found that σ_s increased with decreasing annealing temperature, due to the presence of fine coherent precipitates. In contrast, semi-coherent precipitates, such as spherical Ti_2Ni, encouraged plastic deformation with a consequent decrease in σ_s.

The recoverable strain ($\mathcal{E}_R$) was found to be strongly dependent on the sequence of transformation, in particular for a Cu content ranging between 10 – 20 at.% the B2 – B19 phase transition was characterized by a low and almost constant $\mathcal{E}_R$ (2.5 – 3 %), whereas for a Cu content lower than 10 at.%, the B2 – B19' transformation was characterized by a higher $\mathcal{E}_R$ (2.5 – 5 %). Regardless of the Cu content, $\mathcal{E}_R$ decreased with increasing annealing temperature, especially for Cu content below 20 at.%, owing to the formation of semi-coherent precipitates with the B2 matrix, which promoted plastic deformation. Annealing at 700°C caused the formation of grain boundary precipitates, which probably resisted the deformation of the grains caused by the reorientation of the martensitic variants.

The martensite start temperature (M_s) increased with increasing Cu content, although it levelled off as shown in Figure A.10 (c), while more pronounced changes in M_s were observed by increasing annealing temperature. It was though that the GP zones formed in films annealed at 500°C tend to suppress the martensitic transformation, thus lowering the M_s. In fact the change in M_s was more pronounced on the films annealed at 500°C, especially for Cu content below 10 at.%. The dependence of the M_s on the Cu content was ascribed also to the lower lattice deformation required for the B2↔B19 transformation (Cu $>$ 10 at.%) compared to the B2↔B19' transformation (Cu $<$ 10 at.%).

The temperature hysteresis (T_H) was found to decrease sharply with increasing Cu content up to 6.5 at.% (Figure A.10). In particular T_H saturated at about 15 – 17°C for a Cu content of about 6.5 at.%. In fact despite the B2 – B19' transformation, the film

with 6.5 at.% Cu showed a small temperature hysteresis and the reason behind this observation was not clear. T_H decreased slightly with further increase in Cu content up to 23.3 at.%. On the other hand, a slight increase was observed when Cu content was increased up to 37.3 at.%. With increasing annealing temperature and for a Cu content lower than 23.3 at.%, T_H slightly decreased due to the presence of coherent precipitates such as GP zones and Ti_2Cu phase. On the other hand, for higher Cu contents the grain sizes seemed to affect T_H, as no precipitates were observed in the grain interiors.

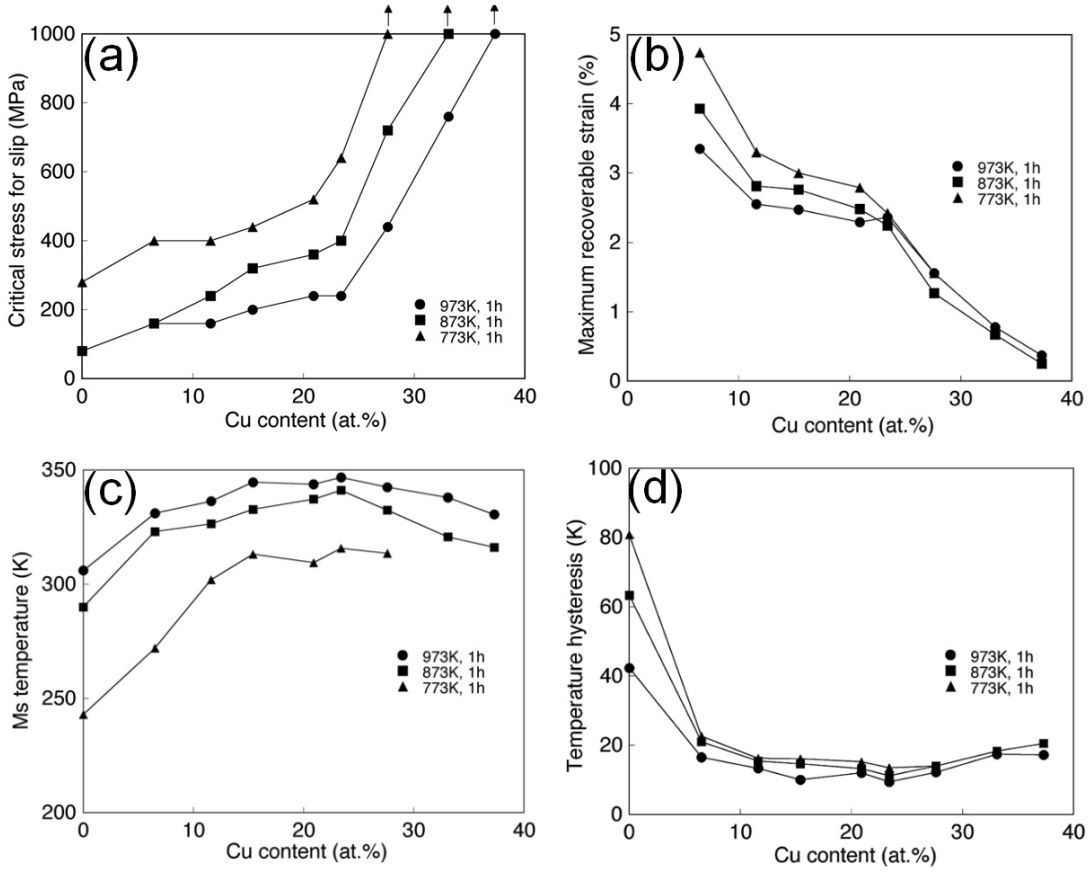

Figure A.10 – Shape memory characteristics as a function of Cu content for $Ti_{51.5}Ni_{48.5-x}Cu$ (x = 0 – 37.3) films annealed at 500, 600 and 700°C for 1 hour [1].

The shape memory behaviour was similarly assessed for films with high Cu content up to 37.3 at.% [1]. Films with Cu content above 20 at.% exhibited basically two different microstructural features compared to the films with lower Cu content, i.e. the presence of a TiCu phase, which formed a duplex structure with the B2 phase, and the smaller grain size (700 nm for 27.6 at.% Cu). The critical stress for slip reported in Figure A.10 for high Cu content, was not ascribed only to the presence of the duplex structure mentioned above, as the TiCu phase alone, as also assumed for GP zone, is

unlike to produce a large increase in σ_S. Therefore the trend observed in Figure A.10 (a) was associated with both the presence of TiCu, which increases with Cu content, and to the finer grains. The $\mathcal{E}_R$ decreased with increasing Cu content in the range 20 – 30 at.% and no evident dependence on the annealing temperature was observed; the reason behind this behaviour was attributed to the effects of composition on the grain size when annealing at different temperatures, although this dependence was not clear. M_s slightly decreased with increasing Cu content in the range 20 – 40 at.%, and this behaviour was also attributed to the grain size and in particular to the suppression of the deformation required for the martensitic transformation with decreasing grain size.

The results reported so far are related to Ti-rich Ni-Ti-Cu film compositions, while only a few studies investigated the functional behaviour of (Ni, Cu)-rich Ni-Ti-Cu thin films.

Ishida et al. [16] compared the shape memory behaviour of different Ti-rich and (Ni, Cu)-rich Ni-Ti-Cu thin films with different Cu contents and annealing temperatures (i.e. 500, 600 and 700°C for 1 hour). (Ni, Cu)-rich films exhibited always a lower M_s compared to the Ti-rich compositions for a specific annealing temperature in the range 500 – 700°C [16]. In (Ni, Cu)-rich films, it was found that M_s increased with increasing Cu content and annealing temperature, as shown in Figure A.11 (c). The increase in M_s with Cu content was attributed to the decrease of Ni solubility in the B2 phase due to Cu addition. In the films annealed at 500°C, it was assumed that M_s was mostly affected by the change in chemical composition in the B2 matrix owing to the formation of precipitates, and possibly by the coherent strain field generated around the precipitates, which suppressed the deformation associated with the martensitic transformation. On the other hand, for annealing at higher temperatures a less evident change with Cu content was observed, which was not attributed to the grain refinement induced by Cu addition.

The critical stress for slip increased with increasing Cu content for Ti-rich and (Ni, Cu)-rich systems, although no obvious differences were found between these compositions by changing the Cu content. *Ishida et al.* [18] reported that for a $Ti_xNi_{(84.5-x)}Cu_{15.5}$ (x = 44 – 56 at.%), σ_S increased with deviation from 50 at.% Ti and with decreasing annealing temperature. In particular, a higher σ_S was reported for Ti-rich compositions, which was attributed to the higher coherency of Ti_2Cu precipitates formed in Ti-rich

compositions compared to the Ti(Ni, Cu)$_2$ precipitates formed in (Ni, Cu)-rich compositions when the annealing temperature was increased in the range 500 – 700°C. Moreover, the smaller grains found in Ti-rich compositions also contributed at increasing σ_S.

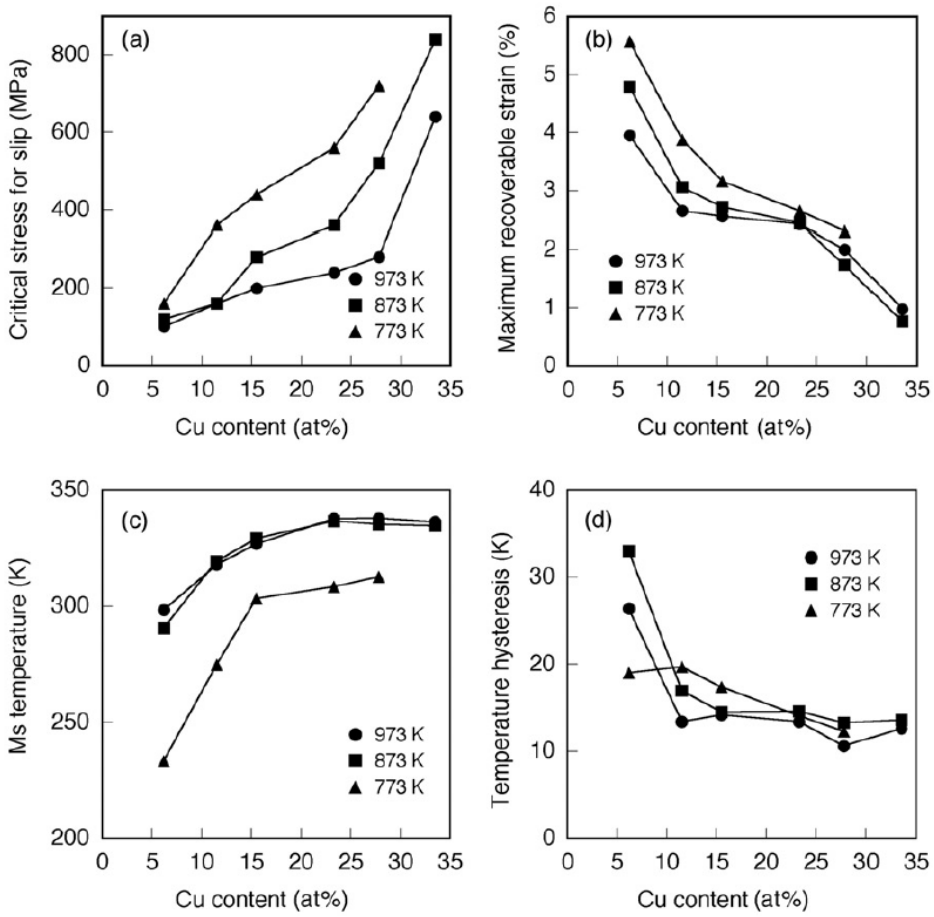

Figure A.11 – Shape memory characteristics as a function of Cu content for Ni-Ti-Cu thin films with nearly 48.5 at.% Ti: (a) critical stress for slip, (b) maximum recoverable strain, (c) martensitic transformation start temperature, (d) temperature hysteresis measured at 120 GPa [17].

In (Ni, Cu)-rich films annealed at 500°C, the increase of σ_S in Figure A.11 (a) was attributed to the presence of coherent precipitates with the B2 matrix. These precipitates were identified to be Ti(Ni, Cu)$_2$ plate with a body-centred tetragonal structure (b.c.t.) for Cu content below 27.8 at.%, and TiCu plate precipitates for Cu content above 33.5 at.% [17]. Cu addition was found to stabilise these plate-like coherent precipitates when annealing at higher temperatures. It was seen that these coherent precipitates contribute more at increasing σ_S compared to the semi-coherent Ti_2Ni spherical precipitates formed in Ti-rich compositions. On the other hand, for

higher annealing temperatures (i.e. 700°C), as found for Ti-rich Ni-Ti-Cu films, the increase in σ_S with Cu content was associated with the solid solution hardening and the grain size, which decreased with increasing Cu content, as no precipitates were found in the grain interior of films annealed at 700°C.

The maximum recoverable strain (ε_R) shown in Figure A.11 (b) decreased for Ti-rich and (Ni, Cu)-rich systems with increasing Cu content owing to the change in native phase from B19' to B19 (typically B2↔B19' is characterised by a higher ε_R than B2↔B19). In fact for (Ni, Cu)-rich films exhibited the B2↔B19' transformation for Cu content of 6.5 at.%, a two-stage transformation B2↔B19↔B19' for a Cu content between 11.5 – 15.5 at.%, and a single stage B2↔B19 transformation for Cu content above 23.3 at.%. However, for the same transformation path the (Ni, Cu)-rich system exhibited slightly higher ε_R, especially for films annealed at 500°C. On the other hand, with increasing annealing temperature the critical stress for slip decreases and plastic deformation appear before that the transformation saturates, thus lowering ε_R. Furthermore, it was assumed that the grain boundary precipitates, which become prominent when annealing at higher temperatures (i.e. 700°C) may reduce the transformation strain. In Figure A.11 (d) the temperature hysteresis (T_H) is reported in relation to the Cu content, where a T_H as low as 15°C was measured for a Cu content above 10 at.%. A slightly higher T_H was found for Ti-rich compositions and the main reason behind this behaviour was related to the different native phase in Ti-rich compositions (B19') compared to that in (Ni, Cu)-rich compositions (B19).

2. Details on the mechanical properties of free-standing Ni-Ti thin films

The functional behaviour, i.e. superelasticity and shape memory effect, of Ni-Ti thin films has been demonstrated experimentally by *Ishida et al.* [19] in 1996 by thermo-mechanical testing of free-standing Ni-Ti films. In particular three different films compositions were investigated (Ti – 48 at.% Ni, Ti – 50 at.% Ni and Ti – 51 at.% Ni) after annealing for 1 hour at 500°C.

The Ti-rich film exhibited macroscopically perfect shape memory behaviour when tested below M_f (-124°C), where a deformation above 6 % was fully recovered upon heating above A_f (46°C). The critical stress (stress plateau) was affected by the test temperature, or in other words by the stable phase at the testing temperature, owing to the different strain energies required to induce phase transformation (B2→B19' or R→B19') or martensitic reorientation (detwinning). When the film was tested at a temperature above A_f, superelastic behaviour was observed, although upon unloading a small permanent deformation of about 0.4 % (of the 6.8 % total deformation) was observed. This deformation was attributed to the fact that Ti_2Ni precipitates found in the film provided good resistance to plastic deformation during the shape memory effect, but not during the superelastic effect. It is because less energy is required for martensitic reorientation compared to the B2→B19' transformation, thus higher energy is necessary to induce plasticity.

The equi-atomic Ni-Ti film tested at temperatures below M_f (22°C) did not exhibit a full strain recovery upon heating, suggesting plastic deformation had taken place, thus a non-perfect shape memory effect is exhibited. When the film was tested at temperatures above A_f (118°C) the critical stress for inducing the B2 → B19' transformation increased with increasing test temperature (Clausius – Clapeyron relationship). However, plastic deformation was produced in the film at a stress level of 500 MPa, which was not recovered upon heating, thus suggesting a non-perfect superelasticity. The reason behind the poorer functional behaviour of equi-atomic Ni-Ti films was attributed to the sensitivity of this film to plastic deformation, i.e. no precipitation hardening effect in near-equiatomic Ni-Ti composition and consequently poor resistance to slip.

The Ni-rich Ni-Ti film exhibited a perfect shape memory effect when tested at temperatures below M_f (-111°C) and a perfect superelasticity for test temperatures above A_f (-1°C). The absence of plastic deformation was attributed to the presence of homogenously distributed Ti_3Ni_4 precipitates in the Ni-Ti grains, which provided a certain resistance against slip.

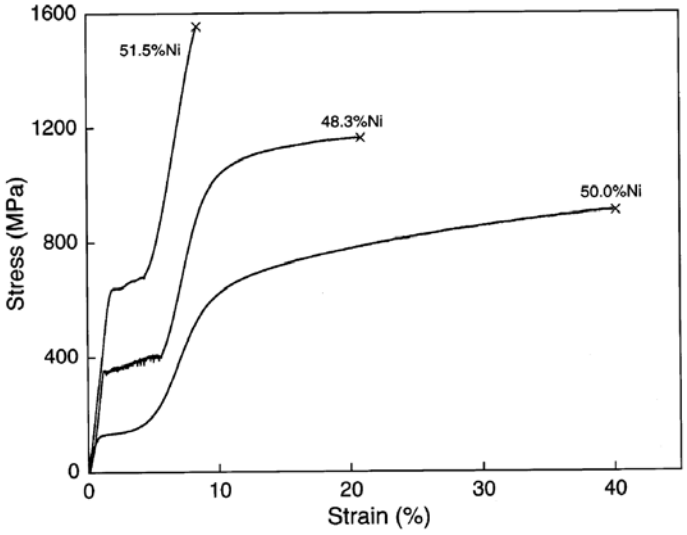

Figure A.12 – Stress-strain curves of Ti – 48.3, 50.0, 51.5 at.% Ni thin films at 42°C. The Ti – 48.3, 50.0 at.% Ni films were annealed at 500°C for 300 seconds and for 1 hour, respectively, and the 51.5at.%Ni film was aged treated at 400°C for 1 hour after solution treatment at 700°C for 1 hour [20].

Figure A.12 shows the stress – strain curves of Ni-Ti films with the following chemical composition: Ti – 48.3, 50.0, 51.5 at.% Ni, similar to the compositions of the films described previously. The Ni-rich films fractured before yielding and a high yield stress (~ 1.5 GPa), owing to the presence of fine Ti_3Ni_4 precipitates, was estimated. The equi-atomic film exhibited a yield stress of about 700 MPa and a very large elongation (40%) before fracture. The Ti-rich film showed a good balance between ductility (elongation of 20 % before fracture) and strength (yield stress of 1.1 GPa) and thus was suggested as the best compromise for applications. However, the ductility of the films in particular of the Ti-rich film was found to be affected by the annealing process. In fact, elongation as large as 20 % was found for the film annealed at 500°C for 300 seconds and 1 hour, while almost no ductility (fracture after yield) was found for the same film annealed at 600°C for 1 hour. This behaviour was attributed to the absence of grain boundary Ti_2Ni precipitates in the film annealed at the lower temperature [20].

Rumpf et al. [21] fabricated a Ni-rich $Ni_{51}Ti_{49}$ film by heating the substrate during deposition to a temperature of 450°C. This deposition process led to a nano-grained structure with an average grain size of 100 nm. In the grain interior no precipitates were observed and a selected area diffraction pattern revealed a polycrystalline structure. The film tested at a temperature above A_f (37°C) exhibited an ultimate tensile strength of 1180 MPa and an elongation of 11.5 %. Furthermore, the film was

subject to a cyclic test (6 cycles) and no significant differences were observed on the different curves. For comparison, a Ni-Ti film with similar composition was deposited at 220°C and annealed for 1 hour at 500°C. This film exhibited larger grains (2 µm) as well as Ti_3Ni_4 precipitates in the grain interior, and showed an ultimate tensile strength of 960 MPa. The different mechanical behaviour of these films was attributed to the different microstructures observed, although no detailed explanation was provided.

References

[1] A. Ishida and M. Sato, “Shape memory behaviour of Ti51.5Ni(48.5-x)Cux (x=23.4-37.3) thin films with submicron grain sizes,” *Intermetallics,* no. 19, pp. 1878-1886, 2011.

[2] Z. Y. Gao, M. Sato and A. Ishida, “Formation of B19' martensite in annealed Ti44.6Ni40.1Cu15.3 thin films and their shape recovery characteristic,” *Journal of Alloys and Compounds,* vol. 505, pp. 81-85, 2010.

[3] S. Miyazaki and A. Ishida, “Martensitic transformation and shape memory behaviour in sputter-deposited TiNi-base thin films,” *Materials Sciences and Engineering A,* Vols. 273-275, pp. 106-133, 1999.

[4] I. Akira, S. Morio, T. Atsushi and M. Shuichi, “Effect of Heat Treatment on Shape Memory Behaviour of Ti-rich Ti-Ni Thin Films,” *Materials Transactions, JIM,* vol. 36, no. 11, pp. 1349-1355, 1995.

[5] K. Ogawa, T. Kikuchi, S. Kajiwara, T. Matsunaga and S. Miyazaki, “Coherent Subnanometric Plate Precipitates Formed during Crystallisation of As-Sputtered Ti-Ni films,” *J. Phys. IV France 7,* vol. C5, p. 221, 1997.

[6] J. X. Zhang, M. Sato and A. Ashida, “The effect of two types of precipitates upon the structure of martensite in sputter-deposited Ti-Ni thin films,” *Smart Materials and Structures,* vol. 13, pp. N37-N42, 2004.

[7] S. Sanjabi and Z. Barber, “The effect of film composition on the structure and mechanical properties of NiTi shape memory thin films,” *Surface & Coatings Technology,* vol. 204, pp. 1299-1304, 2010.

[8] M. Sato, A. Ishida and S. Miyazaki, “Two-way shape memory effect of sputter-deposted thin films of Ti 51.3 at. % Ni,” *Thin Solid Films,* vol. 315, pp. 305-309, 1998.

[9] A. Gyobu, Y. Kawamura, T. Saburi and M. Asai, “Two-way shape memory effect of sputter-deposited Ti-ruch Ti-Ni alloy films,” *Materials Science and Engineering A,* vol. 312, pp. 227-231, 2001.

[10] A. Ishida and M. Sato, “Thickness effect on shape memory behaviour of Ti-50.0at.%Ni thin film,” *Acta Materialia,* no. 51, pp. 5571-5578, 2003.

[11] A. Ishida, M. Sato, A. Takei, K. Nomura and S. Miyazaki, “Effect of Aging on Shape Memory Behaviour of Ti-51.3 At. Pct Ni Thin Films,” *Metallurgical and Materials Transactions A,* vol. 27 A, p. 3753, 1996.

[12] T. Matsunaga, S. Kajiwara, K. Ogawa, T. Kikuchi and S. Miyazaki, “Internal structures and shape memory properties of sputter-deposited thin films of a Ti-Ni-Cu alloy,” *Acta*

Materialia, vol. 49, pp. 1921-1928, 2001.

[13] A. Ishida, M. Sato and K. Ogawa, "Microstructure and shape-memory behaviour of annealed Ti51.5Ni33.1Cu15.4 thin films," *Philosophical Magazine Letters,* vol. 86, no. 1, pp. 13-20, January 2006.

[14] A. Ishida and M. Sato, " Microstructure and shape memory behaviour of annealed Ti51.5Ni(48.5-x)Cux (x=6.5-20.9) thin films," *Philosophical Magazine,* vol. 87, no. 35, pp. 5523-5538, 11 December 2007.

[15] A. Ishida, M. Sato and K. Ogawa, "Microstructure and shape memory behaviour of annealed Ti-36.8at.% Ni-11.6at.% Cu thin film," *Materials Sciences and Engineering A,* Vols. 481-482, pp. 91-94, 2008.

[16] A. Ishida, M. Sato, K. Ogawa and K. Yamada, "Shape memory behaviour of Ti-Ni-Cu thin films," *Materials Science and Engineering ,* vol. A, no. 438-440, pp. 683-686, 2006.

[17] A. Ishida and M. Sato, "Shape Memory behaviour of annealed Ti48.5Ni(51.5-x)Cux (x=6.2-33.5) thin films," *Philosophical Magazine,* vol. 88, no. 16, pp. 2439-2448, 1 June 2008.

[18] M. S. Z. G. A. Ishida, "Effects of Ti content on microstructure and shape memory behaviour of TixNi(84.5-x)Cu15.5 (x = 44.6-55.4) thin films," *Acta Materialia,* vol. 69, pp. 292-300, 2014.

[19] A. Ishida, A. Takei, M. Sato and S. Miyazaki, "Stress-strain curves of sputtered thin films of Ti-Ni," *Thin Solid Films,* Vols. 281-282, pp. 337-339, 1996.

[20] A. Ishida, M. Sato and S. Miyazaki, "Mechanical properties of Ti-Ni shape memory thin films formed by sputtering," *Materials Sciences and Engineering A,* Vols. 273-275, pp. 754-757, 1999.

[21] H. Rumpf, T. Walther, C. Zamponi and E. Quandt, "High ultimate tensile stress in nano-grained superelastic NiTi thin films," *Materials Science and Engineering A,* vol. 415, pp. 304-308, 2006.

Chapter 2 EXPERIMENTAL METHODS AND PROCEDURES

2.1 Chapter summary

In this study, thin films were deposited by a PVD method and several microstructural analyses were performed by X-Ray and Electron Microscopy based techniques. Nano-mechanical and tribological properties were investigated by nanoindentation, nano-scratch and pin-on-disk, respectively. In this chapter a brief description of the equipment and of the experimental procedures followed in this study are given. Particularly, more details are provided regarding the deposition system, electron microscopy including TEM sample preparation, and the instruments used for nano-mechanical testing.

2.2 Plasma-assisted Middle-Frequency Dual Magnetron Sputtering System

During this research, PVD depositions of Ni-Ti(-Cu) layers have been carried out in the cleanroom at the Southampton Nanofabrication Centre (SNC) of the School of Electronic and Computer Science (ECS) at the University of Southampton (UK). On the other hand, W-S-C transition metal dichalcogenide coatings have been deposited at the University of Coimbra (Portugal). In this section a brief overview is provided on the high-vacuum systems used to fabricate Ni-Ti(-Cu) and W-S-C thin films.

The sputtering system used to deposit shape memory alloy layers consists of three main components: a switch cabinet which contains the current unit distribution that serves as an interface between the electrical power supply and the equipment; the

process module (Figure 2.1 a) consisting of a vacuum chamber in which the sputtering processes take place (Figure 2.1 b) and the operator terminal through which the process is monitored and controlled. The equipment also has a RF plasma source and a substrate heater which is used to clean the substrate surface before deposition, and to heat the substrate, respectively.

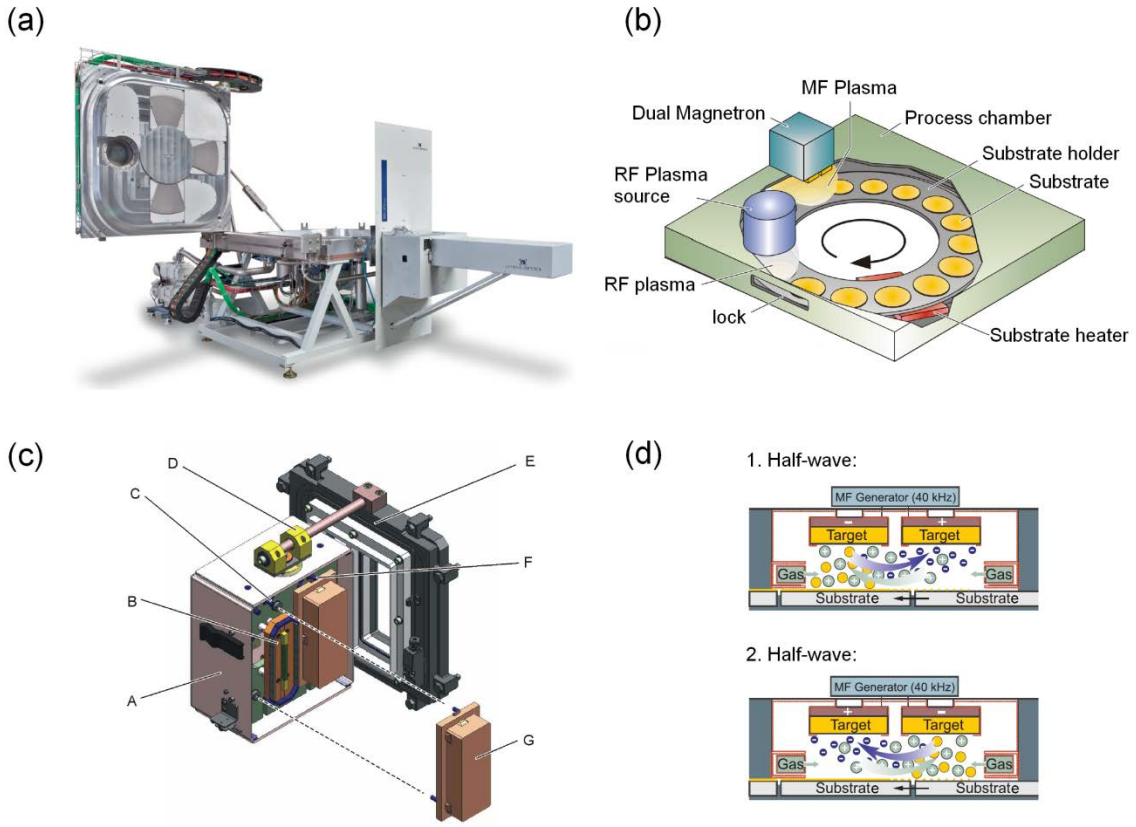

Figure 2.1 – Sputtering system: ***(a)*** *process module,* ***(b)*** *schematic representation of the deposition chamber,* ***(c)*** *MF sputter source: (A) Cathode hood, (B) Magnets (cover), (C) Cooling water connection, (D) Pivot unit, (E) HF seal, (F)Target holder (cathode tank), (G) Target unit,* ***(d)*** *Principle of the dual magnetron technology* [1].

The process module is equipped with one DC plasma source and two MF dual magnetron sputter sources (Figure 2.1 c) consisting of two separate sputter electrodes that serve as sputter cathodes alternately (Figure 2.1 d). The alternating electrical field for the alternating polarity of the sputter electrodes is provided by a mid-frequency generator (40 kHz). The sputter sources are supplied by the same generator and cannot be operated simultaneously. Each of the sputter electrodes (Figure 2.1 c) is equipped with a rectangular target, which is constrained on a steel plate and connected to a water-cooled cover. The cover contains the magnetic system used to increase the plasma density. Each MF source can be controlled by power (the input

power is maintained at constant value), or by partial oxygen pressure (the power is controlled in such a way that the partial oxygen pressure is maintained constant).

The process modulus is also equipped with an RF plasma source (Figure 2.1 b), which due to the application of a static magnetic field and the simultaneous use of a wave resonance, the plasma source generates an extremely dense plasma. This plasma is used for ion-assisted coating and for pre-treating the substrate. The plasma ion assisted coating supports the coating process by providing layers with higher density and improved adhesion, hardness and scratch resistance, as well as high deposition rates and lower operating temperatures. Substrate pre-treatments are carried out with the aid of the RF plasma source, where the impurities on the substrate surface are removed by argon bombardment and then pumped away along with the working gas, or deposited on the wall. In the vacuum chamber a turntable in installed (Figure 2.1 b) which can hold up to 16 substrate holders. The substrate holder is rotated by a rotary drive installed on the chamber floor at a maximum rotation speed is 500 rpm. The temperature of the substrate is measured by a pyrometer installed on the chamber floor.

W-S-C transition metal dichalcogenide layers were deposited by using a carousel-type sputtering system (Teer Coating Ltd, Droitwich, United Kingdom) with DC power supply for the targets and a pulsed power supply for the substrate bias. The deposition system was equipped with two WS_2 targets, one C (graphite) target and one Cr target for the bonding layer. Before the deposition of the top layer, targets and Ni-Ti(-Cu) substrates were plasma cleaned for 40 minutes in order to remove the thin TiO_2 layer (< 10 nm thick) formed on Ni-Ti(-Cu) surfaces after annealing, while a bias voltage of – 600 V was applied to the substrate. Bias voltage was lowered to – 50 V during the deposition (partial pressure of 3×10^{-3} mbar) of a bonding layer consisting of pure Cr first and of Cr with increasing amount of W-S-C at the interface with the top layer. No bias was used during the deposition of the W-S-C top layer, which was deposited at a pressure of 4.5×10^{-3} mbar. To facilitate reading, the W-S-C coating deposited with Cr interlayer on Si wafer is denominated as W-S-C single layer, whereas the W-S-C/Cr films deposited on Ni-Ti(-Cu) layers are denominated as bilayers in chapter 5 and chapter 6.

2.2.1 Calibration of the Ni-Ti(-Cu) deposition processes

In this research, as no historical data were available on the co-sputtering of Ni, Ti and Cu for the equipment described in the previous section, preliminary depositions were performed firstly to assess the behaviour of the equipment, in relation to the materials being sputtered, taking as the main variable the deposition rate. This parameter can be, to a first approximation, considered as proportional to the sputtering yield, especially for flat configurations (target/substrate), as is the case for the sputtering system previously described. Although tabulated sputtering yields are notoriously questionable because over the years this parameter has been measured in flawed experiments [2], it is well known that the sputtering yield roughly doubles in the following order: titanium, nickel and copper, for specific argon ion energies. Based on this information, the deposition rate of each target material (Ni, Ti and Cu provided by Leybold Optics GmbH, Germany) was measured in an appropriate power range within 0.5 – 8 kW, by taking the thickness measured by a stylus profilometer and dividing by the deposition time.

Due to the known lower sputtering yield of titanium compared to the other materials, during co-sputtering, it was considered appropriate to maintain constant and at maximum value the power supply to the titanium target and vary the other two power supplies in order to obtain the desired chemical composition. At a power level of 8 kW the titanium target exhibited a deposition rate of 0.33 nm/sec., while the nickel target exhibited a deposition rate which changed linearly ($dep.rate = 0.06 \times power$) in the power range between 2 – 8 kW. As expected, Cu exhibited the highest deposition rate, which changed linearly ($dep.rate = 0.14 \times power$) in the power range between 0.5 – 2.8 kW.

Preliminary co-sputtering depositions of Ni and Ti were performed, under the conditions reported in Table 5, to determine the Ni/Ti power ratio to be adopted to achieve a near-equiatomic composition. The reason behind this choice of atomic ratio is that shape memory and superelastic properties, in the crystalline thin films, are exhibited only in a narrow range around a Ni/Ti (at.%) ratio of one.

Table 2.1 - The Deposition parameters adopted during fabrication of Ni-Ti-Cu films.

Ti power [kW]	8
Ni power [kW]	2.3
Cu power [kW]	0 – 0.31
Process time [sec.]	~ 2000
Rotation speed [rpm]	180
Ar gas flow [sccm]	15 – 35
Pre-sputtering [sec.]	300
Base pressure [mbar]	1×10^{-7}
Deposition pressure [mbar]	5×10^{-4}

After the deposition of the binary Ni-Ti films had been optimised, Ni-Ti-Cu thin films were deposited on (100) Si wafers (450 μm thick) according to the deposition parameter reported in Table 2.1. The power for every target was set based on preliminary estimates on the atomic percentage obtainable at different power levels for each material being sputtered once their deposition rates had been measured. In order to obtain films with different Cu content, the power on the Cu target was increased linearly, while the deposition time was set in order to fabricate thin films with similar thickness. A high vacuum base pressure was chosen in order to reduce, as much as possible, the oxygen content in the vacuum chamber, as well as to increase the mean free path of the impurities present in the chamber. The rotation speed of the turntable was set in order to avoid the formation of multilayer-type structures. The argon gas flow adopted in all these depositions was a trade-off in order to guarantee a reasonable deposition rate from the three targets as well as to have a good vacuum during depositions. In order to produce films with an amorphous structure, depositions were performed without any deliberate heating of the substrate; moreover the balanced configuration of the sputtering system does not promote excessive heating of the substrate. Eight Ni-Ti-Cu thin films 1.4 μm thick with Cu content in the range 0 – 20.4 at.% were produced (Figure 2.2).

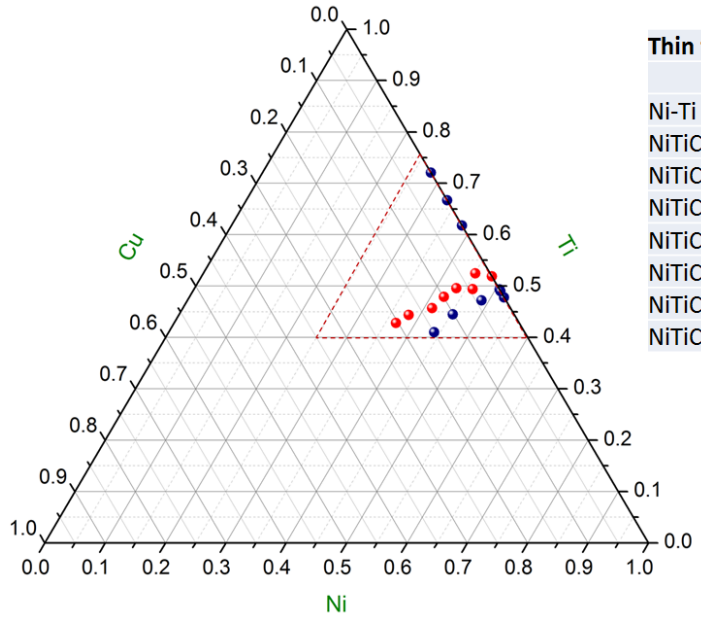

Thin films	Chemical composition [at.%]		
	Ni	***Ti***	***Cu***
Ni-Ti	48.1	51.9	0.0
NiTiCu1	45.1	52.5	2.4
NiTiCu2	46.2	49.4	4.4
NiTiCu3	43.4	49.6	7.0
NiTiCu4	42.2	47.9	9.9
NiTiCu5	41.3	45.7	13.0
NiTiCu6	38.1	44.4	17.5
NiTiCu7	36.8	42.8	20.4

Figure 2.2 – Ternary chemical composition diagram of the Ni-Ti-Cu thin films measured by EDX on the as-deposited films with an error of ± 0.2 at.%. The red dots represent the compositions, summarized in the table, investigated more in depth in this research.

It was noted that when the power to the Cu target was increased, Ni and Ti content decreased approximately at the same rate, indicating no preferential re-sputtering effect of Ni and Ti atoms on the growing structure. For Cu content ≥ 4 at.% the chemical composition of the thin films changed from being Ti-rich to (Ni, Cu)-rich.

2.2.2 Phase transformation in the binary Ni-Ti thin film

Before studying and using of Ni-Ti(-Cu) thin films for tribological coatings, the capability of the Ni-Ti(-Cu) films produced in this study to experience phase transformation was investigated and assessed by hot-stage optical microscopy. The hot-stage consists of a heating unit and a temperature controller (Eurotherm 91e); temperature being measured by a thermocouple installed underneath the sample location. A temperature range between ambient temperature and 80°C is scanned with an error in temperature of ±3°C. The heating unit is fitted underneath the objective lens of the optical microscope (Olympus BX51). A series of images of the surface are captured as the temperature is varied slowly in steps of 5°C in order to

record the changes in surface morphology. The surface changes are also monitored when the sample is left to cool down naturally to ambient temperature, in order to assess the reversibility of the phase transformation.

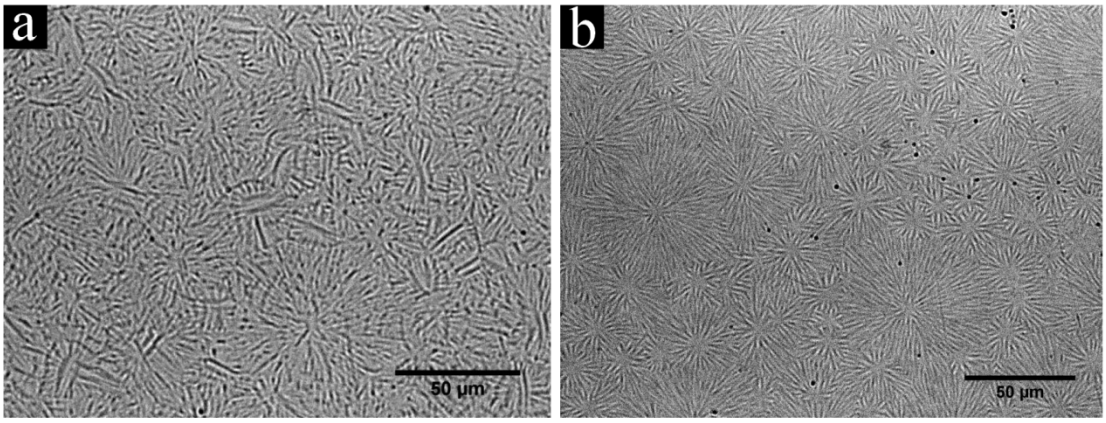

Figure 2.3 – Binarised Bright Field optical images of the Ni-Ti thin film, annealed for 1 hour at 600°C, taken at: (a) ambient temperature (~ 25°C) before and after cooling; (b) at 84±3°C.

Figure 2.3 a shows the surface morphology of the Ni-Ti thin film annealed for 1 hour at 600°C. Such a surface morphology consists of many randomly oriented martensitic plates, with an average size ranging between 3 – 4 µm, nucleated in the austenitic matrix at the free surface. With increasing temperature, the number and size of the plates is observed to decrease and this effect is accompanied by the appearance of radial wrinkles (Figure 2.3 b). The change in surface morphology is accompanied by a change in brightness of the surface. In fact, as observed also by the naked eye, while at room temperature the film shows an opaque surface, a much shinier surface appears when the film is heated to higher temperatures, as also reported in other studies. Figure 2.4 shows some dark field optical images at different temperatures displaying the effect mentioned above[1]. A transformation boundary is clearly visible in Figure 2.4 b (dashed white line) between a dark (austenite) area and a bright (martensite) area. While in Figure 2.4 a, the film is still mostly martensitic and in Figure 2.4 c the film is fully austenitic.

[1] The shiny austenitic surface appreciable even by naked eye is dark in the dark field optical images.

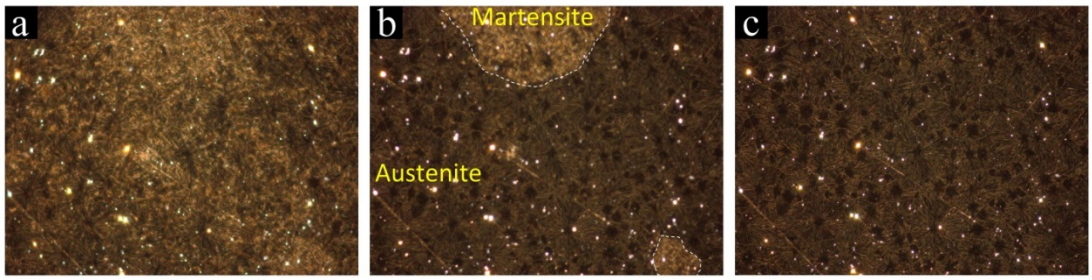

Figure 2.4 – Dark Field optical images of the Ni-Ti thin film, annealed for 1 hour at 600°C, at different temperatures: (a) 62°C, (b) 65°C and (c) 71°C.

The same surface morphology shown in Figure 2.3 a before heating is found after cooling back to room temperature, thus demonstrating the reversible nature of the martensitic transformation. This reversible change in surface morphology makes Ni-Ti-based thin films attractive materials for the fabrication of smart mirrors, where the reflection capability of the Ni-Ti mirror is controlled electrically, by exploiting the Joule effect to activate the phase transformation.

Similar results are found for some Cu-doped Ni-Ti thin films, where the analyses of the surface by optical microscopy was limited owing to the resolution of the microscope, as with increasing Cu content the surface features shown in Figure 2.3 and 2.4 become much smaller.

2.3 Post-deposition heat treatments

The functional properties (i.e. shape memory and superelasticity) in Ni-Ti-based alloy thin films are associated with the martensitic transformation and thus to a transformation between two phases. Therefore a crystalline structure is required and the crystallisation process can be induced by heat treating the ad-deposited films at a temperature above that of crystallisation for an appropriate annealing time. In this research, the as-deposited thin films were isothermally annealed by means of a high vacuum (8×10^{-5} mbar) furnace at different temperatures, in order to induce a crystalline structure as well as to promote different microstructures according to the results reported in the literature. In order to avoid delamination induced by thermal

stresses a heating/cooling rate of 5°C/min was adopted above 400°C while below this temperature samples were allowed to cool down naturally to ambient temperature. Moreover, so as to limit as much as possible the formation of oxide on the film surface, a sacrificial material (titanium) which will be preferentially oxidised has been introduced in the vacuum chamber during every heat treatment. Every process has been performed without argon gas in the chamber to limit as much as possible the presence of impurities in the chamber itself.

In view of the chemical affinity of Ti and O, the chemical composition as well as the surface morphology of some of the Ti-rich thin films was evaluated by SEM/EDX after the heat treatments and no oxygen was detected.

2.4 Microstructural and chemical characterisation

The microstructure and chemical composition of the Ni-Ti(-Cu) thin films were investigated by X-ray based techniques (XRD, XPS, EDX). X-ray diffraction has been used mainly to identify the different phases formed as a consequence of the post-deposition heat treatments. XPS analyses were used to identify chemical bonding, while EDX was used to measure chemical composition. A more in depth microstructural characterisation has been carried out by means of electron microscopy such as SEM and (S)TEM.

2.4.1 X-ray based techniques

The microstructure and the phases produced by annealing were investigated by grazing incidence X-ray diffraction (GIXRD) by means of two different diffractometers.

In particular, the diffraction data were collected by using an X'Pert-Pro Philips diffractometer (PANalytical, ALMELO, The Netherland) [3] with a Cu anode (λ=1.540598 Å). The tube was set at an accelerating voltage of 40 kV and a current of 30 mA. The GIXRD spectra, acquired with an incidence angle of 5°, were analysed by

the X'Pert HighScore Plus software together with a ICDD PDF-2 database (chapter 3). The diffraction data were also collected by using the Rigaku SmartLab diffraction system (Rigaku Corporation, Japan) [4] in grazing incidence mode (incidence angle between 1 – 5° depending on the coating – see chapter 5) with Cu Kα radiation (λ=1.540593 Å) and the X-ray tube operating at an accelerating voltage of 45 kV and with a current of 200 mA. XRD patterns were analysed by the PDXL software together with a ICDD PDF-2 database. Grazing angles were set between 1 – 5° in order to maximise the volume of material being interrogated as well as to avoid diffraction from the substrate. XRD scans were performed with a scan step size of 0.02°over different angle ranges.

The chemical composition of the as-deposited, annealed and tested coatings was measured by Energy dispersive X-ray spectroscopy (EDX, semi-quantitative analysis, Oxford Instruments) attached to a JEOL JSM 6500F field emission gun scanning electron microscope (FEG-SEM). Oxford INCA 300 software was used to acquire and process EDX spectra.

Surface chemical analysis was carried out with a ThermoVG Thetaprobe X-ray Photoelectron Spectroscopy (Thermo Scientific) [5]. Results were obtained using monochromated, micro-focused Al K-Alpha x-ray source, with a spot size of 400 µm. A flood gun was used for charge neutralization. Sample surfaces were gently cleaned for 30 seconds with an ion gun (1 keV, Ar^+, 1 µA). Spectra analysis was performed with Avantage software provided by the instrument manufacturer.

2.4.2 Electron Microscopy

A JEOL JSM 6500F field emission gun scanning electron microscope (FEG-SEM) was used to analyse surfaces and cross-sectional morphology of the as-deposited, annealed and tested coatings. Microstructural properties are first investigated for some films by using a Zeiss NVision40 Focused Ion Beam (FIB) system at the Southampton Nanofabrication Centre (University of Southampton). The FIB system is used to deposit a tungsten protective layer by ion-induced deposition from a precursor gas to prevent damage and Ga^+ implantation on the top surface of the thin films. After W deposition,

the film surface is tilted to 54° to align the surface normal to the axis of the ion gun column (accelerating voltage of 30 kV). The milling process consisted in the creation of a trapezoidal volume used to accommodate the sputtered material and after by a polishing process of the cross-section with a decreasing probe current from 700 to 80 pA. Imaging of the polished cross-section (tilted 36° away from the electron gun axes) is performed by using the electron beam.

The structure of the annealed and tested coatings was also characterised by transmission electron microscopy (TEM) using a FEI Tecnai F20ST/STEM scanning transmission electron microscope (STEM) operating at an accelerating voltage of 200 kV. These investigations were performed at the National Centre for High Resolution Electron Microscopy at the Kavli Institute of Nanoscience (Technical University Delft).

A brief overview is provided here on imaging in (scanning) transmission electron microscopy while for a detailed explanation reference should be made to [6]. Figure 2.5 a shows the (S)TEM microscope used to analyse the microstructure of W-S-C and Ni-Ti(-Cu) coatings. Transmission electron microscopes consist of an electron gun through which electrons are generated and accelerated down the column of the microscope which is kept under ultra-high vacuum so that electrons are not scattered due to the surrounding atmosphere. The probing signal passes through a series of condenser lenses and apertures before reaching the specimen, where the most important phenomenon, i.e. the interaction electrons-matter (Figure 2.5 b), takes place. The signal transmitted through the specimen goes through the lens system towards the detector, where the information from the specimen is visualised (Figure 2.5 c). The lens system consists of the objective-intermediate and projector lenses used to form the image on the detector. When the electron beam interacts with the specimen, incoming electrons are scattered by the specimen and in this process several signals are generated as shown in Figure 2.5 b. A large fraction of the electrons are elastically scattered, i.e. there is a deviation of the transmitted electrons due to the specimen without any loss of energy. The remaining fraction of electrons is inelastically scattered thus losing energy and consequently generating several other signals such as X-rays and inelastically scattered electrons.

In conventional TEM (imaging and diffraction), we use the transmitted electrons or the forward scattered electrons for most of the studies. In diffraction, the electron beams that satisfy Bragg's law in a crystalline specimen are diffracted at specific angles

forming a periodic diffraction pattern. The imaging in a TEM is realised by one of the following methods: static beam and scanning beam. In the first case, all the forward scattered electrons are collected on the detector to form the image (Figure 2.5 c). Scanning in TEM is achieved by incorporating electromagnetic beam deflection coils in the illumination system, as shown in Figure 2.5 d. Basically, the electron beam is converged by the condenser lens to a spot called "probe" (typical probe sizes range between 0.05 – 0.2 nm). The probe is scanned over the specimen and the forward scattered electrons are collected using an annular detector to form the image.

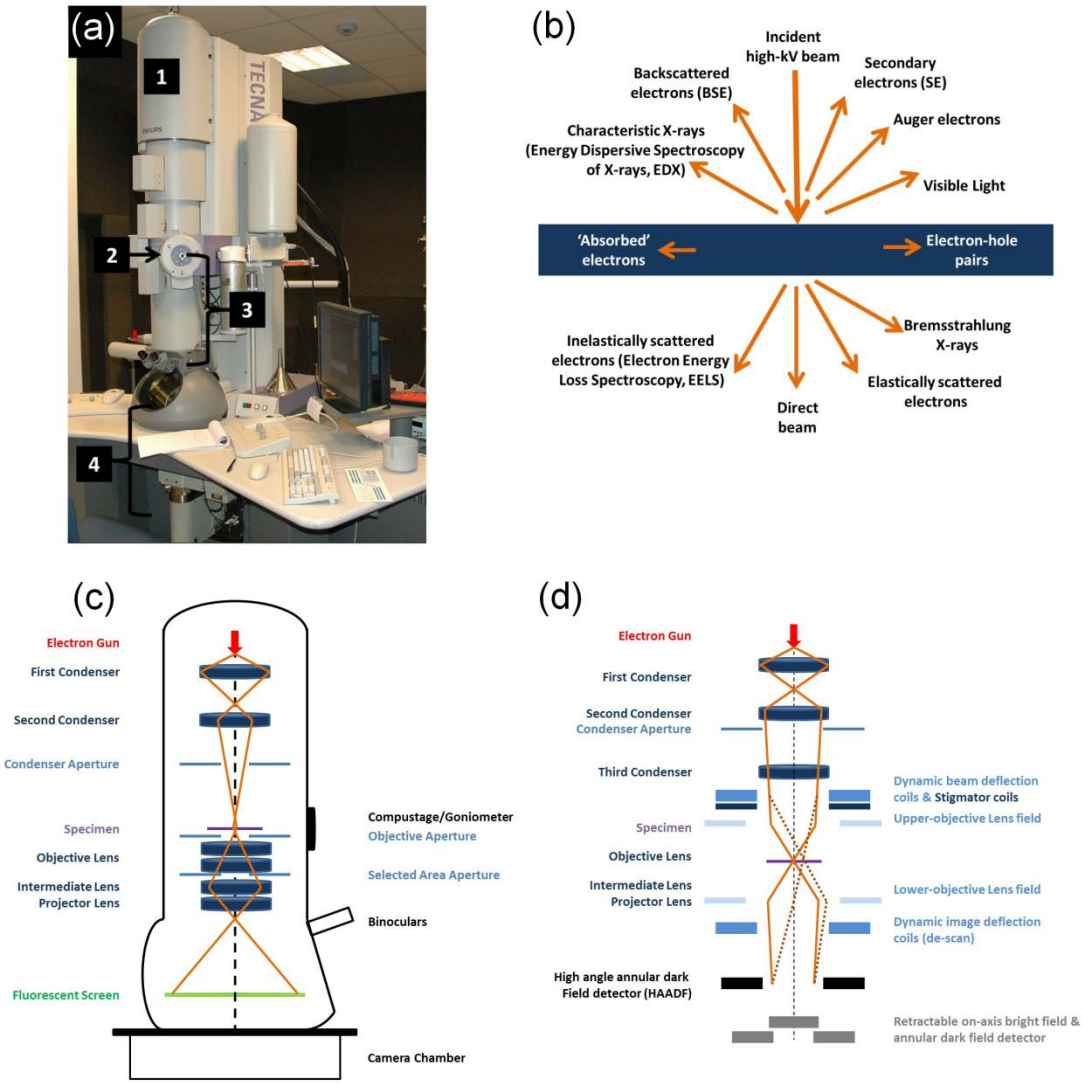

Figure 2.5 – Transmission electron microscope: ***(a)*** *FEI Tecnai F20ST/STEM scanning transmission electron microscope (STEM: (1) illumination system, (2) specimen area, (3) lenses, (4) fluorescent screen and CCD camera;* ***(b)*** *Signals generated when a high-energy beam of electrons interacts with a thin specimen;* ***(c)*** *ray diagram of a typical TEM to form an image on the detector;* ***(d)*** *ray diagram for STEM mode with a three-condenser lens TEM* [7].

One of the most important aspects in interpreting (S)TEM images is the contrast, which can be classified as either amplitude or phase contrast. Most of the images in the TEM are obtained by a combination of both of these contrasts. The amplitude contrast has two principal types, i.e. diffraction contrast (TEM, STEM) and mass-thickness contrast (TEM, STEM). Z-contrast is another term that arises while looking at high-resolution STEM images, where detectable scattering arises from single atoms or column of atoms. Any differences in the specimen such as: the presence of precipitates, defects such as dislocations, grain boundaries or orientation differences between the electron beam and specimen due to tilting lead to a change in diffraction conditions which give rise to diffraction contrast. Any microstructural variations causing a change in diffraction contrast can be imaged by using a suitable objective aperture. For instance, the contrast of an image can by enhanced by just selecting the direct beam, also called bright-field (BF) imaging; or by suitably selecting a diffraction spot, the features corresponding to that particular spot can be highlighted, called dark-field (DF) imaging.

Each element has its own scattering power and heavy atoms have a stronger interaction with electrons than lighter atoms. If the specimen thickness is homogeneous, variations in the atomic mass of the constituent elements results in mass and atomic number contrast. On the other hand, if there is a variation in the thickness of the specimen, the electrons are scattered more in thicker areas than in thinner areas resulting in thickness contrast.

Phase contrast arises from the interference of the primary beam and the diffracted beams. Phase contrast is responsible for the appearance of lattice fringes in TEM images. The diffracted beams from the parallel planes of the crystalline specimen can be imaged at the back focal plane of the objective lens as spots, which recombine in the image plane and are then magnified by the projector lenses resulting in an image with periodic lattice fringes. These images are referred to as lattice images and under certain conditions these peaks correspond to the atom columns. The phase relationship between the electrons leaving the specimen is responsible for the contrast obtained in these images and it critically depends on the thickness of the specimen. This technique of obtaining atomic-resolution images is called high-resolution transmission electron microscopy (HRTEM).

While imaging in STEM mode, using the high angle annular dark field (HAADF) detector, it is possible to visualise the lattice with Z-contrast (atomic number contrast).

It is understood that the images collected from beams elastically scattered at higher angles (50 – 150 mrad) show a dependency on the atomic number approximately as $Z^{1.7}$. In these images, there is no coherency between the high angle scattered beams which are collected on an annular detector. Therefore in a high resolution STEM (HRSTEM) image obtained with a HAADF detector, the intensities from individual scattering centres (atoms) along the beam path can be added enabling a direct interpretation of atom types and positions. Combining all these imaging techniques, it is possible to get complete morphological and structural information of a specimen at the atomic scale.

2.4.3 Microanalysis in TEM

When the accelerating electrons ionise an atom in the TEM specimen, each of the possible transitions within the internal shells of the atom is associated with the emission of a characteristic X-ray, which has an energy unique to that element. The emitted X-ray photons are collected using special detectors and plots of X-ray counts versus X-ray energy are generated. From the intensities of the peaks corresponding to specific elements, it is possible to quantify and estimate the elemental composition of specimen. Conventional X-ray detectors are semiconductor based, lithium (Li) doped silicon (Si), protected by an ultrathin window cooled to liquid nitrogen (N_2) temperature to prevent thermal noise during the collection.

Once the intensity-energy plots for the X-rays are generated after detection, the amounts of elements present in the specimen are estimated from the relation between the weight fraction and generated intensities (ionisation cross section), which is given by the Cliff-Lorimer equation.

The equation mentioned above is valid when the fluorescence and the absorption effects are negligible. In case of the TEM specimens, as they are quite thin the absorption effects are usually negligible, and hence the Cliff-Lorimer method gives a reasonable compositional estimate [8].

2.4.4 (S)TEM samples preparation

A successful TEM experiment depends largely on the quality of the specimen being investigated. As we need the electrons to transmit through the specimen, the specimen has to be as thin as possible. The ideal specimen thickness depends on several factors such as the imaging technique being used, the atomic weight of the specimen. In general, the accepted thicknesses for TEM investigation are ≤ 100 nm. For HRTEM studies, the specimen thicknesses should be even less than 50 nm. An important factor that has to be considered while investigating the TEM specimens is the influence of surfaces. As the TEM specimens are nearly 2-dimensional in nature as they have a very large surface area to volume ratio and lacking the constraints of the surrounding material found in bulk samples, one has to be very careful when interpreting the observations from a TEM specimen.

TEM samples for this study have been prepared using two techniques, i.e. ion milling and focused ion beam (FIB), which are described below very briefly.

In ion milling, 3 mm discs ~ 10 µm thick (cross-section in this case) are further thinned down by bombarding with a beam of argon ions with low energies of 2 – 5 kV. To have an electron transparent area as large as possible, the Ar ions are directed at a low incidence angle of 5 – 10°. For the final thinning, we have used the Gatan precision ion polishing system (PIPS, model 691).

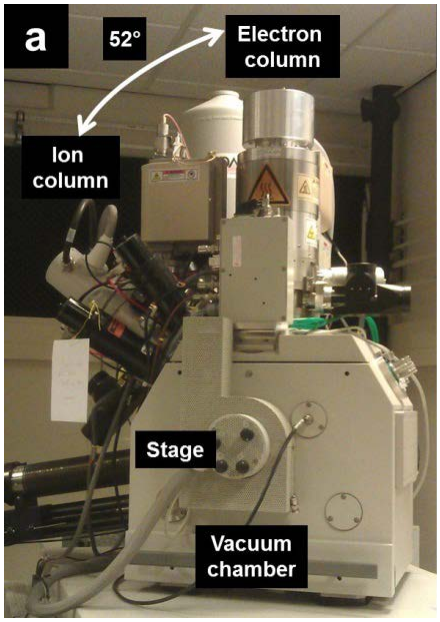

Figure 2.6 –Dual beam FIB-SEM FEI strada DB 235 [7].

A focused ion beam (FIB) is an instrument that looks like a scanning electron microscope and is built upon similar principles and operates like an SEM except that ions are accelerated in a FIB for imaging and specimen modification. In fact the modern day FIBs are integrated with an SEM and the instrument is called a dual beam (SEM-FIB), Figure 2.6. While the electron beam allows conventional SEM imaging, the ion beam is used to modify the sample surface by milling. Common FIBs run on a gallium (Ga) ion source as it is liquid close to room temperature and the beam can be focused to a very fine probe. The typical operating voltages for FIB range between 5 – 30 kV. By controlling the strength of the electrostatic lenses and adjusting the aperture sizes, the probe current density can be altered from few tens of pA to nA corresponding to beam diameters ranging from 5 nm to 0.5 µm.

The principle involved in a FIB is that the heavy Ga ions accelerated towards the sample sputter the surface and cause a modification. Typically the penetration depth is ~ 25 nm for ~ 25 keV Ga ions. By using scripts to control the path of the ion beam, it is possible to precisely define the shapes and sizes of interest and modify the samples accordingly. Using this method, cross-sectional TEM lamellae of sizes ~ 15 µm × 5 µm × 100 nm were produced. The primary advantage of this method is that lamella can be localised in a very specific areas of interest, such as: across a specific interface (i.e. grain boundary, different phases), in the wear track, across an indent.

In this study lamellae produced in the wear tracks are transferred from the sample to the TEM grid (grid plus carbon film) by using an external micromanipulator with a glass capillary and an optical microscope.

2.5 Nanomechanical characterisation: Nanoindentation and nano-scratch

In this research nanoindentation and nano-scratch measurements are carried out by using depth-sensing nanoindentation. In particular two different instruments are used, i.e. Nano-Test Platform 2, for multiple-load nanoindentation measurements and Nano-Test Vantage Platform 4 for single hysteresis nanoindentation measurements and nano-scratch tests (Micro Materials Ltd., Wrexham, UK) [9]. A very brief description of

the principle at the heart of the nanoindenters used in this study is provided here. Figure 2.7 shows the Nano-Test Vantage, platform 4 as well as a schematic representation of the nano head used for nanoindentation and nano-scratch experiments. In the indentation module, a very small and calibrated diamond probe is brought into contact with the specimen surface and load is applied by means of a coil and magnet located at the top of the pendulum. The pendulum is supported by a frictionless spring flexure. The resultant displacement of the probe into the surface is monitored with a sensitive capacitive transducer and displayed in real time as a function of the load.

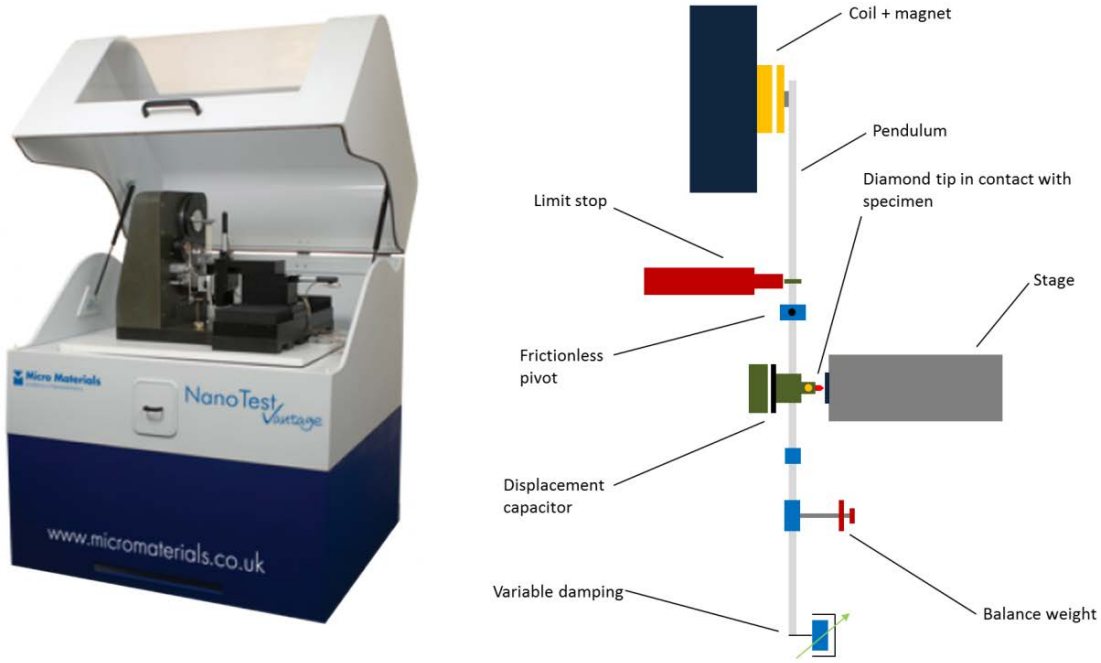

Figure 2.7 –Nanoindenter Nano-Test Vantage Platform, 4 Micro Materials and on the right hand side a schematic representation of the nano head [9].

Mechanical properties reported in Chapter 3 have been measured using the Nano-Test Platform 2, where a diamond Berkovich indenter (nominal tip radius < 100 nm) was used to perform multiple-load nanoindentation experiments at ambient temperature (~ 20°C). Each indent consists of 12 cycles, starting with a penetration depth (first cycle) of approximately 25 nm and with a depth step of ~ 25 nm per cycle. A final penetration depth greater than 10 % of the film thickness is deliberately chosen in order to understand how mechanical properties change in relation to the penetration depth and especially at which depth the substrate affects the hardness values. Mechanical properties for the thin films are evaluated at a depth such that the

substrate effect on the hardness is minimised. The experiments are carried out using a loading rate of 0.1 mN/s whereas an unloading rate of 0.05 mN/s is set in order to have a larger number of points which can be fitted accordingly to the procedure outlined by *Oliver and Pharr* [10, 11]. A partial unloading of 30% relative to the maximum load per cycle is assessed to be sufficient for the application of the procedure referred to above. A holding time of 20 seconds at every maximum load is selected to saturate creep effects before unloading. Thermal drift correction on the load-displacement curves is performed using the mean value of the pre- and post-indentation drift calibration data collected during a holding time of 60 seconds. For each film nano-hardness is determined as the average of the hardness values measured after the size effect is saturated and before the appearance of substrate effects. The selected curves for hardness measurement are also used to calculate the Young's moduli by assuming for the diamond tip an elastic modulus of 1141 GPa and a Poisson's coefficient of 0.07 (values provided by the manufacturer).

Mechanical properties of single layers, i.e. Ni-Ti(-Cu) and W-S-C, reported in chapter 5 and chapter 6, have been measured by using the Nano-Test Platform 4. A diamond Berkovich tip (nominal tip rounding of 250 nm) was used to perform the measurements at ambient temperature (~ 20°C). The mechanical properties for the single layers are evaluated from single hysteresis load-displacement curves for penetration depths within 10% of the layer thickness to avoid substrate effects on the hardness measurements; however small substrate effects on the reduced Young's modulus were expected at this penetration depth. Nanoindentation experiments and data analyses are carried out by using the same indentation parameters (i.e. loading/unloading rate, dwell time at maximum load and data acquisition time for thermal drift correction) and procedures as those reported above.

Mechanical properties of the W-S-C/Ni-Ti(-Cu) bilayers are measured by following the same procedure as that described above. Especially, with the aim of investigating the response to the nanoindentation of these systems characterised by different superelastic interlayers, nanoindentation experiments are carried out at different penetration depths up to 500 nm. This is done in order to gradually extend the strain field produced by indentation through the superelastic interlayer.

The set up shown in Figure 2.7 (Nano-Test Platform 4) is also used to perform nano-scratch tests by using a suitable probe. Furthermore, when friction measurement is also required a friction probe is interposed between the diamond tip and the pendulum as revealed in Figure 2.8. Basically the specimen is moved perpendicularly to the axis of the indenter movement allowing either single or repetitive scratch tests. It is important to note that the pendulum spring support is extremely stiff in the scanning direction[2], thus minimising errors due to the tilt of the loading head as the scratch load is increased. Accurate repositioning of the sample enables complex multi-pass scratch tests to be performed as well as scanning the surface at a very low load (0.1 mN) to have surface topography before and after the scratch test.

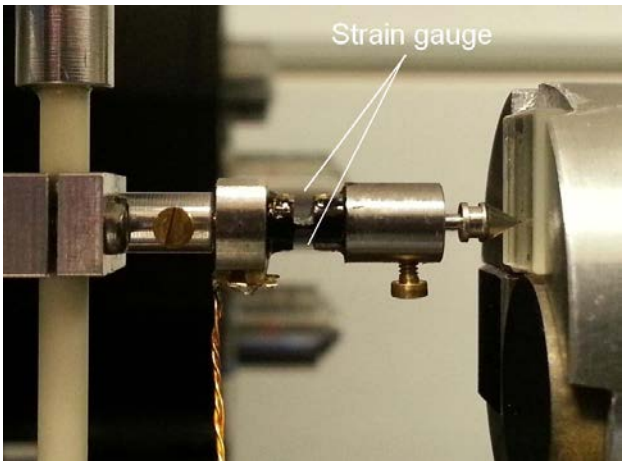

Figure 2.8 –Friction probe in position on the pendulum. The strain gauge consists of two very thin wires highlighted by arrows.

The instrument is equipped with an optical microscope (magnification up to x40), particularly useful when nanoindentation or nano-scratch measurements are required in a specific area on the surface according to the resolution of the microscope and of the stage (~ 5 µm). The nano head allows 100 different schedule with a load ranging between 0 – 500 mN and a displacement between 0 – 20 µm to be set up. The resolution in terms of force and displacement are as low as 3 nN and 0.001 nm, respectively.

The instrument requires three essential calibrations in order to produce accurate results, i.e. load calibration, diamond area function, frame compliance calibration and cross hair calibration. Calibration of the friction probe is also required before testing.

[2] Direction parallel to the axis of the pendulum.

While frame compliance is required only if any part of the instrument is replaced, the other calibrations need to be performed with a certain frequency following the instruction provided by the manufacturer. In this study the calibration above reported, with particular regard to the diamond area function and friction probe calibration have been performed before testing.

Nano-scratch tests reported in chapter 5 are performed on the W-S-C single layer and on the bilayers in order to evaluate the role of different superelastic interlayers when the bilayers are under complex stress conditions. A conical diamond tip with a nominal radius of 5 µm is used to scratch the films surface with a scanning speed of 1 µm/s over a 250 µm track. A rounded tip is chosen in order to avoid high stress concentrations, usually induced by sharp tips, this test being aimed at investigating the response of the superelastic interlayers. The tip is scanned for 50 µm on the surface at low load (0.1 mN), after which the load is ramped at a constant rate of 0.5 mN/s up to a maximum load of 100 mN. At least 10 scratches are performed on each sample, with adjacent tracks 60 µm apart to avoid mutual effects. Tests are performed as multi-pass (3 scans) experiments (topography-scratch-topography) through which, scratched surfaces are compared before, during and after every scratch. The surface topography of the bilayers is evaluated by scanning the surface with a low load (0.1 mN) so as to avoid damaging the surface. Scratch data are corrected for topography through the Nano-Test Platform 4 software (Micro-Materials Ltd., Wrexham, UK), by taking into account the instrument compliance and the sample slope, so as to have the true depth profiles under the applied load and during topography measurements.

2.6 Tribological characterisation

Tribological properties of the coatings such as: friction coefficient, wear rate, wear track morphology (depth/width) and chemical changes induced by sliding are characterised by using a combination of standard pin-on-disk wear instrument (CSM Instruments) with other characterisation equipment such as a 3D optical profiler (Zygo NewView 7200) and FEG-SEM for tribological characterisation, and Raman

spectroscopy for investigating the chemical and microstructural changes in/out the wear tracks on the coatings and correspondent pins.

The pin-on-disk wear instrument consisted of a data acquisition system and the tribometer itself (simply a ball pressed against a rotating sample) as shown in Figure 2.9.

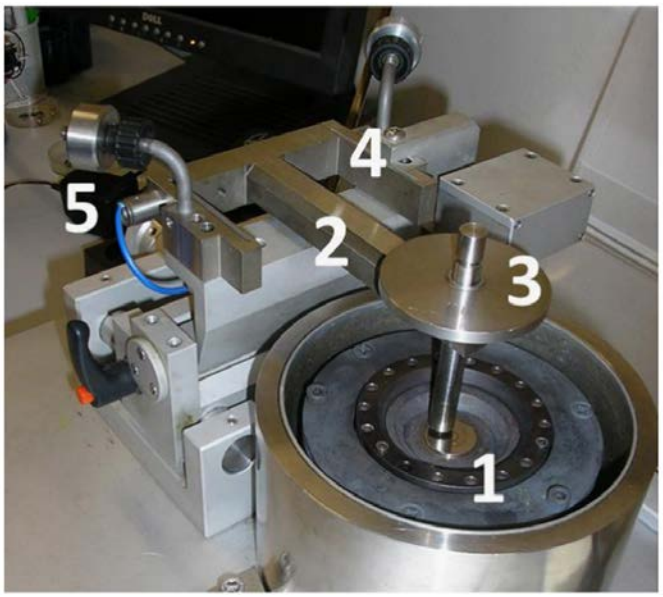

Figure 2.9 – Tribometer measuring head: (1) pin, (2) stiff lever, (3) dead weight, (4) elastic arm, (5) inductive displacement transducer [12].

The pin (1) is mounted on a stiff lever (2) designed as a frictionless force transducer, while the dead weight (3) produces the normal force. The friction force is evaluated from the deflection of the elastic arm (4) measured by the inductive displacement transducer (5).

The tribological measurements on W-S-C and W-S-C/Ni-Ti(-Cu) coatings (chapter 6) are carried out in humid air (relative humidity 27%) using the tribometer in Figure 2.9 with 100Cr6 balls (diameter of 6 mm) as a counterbody. This material was selected as counterpart as mostly used in the literature to test tribological properties of self-lubrication coatings, thus allowing us to compare our results with those reported in the literature. Three normal loads, 1, 5 and 18 N, are used to generate different stress levels in the coatings on wear tracks with a radius of 2, 3 and 4 mm, respectively. The sliding speed is set at 5 cm/s, while the number of laps is 2500 for the highest load and 5000 for the lower loads. The friction coefficient is evaluated in this study as the mean value of the entire test for every testing condition.

Wear tracks are analysed by 3D optical profiler (Zygo NewView 7200) and optical microscopy through which wear track morphology and quantification of the wear loss are performed by integration of at least 3 cross-sections per wear track, load and sliding distance. FEG-SEM and EDX are also used to investigate the wear track morphology. Surface chemical analysis is performed on both the as-deposited and on the wear tracks of the tested coatings by Raman spectroscopy (DPSS laser, wavelength 532 nm), where laser power and acquisition time were set so as to avoid graphitization and microstructural changes in the wear tracks.

References

[1] "HELIOS - Sputtering system for creating optical coatings," Leybold Optics, Germany, 2009.

[2] K. Seshan, Handbook of Thin-Film Deposition Process and Techniques, Santa Clara: WILLIAM ANDREW PUBLISHING, 2002 .

[3] "http://www.panalytical.com," Panalytical. [Online]. [Accessed 20 06 2014].

[4] "http://www.rigaku.com//products/xrd/smartlab," Rigaku Corporation. [Online]. [Accessed 20 06 2014].

[5] "http://www.thermoscientific.com/en/product/theta-probe-angle-resolved-x-ray-photoelectron-spectrometer-arxps-system.html," Thermo Scientific. [Online]. [Accessed 30 06 2014].

[6] D. B. Williams and C. B. Carter, Transmission Electron Microscopy: A Textbook for Materials Science, Springer, 2009.

[7] S. R. K. MALLADI, "IN-SITU TEM STUDIES: Heat-Treatment and Corrosion," Technical University Delft, Delft, 2014.

[8] D. BRANDON and W. D. KAPLAN, Microstructural Characterisation of Materials, 2nd Edition, Chichester, England: John Wiley & Sons Ltd, The Atrium, Southern Gate, , 2008.

[9] "http://www.micromaterials.co.uk/the-nano-test/nanotest-vantage/," Micro Materials Ltd.. [Online]. [Accessed 25 06 2014].

[10] W. Oliver and G. Pharr, "Measurement of hardness and elastic modulus by instrumented indentation: Advances in understanding and refinements to methodology," *Journal of Materials Research,* vol. 19, no. 1, pp. 3-20, 2004.

[11] W. Oliver and G. Pharr, "An improved technique for determining hardness and elastic modulus using load and displacement sensing indentation experiments," *Journal of Materials Research,* vol. 7, no. 6, pp. 1564-1583, 1992.

[12] R. Novak and T. Polcar, "Tribological analysis of thin films by pin-on-disc: Evaluation of friction and wear measurement uncertainty," *Tribology International,* vol. 74, pp. 154-163, 2014.

Chapter 3 MICROSTRUCTURE AND MECHANICAL PROPERTIES OF Ni-Ti(-Cu) THIN FILMS[♣]

3.1 Chapter summary

The microstructure of sputter deposited Ti-rich Ni-Ti thin films doped with Cu in the range 0 –20.4 at.% and annealed for 1 hour at 500 and 600°C is investigated and correlated with the mechanical properties of the films measured by depth-sensing nanoindentation. X-ray diffraction analyses show the microstructural evolution of Ni-Ti thin films when doped with Cu and annealed at different temperatures. Heat treatments promote the nucleation and growth of Ti_2Ni precipitates in Ti-rich Ni-Ti thin films, which affect the stability of austenitic and martensitic phases at ambient temperature. Cu-doped Ni-Ti thin films show a columnar grain morphology extended through the whole films thickness, and with increasing Cu content a noticeable lateral grain refinement is induced by segregation of a (Ni, Cu)-rich Ni-Ti-Cu phase to grain boundaries. The lateral grain size decreases from an average of 3.5 µm for the Ni-Ti film to 220 nm when this film is doped with 17.5 at.% Cu and annealed at 500°C. Doping with Cu causes also the formation of $Ti(Ni, Cu)_2$ plate precipitates, which become more finely and densely dispersed in the grains with increasing Cu content. These plate precipitates coarsen and their density distribution in the grains decreases with increasing annealing temperature.

The nano-hardness increases almost linearly with increasing Cu content owing to the observed grain refinement, though differences between samples annealed at different temperatures are found which can be related to the volume fraction of martensite and

[♣] Expanded from: M. Callisti, F. D. Tichelaar, B. G. Mellor, T. Polcar, "Effects of Cu on the microstructural and mechanical properties of sputter deposited Ni-Ti thin films", Surface & Coatings Technology 237 (2013) 261-268.

to the microstructural evolution of Ti(Ni, Cu)$_2$ plate precipitates with annealing temperature and Cu content. The Young's modulus exhibits a similar dependence on Cu content as nano-hardness, though no significant differences are observed for different annealing temperatures. Therefore, alloying Ni-Ti compositions with a third element such as Cu, allows their mechanical properties to be modified by a certain extent, thus improving properties such as hardness and elastic modulus.

3.2 Coatings chemical composition and surface morphology

Eight Ni-Ti(-Cu) thin films with increasing Cu in the range 0 – 20.4 at.% and a thickness of ~ 1.4 μm were produced. Table I reports the chemical compositions measured by EDX on the as-deposited films. It is noted that when the power to the Cu target was increased Ni and Ti content decreased at approximately the same rate, indicating no preferential re-sputtering effect of Ni and Ti atoms on the growing structure. For Cu content higher than 4 at.% the chemical composition of the thin films changed from being Ti-rich to (Ni, Cu)-rich. In view of the chemical affinity of Ti and O, the chemical composition of some of the Ti-rich thin films was also measured by EDX after heat treatments at 500 and 600°C and no oxygen was detected on the surface.

Table 3.1 – Average chemical composition of the as-deposited thin films measured by EDX with an error of ± 0.2 at.%.

Thin films	**Chemical composition [at.%]**		
	Ni	Ti	Cu
NiTi	48.1	51.9	0.0
NiTiCu1	45.2	52.5	2.4
NiTiCu2	46.2	49.4	4.4
NiTiCu3	43.4	49.6	7.0
NiTiCu4	42.1	47.9	9.9
NiTiCu5	41.3	45.7	13.0
NiTiCu6	38.1	44.4	17.5
NiTiCu7	36.8	42.8	20.4

However, annealing at different temperatures promoted the formation of precipitates with different structure and chemical composition, thus altering the chemical

composition of the matrix, i.e. the material exhibiting phase transformation, and consequently its microstructure.

As-deposited films exhibit a featureless surface, while after annealing at 500 and 600°C, the Ni-Ti film exhibited striations on the surface (Figure 3.1). It is known that crystalline Ni-Ti based thin films exhibit particular surface features resulting from large deformation accommodated by martensitic transformation [1].

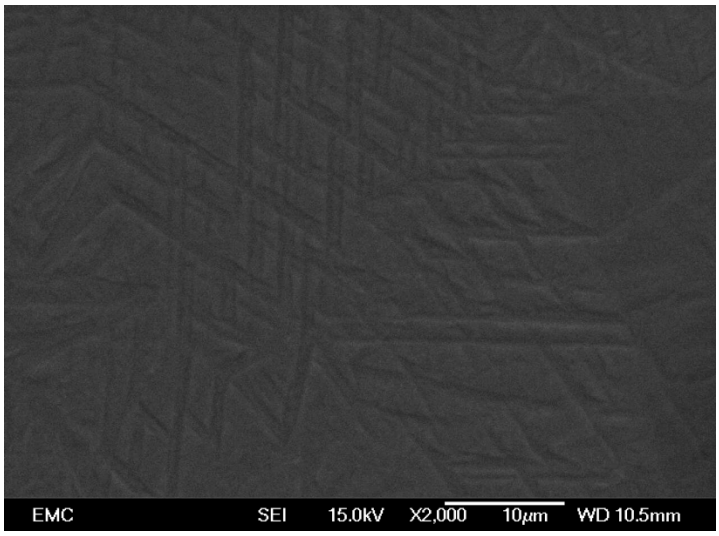

Figure 3.1 – Striations formed on the surface of the Ni-Ti film after cooling from 600°C.

Therefore the features shown in Figure 3.1 are attributed to the formation of step-like shape features associated with martensite nucleation at the free surface in the B2 matrix [2, 3] during cooling from the annealing temperature. Further details about the thermally-induced martensite on the Ni-Ti thin film are reported in the appendix A. TEM observations of the present films revealed a thin oxide layer (~ 10 nm) on top of the annealed films.

3.3 Structure

Figure 3.2 shows the cross sectional scanning electron micrographs of the as-deposited and annealed Ni-Ti thin film. Figure 3.2 (a) illustrates a featureless and homogeneous cross-section morphology for the as-deposited film, indicating a dense amorphous

structure. The amorphous film is noted to exhibit relatively ductile fracture behaviour during SEM sample preparation. In fact when the Si substrate is broken the amorphous thin film still keeps the broken parts together; this provides an indication of the good quality of the as-deposited films.

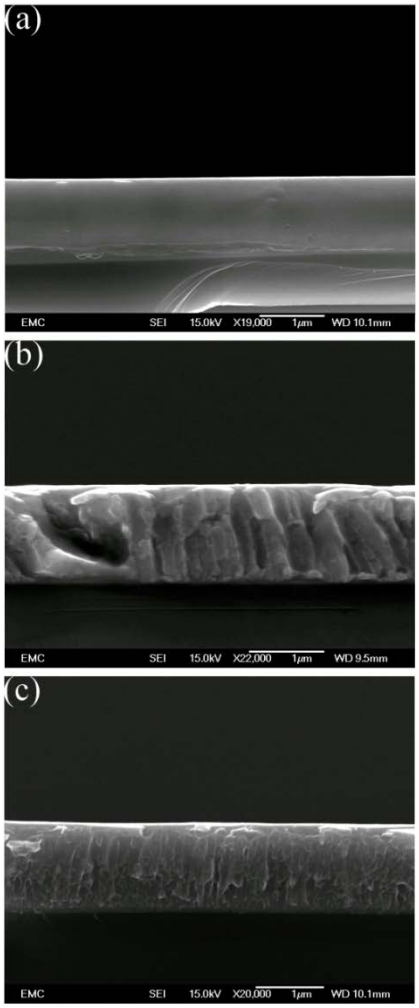

Figure 3.2 – Cross-sectional SEM images of the Ni-Ti-base thin film: (a) as-deposited, (b) annealed at 500°C and (c) annealed at 600°C.

Films annealed at 500°C, Figure 3.2 (b) and 600°C, Figure 3.2 (c) have a fibrous texture across the whole film thickness suggesting the presence of relatively large columnar grains. The Ni-Ti film annealed at 600°C exhibits a slightly more brittle fracture behaviour during cross-sectional SEM sample preparation, which might indicate intergranular fracture owing to the embrittlement of the grain boundaries attributed to the presence of gran boundary precipitates.

3.3.1 X-ray diffraction analysis

The effects of annealing on the microstructure of the Ni-Ti(-Cu) thin films are analysed first for the Ni-Ti film. Figure 3.3 shows the XRD pattern of the Ni-Ti film in the as-deposited and annealed conditions. The as-deposited film exhibits an amorphous structure resulting from the relatively low deposition temperature (~ 80°C, measured by the pyrometer installed in the deposition chamber floor). After annealing for 1 hour at 500°C the XRD pattern revealed the coexistence of the austenitic (B2) and martensitic (B19') phases at ambient temperature indicating that nucleation of martensite in the austenitic matrix took place during cooling from the annealing temperature. However, the martensitic transformation is incomplete, i.e. ambient temperature is between the martensite start (M_s) and finish (M_f) temperatures. Small peaks related to the metastable Ti_2Ni phase are also identified in the film annealed at 500°C. This phase is thought to have a spherical morphology with a semi-coherent interface with the matrix [4].

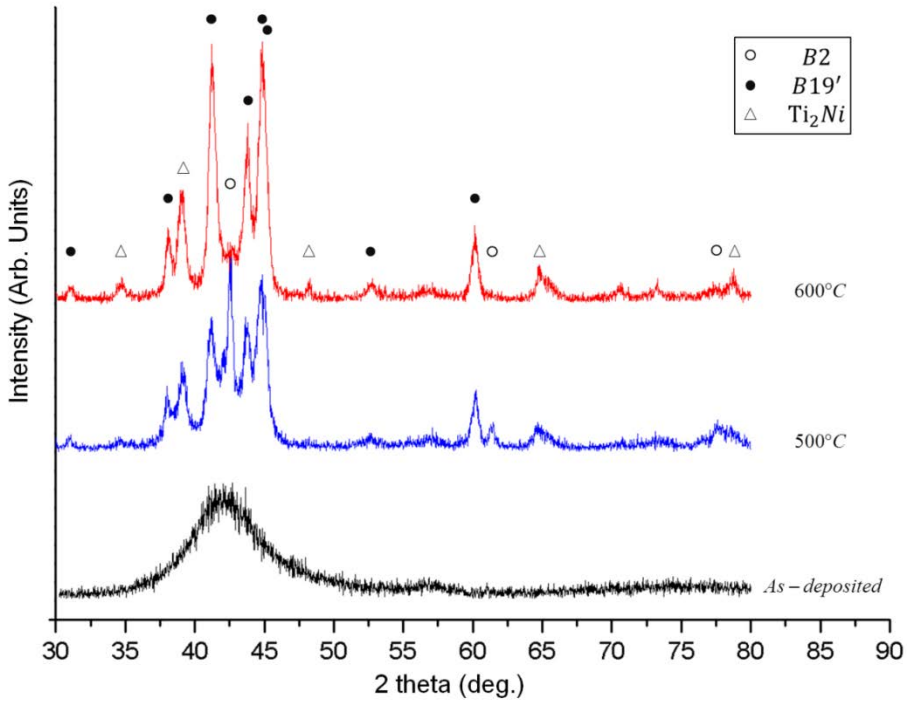

Figure 3.3 – Grazing incidence X-ray diffractograms of the Ni-Ti thin film in the as-deposited and annealed conditions (B2: austenite, B19': martensite); grazing angle ω = 5°.

On the other hand, the film annealed at 600°C exhibits a martensitic structure (upon cooling from the annealing temperature, austenite transformed to martensite and a Ti_2Ni intermetallic phase was also formed in the grain interior) as revealed by the XRD pattern (Figure 3.3), thus indicating M_f above ambient temperature, which was found also in other studies for a similar composition and heat treatment [5]. It is well known that the transformation temperatures of Ni-Ti alloys are strongly affected by both the chemical composition and by stress according to the Clausius-Clapeyron relationship [6]. In the results reported in Figure 3.3 no appreciable shifts in peaks due to residual stresses are noted for the two annealing temperatures, therefore the shift of transformation temperatures is attributable to the change of chemical composition of the matrix. Figure 3.3 shows that with increasing annealing temperature the peaks related to the Ti_2Ni phase become more intense, indicating an increasing amount of this phase with concomitant Ni and Ti depletion in the matrix. It is well known that the transformation temperatures are strongly dependent on the Ni concentration rather than on Ti content [6], however it has been reported that near-equiatomic Ni-Ti compositions exhibit slightly higher transformation temperatures than Ti-rich and Ni-rich compositions [7, 8, 9]. Therefore, the formation of Ti-rich precipitates in the matrix causes a change in chemical composition toward a near equiatomic condition, thus making the films annealed at 600° martensitic at ambient temperature.

The XRD patterns in Figure 3.4 show the microstructural evolution of the Ni-Ti film annealed for 1 hour at 500 and 600°C, when an increasing amount of Cu is co-sputtered together with Ni and Ti. For the films annealed at 500°C, peak intensity evolution clearly indicates an increase in M_s with increasing Cu content i.e. B19' peaks become more intense at the expense of the B2 peak. This effect is due to the solubility of Ni in the B2 matrix decreasing with increasing Cu content [10], and a decreasing Ni content in the matrix is known to increase the transformation temperatures [11].

The Ni-Ti film annealed at 600°C is already martensitic at ambient temperature (Figure 3.3). By Cu addition to the binary system, a peak associated with the $Ti(Ni, Cu)_2$ phase, which almost overlaps the martensitic peak for $2\theta \approx 41°$, appears in the films annealed at 600°C, as also found in another study [12]. The $Ti(Ni, Cu)_2$ phase, which usually nucleates along two perpendicular planes in the B2 matrix, is thought to have a tetragonal structure ($C11_b$-type); however it was not considered to be a GP zone [13]. It has been reported that this tetragonal phase has a rather thin disk-like morphology

which makes it hardly detectable by XRD analysis at relatively low annealing temperatures, such as 500°C where these plates are expected to be very small.

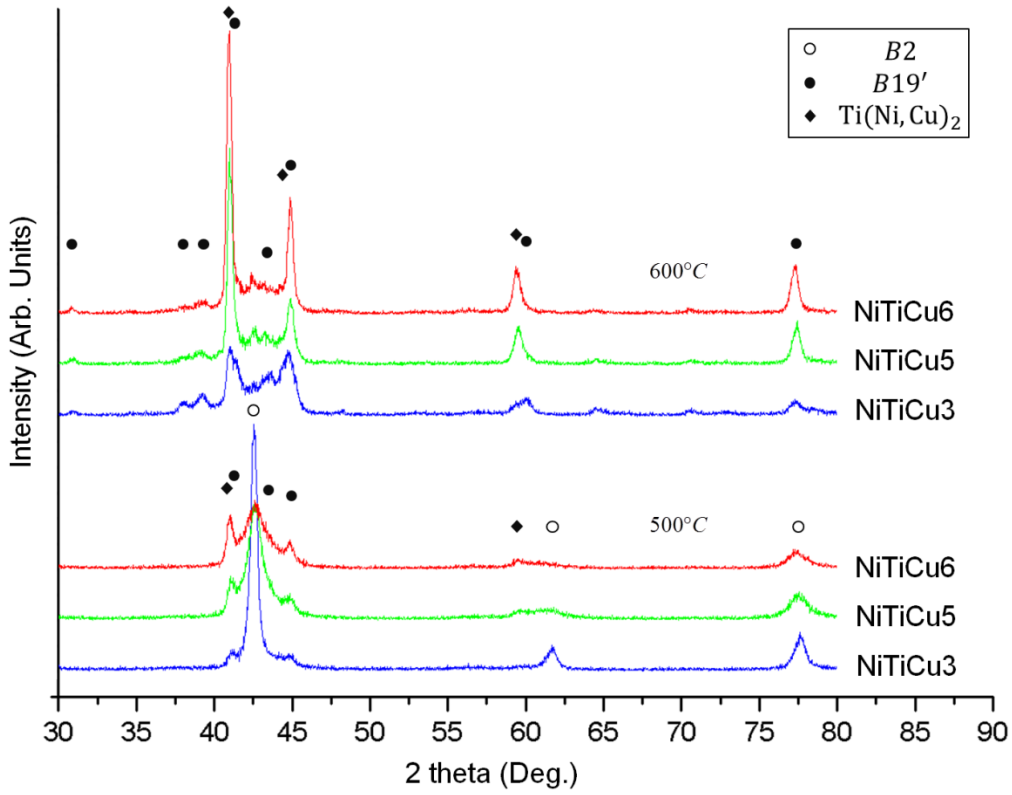

Figure 3. 4 – Grazing incidence X-ray diffractograms of some of the investigated Ni-Ti-Cu thin films annealed for 1 hour at 500 and 600°C; grazing angle ω = 5°.

Although Cu addition further contributes to lowering the solubility of Ni in the B2 matrix with consequent increase of M_s, it has been reported that for a specific annealing temperature the increase of M_s with increasing Cu content saturates [14]. This suggests that when the Cu content increases above a certain limit, the chemical composition of the matrix and consequently the M_s is no longer strongly affected, therefore the Cu atoms may be segregated or present as precipitates in the matrix. This may be another reason for the appearance of intense peaks related to $Ti(Ni, Cu)_2$ phase with increasing Cu content in the films annealed at 600°C (Figure 3.4). We expect that with increasing Cu content and annealing temperature coarsened and more densely dispersed plate precipitates may appear in the grain interior, as well as excess atoms segregated at the grain boundaries.

It has been reported that Ni-Ti thin films with a Cu content higher than 10 at.% exhibit a single or two-stage B2↔B19(↔B19') martensitic phase transition [6]. However, the XRD analysis performed in this study shows only the presence of B19' martensite for NiTiCu5 and NiTiCu6 annealed at 500 and 600°C, as also found by *Gao et al.* [15] for a $Ti_{44.6}Ni_{40.1}Cu_{15.3}$ thin film annealed at similar temperatures. The reason for this may be understood by considering the relative stability between parent and native phases and consequently the path of transformation in terms of the Gibbs free energy. It is known that the relative stability in terms of free energy between parent and native phases can be affected by the chemical composition (i.e. Ni/Ti ratio and by alloying the binary system a third element) and by the internal energy (typically stress due to precipitates and dislocations) [6]. It was reported that by Cu addition the elastic constant c_{44} associated to the shear deformation in the B2 crystal increases, thus destabilising the B19' phase, i.e. the free energy curve moves up, and considering the lower transformation strain required to produce B19 (∼ 8 %, compared to ∼ 10 % for the B19') from the B2 crystal, the B2↔B19 becomes energetically more favourable than B2↔B19'. Similarly, the presence of dislocations and precipitates act as a resistance against lattice distortion (martensitic transformation).

The presence of B19' rather than B19 found in this study suggests that the effects of precipitates and eventually of dislocations (elastic free energy component) are strongly counterbalanced by the other component of the free energy, i.e. the chemical free energy depending on the chemical composition. This means that the formation of (Ni, Cu)-rich precipitates as well as the segregation of excess atoms at the grain boundary may significantly decrease the Cu content in the matrix below 10 at.%; as a consequence, B19' becomes energetically more favourable at ambient temperature than B19.

3.3.2 Transmission electron microscopy

The Ni-Ti film displays grains with a lateral size larger than the film thickness (Figure 3.5 (a)) as also reported in other studies [16], indicating that grain growth normal to the surface was limited by the substrate and the film surface, while lateral grain

boundary migration took place promoting the formation of large grains (two-dimensional grain growth).

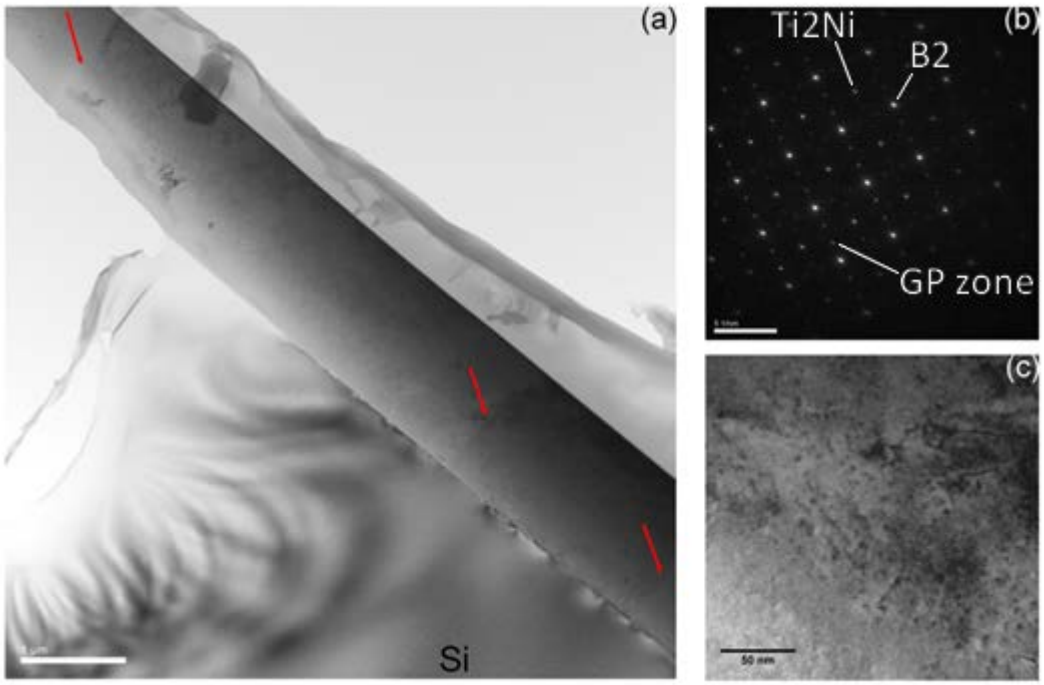

Figure 3.5 – Ni-Ti thin film annealed for 1 hour at 500°C: (a) BF TEM image of the Ni-Ti thin film, arrows highlight the grain boundaries; (b) selected area diffraction pattern from a grain in zone axis; (c) grain interior, where black dots are Ti_2Ni precipitates.

The selected area electron diffraction pattern in Figure 3.5 (b) clearly shows diffraction from the B2 crystals (intense spots), as well as secondary spots (less intense spots) attributed to Ti_2Ni precipitates, which appear as black dots in Figure 3.5 (c). The SAD pattern in Figure 3.5 (b) suggests also the presence of GP zones, although they are not evident in TEM images, thus suggesting GP zones of a very small size (they can be as thin as 0.5 – 1 nm, which corresponds to a very few atomic layers [17]).

The Ni-Ti thin film shows small twin domains in the B2 matrix, attributed to the twinned B19' martensite. Some of these twins are highlighted in Figure 3.6 (a), while one of these is shown in higher resolution in Figure 3.6 (b). These twinned martensitic domains exhibit a zig-zag morphology as also found in other studies [18].

The presence of an array of spots or streaks in the diffraction pattern suggests a structural periodicity in real space [19], which in this case is represented by the twinned structure of B19' martensite as shown in Figure 3.6 (b). The array of spots

shown in Figure 3.6 (c) consists of more intense spots related to diffraction from twin boundaries and by secondary (less intense) spots between the twin spots owing to the interference of the electrons diffracted by the twin boundaries.

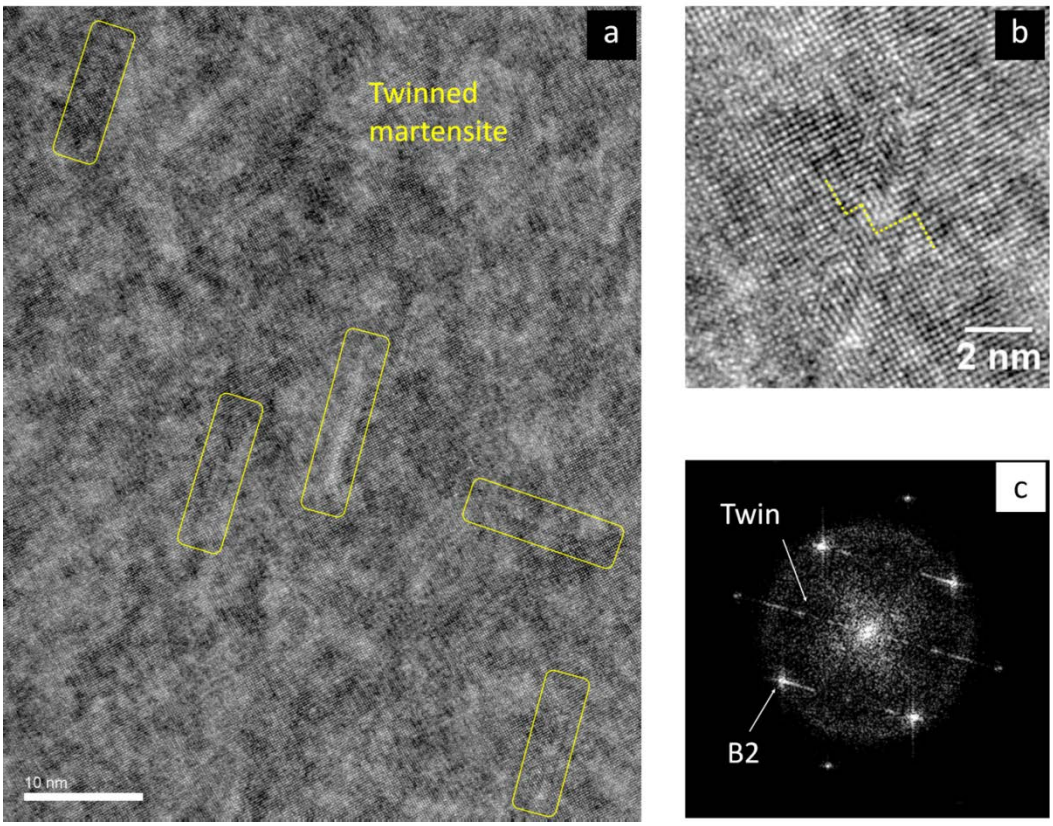

Figure 3.6 – Ni-Ti thin film annealed for 1 hour at 500°C: (a) HR-TEM image showing some twinned martensite domains in the B2 matrix; (b) HR-TEM image of a twinned domain with a zig-zag morphology and corresponding SAD pattern in (c).

With increasing Cu content the lateral grain size of the Ni-Ti-Cu layers gradually decreased reaching an average size of 220 ($\pm$80) nm for 17.5 at.% Cu. Figure 3.7 shows the cross section of films doped with different Cu contents and annealed for 1 hour at 500°C. It is clear that, regardless of the chemical composition, the grains exhibit a columnar morphology extending in most cases through the whole film thickness, whereas their lateral size[1] seems to be strongly affected by the composition. This dependence appears to be related to the Cu content for (Ni, Cu)-rich films with an approximately constant Ni/Ti ratio.

[1] Average size of the columnar grains measured perpendicularly to the column axis on the plane of view of the Cross-sectional TEM sample.

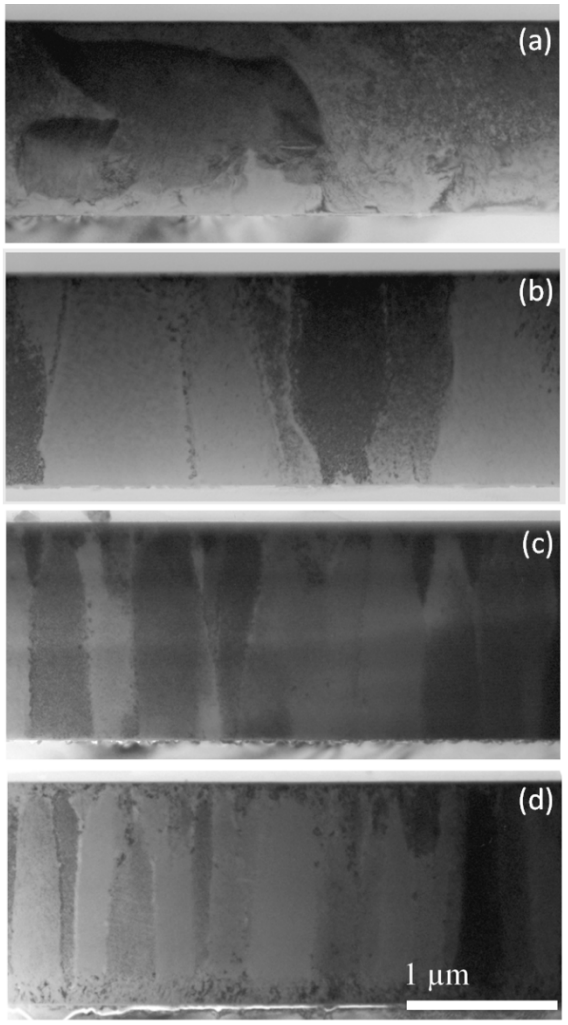

Figure 3.7 – Cross-sectional High Angle Annular Dark Field (HAADF) TEM images of (a) Ni-Ti, (b) NiTiCu3, (c) NiTiCu5 and (d) NiTiCu6 annealed for 1 hour at 500°C.

Figure 3.7 provides some evidence regarding the mechanism of grain growth during the heat treatment. Beneath the surface of the films a competitive growth mechanism from top to bottom took place. It is well known that the boundary mobility can be very sensitive to the presence of solute; therefore the mechanism reported above may be related to the anisotropy in the surface chemical interaction of the solute atoms with the adjacent crystal faces [15]. Based on this, by looking closely underneath the surfaces (Figure 3.8), it seems that the grain II, whose growth was blocked, is surrounded by a more continuous network of segregated particles, approximately 10 – 15 nm wide. Therefore, it is likely that the two adjacent grains (I and III) grew, at least in the early stages, at the expense of grain II, where most of the solute atoms have segregated to its grain boundaries.

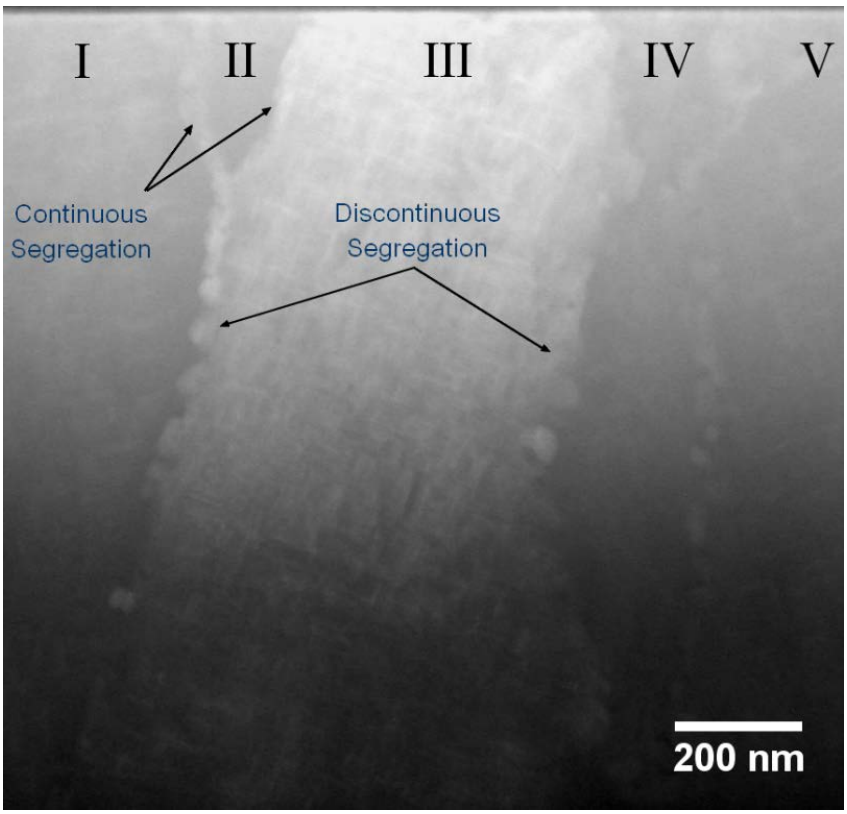

Figure 3.8 – Cross-sectional HAADF TEM image of the NiTiCu3 film annealed for 1 hour at 500°C.Continuous and discontinuous grain boundary segregation are observed along the film thickness.

EDX analyses at the grain boundaries show a (Ni, Cu)-rich Ni-Ti-Cu composition for the phase segregated at the interface. Although the chemical quantification of Ni, Ti and Cu within the grain boundary precipitates may be affected by the surrounding structure, several chemical analyses performed along the grain boundaries both in specific areas as well as across the grain boundaries (EDX line scans), clearly shows a Ni and Cu enrichment corresponding to the segregated particles. The presence of a high Ni concentration may be attributed to the lower solubility of Ni in the B2 matrix with increasing Cu content as previously reported. Therefore it is likely that for a sufficiently large Cu content, segregation of a (Ni, Cu)-rich phase at grain boundaries occurs during annealing, preceding grain coarsening.

By comparing Figure 3.7 (b) to (d) at the films free surface and at the interface with the substrate (energetically more favourable places for crystal nucleation), it is seen that with higher Cu content an increasing amount of small grains (~ 20 nm on average) nucleate at the interfaces. It suggests that Cu addition causes an increase in crystal nucleation rate and the competitive growth mechanism is expected to be further encouraged. Therefore, the grain refinement observed in Figure 3.7 (a) to (d) is very

probably associated mainly with solute atoms (mostly Cu and Ni) segregation at the grain boundaries, which limits grain boundary mobility in the direction parallel to the film surface. This behaviour is the opposite of the case of the Ni-Ti film where, although the chemical composition of the film is off-stoichiometric (Ti-rich), segregated phases are not observed at all along the grain boundaries.

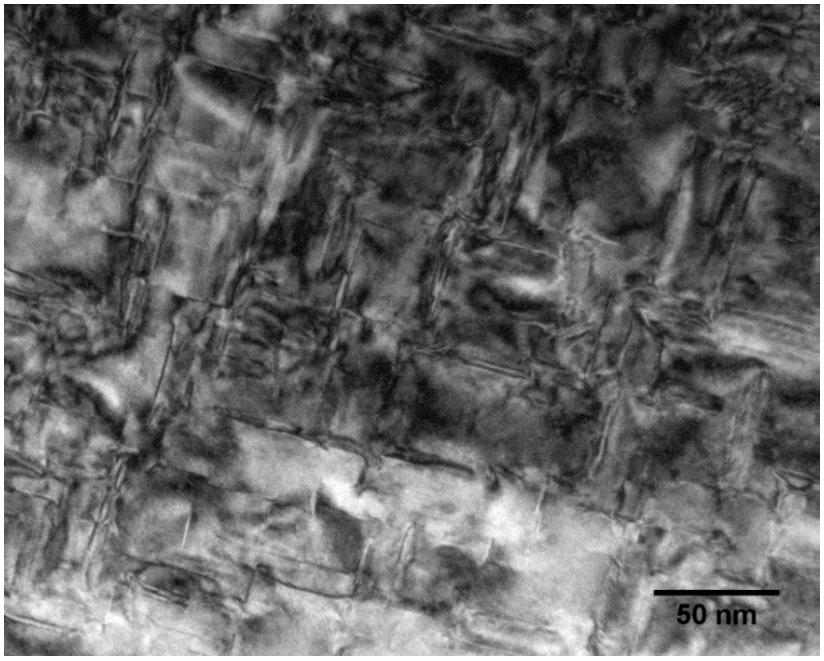

Figure 3.9 – Bright Field TEM image of the grain interior for the NiTiCu3 thin film annealed for 1 hour at 500°C.

Figure 3.9 shows the microstructure in the grain interior of the NiTiCu3 thin film annealed at 500°C. Uniformly distributed streaks along two perpendicular directions can be appreciated within the grain. EDX line scan across these bright streaks showed a (Ni, Cu)-rich Ni-Ti-Cu composition, as shown in Figure 3.10; thus, they are believed to be Ti(Ni, $Cu)_2$ precipitates (b.c.t. structure) [20]. Since the precipitates are very thin, they are barely identified in the XRD patterns of films annealed at 500°C.

These plate precipitates are found to lie on the {100} planes of the cubic B2 structure with a measured d-spacing[2] of $\sim$ 1.49 Å, while the B2 matrix exhibited a lattice parameter of $\sim$2.98 Å, as also reported in other studies [6]. High coherency is therefore produced at the interface matrix/precipitate. Notwithstanding the highly

[2] SAD and CBED patterns are used to calculate the d-spacing of the crystals according to the equation d = λL/D, with an error of about 1 %.

coherent interface, a small lattice mismatch generates a strain field around these precipitates as suggested by the blurred area surrounding the plates (Figure 3.9).

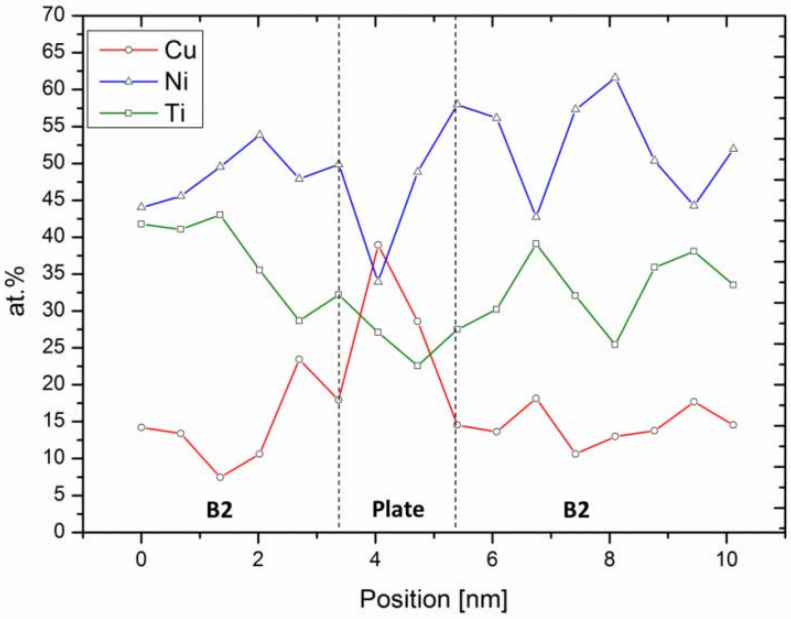

Figure 3.10 – Representative EDX line scan across a plate precipitate in the NiTiCu3 thin film annealed for 1 hour at 500°C.

Figure 3.11 (a) shows an atomic resolution image of a plate precipitate formed in the NiTiCu3 film, and in Figure 3.11 (b) the corresponding Inverse Fast Fourier Transform (IFFT) where the strain field along the interface matrix/precipitate is very clear (darker areas at the interface). In the one-dimensional Fourier-filtered image in Figure 3.11 (d) (obtained by filtering the diffraction spots highlighted in Figure 3.11 (c)) some misfit dislocations are highlighted at the interfaces plate/matrix, which confirms that although the coherency is very high, a very small misfit, hardly quantifiable, exists between the matrix and the precipitates. This lattice misfit is expected to be due to the stretching of the cubic crystal (B2) to form the b.c.t. structure caused by the Cu and consequently Ni enrichment in the precipitate. It is in agreement with the result found by *T. Fukuda et al.* [21], which reported that with increasing Cu content in Ni-Ti-Cu alloys the interfacial coherency becomes worse.

However, the presence of this coherent strain field as well as the presence of uniformly distributed precipitates in the matrix is expected to increase the strength of the B2 matrix without impeding the martensitic transformation, as it is found for GP zones formed in binary Ni-Ti systems [22].

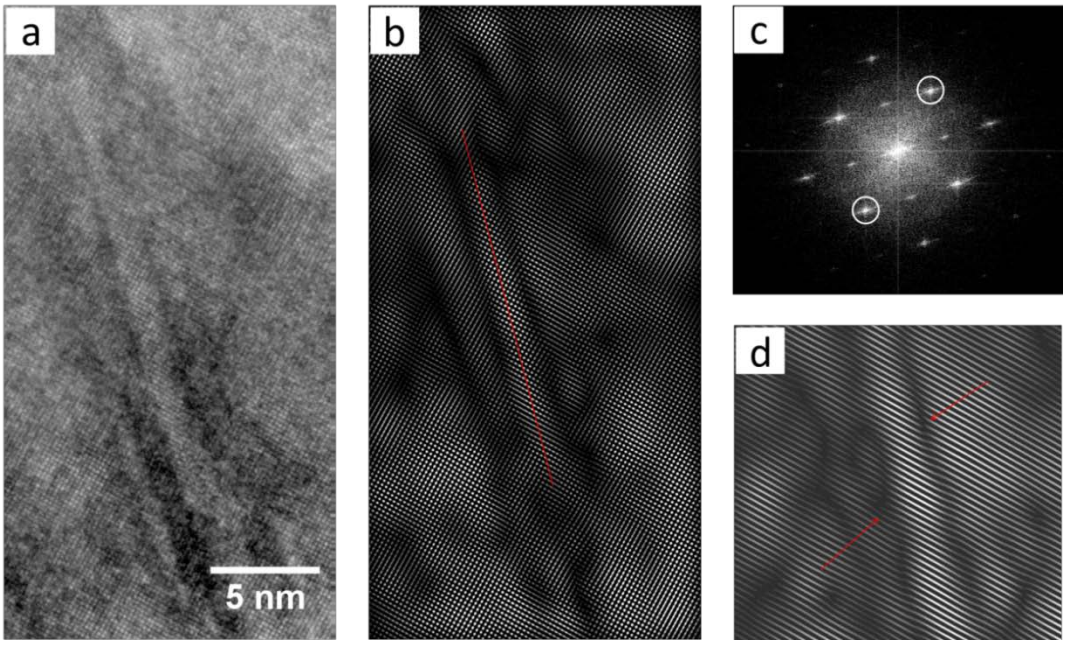

Figure 3.11 – Plate precipitates in the NiTiCu3 thin film annealed for 1 hour at 500°C: (a) HR-TEM image; (b) Inverse Fast Fourier Transform of the HR-TEM image obtained by filtering the main spots in the power spectrum of the HR-TEM image (the line indicates the position of the plate precipitate); (c) FFT spectrum of the HR-TEM image; (d) One-dimensional Fourier-filtered image obtained by using the diffraction spots highlighted in (c).

However, as also evident from Figure 3.9 plate precipitates can cross each other or can generate a cage-like structure[3], which may have some negative effects on the martensitic transformation. The reason is attributed to the fact that as shown in Figure 3.12, where two crossing plates (Figure 3.12 b) and two spaced plates (Figure 3.12 a) are imaged on the atomic scale, much more lattice distortions are generated at the interface and in the surrounding B2 matrix when two plates meet each other, compared to the case of single plates. Even though the growing martensite may pass through the crossing plates, the energy required for the inverse[4] martensitic transformation might be such that plastic deformation become energetically more favourable, or the elastic energy stored in the system is not sufficient to drive a complete inverse transformation and thus stabilised martensite may form around the precipitates.

[3] Three or four plate precipitates crossing each other or close each other.
[4] Phase transformation from martensite to austenite during unloading or upon heating.

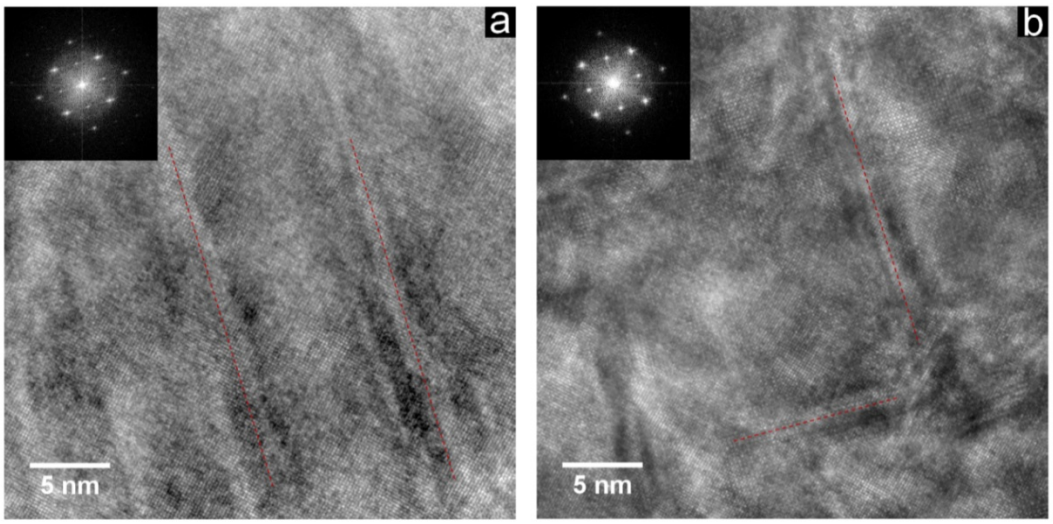

Figure 3.12 – HR-TEM images of (a) single and (b) double Ti(Ni, Cu)$_2$ plate precipitates formed in the NiTiCu3 thin film annealed for 1 hour at 500°C; the dashed lines highlight the position of the plate precipitates. The insets show the electron diffraction pattern.

Figure 3.13 demonstrates that with increasing Cu content Ti(Ni, Cu)$_2$ plate precipitates decrease in size and become more densely distributed in the matrix. This observation may further suggest that Cu significantly affects the kinetics of crystallisation of binary Ni-Ti systems. The presence of more densely distributed plates of smaller size is in agreement with the hypothesis that Cu addition increases the nucleation rate while decreasing the crystal growth rate.

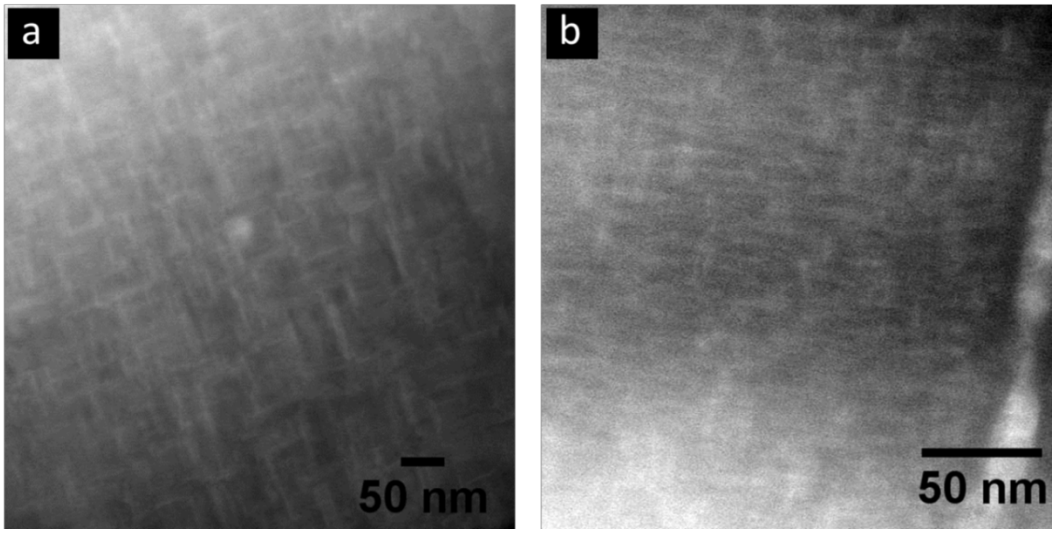

Figure 3.13 – Cross-sectional HAADF TEM images of the (a) NiTiCu3 and (b) NiTiCu5 thin films annealed for 1 hour at 500°C. Smaller and more densely distributed Ti(Ni, Cu)2 plate precipitates are observed for the NiTiCu5 film.

Regardless of the annealing temperature, the presence of the Ti(Ni, Cu)$_2$ precipitates and of the (Ni, Cu)-rich phase segregated at the grain boundaries reinforces the hypothesis regarding the appearance of the B19' rather than B19 phase as a result of the lower Cu content in the matrix owing to the formation of these Cu-rich phases.

Some of the Cu-doped Ni-Ti thin films annealed for 1 hour at 600°C are investigated by FIB, in order to evaluate the effects of annealing temperature on the microstructure of these films. A comparison is made here between the NiTiCu3 film annealed at 500 (described above) and 600°C. Figure 3.14 shows the cross-section of the NiTiCu3 film annealed at 600°C, where some microstructural features are clearly visible. With respect to the NiTiCu3 film annealed at 500°C (see Figure 3.7 (b)), the film annealed at 600°C (Figure 3.14 (a)) exhibited slightly larger grains and a significantly thicker diffusion layer at the interface with the silicon substrate (the diffusion layer for films annealed at 500°C is ~ 20 nm thick).

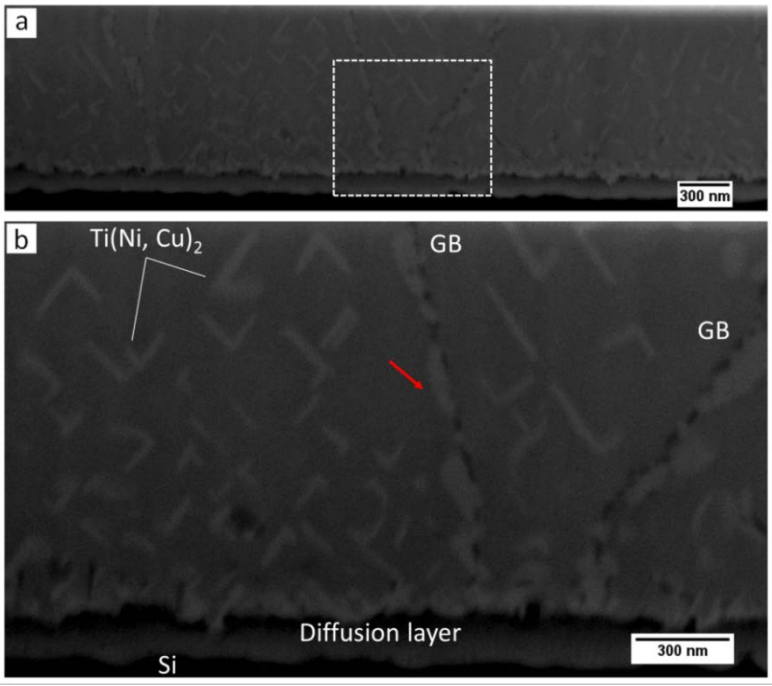

Figure 3.14 – NiTiCu3 film annealed for 1 hour at 600°C: (a) cross-sectional secondary electron image (Zeiss NVision 40 CrossBeam FIB System), (b) high magnification image of the inset in (a). The arrow highlights very likely the diffusion of Ni and Cu atoms toward the grain boundary (GB).

Interesting changes are observed in the grain interior in relation to the annealing temperature. In fact, by comparing Figure 3.14 (b) with Figure 3.12 and 3.13, it is clearly seen that the Ti(Ni, Cu)$_2$ plate precipitates coarsen at higher annealing

temperature and their density distribution in the grain interior decreases. Such a decrease is attributed to the fact that the chemical composition of the matrix must remain the same; therefore the diffusion of solute atoms toward the grain boundary (highlighted in Figure 3.14 (b) by the red arrow) is counterbalanced by a decrease in the density distribution of plate precipitates in the grain interior. Diffusion of solute atoms is also observed at the interface film/substrate.

3.4 Mechanical properties versus microstructure

The mechanical response of the films is probed by multiple-loading nanoindentation through which nano-hardness and Young's modulus were measured. Figure 3.15 shows a representative multiple-load versus displacement curve for the Ni-Ti thin film annealed for 1 hour at 500°C. Every partial unloading is used to calculated hardness and elastic modulus.

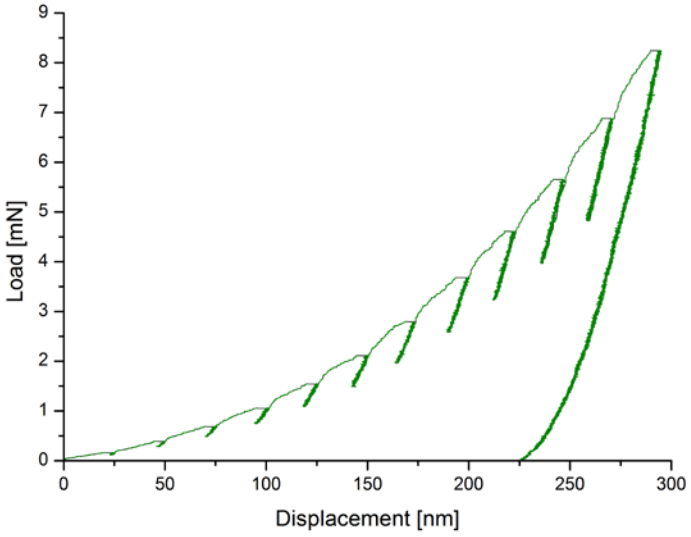

Figure 3.15 – Multiple load – displacement curve for the Ni-Ti thin film annealed for 1 hour at 500°C.

Figure 3.16 shows a typical trend of the hardness in relation to the penetration depth as determined by the curve shown in Figure 3.15. The curve in Figure 3.16 can be subdivided in three stages. In particular, for very shallow penetration depths ($<$ 70 nm) the hardness first decreases, thus suggesting indentation size effect. For depths ranging between 70 – 130 nm the hardness is about constant and it is the range of

depths where the hardness is calculated of every film and averaged over at least 10 measurements. This experimental result suggests that that 10 % rule generally used to avoid substrate effects on the hardness is roughly valid for Ni-Ti(-Cu) thin films.

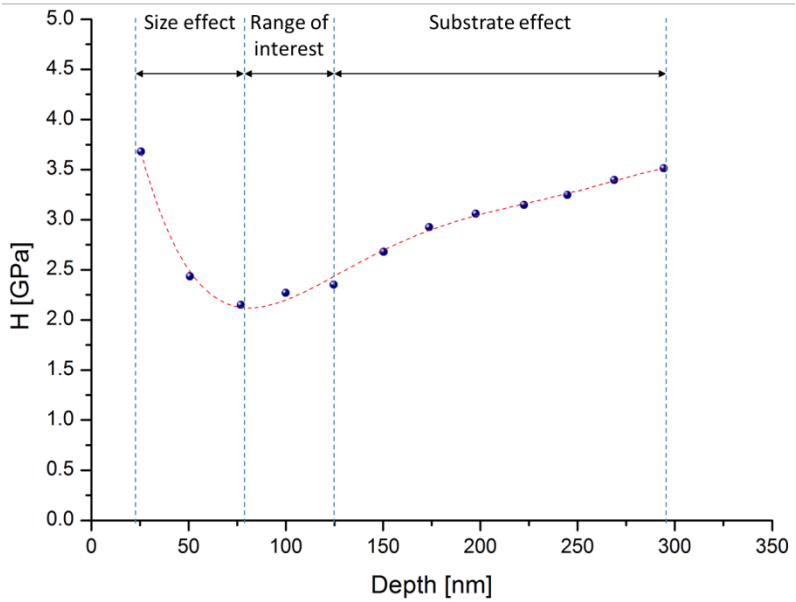

Figure 3.16 – Hardness in relation to the penetration depth for the Ni-Ti thin film annealed for 1 hour at 500°C. The dashed line is reported only as guideline.

For penetrations depths larger than 130 nm the substrate effect becomes prominent, thus causing an increase in hardness. The reduced elastic modulus, used to calculate the elastic modulus as described previously, is also calculated in the depth range mentioned above, although at this depth minor substrate effects on elastic modulus of the film might be expected.

Figure 3.17 (a) shows the hardness as a function of the Cu content for two annealing temperatures; the vertical error bars may also include the effects of crystal anisotropy together with measurement errors.

The Ni-Ti film exhibits almost the same hardness value on both annealing temperatures being very close to the value reported by *Huang et al.* for a martensitic Ti–48.3 at.% Ni thin film [23]. These results indicate that though the austenitic phase is still partially present in the film annealed for 1 hour at 500°C (see Figure 3.3), its nanoindentation response is mainly controlled by the martensitic reorientation process (detwinning) rather than by stress-induced martensitic transformation. This is in agreement with the fact that the energy level required to activate the detwinning

process of martensite is lower compared to that required to activate the B2→B19' transformation [6], thus the first process results energetically more favourable.

Regarding the role of precipitates on the mechanical properties, as shown in Figure 3.3, Ti_2Ni precipitates are already formed in the film annealed at 500°C together with thin coherent plate precipitates (GP zones), while only Ti_2Ni precipitates are expected in the film annealed at 600°C. As a consequence of this, no evident differences are observed in the hardness for annealing at different temperatures. It suggests that even if GP zones are present in the film annealed at 500°C, their beneficial effect on mechanical properties is suppressed by the presence of the semi-coherent Ti_2Ni precipitates.

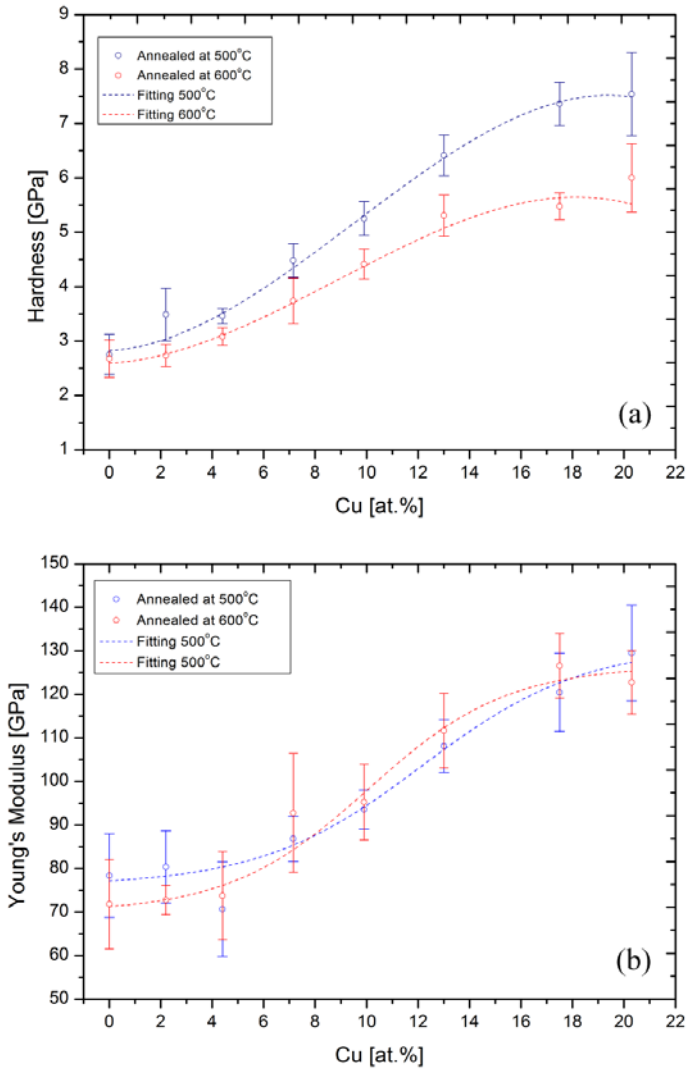

Figure 3.17 – Mechanical properties measured by multiple-loading nanoindentation experiments: (a) Nano-hardness and (b) Young's modulus (calculated assuming E = 1141 GPa and v = 0.07 for the diamond tip and v = 0.3 for the films) as a function of Cu content and annealing temperature. Dashed lines are reported as guideline.

In the literature very few studies investigated the hardness of ternary Ni-Ti-Cu thin films and to the best of our knowledge no systematic investigations were performed to understand the effects of Cu on mechanical properties. It was reported an average hardness of about 4 GPa for a $Ti_{48}Ni_{42}Cu_{10}$ film (600 nm thick) annealed in vacuum for 1 hour at 500°C [23], which is lower compared to the hardness found here (5.2$\pm$0.3 GPa) for the NiTiCu4 film annealed for 1 hour at 500°C.

Regarding the Cu-doped Ni-Ti films, no significant changes in grain size are expected for annealing at different temperatures, as reported in literature [14, 24, 13] and also found in this study (see section 3.2.2). Therefore, we expect that three different microstructural aspects may play a role in the mechanical properties of these films in relation to the Cu content and/or annealing temperatures that are: grain refinement as a consequence of Cu addition (Figure 3.7), change in martensite/austenite volume fraction as a consequence of both Cu addition and annealing temperature (see Figure 3.4 for a qualitative understanding) and microstructural evolution in the grain interior, even in this case in relation to the Cu content and annealing temperature (see Figure 3.13 and Figure 3.14).

The main reason behind the observed increase in hardness with Cu content, regardless of annealing temperature, is attributed mostly to the grain refinement in Cu-doped films. By increasing Cu content the grain refinement as well as the constraining effect of the neighbouring grains becomes prominent, thus decreasing the deformation accommodated during the indentation process regardless of the austenite/martensite volume fraction and microstructural evolution in the grain interior. However, it is seen that for high Cu content ($>$ 13 at.%), hardness tends to saturate regardless of the annealing temperature. It suggests that neither annealing temperature nor microstructure in the grain interior (i.e. martensite volume fraction and precipitate evolution) affect the hardness trend. Therefore, the observed hardness saturation for higher Cu content is likely attributable to the evolution of grain boundaries with Cu content. As observed in Figure 3.7, with increasing Cu content, grain boundaries become populated by (Ni, Cu)-rich precipitates, which for a Cu content above 17 at.% form dense and continuous chains along grain boundaries. The presence of solute atoms at the grain boundaries is further encouraged for higher annealing temperatures (Figure 3.14). It is expected that when the grain size becomes small,

where its deformation becomes energetically more demanding, the high compressive stress generated underneath the indented surface likely is in part relaxed at grain boundaries (likely plastic deformation). Such a physical phenomenon is expected to be the cause of the hardness saturation observed in Figure 3.17.

Films annealed at 500°C exhibit a higher hardness compared to those annealed at 600°C. This is related to the austenitic phase presents in the Cu-doped Ni-Ti thin films annealed at the lower temperature. The XRD patterns in Figure 3.4 show that with increasing Cu content the presence of the B19' phase becomes prominent at the expense of the austenitic phase in films annealed at 500°C. On the other hand, films annealed at 600°C are martensitic at ambient temperature and thus exhibit a lower hardness regardless of the Cu content.

However, it is interesting to note that although in the films annealed at 500°C the B19' phase becomes prominent with increasing Cu content, which should, in principle, correspond to a more similar mechanical response between films annealed at 500 and 600°C (already martensitic), the difference in hardness tends instead to increase with increasing Cu content. This aspect led us to believe that another factor is also responsible for the observed differences in hardness for annealing at different temperatures. This physical factor is thought to relate to the microstructural evolution of the $Ti(Ni, Cu)_2$ plate precipitates in the grains in relation to the Cu content and annealing temperature, as schematically illustrated in Figure 3.18. In particular, these plate precipitates are found to be more finely and densely dispersed in the grains with increasing Cu content in films annealed at 500°C (see Figure 3.13). While with increasing annealing temperature coarsened and less densely distributed plate precipitates with a semi-coherent interface with the matrix are found here (Figure 3.14) and elsewhere [13]. The interfacial coherence was also reported to be affected by the Cu content, i.e. it becomes worse with increasing Cu content even for annealing at low temperatures owing to the increasing lattice mismatch between precipitate and matrix [23].

This highlights the fact that with increasing both Cu content and annealing temperature the strengthening effect gained by formation of coherent plate precipitates is worsened, consequently pronounced differences may be observed in mechanical properties, as is the case reported in Figure 3.17. Such dissimilarity is not only associated with the difference of the relative amount of austenitic and martensitic

phase present in the films annealed at different temperatures, it is because in that case the difference in hardness would decrease owing to the increasing amount of martensite with increasing Cu content in films annealed at 500°C (see Figure 3.4). The difference in hardness becomes prominent in the range 13 – 20.4 at.% Cu, where the nature of precipitates play also an important role in the deformation behaviour of the structure of the grain interior in response to stress.

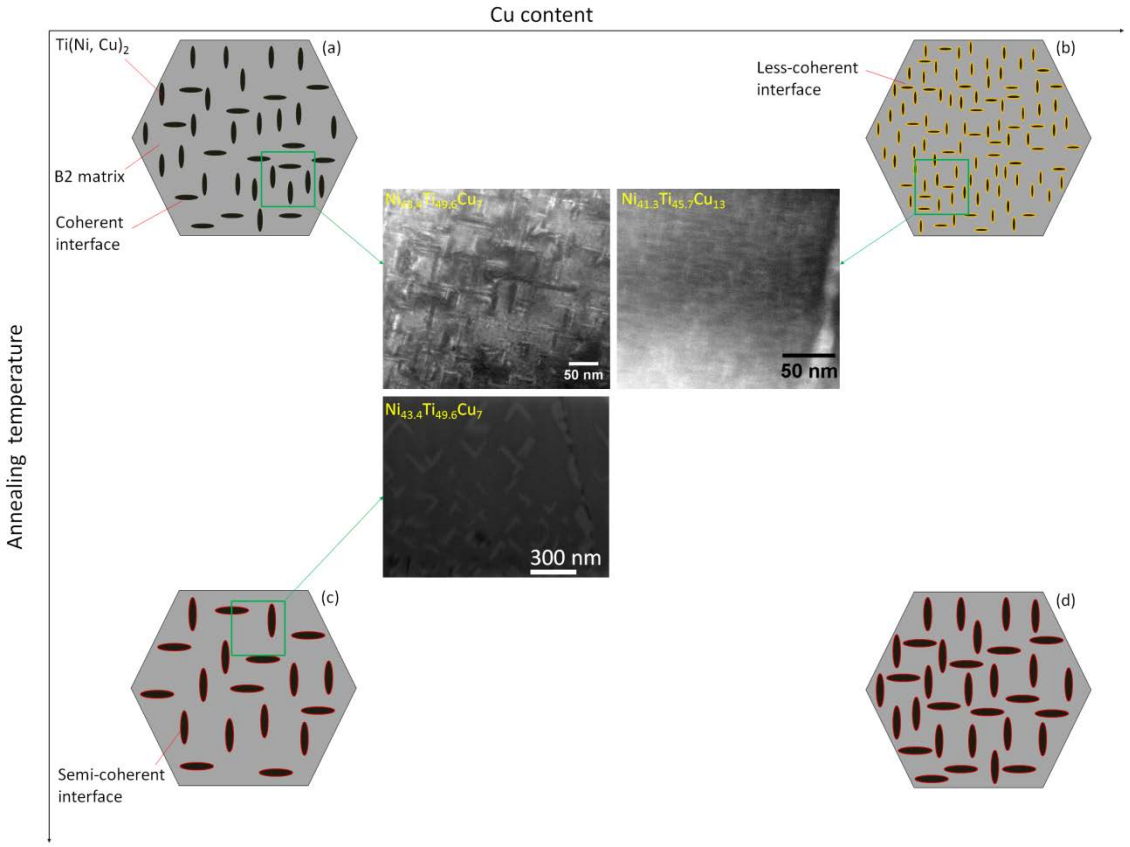

Figure 3.18 – Schematic representation (arbitrary shapes and precipitates distribution) with associated micrographs of the microstructural evolution of the Ti(Ni, Cu)$_2$ plate precipitates, formed in the grain interior of Ni-Ti-Cu thin films, in relation to the Cu content and annealing temperature: (a) for lower Cu content and lower annealing temperature plate precipitates homogenously distributed in the B2 matrix exhibit a coherent interface; (b) for higher Cu content at lower annealing temperature the plate precipitates become more finely and densely distributed in the B2 matrix; (c) for lower Cu content and higher annealing temperature less densely distributed coarsened plate precipitates with a semi-coherent interface are formed in the B2 matrix; (d) for both high Cu content and annealing temperature densely distributed semi-coherent and coarsened plate precipitates are formed in the B2 matrix. The "less-coherent" interface is an intermediate condition between coherency and semi-coherency.

The elastic moduli for the films annealed at different temperatures and doped with Cu are reported in Figure 3.17 b. These results suggest that the Young's modulus increases with increasing Cu content owing to the induced grain refinement. On the other hand, no significant effects of the annealing temperature are observed in Figure 3.17 b, as the two curves are almost superimposed. The average elastic moduli reported in this study for the Ni-Ti films annealed at 500 and 600°C are close to those reported in other studies [23, 25] for austenitic and martensitic Ni-Ti thin films, respectively. However, the error bars associated with the elastic moduli in Figure 3.17 b are almost superimposed, making it difficult to distinguish and explain the differences on the elastic modulus of the binary Ni-Ti system.

Generally, it is observed that doping with an amount of Cu below 4 at.% does not produce significant changes in mechanical properties while when the Cu content is increased above this threshold a clear increase in elastic modulus is observed and associated with both grain refinement and the constraining effect of neighbouring grains, which limit the deformation during indentation. *Zarnetta et al.* [26] reported an average elastic modulus of approximately 115 GPa for a $Ti_{48}Ni_{42}Cu_{10}$ film, ~ 600 nm thick, annealed in vacuum for 1 hour at 500°C. In this study a lower average value (~ 95 GPa) is measured for the NiTiCu4 film annealed at 500°C. This difference is attributed to smaller and equiaxed grains as well as to the very high precipitate/grain size ratio[5] found in the film mentioned above compared to those investigated in this study.

[5] Size of the plate precipitates in relation to the grain size.

References

[1] S. Miyazaki, Y. Fu and W. Huang, Thin film shape memory alloys: fundamentals and device applications, Cambridge (UK): Cambridge University Press, 2009.

[2] Y. Q. Fu, S. Sanjabi, Z. H. Barber, T. W. Clyne, W. M. Huang, M. Cai, J. K. Luo, A. J. Flewitt and W. I. Milne, "Evolution of surface morphology in TiNiCu shape memory thin films," *Applied Physics Letters,* vol. 89, no. 17, 2006.

[3] K. Otsuka and C. Wayman, Shape Memory Materials, Cambridge: Cambridge University Press, New York, 1998.

[4] A. Ishida, M. Sato and S. Miyazaki, "Mechanical properties of Ti–Ni shape memory thin films formed by sputtering," Vols. 273-275, pp. 754-757, 1999.

[5] P. Surbled, C. Clerc, B. L. Pioufle, M. Ataka and H. Fujita, "Effect of the composition and thermal annealing on the transformation temperatures of sputtered TiNi shape memory alloy thin films," *Thin Solid Films,* vol. 401, no. 1-2, pp. 52-59, 2001.

[6] K. Otzuka and X. Ren, "Physical metallurgy of Ti-Ni-based shape memory alloys," *Progress in Materials Science,* vol. 50, pp. 511-678, 2005.

[7] J. Chu, Y. Lai, T. Lin and S. Wang, "Deposition and characterization of TiNi-base thin films by sputtering," *Materials Science and Engineering: A,* vol. 277, no. 1-2, pp. 11-17, 2000.

[8] H. D. Y. Fu, "Relaxation and recovery of stress during martensite transformation for sputtered shape memory TiNi film," *Surface and Coatings Technology,* vol. 153, no. 1, pp. 100-105, 2002.

[9] S. Sanjabi, S. Sadrnezhaad, K. Yates and Z. Barber, "Growth and characterization of TixNi1−x shape memory thin films using simultaneous sputter deposition from separate elemental targets," *Thin Solid Films,* vol. 491, no. 1-2, pp. 190-196, 2005.

[10] A. Ishida, M. Sato, K. Ogawa and K. Yamada, "Shape memory behavior of Ti–Ni–Cu thin films," *Materials Science and Engineering: A,* Vols. 438-440, pp. 683-686, 2006.

[11] S. Sanjabi and Z. Barber, "The effect of film composition on the structure and mechanical properties of NiTi shape memory thin films," vol. 204, no. 8, pp. 1299-1304, Surface and Coatings Technology.

[12] Z. Gao, M. Sato and A. Ishida, "Formation of B19' martensite in annealed Ti44.6Ni40.1Cu15.3 thin films and their shape recovery characteristic," *Journal of Alloys and Compounds,* vol. 505, no. 1, pp. 81-85, 2010.

[13] A. Ishida, M. Sato and K. Ogawa, "Microstructure of annealed Ti48.5Ni(51.5–x)Cux (x=6.2–33.5) thin films," *Philosophical Magazine,* vol. 88, no. 16, pp. 2427-2438, 2008.

[14] A. ISHIDA and M. SATO, “Microstructure and shape memory behaviour of annealed Ti51.5Ni(48.5-x)Cux (x=6.5–20.9) thin films,” *Philosophical Magazine,* vol. 87, no. 35, pp. 5523-5538, 2007.

[15] Z. Gao, M. Sato and A. Ishida, “Formation of B19’ martensite in annealed Ti44.6Ni40.1Cu15.3 thin films and their shape recovery characteristic,” *Journal of Alloys and Compounds,* vol. 505, no. 1, pp. 81-85, 2010.

[16] A. Ishida and M. Sato, “Thickness effect on shape memory behaviour of Ti-50at.%Ni thin film,” *Acta Materialia,* vol. 51, pp. 5571-5578, 2003.

[17] K. Ogawa, T. Kikuchi, S. Kajiwara, T. Matsunaga and S. Miyazaki, “Coherent Subnanometric Plate Precipitates Formed during Crystallization of As-Sputtered Ti-Ni films,” *Journal of Physics IV,* vol. C5, no. 7, pp. 221-226, 1997.

[18] T. Waits, V. Kazykhanov and H. P. Karnthaler, “Martensitic phase transformations in nanocrystalline NiTi studied by TEM,” *Acta Materialia,* vol. 51, pp. 137-147, 2004.

[19] W. D. B. and C. C. Barry, Transmission Electron Microscopy: A Textbook for Materials Science, 2nd ed., New York, USA: Springer, 2009.

[20] X. Meng, M. Sato and A. Ishida, “Structure of martensite in sputter-deposited (Ni,Cu)-rich Ti–Ni–Cu thin films containing Ti(Ni,Cu)2 precipitates,” *Acta Materialia,* vol. 57, no. 5, pp. 1525-1535, 2009.

[21] T. Fukuda, T. Kakeshita and T. Saburi, “Copper content dependence of the lattice parameters of Ti(Ni, Cu)2,” *Materials Transactions,* vol. 41, no. 7, pp. 837-840, 2000.

[22] J. Zhang, M. Sato and A. Ishida, “Influence of Guinier-Preston zones on deformation in Ti-rich Ti-Ni thin films,” *Philosophical Magazine Letters,* vol. 82, no. 5, pp. 257-264, 2002.

[23] X. Huang, J. Nohava, B. Zhang and A. Ramirez, “Nanoindentation of NiTi shape memory thin films at elevated temperatures,” *International Journal of Smart and Nano Materials,* vol. 2, no. 1, pp. 39-49, 2011.

[24] A. Ishida and M. Sato, “Microstructures of crystallized Ti51.5Ni48.5−xCux (x = 23.4–37.3) thin films,” *Intermetallics,* vol. 19, no. 7, pp. 900-907, 2011.

[25] P. Tall, S. Ndiaye, A. Beye, Z. Zong, W. Soboyejo, H.-J. Lee, A. Ramirez and K. Rajan, “Nanoindentation of Ni–Ti Thin Films,” *Materials and Manufacturing Processes,* vol. 22, no. 2, pp. 175-179, 2007.

[26] R. Zarnetta, S. Kneip, C. Somsen and A. Ludwig, “High-throughput characterization of mechanical properties of Ti–Ni–Cu shape memory thin films at elevated temperature,” *Materials Science and Engineering: A,* vol. 528, no. 21, pp. 6552-6557, 2011.

Chapter 4 GRAIN REFINEMENT IN Cu-DOPED Ni-Ti THIN FILMS♦

4.1 Chapter summary

The mechanism of grain refinement as a function of copper content in Ni-Ti-Cu thin films is investigated by (scanning) transmission electron microscopy (STEM). Sputter deposited (Ni,Cu)-rich Ni-Ti-Cu thin films exhibit a columnar structure consisting of grains whose lateral size decreases with increasing Cu content. Cu-rich grain boundary segregation is found to become prominent in films containing higher Cu contents. This segregation is attributed to a non-polymorphic crystallisation, which consists of two steps: diffusion across a transition volume surrounding the growing grains followed by crystallisation at the interface between the transition volume and the already crystallised structure. The smaller grain size observed in films containing higher Cu at.% is attributed to the greater amount of excess atoms that have to diffuse before the crystallisation can take place. A simple model describing such a crystallisation process is proposed in this study.

♦ Published as: M. Callisti, B. G. Mellor, T. Polcar, "Microstructural investigation on the grain refinement occurring in Cu-doped Ni-Ti thin films", Scripta Materialia 77 (2014) 52-55.

4.2 Results and discussion

Three (Ni,Cu)-rich Ni-Ti-Cu thin films (~ 1.4 µm thick) were deposited with an approximately constant Ni/Ti ratio and different Cu contents with the resulting following chemical compositions: $Ni_{43.4}Ti_{49.6}Cu_7$, $Ni_{42.2}Ti_{47.9}Cu_{9.9}$ and $Ni_{38.1}Ti_{44.4}Cu_{17.5}$. The reference binary composition used as a base system to be doped by Cu is a Ti-rich composition ($Ni_{48.1}Ti_{51.9}$), which is mostly austenitic at ambient temperature (see chapter 3). The as-deposited films show a fully amorphous and homogeneous structure. After annealing, the $Ni_{48.1}Ti_{51.9}$ film exhibits an average lateral grain size about three times larger than the film thickness (see chapter 3 for further details). It indicates that grain growth is obstructed by both the film/substrate interface and the film free surface, while lateral growth takes place till neighbouring grains impinge each other (two-dimensional growth), as also found by A. Ishida et al. [1]. Much narrower columnar grains are clearly observed in Cu-doped Ni-Ti films, which exhibit an austenitic structure (see chapter 3). In particular, the average lateral grain size (L) scales with Cu content according to an exponential model ($L = A \cdot e^{-\frac{X}{t}} + B$, with constants A = 3400, t = 3.4 and B = 200; X is the Cu content in at.%). Thus, a significant grain size refinement compared to the binary system is induced in films with high Cu content (i.e., L = 220 nm → 17.5 at.% Cu).

In all the Ni-Ti-Cu films many small and randomly distributed grains (10 – 40 nm) are observed close to the film free surface (Figure 4.1), since the free surface is the most energetic location for crystal nucleation [2]. Such a heterogeneous crystallisation process was reported also for a near-equiatomic Ni-Ti film [3], although not as pronounced as for the Ni-Ti-Cu reported here. These nano-grains close to surface are more densely distributed in films with higher Cu content. Larger columnar grains, whose lateral size (L) is strongly affected by Cu content, grow normal to the free surface just below the nano-grains referred to above.

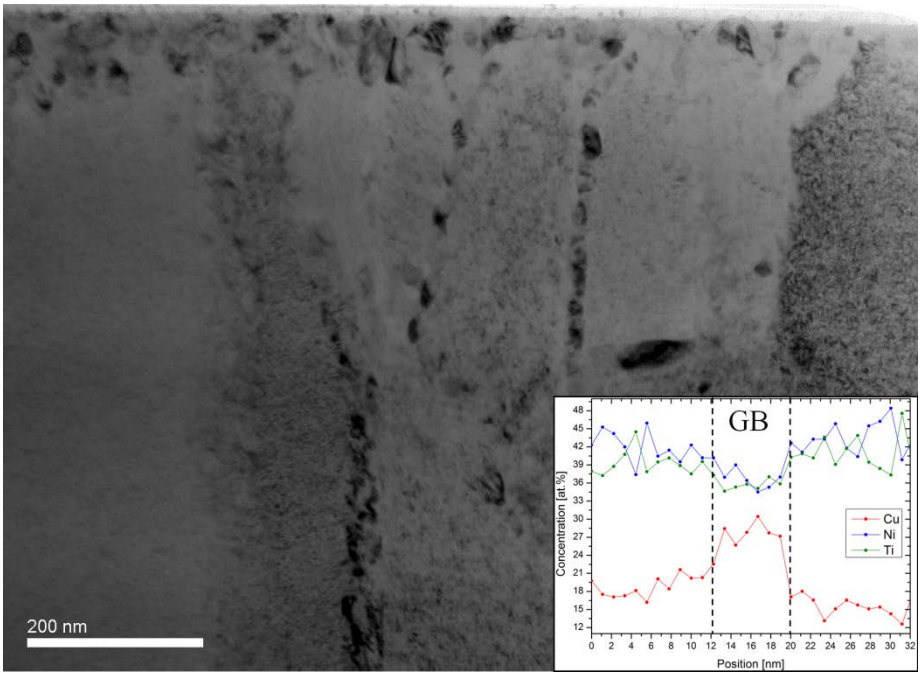

Figure 4.1 – Bright Field TEM image of the $Ni_{42.2}Ti_{47.9}Cu_{9.9}$ thin film; the inset shows the chemical composition across the grain boundary (GB).

The grain boundaries with a thickness of 10 – 30 nm are clearly visible in Figure 4.1. Several particles are distributed along the grain boundary and the higher contrast suggests an enrichment of heavier atoms within the particles. In fact, EDX measurements (inset in Figure 4.1 shows a representative case) performed across the grain boundary reveals Cu enrichment, while almost no changes in Ni and Ti content are observed. It indicates that during the crystallisation process Cu atoms are preferentially segregated to the grain boundary.

Figure 4.2 shows a representative case of the grain boundary for the $Ni_{43.4}Ti_{49.6}Cu_7$ film. In order to characterise the grain boundary microstructure, Fast Fourier Transform (FFT) is performed in different areas across the grain boundary and within the adjacent grains. The grain interior (Figure 4.2 I) as well as the grain boundary particles (Figure 4.2 II) exhibit a fully crystalline structure (see related FFTs). These particles are embedded in a composite structure consisting of randomly oriented nano-crystalline domains surrounded by an amorphous matrix (Figure 4.2 III, IV). Although a partial coherency is observed at the interface between this specific particle and the adjacent grain (larger particle in Figure 4.2), the formation of these crystalline particles is not correlated to the crystallisation of the B2 structure within the grains. This might suggests that a secondary crystallisation takes place along the grain

boundary once they are formed, although a partially amorphous boundary structure is almost always observed.

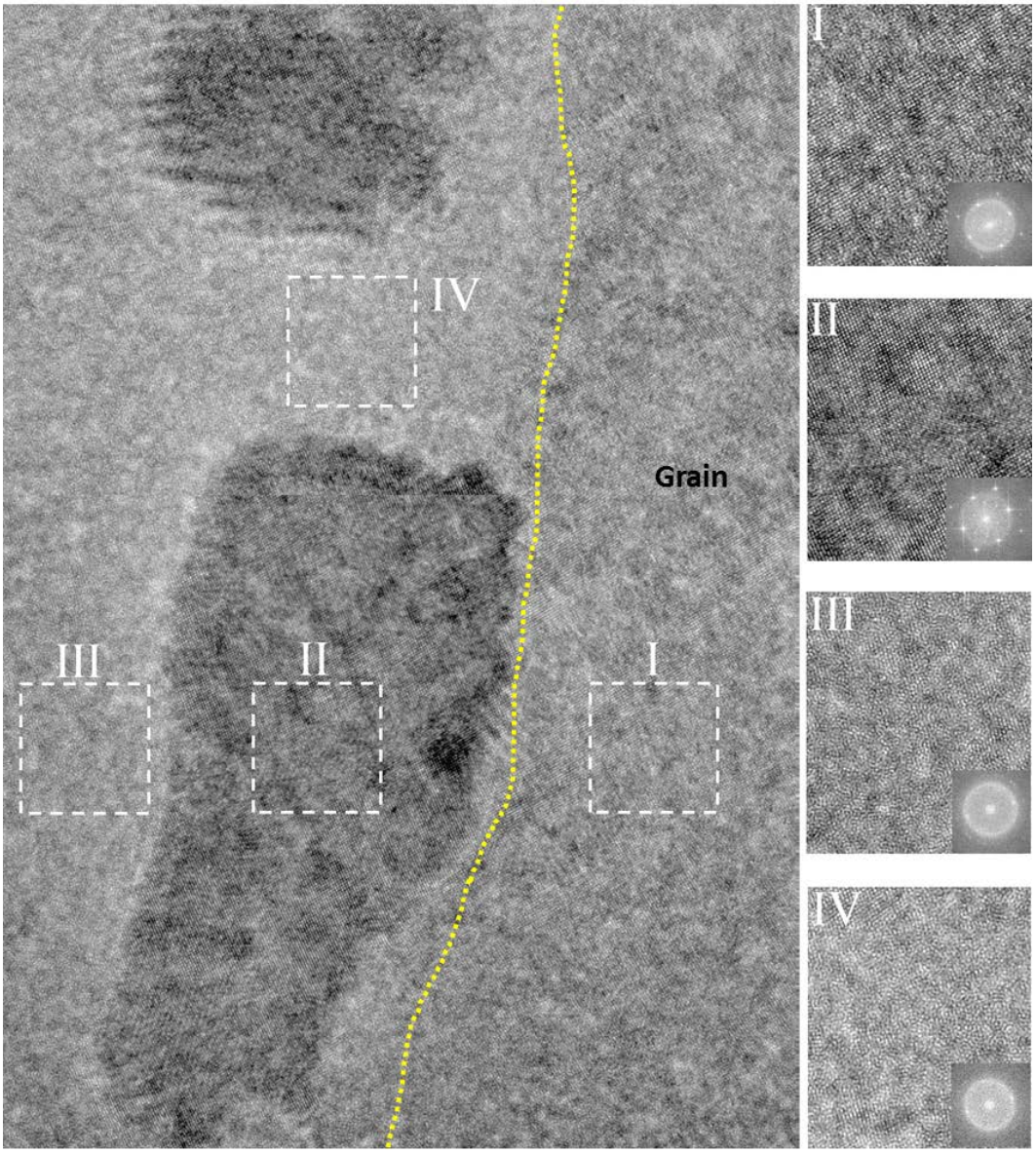

Figure 4.2 – High resolution TEM image along grain boundary in the $Ni_{43.4}Ti_{49.6}Cu_7$ thin film annealed for 1 hour at 500°C. The yellow line indicates the interface between the grain and the grain boundary. FFT was performed in different areas as follow: (I) grain interior, (II) Cu-rich particle, (III)-(IV) grain boundary.

Y. Xu et al. [4] reported that a small Cu addition (1.3 at.%) in Ni-Ti-Cu films did not produce any significant change in the crystallisation temperature and in the overall activation energy compared to pure Ni-Ti films. However, *in-situ* TEM observations suggested that Cu addition may decrease the activation energy for crystal growth and increase it for nucleation [4]. Therefore, the Cu enrichment observed along the grain boundary (inset in Figure 4.1) can alter the kinetics of crystallisation of the amorphous structure observed in Figure 4.2, although its effect is not clearly understood.

Plate-like precipitates are found in the grain interior of the Ni-Ti(-Cu) after the heat treatment (see chapter 3 for details on microstructure). Therefore, the annealing has not been sufficient to promote long range diffusion and metastable precipitates are formed in the grains interior as also reported in other studies [9, 10, 11].

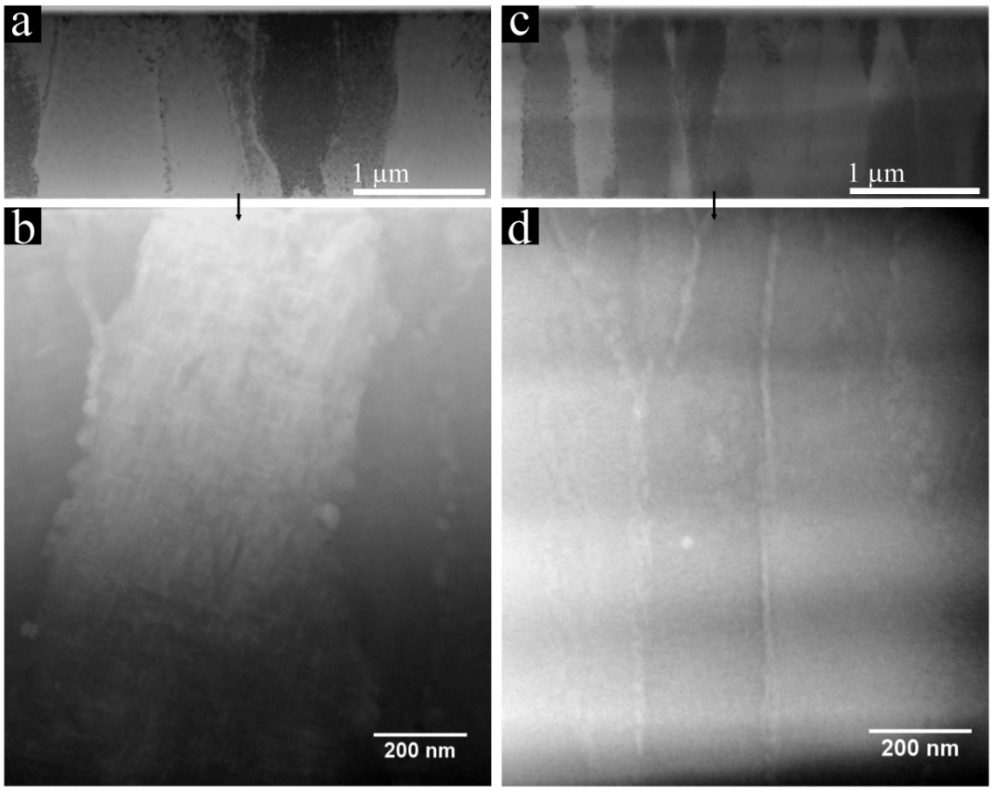

Figure 4.3 – Cross-sectional High Angle Annular Dark Field (HAADF) TEM images of the (a) $Ni_{43.4}Ti_{49.6}Cu_7$ and (c) $Ni_{42.2}Ti_{47.9}Cu_{9.9}$ thin film together with corresponding HAADF images of the films showing different grain boundary morphologies.

These precipitates are found to be $Ti(Ni,Cu)_2$ for (Ni,Cu)-rich Ni-Ti-Cu compositions. According to Ostwald's step rule [2] and to the precipitation process occurring in Ni-Ti-Cu thin films (for annealing temperature in the range 500 – 700°C) [8, 5, 6], it is deduced that the formation of prominent grain boundary precipitates represents the last steps of the precipitation process to occur when Ni-Ti(-Cu) compositions are annealed at a temperature well above that of crystallisation, i.e. above 700°C. The Ni-Ti(-Cu) films studied here are annealed at a temperature very close to the narrow range of crystallisation temperatures reported for Ni-Ti(-Cu) compositions in independent studies [9, 10, 11]. Therefore we can conclude here that the co-existence

of the $Ti(Ni,Cu)_2$ plate precipitates in the grain interior and the segregation at the grain boundaries is not a consequence of the precipitation process.

H. Ni et al. performed an *in-situ* TEM investigation to study the crystallisation behaviour of amorphous Ni-Ti thin films [12]. They reported that stoichiometric binary Ni-Ti films underwent a polymorphic crystallisation, while a more complex behaviour took place in off-stoichiometric compositions owing to the formation of precipitates, which made the crystallisation process sluggish. In our Ni-Ti-Cu films, the presence of a relatively large number of Cu-rich particles at the grain boundaries leads us to conclude that, in contrast to near-equiatomic Ni-Ti films [12], the crystallisation process in Cu-doped Ni-Ti film is not polymorphic.

In such a non-polymorphic crystallisation process, diffusion followed by grain growth plays an important role in the grain refinement observed in Cu-doped Ni-Ti films. In particular, a transition volume covering the growing crystal (i.e. shell-like structure) forms and hence separates the growing crystal itself from the surrounding amorphous structure as shown schematically in Figure 4.4 b. Within this transition volume diffusion of Ni, Ti and Cu atoms is required to start the crystallisation process. Such a two-step mechanism consisting of diffusion followed by the formation of new crystals decreases the grain growth rate and prevents grain coarsening. Based on this mechanism and on TEM observations (Figure 4.1), the crystallisation occurring in Ni-Ti-Cu thin films can be subdivided in three stages. In the first stage several nano-grains nucleate underneath the film free surface (Figure 4.4 a), surrounded by an amorphous-like structure. In the second stage plate-like grains grow laterally till their transition volumes impinge on each other (i.e. soft impingement – for more details see Ref. [13]) as schematically reported in Figure 4.4 c. At this stage, the expected slower grain growth rate, owing to the above reported two-step process, is the cause of the formation of several smaller grains rather than a few very large grains like those observed for the $Ni_{48.1}Ti_{51.9}$Ni-Ti film.

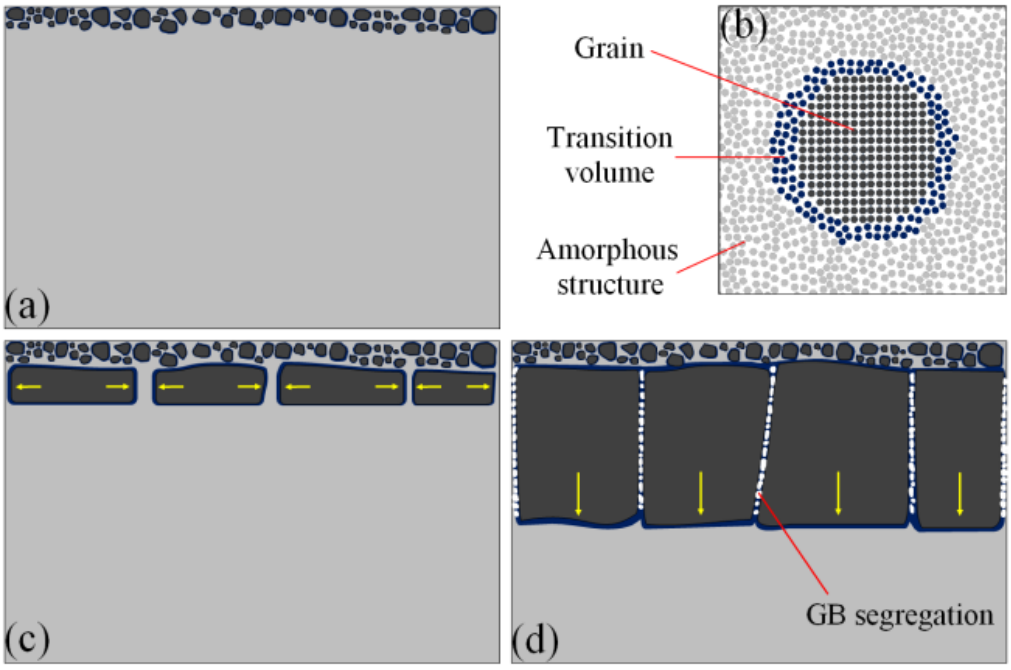

Figure 4. 4 – Schematic representation (arbitrary shapes) of the non-polymorphic crystallisation taking place in Ni-Ti-Cu thin films. The formation of nano-grains at the film free surface and of Cu-rich grain boundary precipitates is enhanced for higher Cu content in the as-deposited film.

After the impingement, the third stage, i.e. grain growth normal to the film free surface (Figure 4.4 d), becomes prominent promoting the formation of columnar grains. During this growth the transition volume surrounding the growing grains, particularly at the interface with neighbouring grains, is likely to mitigate the competitive grain growth mechanism, which is observed in the early stage of columnar grain growth close to the film free surface (Figure 4.3 b and d). This encourages the formation of grains of similar size across the film thickness.

The grain boundary morphology and size depends on Cu content as demonstrated in Figure 4.3, where the films containing 7 and 9.9 at. % Cu (referred as Cu-poor and Cu-rich respectively) are compared. The Cu-poor film exhibits a discontinuous distribution of spherical Cu-rich particles with an average diameter of ~ 25 nm (Figure 4.3 b) along the grain boundaries.

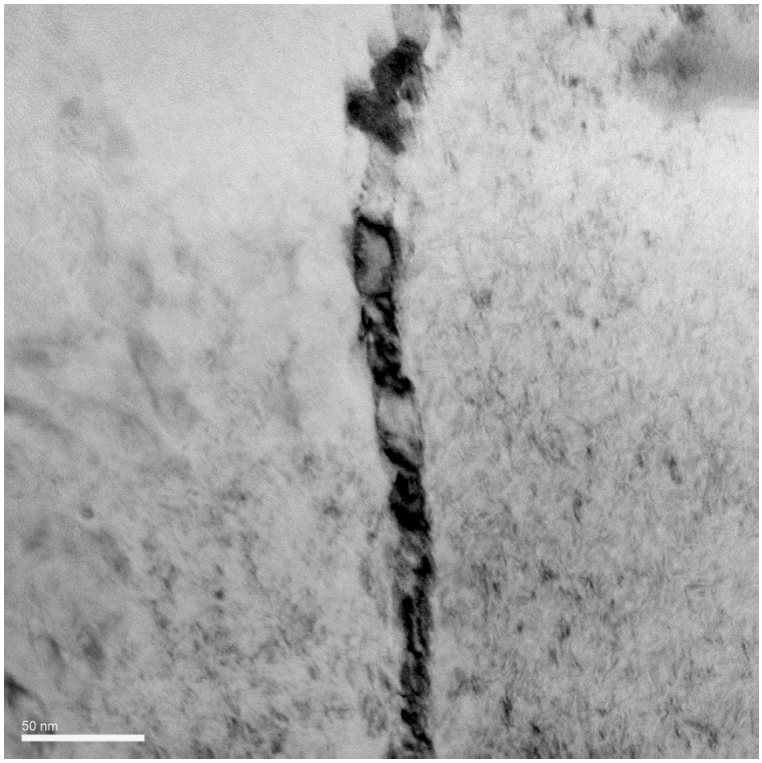

Figure 4.5 –Bright Field TEM image along one of the grain boundaries formed in the $Ni_{42.2}Ti_{47.9}Cu_{9.9}$ thin film annealed for 1 hour at 500°C; a continuous chain of Cu-rich particles is formed along the grain boundary.

On the contrary, the Cu-rich film shows continuous chains of Cu-rich particles, which exhibit an elongated shape along the grain boundary with an average size ~ 14 nm, as can be clearly seen in Figure 4.5. This suggests that diffusion of a greater amount of Cu atoms takes place within the transition volume during grain growth in films richer in Cu, which further limits the grain boundary movement and thus promotes the observed grain refinement.

References

[1] A. Ishida and M. Sato, “Thickness effect on shape memory behavior of Ti-50.0at.%Ni thin film,” *Acta Materialia,* vol. 51, no. 18, pp. 5571-5578, 2003.

[2] E. Machelin, An Introduction to Aspects of Thermodynamics and Kinetics Relevant to Materials Science, t. ed., Ed., Oxford: Elsevier, 2007.

[3] M. Vestel, D. Grummon, R. Gronsky and A. Pisano, “Effect of temperature on the devitrification kinetics of NiTi films,” *Acta Materialia,* vol. 51, no. 18, pp. 5309-5318, 2003.

[4] Y. Xu, X. Huang and A. Ramirez, “Y. Xu, X. Huang, A.G. Ramirez,” *Journal of Alloys and Compounds,* vol. 480, no. 2, pp. L13-L16, 2009.

[5] A. Ishida and M. Sato, “Microstructures of crystallized Ti51.5Ni48.5−xCux (x = 23.4–37.3) thin films,” *Intermetallics,* vol. 19, no. 7, pp. 900-907, 2011.

[6] A. Ishida, M. Sato and K. Ogawa, “Microstructure of annealed Ti48.5Ni(51.5– x)Cu x (x = 6.2–33.5) thin films,” *Philosophical Magazine,* vol. 88, no. 16, pp. 2427-2438, 2008.

[7] A. Ishida and M. Sato, “Microstructure and shape memory behaviour of annealed Ti51.5Ni(48.5- x)Cu x (x = 6.5–20.9) thin films,” *Philosophical Magazine,* vol. 87, no. 35, pp. 5523-5538, 2007.

[8] X. Meng, M. Sato and A. Ishida, “Structure of martensite in Ti-rich Ti–Ni–Cu thin films annealed at different temperatures,” *Acta Materialia,* vol. 56, no. 14, pp. 3394-3402, 2008.

[9] J. Chen, S. Wu and J. Non-Cryst, “Crystallization temperature and activation energy of rf-sputtered near-equiatomic TiNi and Ti50Ni40Cu10 thin films,” *Journal of Non-Crystalline Solids,* vol. 288, no. 1-3, pp. 159-165, 2001.

[10] P. Hsu and J. Ting, “Growth and characteristics of TiNiCu thin films,” *Thin Solid Films,* Vols. 420-421, pp. 524-529, 2002.

[11] H. Ni, H. Lee and A. Ramirez, “Compositional Effects on the Crystallization Kinetics of Nickel Titanium Thin Films,” *Journal of Materials Research,* vol. 20, no. 7, pp. 1728-1734, 2005.

[12] J. d. C. Teixeira, D. Cram, L. Bourgeois, T. Bastow, A. Hill and C. Hutchinson, “On the strengthening response of aluminum alloys containing shear-resistant plate-shaped precipitates,” *Acta Materialia,* vol. 56, no. 20, pp. 6109-6122, 2008.

[13] J. d. C. Teixeira, D. G. Cram, L. Bourgeois, T. J. Bastow, A. J. Hill and C. R. Hutchinson, “On the strengthening response of aluminum alloys containing shear-resistant plate-shaped precipitates,” *Acta Materialia,* vol. 56, pp. 6109-6122, 2008.

Chapter 5 MECHANICAL PROPERTIES AND NANO-SCRATCH BEHAVIOUR OF W-S-C/Ni-Ti(-Cu) BILAYERS♥

5.1 Chapter summary

A self-lubricant W-S-C coating with different Ni-Ti(-Cu) interlayers is fabricated by magnetron sputtering following a three-step process. It consists of deposition and annealing of Ni-Ti(-Cu) layers with different Cu content and subsequent deposition of the transition metal dichalcogenide W-S-C coating bonded to the Ni-Ti(-Cu) layer through a gradient Cr-based thin layer. Doping the Ni-Ti interlayer with Cu leads to significant microstructural changes which influence mechanical properties, such as the H/E_r ratio and the resistance against plastic deformation. The response of the bilayers, i.e. W-S-C/Ni-Ti(-Cu) coatings, to indentation is affected by the interlayer material. The resistance to adhesion damage of the W-S-C coating is improved by using Ni-Ti(-Cu) interlayers. It is found that interlayers with lower H/E_r ratio show an improved capability to increase the adhesion of the functional top layer. The different response of the bilayers to the indentation process as well as to the scratch is attributed to the different grain sizes in the Cu-doped Ni-Ti layers. For interlayers with larger grains less energy is required to activate the stress-induced martensitic transformation in the grain interior. On the contrary, for interlayers with smaller grains the austenite-to-martensite phase transformation is limited and part of the deformation is accommodated by the elastic deformation of the austenitic phase before adhesion failure. Based on the presented results, a Ni-Ti-Cu interlayer with a grain size ranging between 0.5 – 1 μm represents a good compromise between resistance to adhesion damage and strain recovery.

♥ Expanded from: M. Callisti, T. Polcar, "The role of Ni-Ti(-Cu) interlayers on the mechanical properties and nano-scratch behaviour of solid lubricant W-S-C coatings", 2014, 10.1016/j.surfcoat.2014.06.028.

5.2 Coatings composition

The Ni-Ti thin films are deposited with different Cu contents in the range 0 – 17.5 at.% (their chemical composition is summarised in Table 5.I) with a thickness of ~ 1.4 µm. EDX measurements show that the amount of Ni and Ti decreases proportionally with increasing Cu content. $Ni_{48.1}Ti_{51.9}$ and $Ni_{45.1}Ti_{52.5}Cu_{2.4}$ are Ti-rich compositions, whereas further increase in Cu leads to (Ni, Cu)-rich coatings.

Table 5.I – Average chemical composition of the as-deposited Ni-Ti-Cu thin films measured by EDX with an error of ±0.2 at.%.

Layers	***Chemical composition [at.%]***				***H [GPa]***	***E [GPa]***
	Ni	**Ti**	**Cu**	**Ti/Ni**		
Ni-Ti	48.1	51.9	0.0	1.08	2.1	63.1
Ni-Ti-Cu 1	45.1	52.5	2.4	1.16	1.9	60.0
Ni-Ti-Cu 2	46.2	49.4	4.4	1.07	2	51.7
Ni-Ti-Cu 3	43.4	49.6	7.0	1.14	3.7	67.1
Ni-Ti-Cu 4	42.2	47.9	9.9	1.14	5	77.2
Ni-Ti-Cu 5	38.1	44.4	17.5	1.17	6.7	128.5

The as-deposited coatings are amorphous and exhibit a dense, homogeneous and featureless cross-sectional morphology. After annealing in a high vacuum furnace and plasma etching, the Ni-Ti(-Cu) substrates are coated by a 250 nm thick bonding layer, i.e. Cr layer with an increasing amount of W-S-C. Finally, the W-S-C top layer is deposited with a resulting thickness of 1.15 µm. EDX measurements performed on the W-S-C layer revealed the following chemical composition: 29.0 at.% C, 41.9 at.% S, 23.7 at.% W and 5.4 at.% O, with an error of ±0.5 at.%. From cross-sectional FEG-SEM micrographs, the as-deposited W-S-C layer exhibited a homogeneous and featureless cross-sectional morphology. Bilayers are characterised by a total thickness of ~ 2.8 µm. The average surface roughness of the bilayers, measured by an optical surface profiler (Zygo NewView 7200) on a length of 1.4 mm, ranged between 1 – 3 nm.

5.3 Microstructure

Figure 5.1 displays the X-ray diffractograms of some representative cases of the Ni-Ti(-Cu) films to show how the microstructure changes in relation to the chemical composition. The $Ni_{48.1}Ti_{51.9}$ film, although Ti-rich composition (Ti/Ni ≈ 1.08), exhibits a predominant austenitic phase (B2). The presence of austenite is ascribed mostly to a change of the Ti/Ni ratio in the matrix owing to the formation of Ti_2Ni precipitates, as found in the XRD pattern and also by TEM analyses (see chapter 3). However, some small martensitic (B19') peaks are found in the diffractogram as well.

In the $Ni_{45.1}Ti_{52.5}Cu_{2.4}$ film the Ti content is still above 50 at.%, while the Ni content is decreased (Ti/Ni ≈1.16) compared to the $Ni_{48.1}Ti_{51.9}$ composition. As a consequence the presence of martensitic peaks in the XRD pattern for $Ni_{45.1}Ti_{52.5}Cu_{2.4}$ is much more pronounced compared to the undoped $Ni_{48.1}Ti_{51.9}$ film.

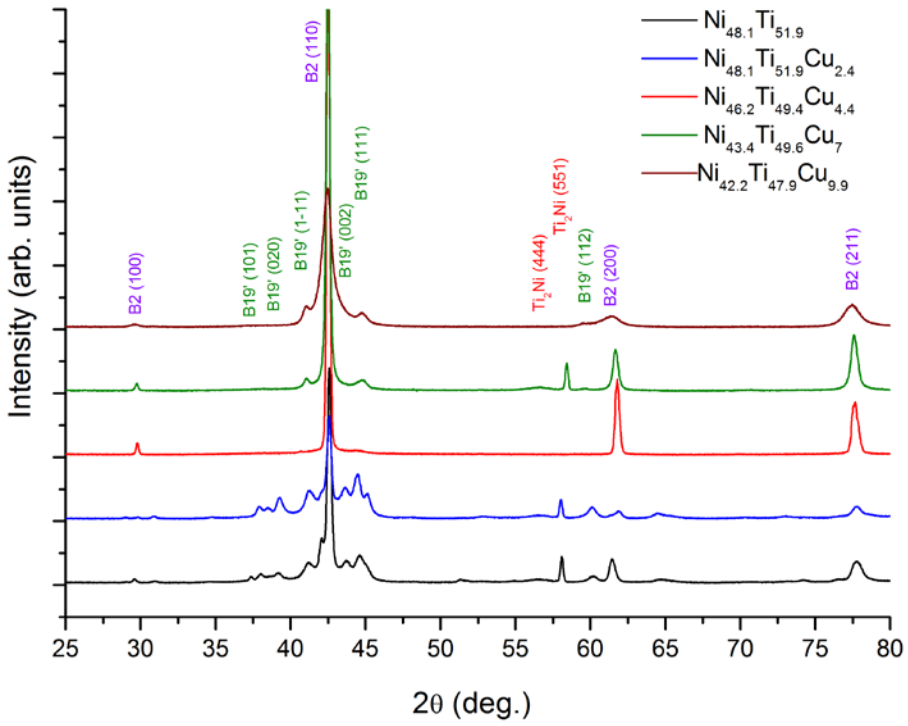

Figure 5.1 – Grazing incidence X-ray diffractograms of Ni-Ti(-Cu) thin films annealed for 1 hour at 500°C; grazing angle ω = 4°.

On the other hand, $Ni_{46.2}Ti_{49.4}Cu_{4.4}$ composition (Ti/Ni ratio of ~ 1.07) exhibits a fully austenitic structure at ambient temperature. With a further increase in Cu content

($Ni_{43.4}Ti_{49.6}Cu_{7.0}$ composition) but with a higher Ti/Ni ratio (~ 1.14) compared to the $Ni_{46.2}Ti_{49.4}Cu_{4.4}$ film, again small traces of martensite (B19') and Ti_2Ni phase appear in the XRD pattern. It is suggested that, compared to the $Ni_{46.2}Ti_{49.4}Cu_{4.4}$ composition, the higher Ti/Ni ratio in $Ni_{43.4}Ti_{49.6}Cu_{7.0}$ contributes to stabilise martensite in the matrix as well as promoting the formation of Ti_2Ni precipitates. With a further increase in Cu content (above 7 at.%), Ti_2Ni precipitates are not detected any more by XRD. Thus, Ti_2Ni phase can be formed in Ni-Ti-Cu systems when the Ti content is $\geq$ 50 at.% or in (Ni, Cu)-rich composition for a Cu content lower than 7 at.% and Ti content between 49.5 – 50 at.%. In chapter 3, we reported that thin $Ti(Ni,Cu)_2$ plate precipitates are also formed during annealing at 500°C in the grain interior of (Ni, Cu)-rich films.

These results are in agreement with the precipitation map suggested by Ishida et al. [1] for annealed sputter-deposited Ni-Ti-Cu films. Cu addition is known to affect slightly the stability of the austenitic (B2) phase [2]; in (Ni, Cu)-rich compositions, with increasing Cu content above 7 at.%, the (110) austenitic peak becomes less intense (Figure 5.1), though it is still the main phase in the films.

By comparing the diffractograms shown in Figure 3.4 (chapter 3) and Figure 5.1 for the $Ni_{43.4}Ti_{49.6}Cu_7$ layer annealed for 1 hour at 500°C, it is seen that a peak (located at $2\theta \approx 58°$) attributed to the Ti_2Ni intermetallic phase appears only in Figure 5.1. As these layers were deposited in the same deposition process but annealed separately, the presence of the Ti_2Ni phase observed in Figure 5.1 is very likely attributed to slightly different heat treatments performed on these layers. In particular heat treatments slightly longer or performed at a slightly higher temperature can encourage the formation of metastable phases in the grain interior (see section 2.4.1 in chapter 1 for details).

The (110) B2 peak slightly shifts to lower angles with increasing Cu content, i.e. $2\theta \approx 42.586°$ for $Ni_{48.1}Ti_{51.9}$, $2\theta \approx 42.510°$ for $Ni_{46.2}Ti_{49.4}Cu_{4.4}$ and $2\theta \approx 42.498°$ for $Ni_{43.4}Ti_{49.6}Cu_{7.0}$. This might be attributed to the solid solution substitution of Ni by Cu atoms in the B2 crystal owing to the chemical affinity of Cu and Ni atoms, which contributes to increase the compressive in-plane stress in the films. In fact, as-

deposited coatings exhibit a compressive in-plane residual stress, which is mitigated when the coatings are annealed[1].

Figure 5.2 (a) shows the XRD pattern of the as-deposited W-S-C single layer, where a loss of crystallinity is observed when compared to the pure WS_2 coatings [3]. A broad peak corresponding to (002) plane of the WS_2 is detected at $2\theta \approx 10°$ (shifted by about 4° compared to the ICDD PDF-2 database), and attributed to the type I structure, i.e. (002) plane perpendicular to the film surface [3]. In the 2θ range between 25 – 60° a broad peak with a long tail toward higher 2θ angles is observed and attributed to a turbostratic stacking of (10*L*) planes (*L* = 1, 2, 3, ..) of the WS_2 phase.

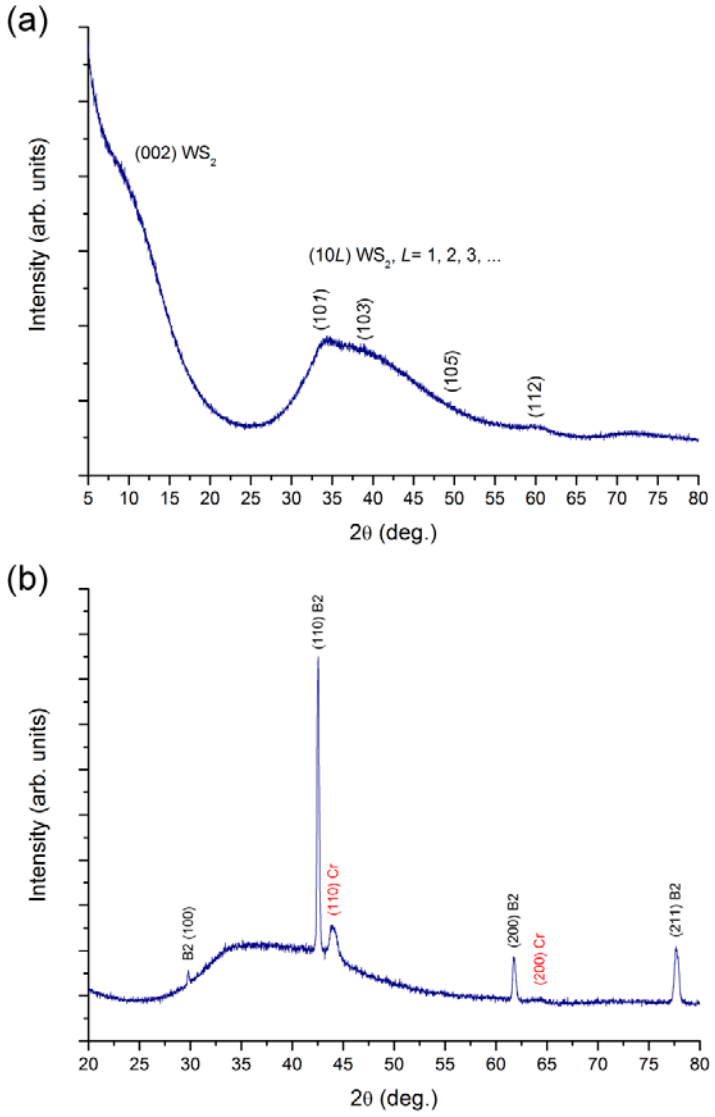

Figure 5.2 – Grazing incidence X-ray diffractogram of the (a) as-deposited W-S-C layer (grazing angle ω = 1°) and of the W-S-C/Cr/$Ni_{46.2}Ti_{49.4}Cu_{4.4}$ bilayer (grazing angle ω = 4°).

[1] Residual stress in the coatings is qualitatively evaluated by observing the bending of the coating attached to a thin aluminium substrate (24 μ m thick).

Some of these (10*L*) are more clearly identified in Figure 5.2 (a), such as: (101) plane around $2\theta \approx 35°$, (103) plane around $2\theta \approx 40°$ and the (105) plane around $2\theta \approx 50°$ followed by a long tail consisting of other peaks associated to the (10*L*) planes for $L > 5$. Some other small peaks, hardly identified, are observed for $2\theta > 60°$.

The XRD patterns of the bilayers consist of a superimposition of a diffractogram shown in Figure 5.1 with that reported in Figure 5.2 (a) with the addition of two peaks attributed to the crystalline Cr bonding layer. In Figure 5.2 (b) a representative diffractogram is shown (W-S-C/Cr/$Ni_{46.2}Ti_{49.4}Cu_{4.4}$), where the (110) peak attributed to the austenitic phase in the superelastic interlayer is superimposed to the broad peak of the W-S-C coating described above.

A microstructural investigation has been also performed by transmission electron microscopy (TEM) in order to assess the microstructure at the interface between layers. Figure 5.3 shows that, despite plasma etching of Ni-Ti(-Cu) layers before the deposition of the Cr layer, a residual thin TiO_2 layer is still present on the surfaces. The Cr layer exhibits a columnar structure with grains extended through the layer thickness (160 nm) and with a diameter ranging between 30 – 40 nm. On top of the Cr layer, the gradient layer about 100 nm thick is clearly observed in the bright field TEM image (Figure 5.3). The W-S-C layer exhibits a nano-composite structure consisting of clusters of heavier elements (black dots), which are supposed to be W-rich domains (possibly WS_2) embedded in the amorphous carbon matrix.

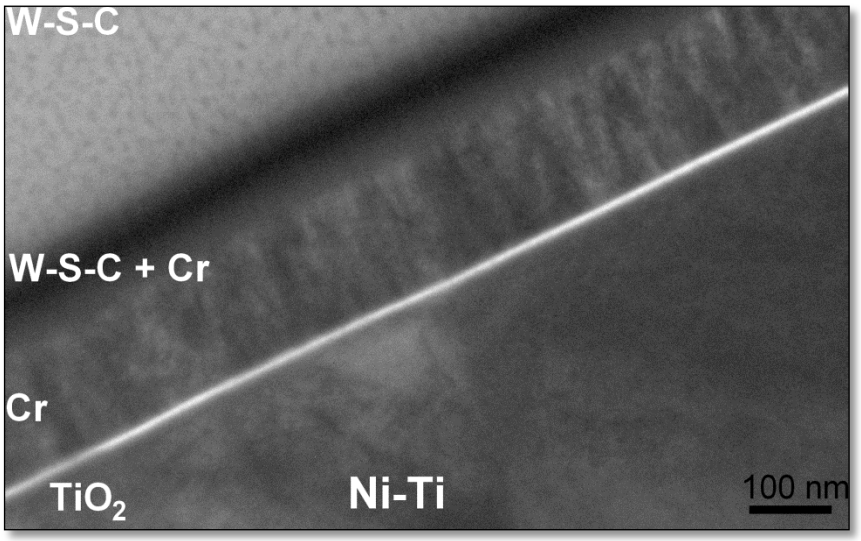

Figure 5.3 – Bright Field TEM image of the W-S-C/Cr/$Ni_{48.1}Ti_{51.9}$ bilayer at the interface between layers.

A detailed description of the Ni-Ti(-Cu) interlayers microstructure can be found in chapter 3 and chapter 4. The TEM analysis is also aimed at assessing the interface between the Ni-Ti(-Cu) layer and the Si substrate. It is observed that during the heat treatment silicides are formed at the interface mostly as the result of diffusion of Ni and Ti atoms toward the Si substrate (see Appendix B for more details). The formation of such a phase is expected to have beneficial effects on the adhesion of the Ni-Ti(-Cu) layers on the Si substrate, without deterioring the functional properties of the Ni-Ti(-Cu) layer itself.

5.4 Mechanical properties

5.4.1 Nanoindentation

The mechanical properties of single layers are measured by nanoindentation and compared for different chemical compositions by evaluating parameters involving hardness (H) and reduced elastic modulus (E_r). It is worth noting that the mechanical properties measured on materials exhibiting stress-induced phase transformation, as is the case of Ni-Ti(-Cu) thin films, result from a complex combination of the parent and native phases involved as well as of the phase transformation itself. The indentation hardness is evaluated through the projected contact area (A_c) at maximum load, where A_c is calculated from the contact depth. Clearly, the displacement measured by instrumented nanoindentation consists of different contributions related to the elastic deformation of austenite, deformation associated with the stress-induced martensitic transformation, and elastic and plastic deformation of martensite. Some pop-in events originating in the phase transformation are observed on the loading curves of Ni-Ti(-Cu) films, thus giving evidence of the stress-induced martensitic transformation taking place underneath the indented surface [4]. Similarly, the reduced elastic modulus is evaluated by the slope of a portion of the unloading curve according to the procedure outlined by Oliver and Pharr [5, 6], where the reversible martensite-to-austenite transformation may take place during the unloading [4].

Therefore, even in this case the resulting elastic modulus is affected by a combination of properties coming from different phases, the stress-induced phase transformation

and the substrate. In this study, our aim is to compare the overall response of these Ni-Ti(-Cu) films to nanoindentation in relation to their microstructure including the microstructural phenomena occurring under stress. Figure 5.4 shows the measured hardness and the lateral grain size measured by TEM (see chapter 3 and chapter 4 for details on microstructure) of the Ni-Ti(-Cu) thin films as a function of the Cu content. The lateral grain size has been further assessed and confirmed by top view FEG-SEM micrographs for coatings with large grains (i.e. Ni-Ti) in order to take into account the fact that the TEM cross-sectional sample does not cut through the diametral plane of the columnar grains, especially when grains are much larger compared to the thickness of the TEM cross-sectional foil.

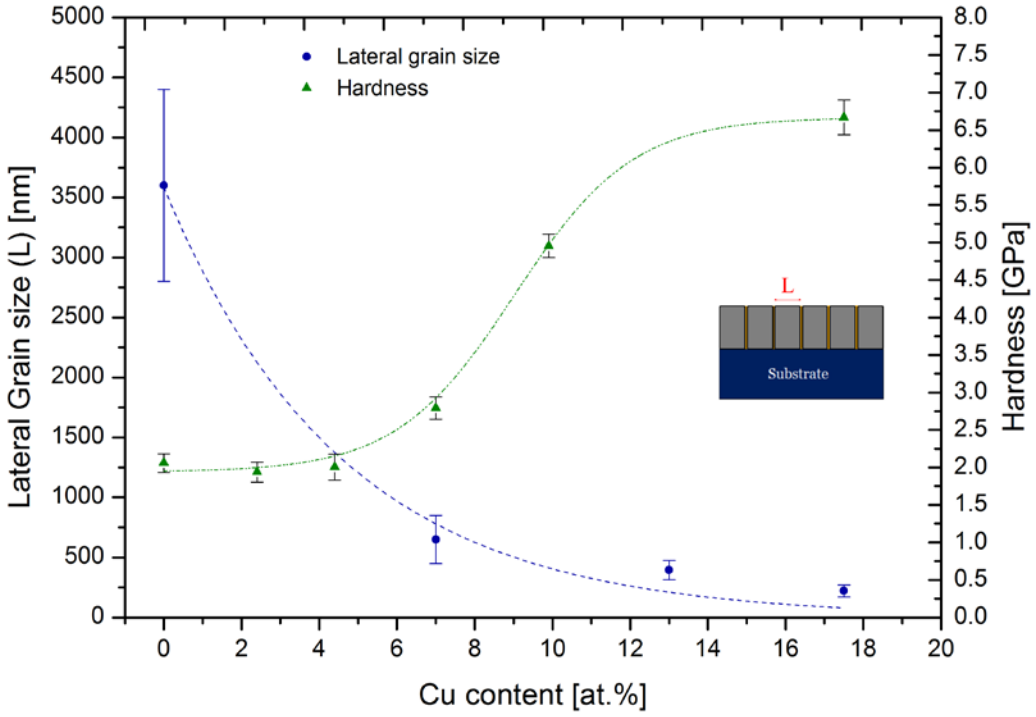

Figure 5.4 – Average lateral grain size (L) and nano-hardness as a function of the Cu content for Ni-Ti(-Cu) thin films annealed for 1 hour at 500°.

The lateral grain size decreases with increasing Cu content following an exponential law. The hardness exhibits a sigmoidal behaviour; for Cu content lower than about 5 at.% no relevant changes are noticed despite the significant decrease in grain size, whereas for a average lateral grain size lower than ~ 700 nm the hardness increases up to ~ 6.6 GPa for the film containing 17.5 at.% Cu.

Assuming a cylindrical shape of the columnar grains, the average cross-sectional size of the grains (A_{grain}) for different Cu contents is calculated and compared to the projected

contact area of the Berkovich tip (A_c), evaluated by the contact depth calculated during the experiments. The hardness increased when A_c and A_{grain} are comparable ($A_c/A_{grain} \approx 0.75$ for 7 at.% Cu). It is suggested that the hardness increase is mostly caused by the constraining effect of the neighbouring grains, which limits the deformation during the indentation process.

Although different types of precipitates (see chapter 3) as well as different amounts of martensite (qualitatively estimated from XRD analyses) are found in the films, their effects on the hardness are expected to be small in comparison to the effects of grain refinement. Similar values of hardness are observed for average grain size larger than 1 μm (Figure 5.4), where the constraining effect from neighbouring grains should be negligible.

The elastic modulus is also affected by the grain size (see Table 5.I), i.e. E increases with decreasing grain size, although not monotonically, especially for low Cu content ($\leq$ 4.4 at.%). In particular, by considering the binary Ni-Ti film as reference, the elastic modulus first decreases probably due to the larger amount of martensite nucleated in the austenitic matrix ($E_A > E_M$ [7]) as a result of Cu addition up to 2.4 at.%. The $Ni_{46.2}Ti_{49.4}Cu_{4.4}$ layer (4.4 at.% Cu), although fully austenitic, exhibits a lower elastic modulus compared to the other films with lower or no Cu content. No significant differences in terms of grain size effects are expected between $Ni_{46.2}Ti_{49.4}Cu_{4.4}$ and the other samples with lower or no Cu content. Therefore, we attribute the lower elastic modulus of $Ni_{46.2}Ti_{49.4}Cu_{4.4}$ to the presence of different types of precipitates in the grains interior compared to films with lower Cu content (see chapter 3). In particular, it is expected that Ti_2Ni spherical precipitates (not detected in $Ni_{46.2}Ti_{49.4}Cu_{4.4}$ layer) prevent martensite plates growth compared to the $Ti(Ni,Cu)_2$ plate precipitates [8, 9], which instead are expected in the $Ni_{46.2}Ti_{49.4}Cu_{4.4}$ layer. The lower elastic modulus measured for the $Ni_{46.2}Ti_{49.4}Cu_{4.4}$ layer may be related to the fact that larger deformation is accommodated when the growth of martensitic plates is not inhibited by the precipitates. It means that the Ti_2Ni spherical precipitates produce a stiffening effect related to the capability of these precipitates to limit the martensitic transformation and promote plastic deformation instead.

Cu content $\geq$ 7 at.% results in pronounced grain refinement and the elastic modulus increases monotonically with decreasing grain size. Recently, it has been reported that

the phase transformation in Ni-Ti thin films is strongly inhibited for a critical grain size in the range 50 – 100 nm [10]. In our case, grains in Cu-rich films are slightly larger compared to above mentioned range; nevertheless, we expect that such inhibition occurs gradually with decreasing grain size. In fact, Zhang et al. [11] found for a Ni-Ti alloy that the stress required to activate the austenite-to-martensite transformation ($\sigma^{A\rightarrow M}$) increased linearly with decreasing grain size from 700 to 50 nm; the observed behaviour was attributed to increased grain boundary density. Therefore, the elastic response of the layer can be affected by the grain size, which in turn affects the phase transformation. In particular, when the phase transformation is limited by the small grain size (high $\sigma^{A\rightarrow M}$), a larger contribution from the austenitic phase to the elastic response of the layer is expected resulting in an increase in the elastic modulus.

Therefore, it is believed that the presence of Ti_2Ni spherical precipitates affects the stiffness of the films and this effect is evident when grain boundary effects are negligible (large grain size – Cu content $\leq$ 4.4 at.%). On the other hand, when the grain boundary effect becomes prominent (small grain size – Cu content $>$ 4.4 at.%), it affects the mechanical properties in a much more significant way compared to the precipitates in the grain interior.

We should point out that the values of hardness and elastic modulus presented in this chapter (single hysteresis nanoindentation measurements) are lower than those obtained on identical coatings by multiple-loading nanoindentation experiments presented in chapter 3 (the mechanical properties were evaluated at a depth corresponding to $\sim$ 10 % of the layer thickness reached through 5 nanoindentation cycles – see chapter 3). This difference is likely associated with the strain hardening behaviour of Ni-Ti based alloys – see Appendix B for further details.

The W_e/W_{tot} ratio (elastic-to-total work ratio evaluated by numerical integration of the load-displacement curves) increases with increasing Cu content owing to the more linear elastic behaviour of the layers. In fact, for higher Cu content, i.e. smaller grain size, larger contribution of the austenitic matrix to the total deformation, at the expense of the pseudo-elastic deformation associated with the phase transformation, is expected. It is related, as mentioned previously, to the effect of the grain size on the $\sigma^{A\rightarrow M}$.

In terms of mechanical behaviour during the contact, based on the H/E_r ratio reported in Figure 5.5, similar response to nanoindentation is expected for films with a Cu content lower than 4.4 at.%. On the other hand, higher ratios are found for interlayers containing a Cu content ≥ 7 at.%; $Ni_{42.2}Ti_{47.9}Cu_{9.9}$ shows the highest H/E_r ratio.

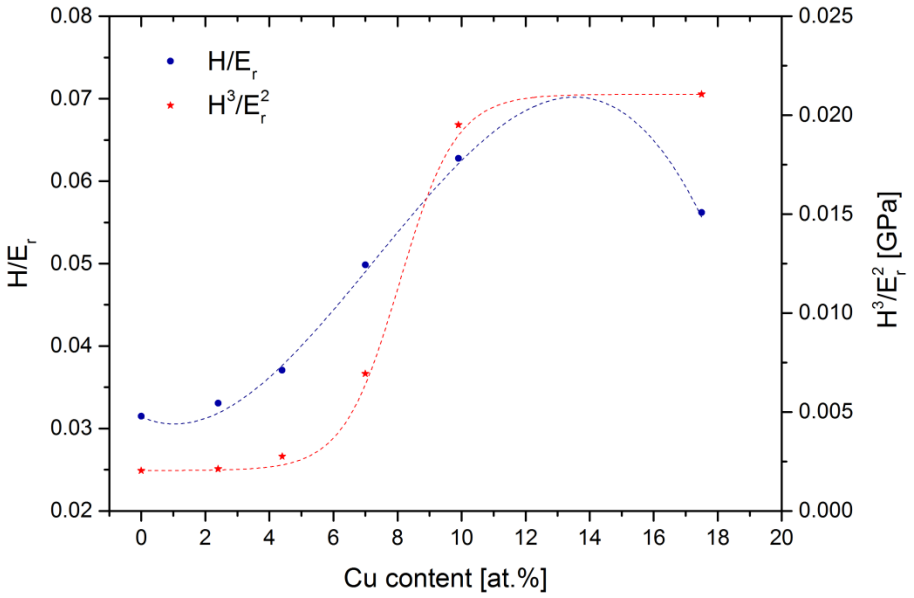

Figure 5. 5 – Mechanical properties of the Ni-Ti(-Cu) layers in relation to the Cu content: hardness-to-reduced elastic modulus (H/E_r) ratio and resistance against plastic deformation (H^3/E_r^2). Dash lines are reported as guideline.

Similar considerations can be drawn concerning the resistance against plastic deformation (H^3/E_r^2) in Figure 5.5, which is even more strongly attributed to the grain size. A higher grain boundary density relative to the volume of material displaced by the tip is expected to provide a stronger resistance against dislocation movement. Relatively thick boundaries between narrow columnar grains (see chapter 4) work as barriers against dislocation movement. Furthermore, energy dissipation can occur within these grain boundaries (i.e. plastic deformation). These aspects suggest that the plastic deformation is confined mostly within the grain, or a few grains, underneath the contact, while the neighbouring grains are expected to support the load mostly through elastic or pseudo-elastic deformation of the austenitic films. Therefore a lower plasticity index, which provides an indication of the energy dissipated during the indentation process [12], is expected for Cu-rich layers. For conventional protective coatings a lower plasticity index normally indicates a more elastic response of the coating to the contact. However, in this study where Ni-Ti(-Cu) interlayers are also

used to limit the transmission of plastic deformation from the top surface down to the substrate, the capability of the interlayer itself to store energy in the form of elastic, pseudo-elastic and eventually plastic deformation, has to be taken into account. The trend in Figure 5.5 suggests that films with lower Cu content (lower H/E_r ratio) are able to dissipate more energy, i.e. accommodate larger deformation (elastic, pseudo-elastic and plastic), and thus provide more protection of the substrate against plastic deformation.

The mechanical properties discussed above only indirectly contribute to the tribological performance of the bilayers. The superelastic interlayer is expected to redistribute the strain field generated during indentation by absorbing part of the deformation and thus mitigating the stress generated in the top layer.

The W-S-C layer exhibits a hardness of 4.9 ± 0.2 GPa and an elastic modulus of 58.9 ± 2.3 GPa measured at a penetration depth corresponding to 10% of the layer thickness (hardness measured for single layer deposited on Si). The W-S-C coating thus shows a H/E_r and H^3/E_r^2 ratios of 8.3 x 10^{-2} and 3.4 x 10^{-2} GPa, respectively. The hardness measured here is higher compared to the value reported in literature, i.e. ~ 3 GPa, for a W-S-C coating with a similar C content [3] and the reason could be related to the denser structure of the film obtained in this study compared to that reported in [3].

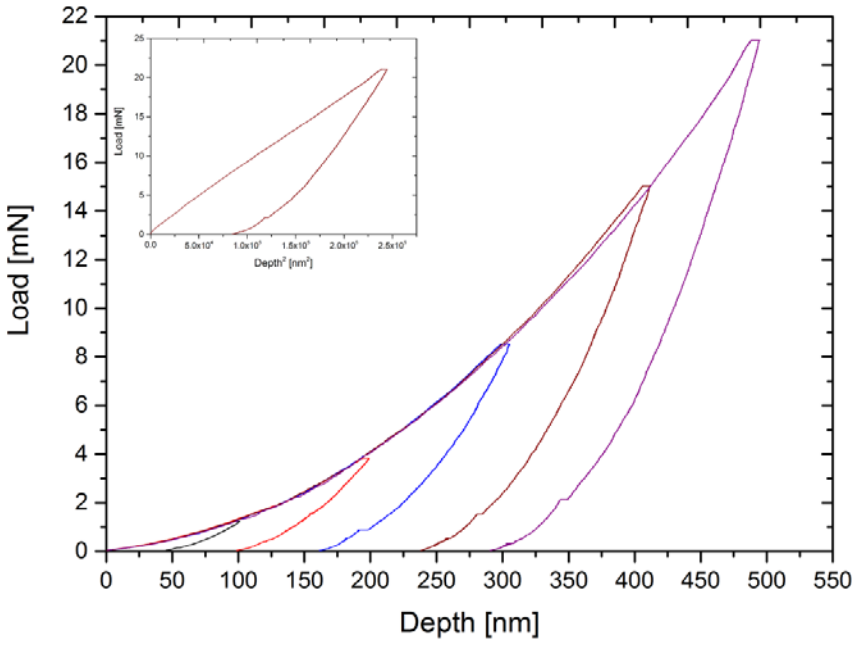

Figure 5.6 – Representative load-depth curves at different depths for the W-S-C/Cr/$Ni_{43.4}Ti_{49.6}Cu_{7.0}$ bilayer. The inset shows the load vs. square of depth curve for a maximum depth of 500 nm.

Figure 5.6 shows some representative load – displacement curves measured on the W-S-C/Cr/$Ni_{43.4}Ti_{49.6}Cu_{7.0}$ bilayer at different penetration depths. Even for penetrations as deep as half of the W-S-C layer thickness, nanoindentation curves are rather smooth and no signs of crack formation are observed for the bilayers studied here. In order to further verify this aspect the load is plotted against the depth squared (see inset in Figure 5.6) and a rather straight loading curve without singularities (i.e. steps) is observed as predicted by the theory of plasticity in contact mechanics [13].

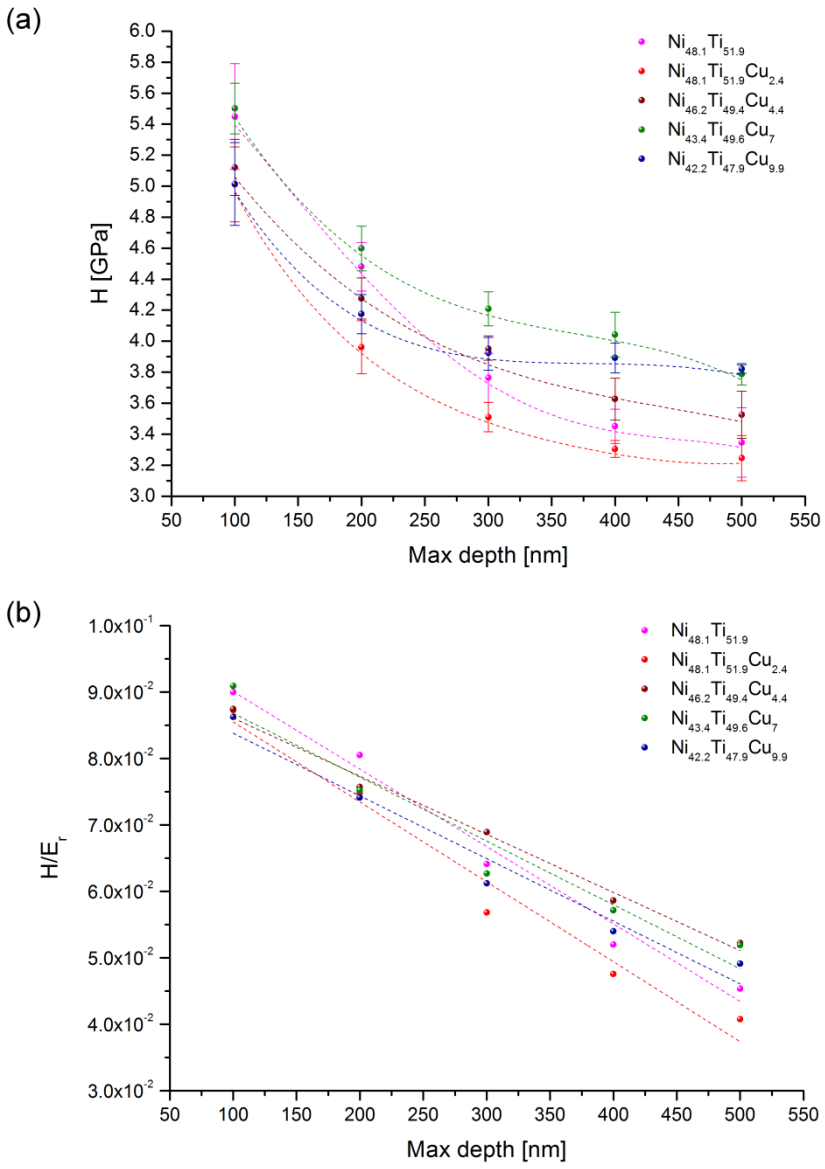

Figure 5.7 – Mechanical properties of the W-S-C/Cr/Ni-Ti(-Cu) bilayers at different depths: (a) hardness and (b) H/E_r ratio.

The hardness of the bilayers at different penetration depths is shown in Figure 5.7 (a). At the lowest penetration depth the composite hardness (i.e. hardness of the bilayer,

5.2 ± 0.3 GPa) corresponds approximately to that of the W-S-C single layer (4.9 ± 0.2 GPa), while with increasing penetration depth the composite hardness drops and for penetration depths larger than 300 nm follows the tendency shown in Figure 5.4. The effect of the interlayer composition on the response of the bilayers to nanoindentation becomes evident at lower penetration depths for harder interlayers – note that for $Ni_{43.4}Ti_{49.6}Cu_{7.0}$ and $Ni_{42.2}Ti_{47.9}Cu_{9.9}$ interlayers the composite hardness has already stabilized at a penetration depth of about 300 nm.

The less pronounced indentation size effect observed when harder interlayers are used is related to the fact that a significant part of the deformation induced by the movement of the tip into the surface is absorbed by the W-S-C layer, which is found here and in other studies [14] to exhibit a weak indentation size effect. On the other hand, by combining the W-S-C layer together with a softer interlayer, most of the deformation is absorbed by the softer interlayer, thus a more pronounced indentation size effect is observed. Although for deep indents (i.e. 500 nm) elastic deformation of the substrate is not excluded, the response of the bilayers at large penetration depths shows a clear dependence on the interlayer material (Figure 5.7 a).

The H/E_r ratio evaluated at different depths for the bilayers is showed in Figure 5.7 (b). H/E_r decreases linearly with the penetration depth regardless of the interlayer material. For low depths (below 200 nm) no significant variations are observed using different interlayers, the deformation being mostly confined within the W-S-C/Cr layer. For depths over 200 nm a larger dispersion of H/E_r ratio is observed for different interlayers. In particular, for depths as large as 500 nm a similar trend to that of the composite hardness in Figure 5.7 (a) is observed for H/E_r except for $Ni_{46.2}Ti_{49.4}Cu_{4.4}$ interlayer. These results show that the response of the W-S-C layer to the contact can be modified, without any detrimental effect on the top layer, by using an appropriate interlayer. The thickness of the top layer is expected to play a role on the dispersion of the H/E_r ratio in relation to the penetration depth, i.e. a thinner W-S-C would cause a larger distribution of the data for a specific depth in relation to the interlayer.

5.4.2 Nano-scratch

Figure 5.8 (a) shows the scratch depth of the W-S-C single layer along the scratch track during and after the test. In the first 50 nm of the track a low load (0.1 mN) is used to scan the surface before and after the test as a reference profile. The scratch depth increases linearly with the applied load, almost from the beginning of the test, till the coating failure. Failure consists of removal of the W-S-C layer, which occurs when the scratch depth reaches a critical value of ~ 470 nm (about 40 % of the W-S-C film thickness). The residual scratch depth increases almost linearly for higher applied loads. The coating exhibits a good elastic recovery for applied loads < 10 mN (scratch distance below 120 µm), as shown in Figure 5.8 (a).

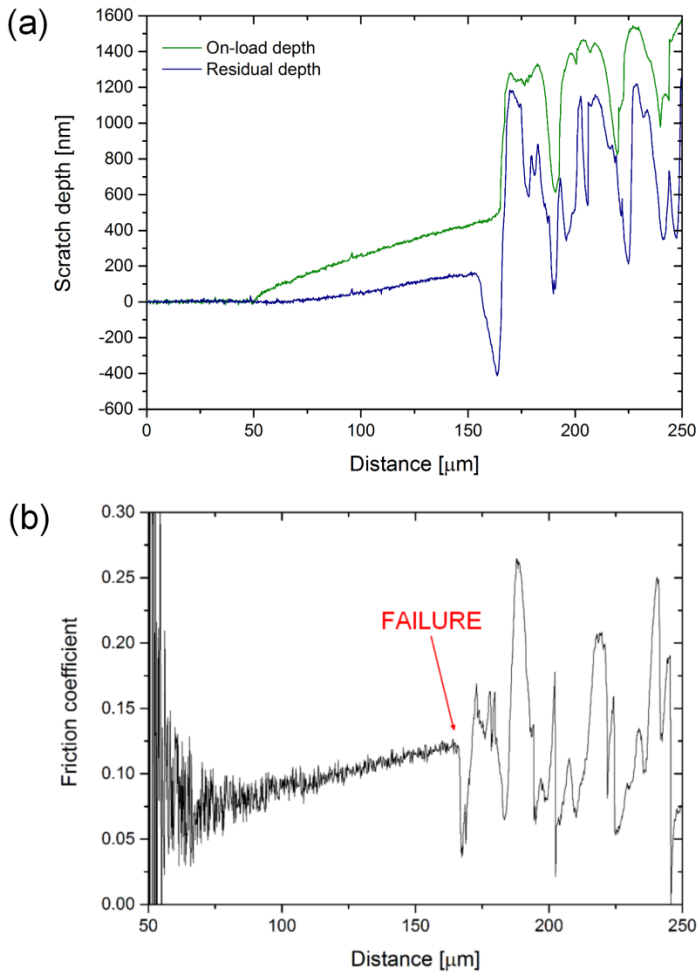

Figure 5.8 – Scratch test on the W-S-C single layer: (a) scratch profiles during and after the test, (b) measured friction coefficient for an applied load in the range 0.1 – 100 mN.

However, this elastic recovery combines both coating and Si substrate elastic deformation; the latter is more pronounced at high applied loads. Hence, rather than the elastic recovery, the residual depth before failure is considered as a more significant factor representing the scratch behaviour of these layers.

By considering that the displacement measured by the instrument consists of different contributions, i.e. elastic and plastic deformation of every layer and deformation of the substrate, the on-load profile showed in Figure 5.8 (a) is not sufficient to identify the actual depth where failure occurs. Therefore, SEM/EDX analyses are performed on the scratches. The SEM micrograph in Figure 5.9 shows some of the scratches performed on the W-S-C coating, where after the critical point, the coating appears chipped. Such a failure mode is typical of crack propagation from the bottom to the surface leading to decohesion of large semi-circular areas formed ahead of the probe (see Figure 5.9). EDX analyses are carried out in different delaminated areas around the critical point in order to understand at which depth delamination takes place. EDX analyses revealed a large amount of Cr (32 at.% in average) and Si (35.5 at.% in average), and smaller amount of C (15 at.% in average). It suggests that the delamination takes place between the W-S-C coating and the Cr bonding layer.

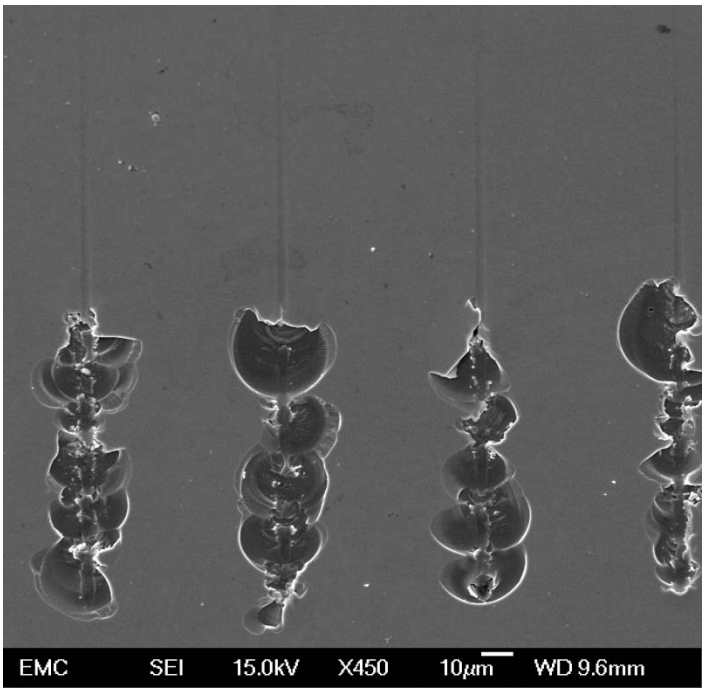

Figure 5.9 – FEG-SEM micrograph of some scratches performed on the W-S-C single layer.

SEM micrographs also show that before the critical point is reached, no cracks are produced on the coating, thus suggesting a good toughness of the W-S-C. Figure 5.8 (b) shows the measured coefficient of friction when the load is ramped from 0.1 to 100 mN. After the initial noise in the signal, friction increases linearly up to about 0.12 just before failure, for an average critical load of 57 mN.

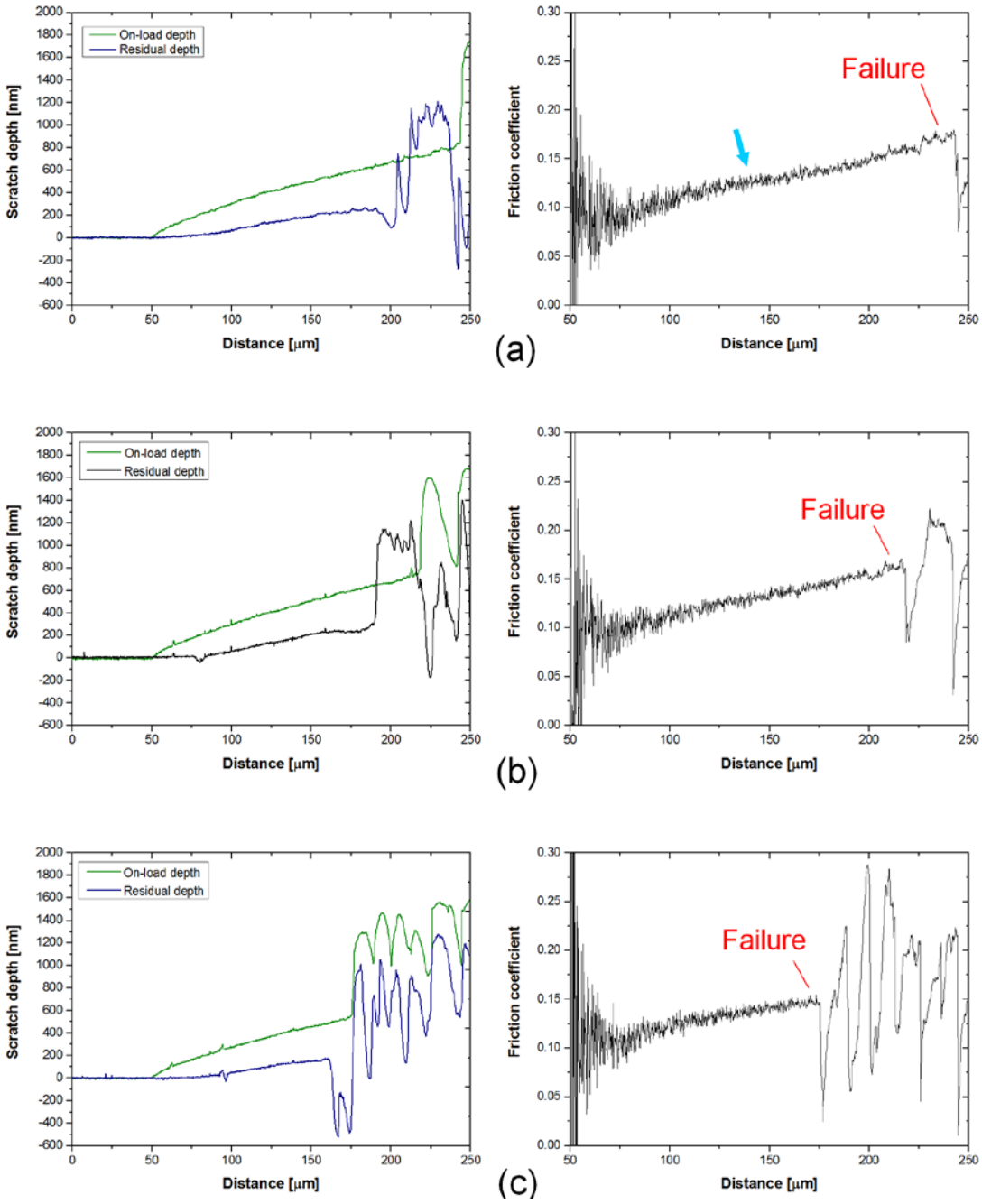

Figure 5.10 – Scratch profiles and corresponding friction coefficient for bilayers using the following interlayers: (a) $Ni_{48.1}Ti_{51.9}$, (b) $Ni_{46.2}Ti_{49.4}Cu_{4.4}$, (c) $Ni_{42.2}Ti_{47.9}Cu_{9.9}$.

Scratch tests are also performed for the bilayers fabricated by using the Ni-Ti(-Cu) interlayers reported in Table 5.I. Bilayers with softer interlayers exhibit a slightly less chipped surface, compared to the W-S-C single layer. Figure 5.10 illustrates the scratch profiles during and after the scratch test and the corresponding coefficient of friction for some bilayers. By comparing the scratch profiles shown in Figure 5.8 (W-S-C single layer) and Figure 5.10 (c) (bilayer) it is evident that the critical points on the on-load and residual depth profiles are almost superimposed (similar distance). It indicates that failure occurrs behind but very close to the probe. On the other hand, for the cases reported in Figure 5.10 (a) – (b) the critical point on the residual depth profile appears at a shorter distance compared to that of the on-load profile. The reason behind this mismatch is related to the fact that a relatively soft interlayer causes the bending of the harder top layer when the critical load is reached.

The combination of SEM micrographs and the measured profiles suggests that when the critical load is reached, cracks generate and propagate even behind the probe, thus extending the delaminated area. When harder interlayers are used, i.e. Figure 5.10 (c), the mechanism described above is mitigated. Figure 5.5 shows that the H/E_r ratio increases with increasing Cu content in the Ni-Ti-Cu layer, which in turn suggests that the response of the layer to the contact becomes more elastic (larger contribution of the elastic deformation of the austenitic phase). By comparing the surface profiles in the range 50 – 100 µm (corresponding load range 0.1 – 25 mN), a more elastic response is observed in Figure 5.10 (c) compared to Figure 5.10 (a). On the other hand, the smaller grains observed for Cu-richer Ni-Ti-Cu layers limit the deformation accommodated by stress-induced martensitic transformation; consequently, most of the shear stress is relaxed at the interface between W-S-C and Ni-Ti(-Cu) layers rather than being accommodated by the Ni-Ti(-Cu) layer.

Figure 5.11 shows the scratch depth profile (on-load depth) of the bilayers as a function of applied load in the range 0.1 – 50 mN. By comparing these profiles, particularly for high applied loads, a clear correlation is observed between the mechanical properties of the Ni-Ti(-Cu) interlayers and the response of the bilayers to the scratch. In fact, deeper scratches are produced on bilayers with Ni-Ti(-Cu) interlayers characterised by lower H/E_r and H^3/E_r^2 ratios. A similar correlation is observed between the scratch depth and the hardness of the bilayers, Figure 5.7 (a).

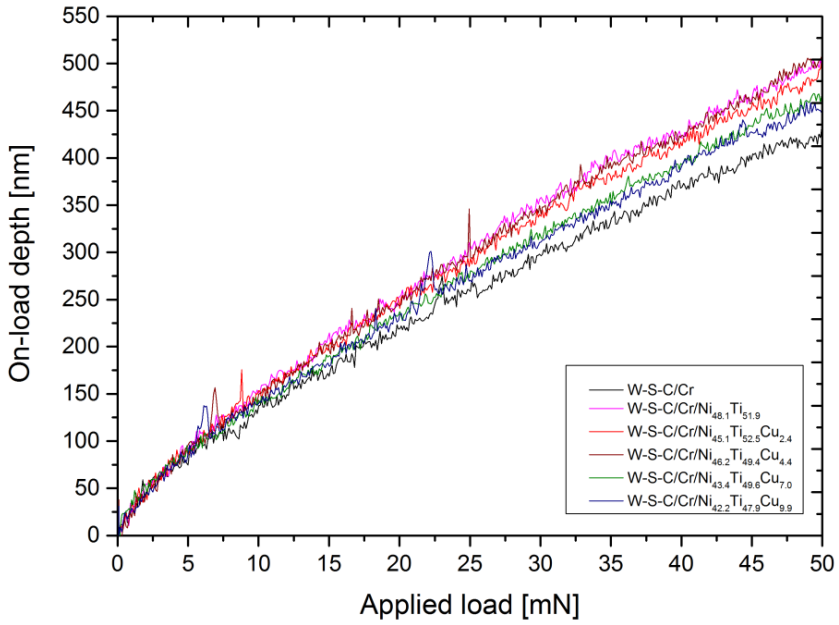

Figure 5.11 – Representative scratch depth vs. applied load in the range 0.1 – 50 mN, for the bilayers.

Regardless of the interlayer material, failure occurs within the Cr-based gradient bonding layer, as confirmed by SEM/EDX analyses. Therefore, the interface between the Ni-Ti(-Cu) interlayer and the W-S-C layer is a critical point. Interestingly, the TiO_2 residual layer observed in Figure 5.3 did not affect the adhesion of the coating. However, we can conclude here that a more robust bonding layer between W-S-C and Ni-Ti(-Cu) can further improve the transmission of the shear strain to the interlayer allowing a better exploitation of its superelastic properties.

In Figure 5.10, although the measured friction coefficient is similar for all the cases studied here, differences in the friction curves are observed. Friction increases linearly for the W-S-C single layer (Figure 5.8) or with interlayers as hard as the W-S-C coating (i.e. $Ni_{42.2}Ti_{47.9}Cu_{9.9}$). On the other hand, the friction curves exhibit a non-linear behaviour attributed to the superelastic interlayer, especially when a relatively soft interlayer is used as can be seen by comparing Figure 5.8 (b) and Figure 5.10 (a). When the normal load is not enough to extend the strain field across the whole bilayer thickness, the response to scratch comes primarily from the top layer. However, when the strain field is extended through the Ni-Ti(-Cu) interlayer, it can accommodate a relatively large part of the shear deformation owing to the phase transformation. This mechanism is likely to lower and/or stabilise the friction coefficient, although the mechanism behind is not fully understood here (see chapter 6 for more depth

analyses). After this transitory behaviour, restricted most likely by the limited transformation strain of the interlayer, friction increases linearly till coating failure.

Figure 5.12 shows the critical load for delamination as well as the measured on-load depth when failure occurs, in relation to the H/E_r ratio of the Ni-Ti(-Cu) interlayers. A Ni-Ti(-Cu) interlayer always improves the adhesion of the W-S-C coating, although significant differences are observed for different Ni-Ti(-Cu) interlayers. These differences are attributed, as discussed previously, to the capability of the interlayer to accommodate deformation through the stress-induced martensitic transformation. This capability is found to be affected by the grain size, which in turn influences the mechanical response of these layers. Films with a grain size larger than ~ 1 μm (Cu content lower than 4.4 at.%) are found to contribute more at improving the layer adhesion. The only exception is the $Ni_{45.1}Ti_{52.5}Cu_{2.4}$ interlayer.

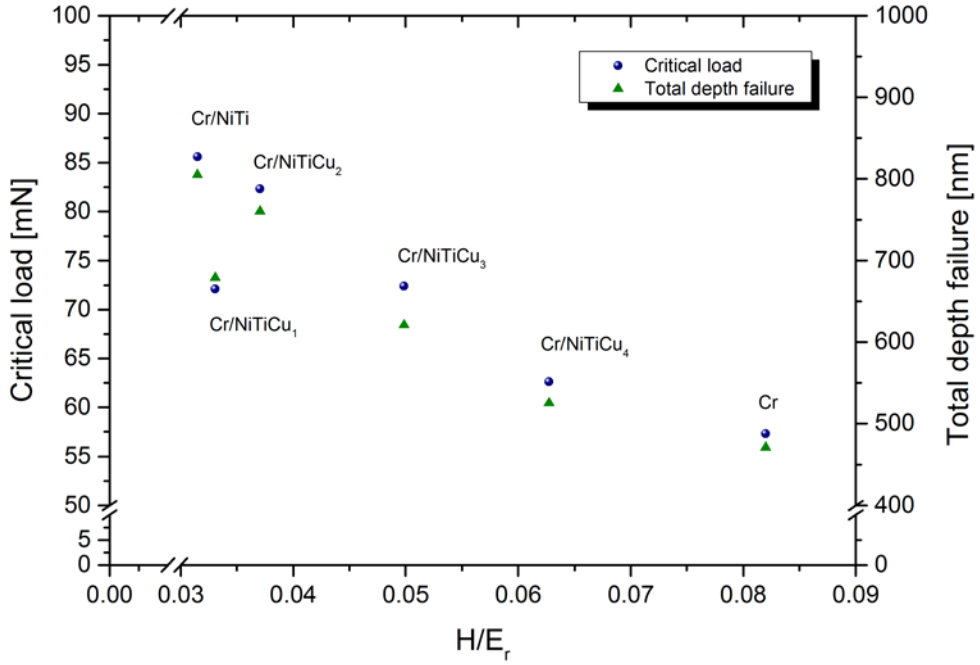

Figure 5.12 – Average critical load (standard deviation < 5 mN) and total depth to failure (measured on the on-load profile with a standard deviation < 15 μm) in relation to the H/E_r ratio of the Ni-Ti(-Cu) interlayers.

The reason behind its poor behaviour compared to the $Ni_{48.1}Ti_{51.9}$ and $Ni_{46.2}Ti_{49.4}Cu_{4.4}$ interlayers is the higher martensitic volume fraction in relation to the austenitic phase (Figure 5.1). Typically, the martensitic phase is softer compared to austenite [7]; thus,

the lower critical load observed for the bilayer with the $Ni_{45.1}Ti_{52.5}Cu_{2.4}$ interlayer is attributed to the fact that bending and consequently crack propagation occurs at lower normal loads for a bilayer with the $Ni_{45.1}Ti_{52.5}Cu_{2.4}$ interlayer. Figure 5.12 shows that a similar trend is observed for the average total depth at coating failure. A lower total depth to failure is observed for the bilayer with the $Ni_{45.1}Ti_{52.5}Cu_{2.4}$ interlayer. As a similar amount of deformation can be accommodated by both stress-induced (austenite-to-martensite) transformation and martensitic reorientation (stress-induced detwinning of martensitic plates) [15], it further supports that the reason behind the poorer performance of the $Ni_{45.1}Ti_{52.5}Cu_{2.4}$ interlayer is associated with its softness.

It seems that the scratch behaviour of the bilayers is more clearly related to the mechanical properties (i.e. H/E_r, H^3/E_r^2) of the Ni-Ti(-Cu) interlayers rather than to the mechanical properties measured directly on the bilayers. It demonstrates that the mechanical and scratch behaviour of such a bilayer design is strongly affected by the interlayer material. Generally, it was observed that to have a suitable toughness for applications the interlayer has to be relatively softer compared to the functional top layer [16, 17] and coatings with high H/E_r ratio do not necessarily represent the optimum solution [12]. However, the reason for such behaviour is different in this study. Compared to conventional interlayers (Cr, Ti), the microstructure and particularly the grain size of the Ni-Ti(-Cu) superelastic interlayers are related not only to mechanical properties, but also to their functional properties, i.e. martensitic transformation. In fact, the grain size controls the energy required to activate the phase transformation and consequently the extent to which deformation can be accommodated by such phase transformation. In smaller grains (higher $\sigma^{A\rightarrow M}$) higher energy is required to activate the phase transformation [11]. Consequently, only limited deformation (i.e. elastic deformation of the austenitic phase, which is significantly lower when compared to the deformation accommodated by the martensitic transformation) can be accommodated by the interlayer before that adhesion failure takes place. On the other hand, for interlayers with relatively large grains less energy is required to activate the phase transformation through which the deformation generated during scratch can be accommodated and consequently stress concentration, in the top layer, mitigated.

Therefore, such an interlayer material needs to be carefully optimised taking into account the loading conditions occurring in the specific application as well as the nature of the functional top layer. The stress field extending through the superelastic interlayer must not exceed the yield stress of the stress-induced martensitic phase, so that most of the strain generated during the contact can be recovered upon unloading. Based on the critical load shown in Figure 5.12 for different interlayers, it is reasonable to assume that the interlayer $Ni_{42.2}Ti_{47.9}Cu_{9.9}$ (small grain size) exhibit poor or no phase transformation before adhesion failure. On the contrary, the $Ni_{48.1}Ti_{51.9}$ interlayer (large grain size) is expected to undergo first phase transformation and subsequently plastic deformation, which is detrimental to the functional behaviour of the layer itself. Therefore, among the bilayers investigated in this study, the one using the $Ni_{43.4}Ti_{49.6}Cu_{7.0}$ as interlayer material might represent a good compromise between adhesion improvement of a top layer and the capability of accommodating and recovering strain upon loading/unloading cycles (limited or no plastic deformation).

References

[1] A. Ishida and M. Sato, “Microstructures of crystallized Ti51.5Ni48.5−xCux (x = 23.4–37.3) thin films,” *Intermetallics,* vol. 19, no. 7, pp. 900-907, 2011.

[2] S. Miyazaki, Y. Q. Fu and W. M. Huang, Thin film shape memory alloys: fundamentals and device applications, Cambridge (UK): Cambridge University Press, 2009.

[3] M. Evaristo, A. Nossa and A. Cavaleiro, “W–S–C sputtered films: Influence of the carbon alloying method on the mechanical properties,” *Surface and Coatings Technology,* vol. 200, no. 1-4, pp. 1076-1079, 2005.

[4] J. Pfetzing-Micklich, N. Wieczorek, T. Simon, B. Maaß and G. Eggeler, “Direct microstructural evidence for the stress induced formation of martensite during nanonindentation of NiTi,” *Materials Science and Engineering: A,* vol. 591, pp. 33-37, 2014.

[5] W. Oliver and G. Pharr, “An improved technique for determining hardness and elastic modulus using load and displacement sensing indentation experiments,” *Journal of Materials Research,* vol. 7, no. 06, pp. 1564-1583, 1992.

[6] W. Oliver and G. Pharr, “Measurement of hardness and elastic modulus by instrumented indentation: Advances in understanding and refinements to methodology,” *Journal of Materials Research,* vol. 19, no. 01, pp. 3-20, 2004.

[7] X. Huang, J. Nohava, B. Zhang and A. Ramirez, “Nanoindentation of NiTi shape memory thin films at elevated temperatures,” *International Journal of Smart and Nano Materials,* vol. 2, no. 1, pp. 39-49, 2011.

[8] J. Zhang, M. Sato and A. Ishida, “On the Ti2Ni precipitates and Guinier–Preston zones in Ti-rich Ti–Ni thin films,” *Acta Materialia,* vol. 51, no. 11, pp. 3121-3130, 2003.

[9] X. Meng, M. Sato and A. Ishida, “Structure of martensite in Ti-rich Ti–Ni–Cu thin films annealed at different temperatures,” *Acta Materialia,* vol. 56, no. 14, pp. 3394-3402, 2008.

[10] M. Kabla, H. Seiner, M. Musilova, M. Landa and D. Shilo, “The relationships between sputter deposition conditions, grain size, and phase transformation temperatures in NiTi thin films,” *Acta Materialia,* vol. 70, pp. 79-91, 2014.

[11] H. Zhang and X. Z. X. Li, “Grain-size-dependent martensitic transformation in bulk nanocrystalline TiNi under tensile deformation,” *Journal of Alloys and Compounds,* vol. 544, pp. 19-23, 2012.

[12] B. Beake, V. Vishnyakov and A. Harris, “Relationship between mechanical properties of thin nitride-based films and their behaviour in nano-scratch tests,” *Tribology*

International, vol. 44, no. 4, pp. 468-475, 2011.

[13] Fischer-Cripps and A. C., Introduction to Contact Mechanics, Second ed., Spring Science, 2007.

[14] T. Koch, M. Evaristo, A. Pauschitz, M. Roy and A. Cavaleiro, "Nanoindentation and nanoscratch behaviour of reactive sputtered deposited W–S–C film," *Thin Solid Films,* vol. 518, no. 1, pp. 185-193, 2009.

[15] K. Otsuka and X. Ren, "Physical metallurgy of Ti–Ni-based shape memory alloys," *Progress inMaterials Science,* vol. 50, pp. 511-678, 2005.

[16] J. Gerth and U. Wiklund, "The influence of metallic interlayers on the adhesion of PVD TiN coatings on high-speed steel," *Wear,* vol. 264, no. 9-10, pp. 885-892, 2008.

[17] K. Holmberg, A. Laukkanen, H. Ronkainen and K. Wallin, "Surface stresses in coated steel surfaces—influence of a bond layer on surface fracture," *Tribology International,* vol. 42, no. 1, pp. 137-148, 2009.

Appendix B

1. Microstructural details of the Ni-Ti-Cu/Si interface

During the annealing process of the Ni-Ti(-Cu) thin films deposited on Si a diffusion layer is formed at the interface. Such a layer exhibts an elongated shape parallel to the interface and a thickness in the range 10 – 15 nm as observed in Figure B.1 (a). EDX line scans across the interface show that this diffusion layer parallel to the substrate surface has a Si-rich Ni-Ti-Si chemical composition as shown in Figure B.1 (b).

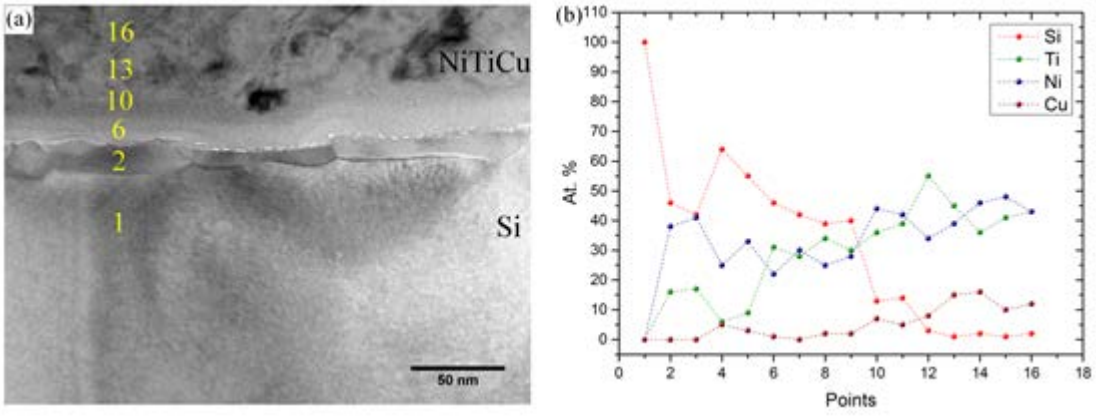

Figure B.1 – Formation of an interdiffusion layer at the interface between Ni-Ti-Cu film and Si substrate: (a) Bright Field TEM image at the interface between the $Ni_{48.7}Ti_{47.2}Cu_{4.1}$ film and Si substrate – numbers provide a rough indication of the points where EDX measurements are performed; (b) representative EDX measurements across the interface.

The EDX measurements across the interfaces suggest that the formation of this diffusion layer involves mostly the diffusion of Ni and Ti, while almost no Cu is found in the layer. Diffusion of Si above these silicides might be possible (see point 10 in Figure B.1) within a few nanometres, although the EDX profile in Figure B.1 (b) shows a clear step at point 10. A similar scenario is found for Ni-Ti-Cu films with different chemical composition.

2. Single versus multiple-loading nanoindentation measurements

Differences in mechanical properties (hardness and elastic modulus) are observed on identical coatings when measurements are performed by single hysteresis and multiple-loading nanoindentation experiments. In particular, higher hardness values are reported in chapter 3 (multiple-loading experiments, Platform 2, Micro Materials) for coatings annealed at 500°C compared to those reported in the current chapter for the same coatings probed by single hysteresis experiments (Platform 4, Micro Materials). In order to make sure that the observed differences are not generated by the different instruments and Berkovich tips used during this study, some Ni-Ti(-Cu) coatings have been tested by the same instrument (Platform 4, Micro Materials) and Berkovich tip by the two testing conditions mentioned above, i.e. single and multiple-loading experiments. The analyses of the selected curves on an average of 10 measurements showed a hardness value, measured by multiple-loading nanoindentation, about 27% higher compared to that measured by single hysteresis experiments. Pan et al. [1] reported that during multiple-loading nanoindentation experiments performed on superelastic Ti 49 ± 0.4 – Ni thin film the formation of dislocations and in general of defects in the structure underneath the indented surface enhances the critical stress for slip of the austenitic matrix and a hardening effect was observed in the first few nanoindentation cycles. Therefore, although this aspect is not investigated in depth in this study, the strain hardening effect might be responsible for the observed behaviour.

Reference

[1] G. Pan, Z. Cao, M. Wei, L. Xu, J. Shi, X. Meng, “Superelasticity of TiNi thin Films induced by cyclic nanoindentation deformation at nanoscale”, Materilas Science & Engineering A, 600 (2014) 8-11.

Chapter 6 Ni-Ti-Cu INTERLAYERS SUPPORTING LOW-FRICTION FUNCTIONAL COATINGS♠

6.1 Chapter summary

In this study we report experimental evidence on the martensitic transformation induced by sliding in Ni-Ti(-Cu) films, when such a film is used as interlayer material between a functional W-S-C top layer and substrate. The stress-induced martensitic transformation occurring in sputter-deposited $Ni_{48.1}Ti_{51.9}$ and $Ni_{43.4}Ti_{49.6}Cu_7$ interlayers, integrated in the W-S-C/Ni-Ti(-Cu) bilayer design, is investigated by transmission electron microscopy, after these bilayers were subjected to different sliding conditions. Martensitic bands across the interlayers are formed depending on the sliding direction with their shape and distribution a function primarily of both applied normal load and grain size.

The $Ni_{48.1}Ti_{51.9}$ interlayer (grain size of ~ 3.5 µm) shows well oriented and ordered martensitic bands extended through the interlayer thickness under low load (5 N). At a higher load (18 N) the growth of these bands is limited by the stabilised martensite formed as a consequence of the high compressive stress, at the interface with the substrate.

The $Ni_{43.4}Ti_{49.6}Cu_7$ interlayer (grain size of ~ 650 nm) exhibits no significant evidence of stabilised martensite under different loading conditions. The martensitic transformation is limited by the smaller grain size and the stress is relaxed by elastic and, to some extent, pseudo-elastic deformation of the austenitic phase. Grain

♠ Extracted from: M. Callisti, T. Polcar, "Stress-induced martensitic transformation in Ni-Ti(-Cu) interlayers controlling stress distribution in functional coatings during sliding", submitted to Applied Surface Science.

boundaries are found to stop the growth of martensitic bands, thus limiting the activation of the martensitic transformation into the neighbouring grains during sliding.

The grain refinement causes a change in the capability of the interlayer to relax shear and compressive stresses. Such a change is found to affect the formation of the WS_2-rich tribolayer on the W-S-C sliding surface, and consequently the shear stress transmitted down throughout the bilayers thickness. Accordingly, different levels of deformation are observed on the top layer.

Despite the similar overall frictional behaviour observed between W-S-C single layer and the W-S-C/Ni-Ti(-Cu) bilayers, in the latter case slightly smoother friction curves, with more stable friction coefficient in the steady-state regime, were observed especially for the W-S-C/Ni-Ti-Cu bilayer. Furthermore, the overall wear behaviour of the functional top layer was significantly improved by using a Ni-Ti(-Cu) interlayer.

6.2 Coatings microstructure

As-deposited bilayers consist of 1.4 µm Ni-Ti(-Cu) interlayer and 1.4 µm functional layer (0.25 µm Cr + W-S-C gradient bonding layer and 1.15 µm W-S-C top layer). Two different interlayers are used in this study, $Ni_{48.1}Ti_{51.9}$ and $Ni_{43.4}Ti_{49.6}Cu_7$ ($\pm$0.2 at.%) and three coatings systems were prepared: W-S-C/Cr used as a reference, W-S-C/Cr/$Ni_{48.1}Ti_{51.9}$ and W-S-C/Cr/$Ni_{43.4}Ti_{49.6}Cu_7$. To facilitate reading these coatings will be denominated as W-S-C, W-S-C/Ni-Ti (binary interlayer) and W-S-C/Ni-Ti-Cu, respectively.

The XRD patterns (see chapter 5) of the annealed Ni-Ti(-Cu) films indicated austenite (b.c.c. structure) as the main phase in these layers; a trace of martensite is detected in the binary interlayer as well. The (110) peak shifted toward lower 2θ angles for the $Ni_{43.4}Ti_{49.6}Cu_7$ film likely suggesting expansion of the B2 crystal normally to the substrate as the result of the solid solution substitution of Ni by Cu atoms [1].

The $Ni_{48.1}Ti_{51.9}$ layer shows a disk-like grain morphology (see Figure 3.5 a in chapter 3) consisting of very large grains (up to ~3 µm in diameter) extended throughout the film thickness. It suggests that grain growth is limited during crystallisation only by both

free surface and film/substrate interface, while lateral growth takes place till grain boundary impingement (two-dimensional growth). On the other hand, the $Ni_{43.4}Ti_{49.6}Cu_7$ film exhibits much narrower columnar grains (650 ± 200 nm) and grain boundaries populated by (Ni, Cu)-rich Ni-Ti-Cu precipitates, see Figure 3.6 (b) in chapter 3. In our previous study (chapter 4), we have attributed the grain refinement to a non-polymorphic crystallisation process, which becomes prominent with increasing Cu content.

Regarding the microstructure in the grain interior, a few small martensitic domains are found in the $Ni_{48.1}Ti_{51.9}$ layer in the form of twin domains observable by HR-TEM (see appendix A in chapter 3) and identified by XRD (see chapter 3 and chapter 5). Furthermore, homogeneously distributed Ti_2Ni spherical precipitates in the grain interior are observed by TEM (see Figure 3.5 (c) in chapter 3) and also identified by XRD in the $Ni_{48.1}Ti_{51.9}$ film. Selected area electron diffraction pattern (SAEDP), in Figure 3.5 (b) (chapter 3), suggested the presence of tiny precipitates in the B2 matrix, which are thought to be GP zones [2, 3, 4, 5]. The presence of Ti-rich precipitates lowers the Ti content in the matrix (Ni/Ti content ratio of the matrix measured by EDX attached to the TEM is about 1.1), thus making the austenitic phase stable at ambient temperature.

On the other hand, in the $Ni_{43.4}Ti_{49.6}Cu_7$ film, plate precipitates (about 10 atomic layers thick and below 100 nm in diameter) are observed (see Figure 3.10 and Figure 3.11 in chapter 3). Several EDX line scan analyses performed across these plate precipitates suggested a (Ni, Cu)-rich Ni-Ti-Cu composition, with a similar Ni and Cu content and lower Ti content (almost half compared to Ni and Cu); therefore these plates are considered to be $Ti(Ni, Cu)_2$ precipitates with a body centred tetragonal structure as also reported elsewhere [6]. In Figure 3.11 (b) in chapter 3, it is observed that plate precipitates can cross each other to form cage-like structures. Such a type of structure is thought to limit to a certain extent the reversible martensitic transformation owing to the more intense lattice distortions, compared to the case of spaced plates (Figure 3.11 (a)), generated at the interface and in the surrounding B2 matrix.

A Ti_2Ni phase is also identified by XRD (see chapter 3 and chapter 5) in the $Ni_{43.4}Ti_{49.6}Cu_7$ film, which is expected considering that the Ti content on average is close to 50 at.%. Ti_2Ni precipitates exhibit a semi-coherent interface with the matrix,

which is found to disturb or even hinder the martensitic transformation, thus promoting plastic deformation, which stabilises martensite [4].

The average chemical composition of W-S-C coating measured by EDX is 23.7 at.% W, 41.9 at.% S, 29.0 at.% C and 5.4 at.% O (± 0.5 at.%). XRD analyses on the W-S-C coating reveals the presence of a turbostratic stacking of (10*L*) planes (*L* = 1, 2, 3, ..) attributed to the WS_x phase with a type I structure (see chapter 5), i.e. basal plane normally oriented with respect to the coating surface. XRD analysis suggested a microstructure mostly consisting of tungsten-sulphur clusters embedded into an amorphous carbon matrix (see chapter 5).

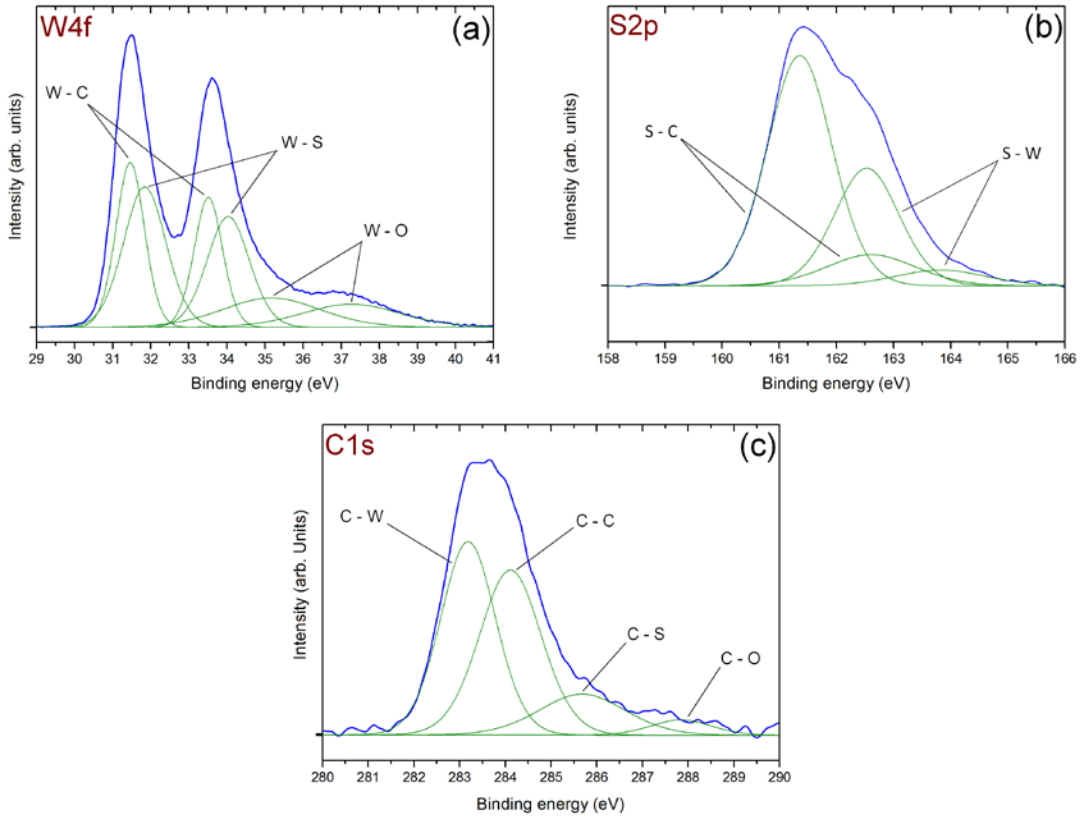

Figure 6.1 – Deconvolution of the W4f, S2p and C1s core level spectra for the W-S-C layer.

Figure 6.1 shows the XPS spectra related to the W4f, S2p, and C1s core levels. It should be pointed out that preferential re-sputtering of sulphur during the etching led to a S/W ratio of ~ 0.93, which is about half of the value estimated by EDX (~ 1.77); therefore the XPS analysis is only qualitative. Figure 6.1 (a) shows the deconvolution in the W4f region with three sets of W4f7 peak doublets, each associated with a W4f5 peak. One peak is associated with WS_2 (W4f7/2 peak located at a binding energy of

about 31.8 eV). In the literature, higher binding energies were reported for WS_2 in the range 32.2 – 33.2 eV [7, 8, 9]. In our case a lower energy level is identified, which is attributed to the sulphur deficiency. In order to fit well the measured spectrum, two more doublets are considered. The first line is located at low binding energy (~ 31.4 eV) and attributed to W – C bond (an energy range of 31.5 – 34.1 eV was reported for W – C [7, 8, 9]). Another peak is introduced at about 35.2 eV and attributed to W – O bond. Therefore, the fitting in Figure 6.1 (a) suggests that W may form carbides and oxides, although the majority of W is bonded to S with a sub-stoichiometric composition (S deficiency). However, we cannot exclude the presence of metallic W (binding energy 30.9 – 31.6 eV [10]).

Figure 6.1 (b) shows the XPS spectrum in the S2p region. S – W bond is identified at a binding energy of about 161.6 eV; in addition, the peak at 161.4 eV is related to the S – C bond, which might exist at the interface between the WS_x clusters and the carbon matrix. Figure 6.1 (c) shows the XPS spectrum in the C1s region, where carbon is found to be mostly bonded to C itself and to W. Furthermore, other two peaks at higher binding energies are required in position of C – S and C – O bonds, although analysis of O1s region suggests that oxygen is almost exclusively bonded to tungsten.

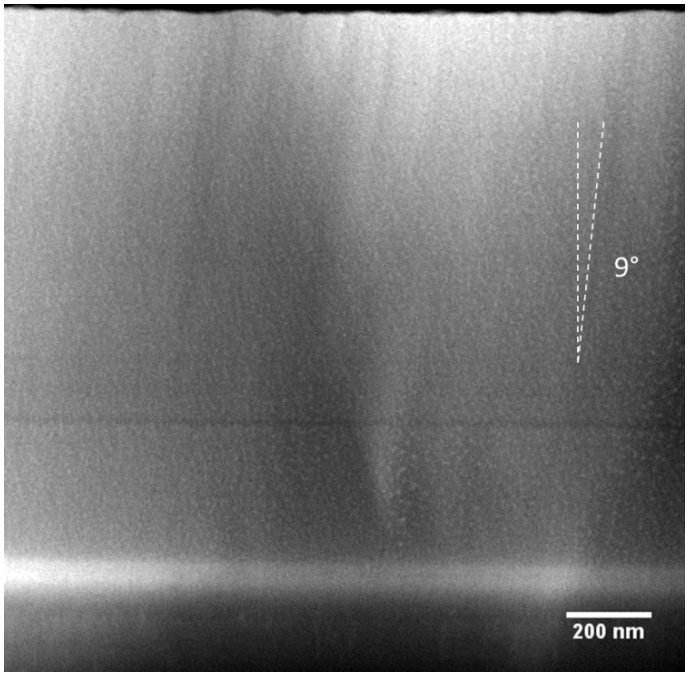

Figure 6.2 – High Angle Annular Dark Field (HAADF) STEM image of the as-deposited W-S-C layer.

TEM analyses are carried out to further assess W-S-C microstructure. Figure 6.2 shows the High Angle Annular Dark Field (HAADF) image of the as-deposited W-S-C layer as well as the Cr-based gradient bonding layer. The latter consists of Cr doped with an increasing amount of W-S-C; the brighter part of the bonding layer is rich in heavier elements. The W-S-C coating exhibits a fine columnar structure (lateral size between 50 – 100 nm) extended throughout the layer thickness. Columns are slightly tilted with respect to the normal to the substrate (~ 9°).

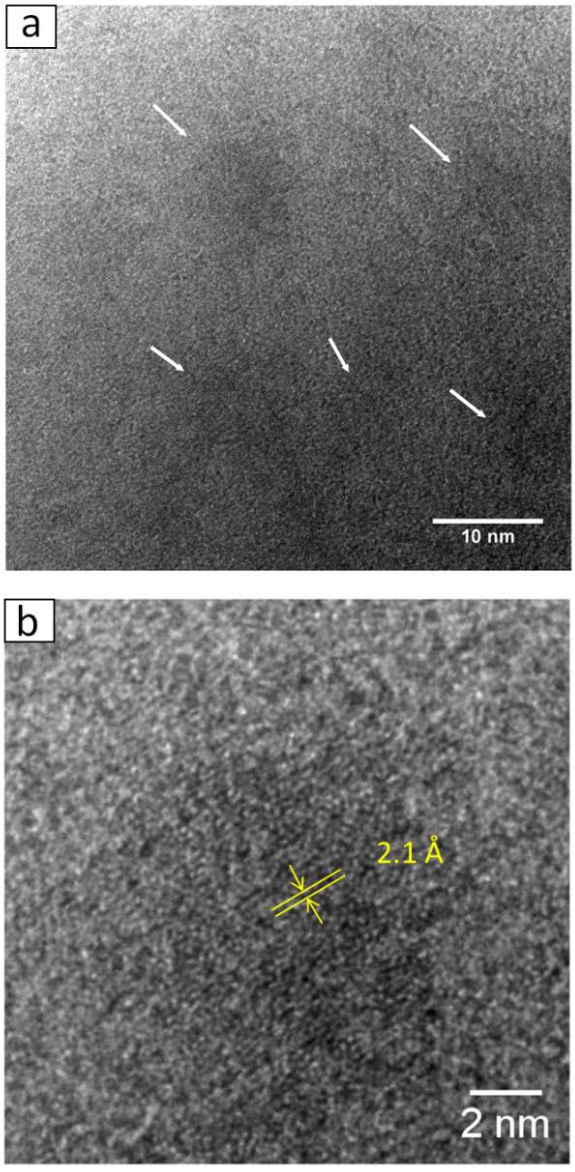

Figure 6.3 – High resolution TEM images of the as-deposited W-S-C layer: (a) WS_x clusters embedded into the amorphous carbon matrix, (b) high resolution TEM image of one of the WS_x clusters in (a).

Regarding nanostructure, clusters of heavier atoms (darker domains in Figure 6.3 (a) with an average size between 6 – 8 nm), embedded into an amorphous carbon matrix

are most likely WS_x crystallites. The fringes spaced ~ 2.1 Å in these clusters (Figure 6.3 (b)) are observed matching well the spacing between W rows in WS_2 nanotubes as reported by *Whitby et al.* [11].

6.3 Mechanical properties

The mechanical properties of every single layer (measured by nanoindentation) and the resistance to adhesion damage of the bilayers (measured by nano-scratch tests) are reported in chapter 5; therefore we only summarize here the main findings (see Table 6.1) in order to support the understanding of the tribological performance of bilayer coatings. The $Ni_{43.4}Ti_{49.6}Cu_7$ film exhibited higher hardness and elastic modulus compared to $Ni_{48.1}Ti_{51.9}$ mainly due to the reduced grain size of the Cu-doped Ni-Ti layer. Moreover, the $Ni_{43.4}Ti_{49.6}Cu_7$ layer exhibited a H/E_r and W_e/W_{tot} ratio (elastic-to-total work ratio evaluated by numerical integration of the load-displacement curves) about 38% and 33% higher when compared to the $Ni_{48.1}Ti_{51.9}$ layer. These differences were attributed to more elastic behaviour of the Cu-doped Ni-Ti layer (i.e. larger contribution of the austenitic matrix to the elastic deformation at the expense of the contribution produced by the phase transformation) during indentation.

Table 6.1 – Summary on the mechanical properties of single layers and critical load against delamination of the corresponding bilayers evaluated by nano-scratch measurements.

	H [GPa]	E [GPa]	H/E_r	H^3/E_r^2 [GPa]
W-S-C	4.9	58.9	$8.3 \times 10 - 2$	$3.4 \times 10 - 2$
$Ni_{48.1}Ti_{51.9}$	2	63	3.1×10^{-2}	2.0×10^{-3}
$Ni_{43.4}Ti_{49.6}Cu_7$	2.8	67	5.0×10^{-2}	6.9×10^{-3}

	Critical load [mN]
W-S-C/Cr	57.3
W-S-C/Cr/$Ni_{48.1}Ti_{51.9}$	85.6
W-S-C/Cr/$Ni_{43.4}Ti_{49.6}Cu_7$	72.4

Similar considerations could be applied to the resistance against plastic deformation (H^3/E_r^2), which is even more strongly related to the grain size. In fact, a higher grain boundary density relative to the volume of material displaced by the indenter is expected to provide a stronger resistance against dislocation movement. This implies that the plastic deformation is confined mostly within the grain, or a few grains, underneath the contact, while the neighbouring grains are expected to support the load mostly through their elastic or pseudo-elastic deformation typical of austenitic films. However, when Ni-Ti(-Cu) films are used as interlayer to absorb energy and limit the transmission of plastic deformation from the top surface down to the substrate, the capability of the interlayer itself to store energy becomes an important property. In our previous study (see chapter 5), we found that Ni-Ti(-Cu) films with lower H/E_r ratio are able to dissipate more energy, i.e. accommodate larger deformation in the form of elastic, plastic and transformation strain. The W-S-C functional layer exhibited higher hardness but lower elastic modulus compared to the Ni-Ti(-Cu) interlayers.

The resistance against adhesion damage for different bilayer coatings as well as for the W-S-C single layer was measured by nano-scratch experiments (see chapter 5). The use of a Ni-Ti(-Cu) interlayer improved significantly the adhesion of the functional W-S-C layer (see Table 6.1), although differences were observed when using different Ni-Ti(-Cu) interlayers. These differences are attributed, as discussed previously, to the capability of the interlayer to accommodate deformation through the stress-induced martensitic transformation. This capability is strongly affected by the grain size.

It is found that the scratch behaviour of the bilayers is strictly related to the mechanical properties (i.e. H/E_r, H^3/E_r^2) of the Ni-Ti(-Cu) interlayers, which are strongly affected by the grain size. In fact, the grain size controls the energy required to activate the phase transformation and consequently the extent at which deformation can be accommodated by phase transformation. In smaller grains higher energy is required to activate the phase transformation [12]. Consequently, less deformation[1]can be accommodated by the interlayer before adhesion failure takes place. On the other hand, for interlayers with relatively large grains less energy is required to activate the phase transformation through which the deformation

[1] It is considered as transformation strain due to the stress-induced phase transformation.

generated during scratch test can be accommodated. These aspects explain the higher critical load found for W-S-C/$Ni_{48.1}Ti_{51.9}$ compared to W-S-C/ $Ni_{43.4}Ti_{49.6}Cu_7$.

6.4 Microstructural changes induced by sliding

Microstructural changes in the coatings could be induced by the simultaneous effect of the compressive and shear stress generated during sliding. While the behaviour of the coatings under compressive stress can be correlated with the nanoindentation response, a much more complex scenario takes place when shear stress is added. Moreover, conversely to conventional materials following Amonton's law, TMD-based coatings exhibit a decrease in friction with increasing load (Figure 6.4) as also reported elsewhere [13]. Therefore the shear component of stress, which is directly related to friction, does not increase linearly with the load.

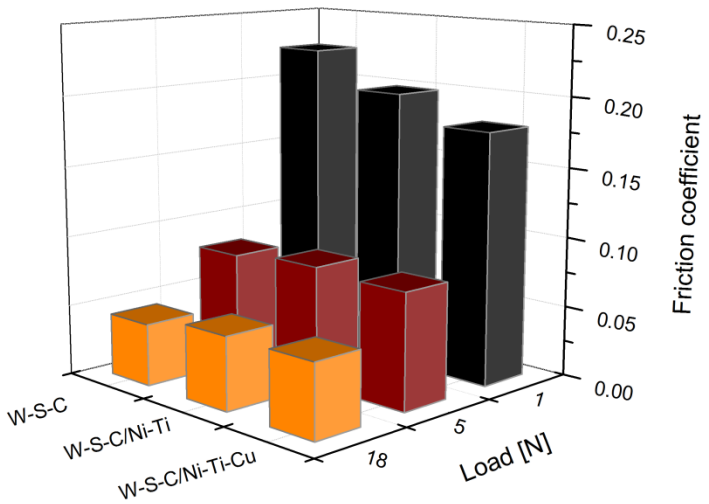

Figure 6.4 – Average friction coefficient as a function of the applied normal load for W-S-C single layer and W-S-C/Ni-Ti(-Cu) bilayers.

In order to shed light on the tribological and mechanical behaviour of these bilayers during sliding, a TEM investigation is carried out on cross-sectional lamellae produced by FIB from the wear tracks of W-S-C/Ni-Ti and W-S-C/Ni-Ti-Cu coatings subjected to different loading conditions. An angle between the FIB cut and the sliding direction of

~ 45° is chosen in order to capture details related to the deformation of the coatings along the sliding direction as well as to have details across the wear track width.

Figure 6.5 (a) shows the cross-sectional morphology of the W-S-C/Ni-Ti coating in the wear track produced with a load of 5 N (~ 0.7 GPa Hertzian pressure). Several bands (darker areas in Figure 6.5 (a)), which are thought to be stabilised martensite, are produced in the interlayer at an angle of ~ 35° away from the normal to the substrate (slightly larger compared to the angle formed by these bands with the sliding direction). The Ni-Ti(-Cu) layers exhibited mainly an austenitic structure, therefore stress-induced martensitic transformation is expected in these interlayers.

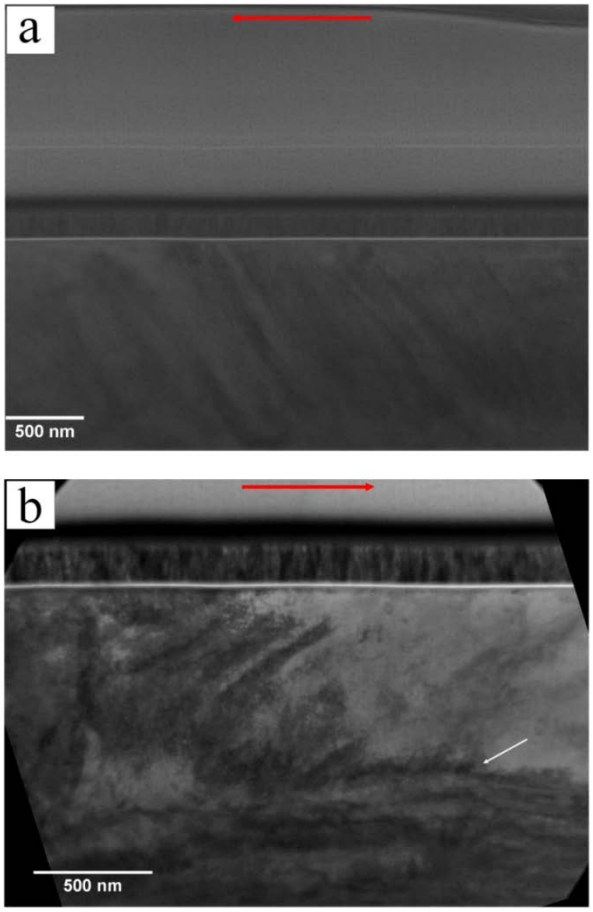

Figure 6.5 – Bright Field TEM cross-sectional images of the W-S-C/Ni-Ti bilayer tested with a normal load of (a) 5 N and (b) 18 N; in (b) the white arrow highlights the boundary between martensitic domains stabilised by shear and those stabilized by compressive stress. Red arrows indicate the sliding direction.

Martensitic bands induced by shear stress are formed mostly away from the interfaces with the substrate and Cr-based bonding layer (Figure 6.5 (a)). At these interfaces the stress-induced phase transformation is inhibited by the constraining effect of the interfaces themselves. The phase transformation in the interlayer takes place without

deforming the interfaces between layers, thus limiting delamination problems eventually generated by out-of-plane (normal to the substrate) stress components. Indeed, the interface between the $Ni_{48.1}Ti_{51.9}$ interlayer and the W-S-C/Cr top layer remained flat and parallel to the substrate during sliding as clearly observed in Figure 6.5 (a). No signs of delamination are found either at the interface with the substrate, where silicide (see appendix B in chapter 5 for further details), contribute at improving the adhesion to the substrate, and with the Cr-based bonding layer.

The average friction coefficient measured for W-S-C/Ni-Ti coating at 5 N is ~ 0.085, which is such that permanent shear deformations (stabilised martensitic bands) in the $Ni_{48.1}Ti_{51.9}$ interlayer were produced. However, understanding at which stage permanent deformation took place in the $Ni_{48.1}Ti_{51.9}$ interlayer was not possible in this study. The running-in stage could be a reasonable candidate, the coefficient of friction ranging between 0.085 – 0.25, thus allowing more shear deformation to be transmitted down toward the substrate.

Figure 6.5 (b) shows the cross-sectional morphology of the W-S-C/Ni-Ti coating tested with a load of 18 N (~ 1 GPa Hertzian pressure). Martensitic bands (darker areas) are still observed in the $Ni_{48.1}Ti_{51.9}$ interlayer, although these bands are in the majority of the cases confined to the upper part of the coating, where shear stress is expected to be higher. In addition, martensitic domains mostly parallel to the interface with the substrate are also found within the $Ni_{48.1}Ti_{51.9}$ interlayer.

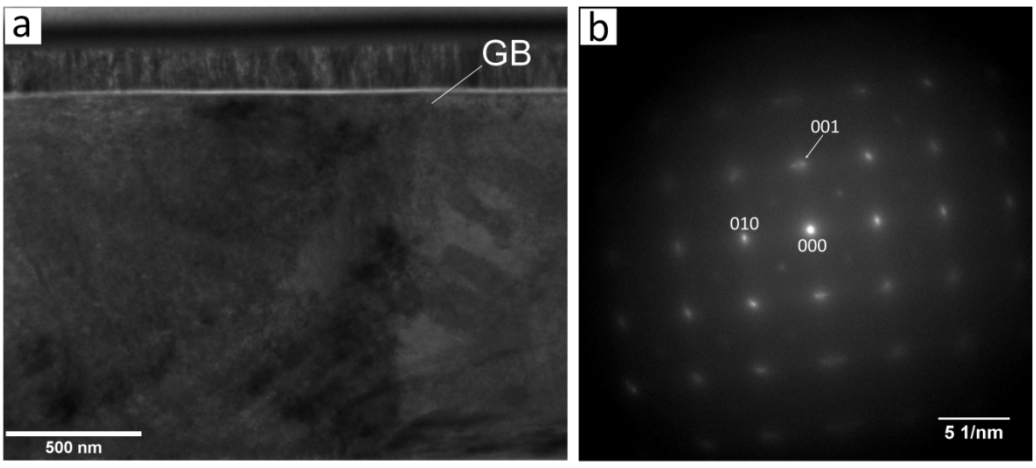

Figure 6.6 – Bright Field TEM image of the W-S-C/Ni-Ti bilayer tested with a normal load of 18 N: (a) microstructure at the grain boundary, (b) Selected Area Electron Diffraction Pattern (SAEDP) acquired in the area close to the grain boundary containing both dark and brighter domains; double spots are attributed to the stress-induced martensitic phase. Electron beam//$[100]_{B2}$.

The presence of stabilised stress-induced martensite close and parallel to the interface with the harder Si substrate (see Figure 6.6 (b)) is mostly attributed to the compressive stress generated underneath the contact area. Contrary to the case shown in Figure 6.5 (a), for a higher load (18 N) the growing martensitic bands from top to bottom are restricted by the stabilised martensite induced by compressive stress (Figure 6.5 (b)). In fact a boundary between these two differently stabilised martensitic domains, as highlighted in Figure 6.5 (b), is clearly observed. Therefore, the deformation induced by compressive stress likely limits the capability of the coating to accommodate shear deformation during sliding.

Interestingly, Figure 6.6 (a) shows how the grain boundaries in the $Ni_{48.1}Ti_{51.9}$ interlayer influence the martensitic transformation. Although shear stress can be transmitted between adjacent grains during sliding, eventually activating the martensitic transformation in the neighbouring grains, we found that the growing martensitic bands are severely obstructed by grain boundaries. Within the grains, martensite nucleates and grows to form parallel bands (particularly visible for a load of 5 N). Close to grain boundaries, a complex scenario is observed, where randomly distributed martensitic domains with a random shape are found together with untransformed austenite. Selected area electron diffraction pattern (SAEDP) acquired in the area containing both the dark bands/domains and bright matrix (Figure 6.6 (a)) shows small diffused spots very close to those generated by the austenitic crystals (Figure 6.6 (b)), and attributed to the stress-induced martensite [14]. On the other hand, SAEDPs acquired on bright areas of the coating (not shown) shows only the cubic structure of the austenitic matrix. These results provide a clear indication of the fact that more energy is required to activate the phase transformation near the grain boundaries; this phenomenon was observed on both sides of the boundary, i.e. regardless of the sliding direction.

The cross-sectional morphology of the W-S-C/Ni-Ti-Cu bilayer after sliding under the same testing conditions as for the W-S-C/Ni-Ti is presented in Figure 6.7. Contrary to the $Ni_{48.1}Ti_{51.9}$ interlayer, no significant evidence of stabilised martensite, caused by sliding or compressive stress, is found in the $Ni_{43.4}Ti_{49.6}Cu_7$ interlayer even for the highest load. $Ni_{43.4}Ti_{49.6}Cu_7$ interlayer absorbed most of the strain energy in a reversible manner by elastic and to some extent pseudo-elastic deformation.

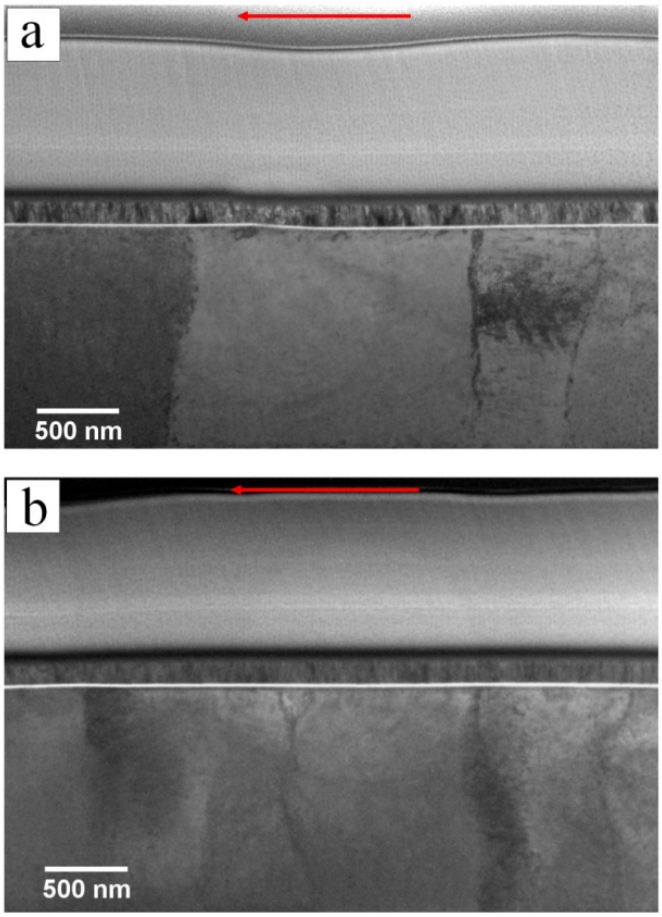

Figure 6.7 – Bright Field TEM cross-sectional images of the W-S-C/Ni-Ti-Cu bilayer tested with a normal load of (a) 5 N and (b) 18 N. Red arrows indicate the sliding direction.

Recently, it has been reported that the phase transformation in Ni-Ti thin films is strongly inhibited for a critical grain size in the range 50 – 100 nm [15]. In our case, grains are larger; nevertheless, we expect that such inhibition occurs gradually with decreasing grain size. In fact, *H. Zhang et al.* [12] found for a Ni-Ti alloy that the stress necessary to activate the austenite-to-martensite transformation ($\sigma^{A\rightarrow M}$) increased linearly as the grain size decreased from 700 to 50 nm; the observed behaviour was attributed to increased grain boundary density. Therefore, differences in the stress-induced martensitic transformation for the films investigated here are expected considering the large difference in grain size.

According to the effects of grain boundaries on the martensitic transformation shown in Figure 6.6, a higher grain boundary density (i.e. smaller grain size) limits the martensitic transformation. In the Cu-doped Ni-Ti thin film, the limited martensitic transformation could be attributed also to other two factors. The first factor (major contribution) is the different nature of the grain boundaries in the $Ni_{43.4}Ti_{49.6}Cu_7$

interlayer compared to the binary $Ni_{48.1}Ti_{51.9}$ layer. As referred to above, Cu addition causes a change in the crystallisation process of the Ni-Ti system resulting in the formation of thick grain boundaries (10 – 20 nm) consisting of Cu-rich precipitates (see chapter 4 for further details). The presence of these precipitates is expected to limit further the activation of the phase transformation in the adjacent grains during sliding.

The second factor limiting martensitic transformation is related to the solid solution substitution of Ni by Cu in the B2 crystal. It was reported that by Cu addition in Ni-Ti alloys the elastic constant c_{44} associated with shear deformation in the B2 crystal increases, thus strengthening the B2 structure against crystal distortions. It makes the martensitic transformation energetically more demanding, i.e. the free energy curve of the native phase moves up [1]. In our previous study (see chapter 5), XRD analyses showed a shift toward lower angles of the B2 (110) peak with increasing Cu content, likely indicating the introduction of Cu into the B2 crystal as solid solution substitution of Ni by Cu atoms [1]. Therefore, the energy required to induce the B2→B19' transformation is expected to be higher for $Ni_{43.4}Ti_{49.6}Cu_7$ interlayer compared to $Ni_{48.1}Ti_{51.9}$.

As a direct consequence of the change in grain size between $Ni_{48.1}Ti_{51.9}$ and $Ni_{43.4}Ti_{49.6}Cu_7$ interlayers, an increase in the anisotropy of the interlayer to accommodate shear and compressive stress is expected. In particular, higher grain boundary distribution density limits the capability of accommodating shear deformation through the martensitic transformation owing to a smaller volume of austenite able to undergo martensitic transformation away from the grain boundaries. Such an anisotropic behaviour is found to have direct consequences on the tribological performance of the W-S-C top layer as will be discussed in the following sections.

6.5 Effects of the interlayer on the performance of W-S-C solid lubricant coating

The friction coefficient, calculated as an average throughout the entire test for different loads and coatings, is shown in Figure 6.4. Increase in load from 1 to 18 N

leads to noticeable decrease in friction coefficient regardless of the coating system (bilayers or single layer). Such behaviour is typical of TMD coatings and suggests the formation of a WS-rich layer (presumably WS_2) on the sliding surface with the basal plane parallel to the sliding direction, i.e. the optimal condition to achieve low friction [13].

Lower friction is observed on the bilayer using the harder interlayer (higher H/E_r ratio, see Table 6.1) at low load (1 N). For higher loads, the average value of the friction coefficient is almost identical for different interlayers. At low load (Figure 6.8 (a)), friction curves are noisy as a result of the polishing process of asperities and surface oxide on the interacting surfaces. $Ni_{48.1}Ti_{51.9}$ interlayer exhibited some wrinkles (see section 2.1.2 in chapter 2) on the surface (martensitic plates nucleated in correspondence of the free surface in the austenitic grains) resulting in an increase in surface roughness of the top W-S-C layer.

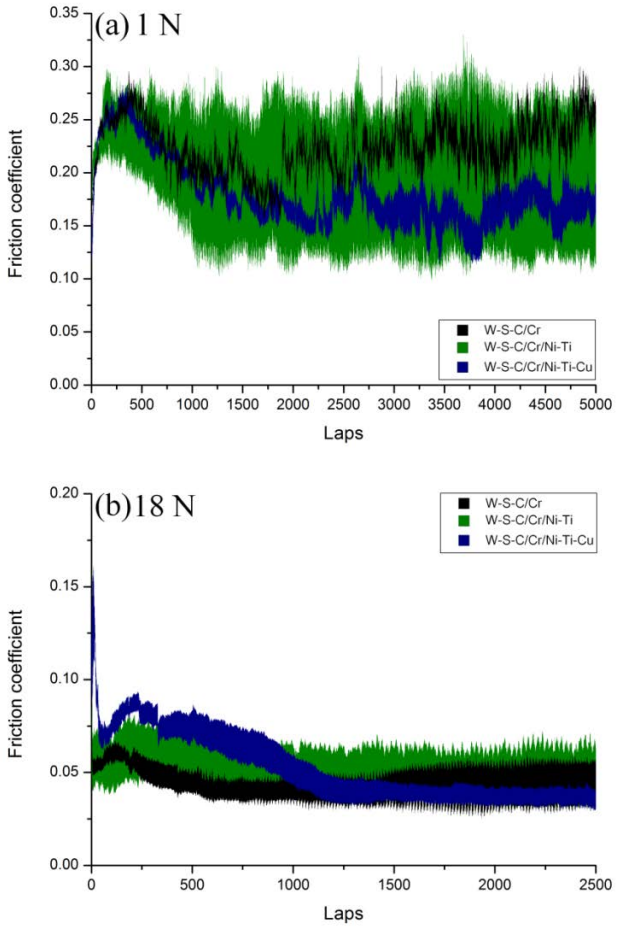

Figure 6.8 – Selected friction curves for W-S-C single layer and W-S-C/Ni-Ti(-Cu) bilayers at a load of (a) 5 N and (b) 18 N.

Much less noisy curves are obtained for W-S-C and, particularly, for the W-S-C/Ni-Ti-Cu coating. The latter exhibits as well lower and stable friction coefficient compared to the increasing friction of W-S-C coating (Figure 6.8 (a)). Higher applied load (18 N, Figure 6.8 (b)) leads to pronounced differences between coating systems in the running-in stage. W-S-C coating shows an initial increase in friction followed by a steady-state regime reached at ~ 600 laps; the W-S-C/Ni-Ti coating shows a more smooth transition from the running-in to the steady-state regime, which takes place also at around 600/700 laps. A rather different behaviour is observed for the W-S-C/Ni-Ti-Cu coating with the running-in stage ending at ~ 1200 laps. On the other hand, more stable and smooth friction coefficient is observed for the W-S-C/Ni-Ti-Cu coating in the steady-state regime compared to the other coatings.

While the W-S-C/Ni-Ti-Cu coating exhibits a similar wear rate for all the testing conditions ($\sim 0.3 \times 10^{-6}\ mm^3/N\ m$), W-S-C/Ni-Ti and W-S-C single layer show similar behaviour with a decrease in average wear rate from $\sim 0.6 \times 10^{-6}\ mm^3/N\ m$ at a load of 1 N to $\sim 0.2 \times 10^{-6}\ mm^3/N\ m$ (for W-S-C/Ni-Ti) and $0.3 \times 10^{-6}\ mm^3/N\ m$ (for W-S-C) at a load of 18 N, as also reported elsewhere [16] for W-S-C coatings. Based on the fact that coatings characterised by a higher H/E_r ratio are expected to exhibit a lower wear rate, the stiffer W-S-C/Cr deposited directly on silicon substrate should exhibit a better wear behaviour. However, the W-S-C single layer exhibits an overall higher wear rate compared to the other coatings. This aspect leads to the conclusion that the presence of the Ni-Ti(-Cu) interlayer plays a role on the tribological behaviour of W-S-C coatings. In fact, the interlayer absorbs and redistributes deformation during sliding due to the stress-induced martensitic transformation, thus mitigating the stress field generated in the functional top layer. Despite the longer running-in stage, the use of a Ni-Ti(-Cu) interlayer prolongs the lifetime of the functional W-S-C top layer and provides a more stable friction coefficient.

Worn surfaces, i.e. the wear tracks and ball wear scars are analysed by optical profilometry and microscopy (Figure 6.9). The wear track of the W-S-C coating (Figure 6.9 (a)) exhibits a rough morphology with several deep scratches (~ 400 nm) along the sliding direction, whereas W-S-C/Ni-Ti coating (Figure 6.9 (b)) exhibits a much smoother morphology and approximately uniform depth (~ 90 nm) across the wear

track width (step-like cross-section) for a load of 18 N. A slightly shallower wear track is observed for the W-S-C/Ni-Ti-Cu coating (Figure 6.9 (c)).

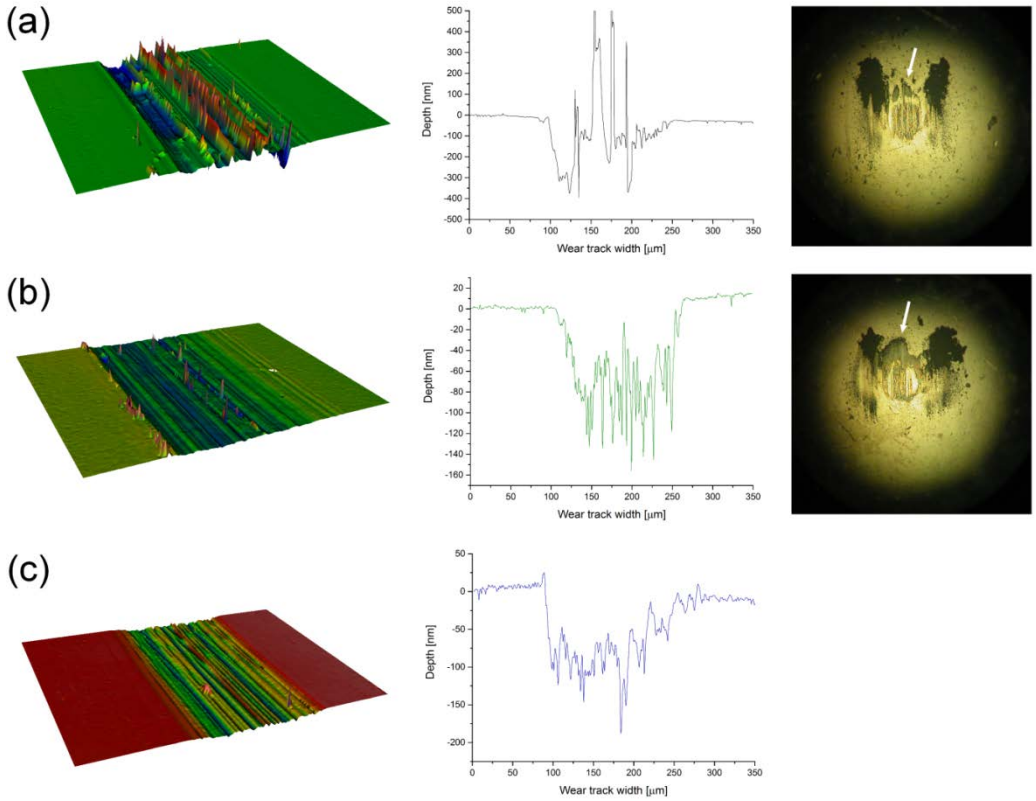

Figure 6.9 – 3D images of the wear tracks produced with a load of 18 N for (a) W-S-C single layer, (b) W-S-C/Ni-Ti and (c) W-S-C/Ni-Ti-Cu, and optical microscopy images of the corresponding counterparts.

Differences are also observed in the counterparts used against the W-S-C/Ni-Ti coating compared to that used for the W-S-C single layer (Figure 6.9). The material accumulated on the sides of the contact area (darker area on the balls in Figure 6.9 (a) and Figure 6.9 (b)) consists mostly of graphitised carbon, whereas a larger amount of W and S is detected in the leading edge and directly in the contact area of the balls [17]. In particular, by comparing Figure 6.9 (a) and Figure 6.9 (b), it is seen as a more homogeneous distribution of the transfer layer on a larger area is formed on the ball, when it is used against the W-S-C/Ni-Ti bilayer. Since EDX measurements performed on the unworn surface and in wear tracks did not reveal any significant difference in S/W chemical composition ratio, the tribolayer should be very thin (if it exists). Therefore, the changes in chemistry on the surface of the wear tracks are studied by more sensitive Raman spectroscopy. Figure 6.10 (a) shows the Raman spectra acquired for

the W-S-C/Ni-Ti coating in the centre of the wear tracks produced with different loads, and on the unworn surface as reference.

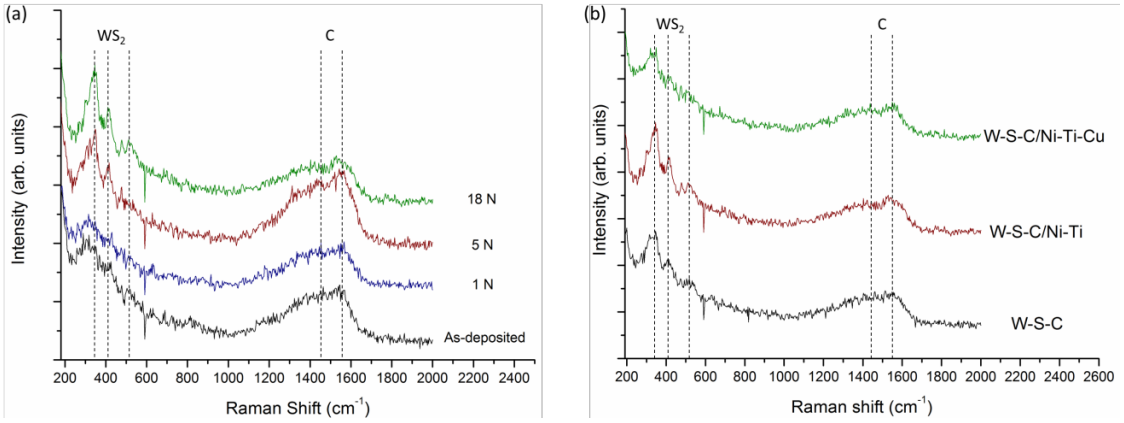

Figure 6.10 – Raman spectroscopy analyses: (a) Raman spectra acquired on the as-deposited and tested W-S-C/Ni-Ti bilayer, (b) Raman spectra acquired on the wear tracks produced by a load of 18 N on W-S-C single layer and W-S-C/Ni-Ti(-Cu) bilayers.

Two or in certain cases three peaks at about 345, 410 and 510 cm^{-1} are identified and associated to the WS_2 phase, while two peaks related to carbon (D and G bands) are found at about 1420 and 1540 cm^{-1}. It is apparent that with increasing applied load the peaks associated to the WS_2 phase become more prominent in comparison with the carbon peaks. The A_C/A_{WS2} ratio, i.e. area of the WS_2 peaks divided by area of carbon peaks, decreases with increasing load from ~ 3.8 in the as-deposited sample to ~ 1.4 in the sample tested with a load of 18 N. It is the typical behaviour observed for W-S-C coatings [16], which indicates the formation of a WS_2-rich layer in the wear track. Interestingly, noticeable differences are observed in the Raman spectra acquired in the wear track of different samples tested with the same load, see Figure 6.10 (b). A significantly larger area (approx. 35 %) of the peaks associated to WS_2 is found for the W-S-C/Ni-Ti compared to the other coatings. This observation suggests that interlayers could affect the thickness of the WS_2-rich transfer layer formed during sliding. Nevertheless, the thickness of tribolayer is in all cases sufficient to provide low friction as documented in Figure 6.4.

6.6 Deformation of the W-S-C functional layer

Different capability of $Ni_{48.1}Ti_{51.9}$ and $Ni_{43.4}Ti_{49.6}Cu_7$ interlayers to store strain energy through the martensitic transformation leads to various microstructural changes of the W-S-C top layer. As-deposited W-S-C layer exhibited a columnar structure with columns tilted by about 9° (Figure 6.2). After sliding the same features are preserved in the W-S-C/Ni-Ti bilayer. On the other hand, significant tilt (∼ 16° at 5 N and ∼ 20° at 18 N) of the columns is observed in the W-S-C coating deposited on top of the $Ni_{43.4}Ti_{49.6}Cu_7$ layer (Figure 6.7). This is a clear consequence of the lower capability of $Ni_{43.4}Ti_{49.6}Cu_7$ to accommodate shear strain compared to the $Ni_{48.1}Ti_{51.9}$. Consequently, a larger amount of shear deformation is absorbed by the W-S-C top layer when it is deposited on the $Ni_{43.4}Ti_{49.6}Cu_7$ interlayer.

Although no large differences are observed in terms of average friction coefficient (Figure 6.4), a careful inspection of the friction curves (Figure 6.8) reveals a different frictional behaviour of the coatings. Low applied load is apparently not sufficient to produce a prominent WS_2-rich tribolayer, as the friction coefficient is relatively high (see Figure 6.8 (a)). Therefore, the slight difference in friction (most notably between W-S-C single layer and W-S-C/Ni-Ti-Cu) should be attributed to varying surface roughness and the presence of wear debris; the intrinsic role of the interlayer should be minimal for low contact pressures.

At a load of 18 N pronounced variations in frictional behaviour (see Figure 6.8 (b)) are found. The running-in stage lasts about 600/700 laps for W-S-C/Ni-Ti and W-S-C single layer. Due to the large amount of stabilised martensite in the $Ni_{48.1}Ti_{51.9}$ interlayer (Figure 6.5 and Figure 6.6), the functional behaviour (superelasticity) of the $Ni_{48.1}Ti_{51.9}$ interlayer progressively degrades resulting in a similar frictional behaviour as that observed for the W-S-C single layer. On the contrary, the $Ni_{43.4}Ti_{49.6}Cu_7$ interlayer exhibits mostly an elastic and/or pseudo-elastic behaviour. The corresponding friction curve (Figure 6.8) exhibits a longer running-in stage (about 1200 laps) for the W-S-C/Ni-Ti-Cu, thus indicating delayed formation of the WS_2-rich tribolayer.

Based on the experimental evidence [18, 19], friction coefficient and consequently the formation of the WS_2-rich tribolayer are strongly affected by the contact pressure. It has been observed that the combination of shear and compressive stress generated

during sliding allows the "coalescence" of WS_2-rich domains on the sliding surfaces, while the worn carbon is accumulated on the lateral side of the pin (see Figure 6.9) and on the sides of the wear track. In other words, carbon is not an active element during sliding [20]. Shear stress promotes as well the alignment of the basal plane of WS_2 tribolayer parallel to the coating surface; such orientation is optimal to achieve low friction and high oxidation resistance [18].

The $Ni_{43.4}Ti_{49.6}Cu_7$ interlayer accommodates compressive deformation in a reversible manner during the entire test (no significant evidence of plastic deformation and/or stabilized martensite), whereas the $Ni_{48.1}Ti_{51.9}$ interlayer undergoes phase transformation followed by plastic deformation, which stabilises martensite. However, the $Ni_{48.1}Ti_{51.9}$ interlayer accommodates a larger amount of shear stress compared to $Ni_{43.4}Ti_{49.6}Cu_7$, which is evidenced by the negligible tilting of the columns in the functional W-S-C layer under different loading conditions.

Increase in load leads to lower friction (see Figure 6.4); therefore, the shear-to-compressive stress ratio decreases significantly when higher loads are applied. However, by using different interlayers further changes in the shear-to-compressive stress ratio in the W-S-C top layer are expected.

Based on the mechanical response of the Ni-Ti(-Cu) layers and on the effects of grain size on the stress-induced martensitic transformation discussed previously, $Ni_{43.4}Ti_{49.6}Cu_7$ interlayer leads to high shear stress and low compressive stress at the W-S-C coating surface. High shear results in coating deformation (column tilt); however, low compressive stress delays the formation of low friction WS_2-rich tribolayer (longer running-in stage). In the case of the $Ni_{48.1}Ti_{51.9}$ interlayer a different scenario is observed, i.e. high compressive stress and low shear stress at the W-S-C surface. It results in accelerated WS_2-rich tribolayer formation (shortened running-in stage) and further reduction of shear stress component (due to decrease of friction force); therefore, the columns in W-S-C coating are not tilted after the sliding process (less deformation) even under high load. It is worth noting that W-S-C coating without Ni-Ti(-Cu) interlayer produces a low-friction tribolayer almost immediately due to high stresses on the top surface. However, such high stresses lead to progressive wear of the film and loss of the required wear resistance.

References

[1] K. Otzuka and X. Ren, "Physical metallurgy of Ti–Ni-based shape memory alloys," *Progress in Materials Science,* no. 50, pp. 511-678, 2005.

[2] S. Miyazaki and A. Ishida, "Martensitic transformation and shape memory behavior in sputter-deposited TiNi-base thin films," *Materials Science and Engineering: A,* Vols. 273-275, pp. 106-133, 1999.

[3] J. X. Zhang, M. Sato and A. Ishida, "Influence of Guinier-Preston zones on deformation in Ti-rich Ti-Ni thin films," *Philosophical Magazine Letters,* vol. 82, no. 5, pp. 257-264, 2002.

[4] J. X. Zhang, M. Sato and A. Ishida, "On the Ti2Ni precipitates and Guinier–Preston zones in Ti-rich Ti–Ni thin films," *Acta Materialia,* vol. 51, no. 11, pp. 3121-3130, 2003.

[5] T. Kikuchi, K. Ogawa and S. Kajiwara, "Strengthening of Ti-Ni shape-memory films by coherent subnanometric plate precipitates," *Philosophical Magazine Letters,* vol. 74, no. 3, pp. 137-144, 1996.

[6] A. Ishida, M. Sato and K. Ogawa, "Microstructure of annealed Ti48.5Ni(51.5– x)Cu x (x = 6.2–33.5) thin films," *Philosophical Magazine,* vol. 88, no. 16, pp. 2427-2438, 2008.

[7] J. V. Pimentel, M. Danek, T. Polcar and A. Cavaleiro, "Effect of rough surface patterning on the tribology of W–S–C–Cr self-lubricant coatings," *Tribology International,* vol. 69, pp. 77-83, 2014.

[8] J. Sundberg, H. Nyberg, E. Sarhammar, F. Gustavsson, T. Kubart, T. Nyberg, S. Jacobson and U. Jansson, "Influence of Ti addition on the structure and properties of low-friction W–S–C coatings," *Surface and Coatings Technology,* vol. 232, pp. 340-348, 2013.

[9] "http://www.xpsfitting.com," [Online]. [Accessed 02 03 2014].

[10] J. Sundberg, R. Lindblad, M. Gorgoi, H. Rensmo, U. Jansson and A. Lindblad, "Understanding the effects of sputter damage in W–S thin films by HAXPES," *Applied Surface Science,* vol. 305, pp. 203-213, 2014.

[11] R. Whitby, W. K. Hsu, C. B. Boothroyd, H. W. Kroto and D. R. M. Walton, "Tungsten disulphide coated multi-walled carbon nanotubes," *Chemical Physics Letters,* vol. 359, no. 1-2, pp. 121-126, 2002.

[12] H. Zhang, X. Li and X. Zhang, "Grain-size-dependent martensitic transformation in bulk nanocrystalline TiNi under tensile deformation," *Journal of Alloys and Compounds,* vol. 544, pp. 19-23, 2012.

[13] T. Polcar and A. Cavaleiro, "Self-adaptive low friction coatings based on transition metal dichalcogenides," *Thin Solid Films,* vol. 519, no. 12, pp. 4037-4044, 2011.

[14] X. L. Meng, M. Sato and A. Ishida, “Structure of martensite in sputter-deposited (Ni,Cu)-rich Ti–Ni–Cu thin films containing Ti(Ni,Cu)2 precipitates,” *Acta Materialia,* vol. 57, no. 5, pp. 1525-1535, 2009.

[15] M. Kabla, H. Seiner, M. Musilova, M. Landa and D. Shilo, “The relationships between sputter deposition conditions, grain size, and phase transformation temperatures in NiTi thin films,” *Acta Materialia,* vol. 70, pp. 79-91, 2014.

[16] J. V. Pimentel, T. Polcar, M. Evaristo and A. Cavaleiro, “Examination of the tribolayer formation of a self-lubricant W–S–C sputtered coating,” *Tribology International,* vol. 47, pp. 188-193, 2012.

[17] T. Polcar, F. Gustavsson, T. Thersleff, S. Jacobson and A. Cavaleiro, “Complex frictional analysis of self-lubricant W-S-C/Cr coating,” *Faraday Discussion,* pp. 156:383-401; Discussion 413-34, 2012.

[18] T. Polcar and A. Cavaleiro, “Review on self-lubricant transition metal dichalcogenide nanocomposite coatings alloyed with carbon,” *Surface and Coatings Technology,* vol. 206, no. 4, pp. 686-695, 2011.

[19] T. Polcar, M. Evaristo and A. Cavaleiro, “Friction of Self-Lubricating W-S-C Sputtered Coatings Sliding Under Increasing Load,” *Plasma Processes and Polymers ,* vol. 4, no. S1, pp. s541-s546, 2007.

[20] T. Polcar, M. Evaristo, R. Colaco, C. S. Sandu and A. Cavaleiro, “Nanoscale triboactivity: The response of Mo–Se–C coatings to sliding,” *Acta Materialia,* vol. 56, no. 18, pp. 5101-5111, 2008.

Chapter 7 Conclusions and Future work

1. Conclusions

In this study Ni-Ti(-Cu) thin films have been fabricated and characterised by several experimental techniques with the aim of investigating the effects of chemical composition and fabrication process on the microstructural and mechanical properties of the films. Furthermore, novel tribological bilayer coatings combining the properties of W-S-C self-lubricant and Ni-Ti(-Cu) layers have been fabricated and characterised from microstructural, mechanical and tribological points of view. This chapter presents the main conclusions from this study.

- The effects of copper and of annealing temperature on the microstructural and mechanical properties of sputter-deposited Ni-Ti thin films have been investigated and the main results are as follows:
  - In Ni-Ti thin films the stability of parent and native phases is affected by the annealing temperature. With increasing annealing temperature the formation of Ti_2Ni metastable precipitates in the grain interior becomes prominent, thus changing the chemical composition of the matrix with consequent increase in transformation temperatures.
  - Films annealed at 500°C and doped with an increasing amount of Cu exhibited a slow phase transition from being primarily austenitic for low Cu content, to being a mixture of martensite and austenite at ambient temperature for high Cu content. The same films annealed at 600°C all exhibited a dominant martensitic structure at ambient temperature; therefore solute atoms had segregated to grain boundaries and in the grain

interior as precipitates, while the formation of martensite was caused by the solid solution of a larger amount of Cu in the Ni-Ti matrix.

- Ni-Ti-Cu thin films exhibited a columnar structure extending through the layer thickness, while the lateral grain size resulted strongly affected by the Cu content. In particular the grain refinement was attributed to the segregation of solute atoms (Cu and Ni) to the grain boundaries. Grain growth took place following a competitive growth mechanism underneath the film surface, which intensified with increasing Cu content.
- Cu-doped Ni-Ti thin films annealed at 500°C exhibited a nanostructure consisting of homogeneously distributed $Ti(Ni, Cu)_2$ plate precipitates embedded in a B2 matrix. Due to interfacial lattice misfit, a strain field is generated in the B2 matrix around plate precipitates. A larger strain field was observed in the surrounding B2 matrix when plate precipitates cross each other to form cage-like structures.
- Grain size resulted unaffected by the annealing temperature, while $Ti(Ni, Cu)_2$ plate precipitates evolved with annealing temperature and Cu content. In fact, it was found that with increasing Cu content these plate precipitates become more finely and densely distributed in the grain interior. On the other hand, plate precipitates coarsened for higher annealing temperature and their density distribution in the grain interior decreased.
- The nano-hardness increased with increasing Cu content owing to the grain refinement observed, although hardness saturation was found for Cu content $>$ 13 at.% regardless of the annealing temperature. This behaviour was attributed to grain boundaries, which, for decreasing grain size, become a weak point where stress can be relaxed.
- For high Cu content ($>$ 13 at.%), films annealed at both 500 and 600°C exhibited mostly a martensitic structure and despite the similar grain size, a significant difference in hardness was observed. Such a difference was attributed to the microstructural evolution of $Ti(Ni, Cu)_2$ plate precipitates in relation to Cu content and annealing temperature. Finely and densely distributed plate precipitates with a coherent interface with the matrix

formed at 500°C were thought to produce a higher strengthening effect of the B2 matrix compared to coarsened and semi-coherent plate precipitates.

- The mechanism of grain refinement in Cu-doped Ni-Ti thin films has been investigated and a simple model describing the crystallisation process resulting in the grain refined structure proposed. The observed grain refinement, which became prominent with increasing Cu content, was attributed to a non-polymorphic crystallisation process caused by Cu addition. In such a crystallisation process, diffusion of solute atoms (mostly Cu and Ni) across a transition volume covering the growing crystal (shell-like structure) followed by grain growth played the major role in the observed grain refinement.

- Ni-Ti(-Cu) layers have been integrated into a novel W-S-C/Ni-Ti(-Cu) tribological system, whose mechanical properties, measured by nanoindentation and nano-scratch test, have been investigated and correlated. The key results are summarised as follows:
  - Calculation of mechanical parameters such as the H/E_r and H^3/E_r^2 ratio suggested that films with a Cu content $<$ 7 at.% (lower H/E_r and H^3/Er^2 ratio) are able to dissipate more energy, i.e. accommodate larger deformation resulting from the sum of elastic, pseudo-elastic and plastic deformation, and thus provide more protection of the substrate against plastic deformation.
  - The response of the W-S-C/Ni-Ti(-Cu) bilayers, with Cu content ranging between 0 – 10 at.%, to nanoindentation resulted affected by the interlayer material. In particular the composite hardness showed a decreasing trend with penetration depth and different hardness values were measured at specific depths, accordingly to the hardness of the Ni-Ti(-Cu) interlayers.
  - Nano-scratch tests performed on the W-S-C/Ni-Ti(-Cu) bilayers showed that improvements to the resistance to adhesive damage of W-S-C coatings can be achieved by using a Ni-Ti(-Cu) interlayer. However, differences in the nano-scratch behaviour of W-S-C/Ni-Ti(-Cu) bilayers have been observed in relation to the mechanical properties of the interlayer. In particular, Ni-Ti(-Cu) interlayers with lower mechanical properties such as: hardness and H/E_r

ratio, which are affected by the grain size (i.e. Cu content), exhibited an improved capability to increase the resistance against adhesive damage of the W-S-C coating. Particularly, a critical load for delamination about 33% higher than that measured for W-S-C single layer was found for W-S-C/$Ni_{48.1}Ti_{51.9}$. Before adhesive failure of the bilayers no damage was observed on the W-S-C layer, which suggested that the use of a Ni-Ti(-Cu) interlayer should not affect the functional properties of the top layer.

- The differences observed in nano-scratch behaviour of bilayer coatings were attributed to the grain size of the Ni-Ti(-Cu) interlayers. Grain size represents an important parameter that affects the energy required to activate the stress-induced martensitic transformation and consequently the amount of deformation that can be accommodated in a reversible manner. Based on the results presented, a Ni-Ti-Cu interlayer with a grain size ranging between 0.5 – 1 µm represents a good compromise between resistance to adhesive damage and strain recovery.

❖ The tribological performance of a W-S-C single layer and of some W-S-C/Ni-Ti(-Cu) bilayers coatings have been investigated by sliding tests carried out in humid air. The resulting properties were correlated with the chemical and microstructural changes induced by stress on the sliding surfaces and on the bilayers microstructure. The main outcomes are summarised as follows:

- The grain size was found to affect significantly the deformation behaviour of the Ni-Ti(-Cu) interlayer in W-S-C/Ni-Ti(-Cu) bilayers subjected to different sliding conditions. In the W-S-C/$Ni_{48.1}Ti_{51.9}$ bilayer tested, ordered and well oriented, with respect to the sliding direction, stabilised martensitic bands were formed during sliding at a load of 5 N. A more complex deformation was observed at a higher load (18 N), where martensitic bands were also stabilised by compressive stress. The formation of these bands close to the interface with the substrate limited the growth of martensitic bands caused by shear stress, thus limiting the overall shear deformation accommodated by the $Ni_{48.1}Ti_{51.9}$ layer.

On the other hand, the W-S-C/$Ni_{43.4}Ti_{49.6}Cu_7$ bilayer tested did not show any significant amount of stabilised martensite, regardless of the load. It is suggested that most of the deformation was, in this case, accommodated by elastic deformation of the austenitic matrix and, to some extent, reversibly by the stress-induced phase transformation.

- The growth of martensitic bands driven by shear stress was severely obstructed by grain boundaries. In fact close to the grain boundaries, a complex scenario was observed, where randomly distributed martensitic domains with a random shape were found together with untransformed austenite. These results provided a clear indication of the fact that more energy is required to activate the phase transformation near the grain boundaries. The different deformation mechanisms observed in the W-S-C/Ni-Ti(-Cu) bilayers tested were attributed mostly to the difference in grain boundary density between the $Ni_{48.1}Ti_{51.9}$ and $Ni_{43.4}Ti_{49.6}Cu_7$ interlayers.
- W-S-C single layer and W-S-C/Ni-Ti(-Cu) bilayers exhibited a similar and decreasing friction coefficient with increasing load, thus suggesting that the use of a Ni-Ti(-Cu) interlayer did not change the typical non-Amonton behaviour of TMD coatings. At the same time, the use of a Ni-Ti(-Cu) interlayer lowered the wear rate of the W-S-C top layer and much less damage was observed on the W-S-C surface during sliding, thus allowing, especially in the case of W-S-C/$Ni_{43.4}Ti_{49.6}Cu_7$, a stable and low friction coefficient to be achieved in the steady-state regime compared to the W-S-C single layer.
- The deformation of the functional W-S-C top layer was found to be affected by the interlayer. This difference was attributed to the capability of the interlayer itself to mitigate shear and compressive stress on the top functional layer during sliding. Based on this property different stress levels were produced on the top layer. In the case of W-S-C/$Ni_{43.4}Ti_{49.6}Cu_7$, owing to the capability of $Ni_{43.4}Ti_{49.6}Cu_7$ to accommodate compressive stress in a reversible manner, but with limited capability to accommodate shear stress, delayed tribolayer formation and consequently more shear deformation on the W-S-C top layer was observed. Conversely, for W-S-C/$Ni_{48.1}Ti_{51.9}$ owing

to the better capability of $Ni_{48.1}Ti_{51.9}$ to accommodate shear stress but not compressive stress due to the large amount of stabilised martensite formed during sliding, the low shear tribolayer was almost immediately formed and consequently no appreciable shear deformation was observed in the W-S-C layer.

2. Suggestions for future work

The mechanical and microstructural investigations performed in this study have highlighted several interesting aspects that warrant further study.

Ni-Ti-Cu films with a Cu content higher than 13 at.% and annealed at 500 and 600°C exhibited mostly a martensitic structure at ambient temperature. The response of these Ni-Ti-Cu films to nanoindentation resulted affected by the microstructural evolution of $Ti(Ni, Cu)_2$ plate precipitates, formed in the grain interior, in relation to the annealing temperature (chapter 3). It is of great interest to the scientific community working on shape memory alloy thin films to understand how the stress-induced martensitic transformation in Ni-Ti(-Cu) films is affected by the nature of these plate precipitates and in particular at their interface with the B2 matrix. This could be studied by investigating the microstructure, with particular regard to the interaction between the growing (stress-induced) martensite variants and the plate precipitates, of the films annealed at different temperatures and tested by nanoindentation. Particular attention should be paid to the deformation mechanism of the matrix/precipitate interface when the martensitic plates grow across the interface produced at different annealing temperatures.

The matrix/precipitate interface is likely affected not only by the annealing temperature but also by the Cu content, i.e. a high Cu content changes the lattice parameter of $Ti(Ni, Cu)_2$ precipitates and thus the lattice misfit at the matrix/precipitate interface; therefore a microstructural investigation should also be aimed at understanding how the lattice misfit at the interface mentioned above affects the martensitic transformation. Such an investigation can be carried out by fabricating

TEM samples by means of FIB facilities in the indented area of the sample and subsequently performing HR-TEM studies underneath the indented surface.

Another interesting microstructural aspect is related to the effects of the Ti(Ni, Cu)$_2$ plate precipitate distribution on the reversible stress-induced martensitic transformation. As shown in chapter 3 and also in Figure I (a), plate precipitates can be both spaced and cross each other in the B2 matrix. A much more complex scenario was observed (chapter 3) owing to the larger strain field generated by crossing plates on the surrounding B2 structure. Therefore, more energy is expected to be required to drive the martensitic transformation through crossed plates. It is interesting to quantify and compare the strain field around the two different precipitate distributions and understand how the stress-induced martensitic transformation proceeds especially when through crossing precipitates. Quantitative analysis of the strain field around the precipitates may require the development of a code to quantify the strain field from Fourier-filtered HR-TEM images.

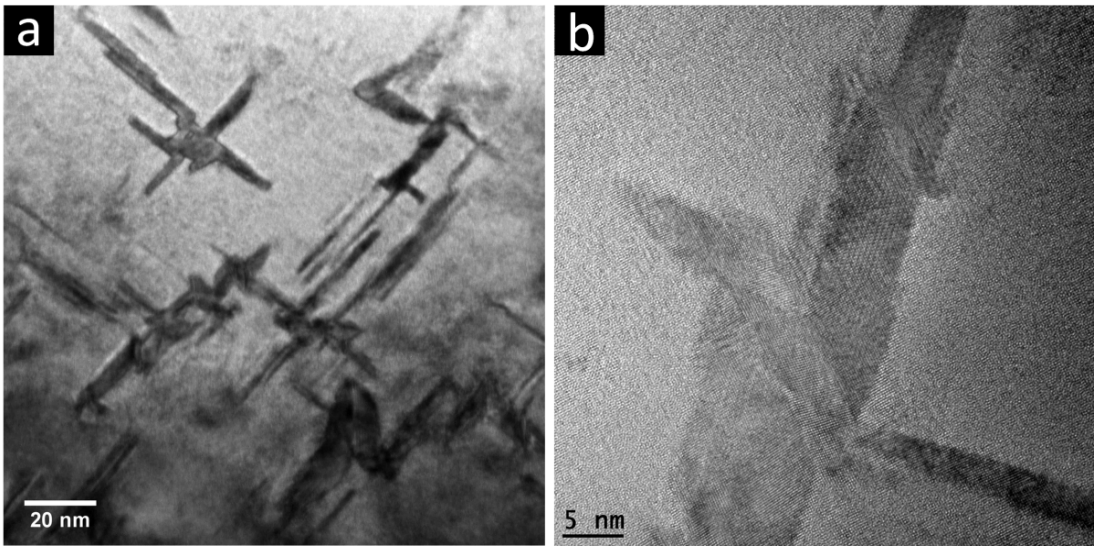

Figure I – Preliminary microstructural investigation on $Ni_{48.7}Ti_{47.2}Cu_{4.1}$ thin film annealed for 1 h at 500°C: (a) Bright Field TEM image of several precipitates formed in the B2 matrix, (b) High resolution TEM image of some of the crossing plate precipitates surrounded by a different phase into the B2 matrix.

The other aspect of relevant interest is related to the effects of the Ti(Ni, Cu)$_2$ plate precipitates, in terms of chemical composition and strain field generated around plate precipitates, on the phase stability (parent and native phases) in the surrounding matrix. In view of the strong dependency of the transformation temperatures on the

chemical composition, the formation of (Ni, Cu)-rich Ni-Ti-Cu precipitates may generate a gradient in chemical composition around precipitates. Such a gradient changes locally the composition of the matrix with a consequent change in transformation temperatures in the surrounding matrix. Similarly, a strain field can complicate/facilitate the martensitic transformation as well as shifting the transformation temperatures based on the Clausius-Clapeyron relationship.

Preliminary TEM and HR-TEM analyses on annealed and untested Ni-Ti-Cu samples showed interesting microstructural features surrounding the plate precipitates – darker domains in Figure I (a), which might be attributed to both stress-induced martensite or martensitic domains formed as a consequence of local change in chemical composition. An *in-situ* TEM study of the formation of $Ti(Ni, Cu)_2$ precipitates during annealing would help at understanding the formation of these precipitates as well as the direct consequence of their formation on the B2 surrounding matrix. A crystallographic analysis of the microstructure surrounding the precipitates (see Figure I (b)) might also help at understanding the formation of the observed features, while high resolution chemical mapping might shed light eventually on chemical composition gradients around the precipitates.

Lack of knowledge on the effects of Cu on the kinetic of crystallisation of Ni-Ti thin films persists in the literature. In this study, experimental evidence on the effects of Cu on fully crystalline Ni-Ti-Cu films has been given and a model on the crystallisation process taking place in Cu-doped Ni-Ti films has been proposed (see chapter 4). The natural extension of this study is to provide experimental evidence on the crystallisation process of Cu-doped Ni-Ti films. Particular interest should be directed to the crystal/amorphous interface during grain growth, where the effects of solute atoms, i.e. mostly copper, are thought to play a major role on the observed grain refinement. In order to highlight the effects of Cu content, films doped with different amounts of Cu should be investigated and compared to off-stoichiometric binary systems, i.e. Ti-rich and/or Ni-rich Ni-Ti. Such a type of investigation has to be performed by *in-situ* TEM experiments, where the use of a special sample holder can allow annealing into the TEM column as well as high resolution analyses (imaging and chemical mapping). This type of investigation has already received funding in the

transnational access to world-leading facilities programme from the European Union Seventh Framework Programme under a contract for an Integrated Infrastructure Initiative (Reference 312483-ESTEEM2). This study will be performed at the National Centre for High Resolution Electron Microscopy at the Delft University of Technology (The Netherlands) in 2015.

Ni-Ti(-Cu) interlayers have been shown to be capable of improving the resistance against adhesive damage and the tribological performance of low-friction W-S-C coatings (see chapter 5 and chapter 6). It is of interest to understand more in depth the stress-induced martensitic transformation that took place under sliding, particularly around the stress-induced martensitic bands and then on the overall deformation of the Ni-Ti(-Cu) interlayer. It was found (chapter 6) that during sliding the interfaces of the Ni-Ti(-Cu) layer with substrate and W-S-C top layer remained flat and parallel to the substrate surface. Therefore, as the habit plane between austenite and martensite has to be a macroscopically unrotated and undistorted plane, in order to maintain flat interfaces a sort of self-accommodating mechanism had to take place in the Ni-Ti(-Cu) structure when martensitic bands have formed.
It is also of interest to deepen the investigation regarding the effects of different Ni-Ti(-Cu) interlayers on the tribological properties of W-S-C coatings, with particular regard to the formation of the WS-rich tribolayer on the W-S-C sliding surface. This would involve HR-TEM investigations on a nanoscale of the sliding surface on W-S-C/Ni-Ti(-Cu) bilayers tested under different loading conditions. This study requires the fabrication of very thin TEM samples by FIB facilities in the wear tracks. It is also interesting to shed light on the formation process of such a tribolayer when different interlayers are used. This implies microstructural investigations on sliding surfaces produced with the same load but different sliding distances.

Based on the capability of Ni-Ti(-Cu) interlayers to absorb energy through the stress-induced martensitic transformation, a quantitative and comparative analysis between different interlayers integrated in W-S-C/Ni-Ti(-Cu) bilayer coatings can be performed by nano-impact tests utilising the impact/fatigue module, with which the Nanoindenter Vantage 4 used in this study is equipped with.

This facility uses a solenoid to accelerate rapidly the impact probe (any type of tip) over a precisely chosen distance to impact the surface at a very high strain rate with a specific applied load. The test can be performed in two different modes, i.e. single and repetitive impacts and materials properties such as: energy absorption, crack resistance, work hardening, dynamic hardness and low cycle fatigue behaviour can be characterised.

These types of tests should help us to understand further and quantify the capability of the Ni-Ti(-Cu) interlayers to absorb energy during abrupt contacts, thus proving the capability of these interlayers to relax also high stress concentrations on the top functional layer. Useful information on the capability of the interlayer to change the fracture toughness of the top functional layer may also be extrapolated.

It is of interest to extend the investigation presented in this study to different types of tribological coatings. Bilayer coatings with W-doped DLC as the functional top layer and Ni-Ti(-Cu) interlayers have already been fabricated and will be tested (mechanical and tribological tests) following an experimental procedure similar to that used in this study, and thus different coatings will be compared.

Publications

The scientific achievements obtained in this study have been disseminated through the following publications and conferences. Some collaborative works are also reported.

Publications related to the thesis:

[1] M. Callisti, F. D. Tichelaar, B. G. Mellor, T. Polcar, "*Effects of Cu on the microstructural and mechanical properties of sputter deposited Ni-Ti thin films*", Surface & Coating Technology 237 (2013) 261-268.

[2] M. Callisti, B. G. Mellor, T. Polcar, *"Microstructural investigation on the grain refinement occurring in Cu-doped Ni-Ti thin films"*, Scripta Materialia 77 (2014) 52-55.

[3] M. Callisti, T. Polcar, *"The role of Ni-Ti(-Cu) superelastic interlayers on the mechanical properties and scratch resistance of solid lubricant W-S-C coatings"*, Surface & Coating Technology 254 (2014), 260-269.

[4] M. Callisti, T. Polcar, *"Stress-induced martensitic transformation in Ni-Ti(-Cu) interlayers controlling stress distribution in functional coatings during sliding"*, accepted in Applied Surface Science.

Other collaborative work:

[1] M.A. Monclus, M. Karlik, M. Callisti, E. Frutos, J. Llorca, T. Polcar, J. M. Molina-Aldareguia, "*Microstructure and mechanical properties of physical vapor deposited Cu/W nanoscale multilayers: Influence of layer thickness and temperature"*, Thin Solid Films, DOI: 10.1016/j.tsf.2014.05.044.

Conferences (oral/poster presentations)

Presentations related to the thesis:

[1] M. Callisti, B.G. Mellor, T. Polcar, "*Effects of Cu on the microstructural and surface properties of sputter-deposited Ni-Ti shape memory thin films*", 1st Engineering Science PG Conference, November 2012. (Oral presentation).

[2] M. Callisti, F. D. Tichelaar, B. G. Mellor, T. Polcar, "*Effects of Cu on the microstructural and mechanical properties of sputter deposited Ni-Ti thin films*", 40th International Conference on Metallurgical Coatings and Thin Films, April 29th – May 3rd, 2013, San Diego, California (CA). (Oral presentation).

[3] M. Callisti, B. G. Mellor, T. Polcar, "*Effects of Cu and of annealing temperature on the microstructural and mechanical properties of sputter deposited Ni-Ti thin films*", Shape Memory and Superelastic Technologies, May 20-24, 2013, Prague, Czech Republic. (Poster presentation).

[4] M. Callisti, F. D. Tichelaar, B. G. Mellor, T. Polcar, "*Effects of Cu on the microstructural and mechanical properties of sputter deposited Ni-Ti thin films*", EUROMAT 2013, September 8-13, Seville 2013, Spain. (Oral presentation).

[5] M. Callisti, B.G. Mellor, T. Polcar, "*The role of a superelastic interlayer on the tribological behaviour of hard coatings: W-S-C/Ni-Ti(-Cu) as case study*", 41st International Conference on Metallurgical Coatings and Thin Films, April 28th – May 2nd, 2013, San Diego, California (CA). (Oral presentation).

[6] M. Callisti, B.G. Mellor, T. Polcar, "*Ni-Ti-Cu superelastic interlayers supporting low-friction W-S-C coatings*", 14th International Conference on Plasma Surface Engineering, September 15 – 19, 2014, Garmish-Partenkirchen, Germany. (Poster presentation).

Other collaborative work:

[1] Emilio Frutos Torres, Mauro Callisti, Miroslav Karlik, Tomas Polcar, "*Incoherent Interface Effect in the Mechanical Properties of Cu/W and Zr/Nb Nanomultilayers*", 41st International Conference on Metallurgical Coatings and Thin Films, April 28th – May 2nd, 2013, San Diego, California (CA). (Oral presentation).

[2] Emilio Frutos Torres, Mauro Callisti, Miroslav Karlik, Tomas Polcar, "*Size-dependent deformation mechanisms and strain-rate sensitivity in irradiated nanostructured metallic multilayers Cu/W coatings*", 14th International Conference on Plasma Surface Engineering, September 15 – 19, 2014, Garmish-Partenkirchen, Germany. (Poster presentation).